

European Federation of
Corrosion Publications
Number 41

Corrosion by carbon and nitrogen

Metal dusting, carburisation
and nitridation

Edited by H. J. Grabke and M. Schütze



WP

Corrosion by carbon and nitrogen

European Federation of Corrosion Publications
NUMBER 41

Corrosion by carbon and nitrogen

Metal dusting, carburisation
and nitridation

Edited by
H. J. Grabke and M. Schütze

**Published for the European Federation of Corrosion
by Woodhead Publishing and Maney Publishing
on behalf of
The Institute of Materials, Minerals & Mining**

**CRC Press
Boca Raton Boston New York Washington, DC**

WOODHEAD PUBLISHING LIMITED
Cambridge England

Woodhead Publishing Limited and Maney Publishing Limited on behalf of
The Institute of Materials, Minerals & Mining

Published by Woodhead Publishing Limited, Abington Hall, Abington
Cambridge CB21 6AH, England
www.woodheadpublishing.com

Published in North America by CRC Press LLC, 6000 Broken Sound Parkway, NW,
Suite 300, Boca Raton, FL 33487, USA

First published 2007 by Woodhead Publishing Limited and CRC Press LLC
© 2007, Institute of Materials, Minerals & Mining
The authors have asserted their moral rights.

This book contains information obtained from authentic and highly regarded sources. Reprinted material is quoted with permission, and sources are indicated. Reasonable efforts have been made to publish reliable data and information, but the authors and the publishers cannot assume responsibility for the validity of all materials. Neither the authors nor the publishers, nor anyone else associated with this publication, shall be liable for any loss, damage or liability directly or indirectly caused or alleged to be caused by this book.

Neither this book nor any part may be reproduced or transmitted in any form or by any means, electronic or mechanical, including photocopying, microfilming and recording, or by any information storage or retrieval system, without permission in writing from the Woodhead Publishing Limited.

The consent of Woodhead Publishing Limited does not extend to copying for general distribution, for promotion, for creating new works, or for resale. Specific permission must be obtained in writing from Woodhead Publishing Limited for such copying.

Trademark notice: Product or corporate names may be trademarks or registered trademarks, and are used only for identification and explanation, without intent to infringe.

British Library Cataloguing in Publication Data
A catalogue record for this book is available from the British Library.

Library of Congress Cataloging in Publication Data
A catalog record for this book is available from the Library of Congress.

Woodhead Publishing ISBN 978-1-84569-232-2 (book)
Woodhead Publishing ISBN 978-1-84569-335-0 (e-book)
CRC Press ISBN 978-1-4200-5894-9
CRC Press order number: WP5894
ISSN 1354-5116

The publishers' policy is to use permanent paper from mills that operate a sustainable forestry policy, and which has been manufactured from pulp which is processed using acid-free and elementary chlorine-free practices. Furthermore, the publishers ensure that the text paper and cover board used have met acceptable environmental accreditation standards.

Typeset by Replika Press Pvt Ltd, India
Printed by TJ International Limited, Padstow, Cornwall, England

Contents

	<i>Contributor contact details</i>	<i>xi</i>
	<i>Series introduction</i>	<i>xv</i>
	<i>Volumes in the EFC series</i>	<i>xvii</i>
1	Metal dusting	1
	H J GRABKE, Max-Planck-Institut für Eisenforschung GmbH, Germany	
1.1	Definition of metal dusting	1
1.2	Thermodynamics and kinetics of gas–metal reactions	1
1.3	Mechanisms of metal dusting	4
1.4	Kinetics of metal wastage and coking on iron and low-alloy steels	8
1.5	Metal dusting of high-alloy steels	10
1.6	Metal dusting of Ni-based alloys	14
1.7	Protection against metal dusting	17
1.8	References	23
2	The metal dusting corrosion of steels with varying concentrations of chromium	25
	C M CHUN, ExxonMobil Research and Engineering Company, USA and T A RAMANARAYANAN, Princeton University, USA	
2.1	Introduction	25
2.2	Experimental procedure	26
2.3	Results	28
2.4	Discussion	40
2.5	Summary	46
2.6	References	48

vi	Contents	
3	Microprocesses of metal dusting on iron–nickel alloys and their dependence on the alloy composition	49
	E PIPPEL and J WOLTERS DORF, Max-Planck-Institut für Mikrostrukturphysik, Germany and H J GRABKE, Max-Planck-Institut für Eisenforschung GmbH, Germany	
3.1	Introduction	49
3.2	Experimental procedure	51
3.3	Results	51
3.4	Discussion	57
3.5	Acknowledgement	58
3.6	References	58
4	Metal dusting behaviour of welded Ni–base alloys with different surface finishes	59
	H J GRABKE and E M MÜLLER-LORENZ, Max-Planck-Institut für Eisenforschung GmbH, Germany and M ZINKE, Institut für Füge- und Strahltechnik, Germany	
4.1	Introduction	59
4.2	Experimental procedure	59
4.3	Results	63
4.4	Conclusions	71
4.5	Acknowledgement	75
4.6	References	75
5	Effect of H ₂ S on metal dusting of iron	76
	A SCHNEIDER and H J GRABKE, Max-Planck-Institut für Eisenforschung GmbH, Germany	
5.1	Introduction	76
5.2	Effect of H ₂ S on carburisation kinetics and graphite formation	77
5.3	Carbon diffusion in cementite and Hägg carbide	81
5.4	Thermodynamics of Hägg carbide formation	83
5.5	Decomposition of Fe ₃ C and Fe ₅ C ₂	84
5.6	Iron sulphide formation in atmospheres containing H ₂ S	86
5.7	Practical aspects of sulphur adsorption	86
5.8	Acknowledgement	87
5.9	References	88

6	Occurrence of metal dusting – referring to failure cases	90
	H J GRABKE and M SPIEGEL, Max-Planck-Institut für Eisenforschung GmbH, Germany	
6.1	Metal dusting – present knowledge	90
6.2	Failure cases	92
6.3	Conclusions	99
6.4	References	101
7	Protective behaviour of newly developed coatings against metal dusting	103
	C ROSADO and M SCHÜTZE, Karl-Winnacker-Institut der DECHEMA e.V., Germany	
7.1	Introduction	103
7.2	Experimental procedure	104
7.3	Results and discussion	109
7.4	Conclusions	146
7.5	Acknowledgements	152
7.6	References	153
8	Metal dusting resistance of high-chromium alloys	154
	H J GRABKE and E M MÜLLER-LORENZ, Max-Planck-Institut für Eisenforschung, Germany and H P MARTINZ, Plansee AG, Austria	
8.1	Introduction	154
8.2	Experimental procedure	154
8.3	Results	155
8.4	Discussion	160
8.5	References	161
9	Study of the metal dusting behaviour of high-temperature alloys	162
	F DI GABRIELE, J R BERNSTEIN, M M AL-QHATANI, Z LIU, M P JORDAN, and F H STOTT, Corrosion and Protection Centre, UK and J A RICHARDSON, Anticorrosion Consulting, UK	
9.1	Introduction	162
9.2	Experimental procedure	163
9.3	Results	164
9.4	Discussion	171
9.5	Conclusions	174
9.6	Acknowledgements	174
9.7	References	174

viii	Contents	
10	Metal dusting of ferritic Fe–Al–M–C (M = Ti, V, Nb, Ta) alloys in CO–H ₂ –H ₂ O gas mixtures at 650 °C	175
	A SCHNEIDER and J ZHANG, Max-Planck-Institut für Eisenforschung, Germany	
10.1	Introduction	175
10.2	Experimental procedure	176
10.3	Thermodynamic calculations	177
10.4	Results	177
10.5	Discussion	181
10.6	Conclusions	185
10.7	Acknowledgements	185
10.8	References	186
11	-Fe layer formation during metal dusting of iron in CO–H ₂ –H ₂ O gas mixtures	187
	J ZHANG, A SCHNEIDER and G INDEN, Max-Planck-Institut für Eisenforschung, Germany	
11.1	Introduction	187
11.2	Experimental procedure	188
11.3	Results	188
11.4	Discussion	194
11.5	Conclusions	197
11.6	Acknowledgements	197
11.7	References	198
12	Coke formation during metal dusting of iron in CO–H ₂ –H ₂ O gas with high CO content	199
	J ZHANG, A SCHNEIDER and G INDEN, Max-Planck-Institut für Eisenforschung, Germany	
12.1	Introduction	199
12.2	Experimental procedure	200
12.3	Results	200
12.4	Discussion	207
12.5	Conclusions	212
12.6	Acknowledgements	213
12.7	References	213
13	Morphologies and mechanisms of metal dusting on high-alloy steels	214
	P SZAKÁLOS, Swedish Institute for Metals Research (SIMR), Sweden	
13.1	Introduction	214
13.2	Experimental procedure	215

13.3	Results	216
13.4	Discussion	225
13.5	Conclusions	235
13.6	Acknowledgements	235
13.7	References	235
14	Filamentous carbon formation caused by catalytic metal particles from iron oxide	237
	F BONNET and F ROPITAL, Institut Français du Pétrole, France; Y BERTHIER and P MARCUS, Laboratoire de Physico-Chimie des Surfaces, France	
14.1	Introduction	237
14.2	Thermodynamic calculations	241
14.3	Experimental procedure	246
14.4	Results	248
14.5	Discussion	254
14.6	Conclusion	257
14.7	References	258
15	Typical failures in pyrolysis coils for ethylene cracking	259
	D JAKOBI, Schmidt + Clemens Group, Germany and R GOMMANS, Gommans Metallurgical Services, The Netherlands	
15.1	Introduction	259
15.2	Damage mechanisms	260
15.3	Metallurgical background of the main failure mechanisms	264
15.4	Process technological background	268
15.5	Conclusions	269
15.6	Acknowledgement	270
15.7	References	270
16	Thermodynamic characteristics and numerical modelling of internal nitridation of nickel-base alloys	271
	H J CHRIST, S Y CHANG and U KRUPP, Universität Siegen, Germany	
16.1	Introduction	271
16.2	Experimental procedure	273
16.3	Results and discussion	274
16.4	Conclusions	284
16.5	Acknowledgement	284
16.6	References	284

x	Contents	
17	Nitridation in $\text{NH}_3\text{-H}_2\text{O}$ mixtures	286
	H J GRABKE, S STRAUSS and D VOGEL, Max-Planck-Institut für Eisenforschung, Germany	
17.1	Introduction	286
17.2	Experimental procedure	286
17.3	Results	287
17.4	Discussion	293
17.5	Acknowledgement	297
17.6	References	297
	<i>Index</i>	299

Contributor contact details

(* = main contact)

Editors

H. J. Grabke
Max-Planck-Institut für
Eisenforschung GmbH
Max-Planck-Str. 1
40237 Düsseldorf
Germany

E-mail: grabke@mpie.de

M. Schütze
Karl-Winnacker-Institut der
DECHEMA e.V.
Theodor-Heuss-Allee 25
60486 Frankfurt
Germany

E-mail: schuetze@dechema.de

Chapter 1

H. J. Grabke
Max-Planck-Institut für
Eisenforschung GmbH
Max-Planck-Str. 1
40237 Düsseldorf
Germany

E-mail: grabke@mpie.de

Chapter 2

C. M. Chun*
Corporate Strategic Research
ExxonMobil Research and
Engineering Company
Annandale, NJ 08801
USA

E-mail:
changmin.chun@exxonmobil.com

T. A. Ramanarayanan
Department of Chemistry
Princeton University
Princeton, NJ 08544
USA

E-mail: trikur@princeton.edu

Chapter 3

E. Pippel* and J. Woltersdorf
Max-Planck-Institut für
Mikrostrukturphysik
Weinberg 2
D-06120 Halle
Germany

E-mail: epip@mpi-halle.de

H. J. Grabke
Max-Planck-Institut für
Eisenforschung GmbH
Max-Planck-Str. 1
40237 Düsseldorf
Germany

E-mail: grabke@mpie.de

Chapter 4

H. J. Grabke* and E. M. Müller-
Lorenz
Max-Planck-Institut für
Eisenforschung GmbH
Max-Planck-Str. 1
40237 Düsseldorf
Germany

E-mail: grabke@mpie.de

M. Zinke
Institut für Füge und Strahltechnik
Otto Van Guericke-Universität
Magdeburg
Germany

Chapter 5

A. Schneider* and H. J. Grabke
Max-Planck-Institut für
Eisenforschung GmbH
Max-Planck-Str. 1
40237 Düsseldorf
Germany

E-mail: schneider@mpie.de
grabke@mpie.de

Chapter 6

H. J. Grabke* and M. Spiegel
Max-Planck-Institut für
Eisenforschung GmbH
Max-Planck-Str. 1
40237 Düsseldorf
Germany

E-mail: grabke@mpie.de
spiegel@mpie.de

Chapter 7

C. Rosado Sainz-Rozas and
M. Schütze*
Karl-Winnacker-Institut der
DECHEMA e.V.
Theodor-Heuss-Allee 25
60486 Frankfurt
Germany

E-mail: schuetze@dechema.de
rosado@dechema.de

Chapter 8

H. J. Grabke*, and
E. M. Müller-Lorenz
Max-Planck-Institut für
Eisenforschung GmbH
Max-Planck-Str. 1
40237 Düsseldorf
Germany

E-mail: grabke@mpie.de

H. P. Martinz

Plansee SE

TZ IO

6600 Reutte

Austria

E-mail:

hans-peter.martinz@plansee.com

Chapter 9

F. Di Gabriele*, J. R. Bernstein,

M. M. Al-Qhatani, Z. Liu,

M. P. Jordan and F. H. Stott

UMIST

Corrosion & Protection Centre

Manchester M60 1QD

UK

E-mail: gab@ujv.cz

J. A. Richardson

Anticorrosion Consulting

Durham DHI 4AL

UK

Chapter 10

A. Schneider* and J. Zhang

Max-Planck-Institute für

Eisenforschung GmbH

Max-Planck-Str. 1

40237 Düsseldorf

Germany

E-mail: schneider@mpie.de

j.zhang@mpie.de

Chapter 11 and 12

J. Zhang*, A. Schneider and

G. Inden

Max-Planck-Institut für

Eisenforschung GmbH

Max-Planck-Str. 1

40237 Düsseldorf

Germany

E-mail: j.zhang@mpie.de

schneider@mpie.de

Chapter 13

P. K. M. Szakálos

Swedish Institute for Metals

Research

Stainless Steel Research Group

Drottning Kristinas väg 48

11428 Stockholm

Sweden

E-mail: szakalos@simr.se

Chapter 14

F. Bonnet and F. Ropital*

Institut Français du Pétrole

1-4 Avenue de Bois Préau

92852 Reuil-Malmaison Cedex

France

E-mail: francois.ropital@ifp.fr

Y. Berthier and P. Marcus
Laboratoire de Physico-Chimie des
Surfaces
CNRS (UMR 7045)
Ecole Nationale Supérieure de
Chimie de Paris
75231 Paris Cedex 05
France

Chapter 15

D. Jakobi*
Schmidt & Clemens GmbH & Co
Edelstahlwerk Kaiserau
51779 Lindlar
Germany

E-mail: d.jakobi@schmidt-clemens.de

R. Gommans
Gommans Metallurgical Services
Stevensweert
The Netherlands

Chapter 16

H. J. Christ*, S. Y. Chang,
U. Krupp
Institut für Werkstofftechnik
Universität Siegen
D-57068 Siegen
Germany

E-mail: christ@ifwt.mb.uni-siegen.de
krupp@ifwt.mb.uni-siegen.de

Chapter 17

H. J. Grabke*, S. Strauss and
D. Vogel
Max-Planck-Institut für
Eisenforschung GmbH
Max-Planck-Str. 1
40237 Düsseldorf
Germany

E-mail: grabke@mpie.de

European Federation of Corrosion (EFC) publications: Series introduction

The EFC, incorporated in Belgium, was founded in 1955 with the purpose of promoting European co-operation in the fields of research into corrosion and corrosion prevention. Membership of the EFC is based upon participation by corrosion societies and committees in technical Working Parties. Member societies appoint delegates to Working Parties, whose membership is expanded by personal corresponding membership.

The activities of the Working Parties cover corrosion topics associated with inhibition, education, reinforcement in concrete, microbial effects, hot gases and combustion products, environment-sensitive fracture, marine environments, refineries, surface science, physico chemical methods of measurement, the nuclear industry, the automotive industry, computer-based information systems, coatings, tribo-corrosion and the oil and gas industry. Working Parties and Task Forces on other topics are established as required.

The Working Parties function in various ways, e.g. by preparing reports, organising symposia, conducting intensive courses and producing instructional material, including films. The activities of Working Parties are co-ordinated through a Science and Technology Advisory Committee, by the Scientific Secretary. The administration of the EFC is handled by three Secretariats: DECHEMA e.V. in Germany, the Société de Chimie Industrielle in France, and the Institute of Materials, Minerals and Mining in the United Kingdom. These three Secretariats meet at the Board of Administrators of the EFC. There is an annual General Assembly at which delegates from all member societies meet to determine and approve EFC policy. News of EFC activities, forthcoming conferences, courses, etc., is published in a range of accredited corrosion and certain other journals throughout Europe. More detailed descriptions of activities are given in a Newsletter prepared by the Scientific Secretary.

The output of the EFC takes various forms. Papers on particular topics, for example reviews or results of experimental work, may be published in scientific and technical journals in one or more countries in Europe. Conference

proceedings are often published by the organisation responsible for the conference.

In 1987 the then Institute of Metals was appointed as the official EFC publisher. Although the arrangement is non-exclusive and other routes for publication are still available, it is expected that the Working Parties of the EFC will use the Institute of Materials, Minerals and Mining for publication of reports, proceedings, etc., wherever possible.

The name of the Institute of Metals was changed to the Institute of Materials on 1 January 1992 and to the Institute of Materials, Minerals and Mining with effect from 26 June 2002. The series is now published by Woodhead Publishing and Maney Publishing on behalf of the Institute of Materials, Minerals and Mining.

P. McIntyre

EFC Series Editor,

The Institute of Materials, Minerals and Mining, London, SW1Y 5DB UK

EFC Secretariats are located at:

Dr B. A. Rickinson

European Federation of Corrosion, The Institute of Materials, Minerals and Mining, 1 Carlton House Terrace, London, SW1Y 5DB, UK

Dr J. P. Berge

Fédération Européenne de la Corrosion, Société de Chimie Industrielle,
28 rue Saint-Dominique, F-75007 Paris, France

Professor Dr G. Kreysa

Europäische Föderation Korrosion, DECHEMA e. V., Theodor-Heuss-Allee
25, D-60486, Frankfurt, Germany

Volumes in the EFC series

- 1 **Corrosion in the nuclear industry**
Prepared by the Working Party on Nuclear Corrosion
- 2 **Practical corrosion principles**
Prepared by the Working Party on Corrosion Education (out of print)
- 3 **General guidelines for corrosion testing of materials for marine applications**
Prepared by the Working Party on Marine Corrosion
- 4 **Guidelines on electrochemical corrosion measurements**
Prepared by the Working Party on Physico-Chemical Methods of Corrosion Testing
- 5 **Illustrated case histories of marine corrosion**
Prepared by the Working Party on Marine Corrosion
- 6 **Corrosion education manual**
Prepared by the Working Party on Corrosion Education
- 7 **Corrosion problems related to nuclear waste disposal**
Prepared by the Working Party on Nuclear Corrosion
- 8 **Microbial corrosion**
Prepared by the Working Party on Microbial Corrosion
- 9 **Microbiological degradation of materials – and methods of protection**
Prepared by the Working Party on Microbial Corrosion
- 10 **Marine corrosion of stainless steels: chlorination and microbial effects**
Prepared by the Working Party on Marine Corrosion
- 11 **Corrosion inhibitors**
Prepared by the Working Party on Inhibitors (out of print)

12 Modifications of passive films

Prepared by the Working Party on Surface Science and Mechanisms of Corrosion and Protection

13 Predicting CO₂ corrosion in the oil and gas industry

Prepared by the Working Party on Corrosion in Oil and Gas Production (out of print)

14 Guidelines for methods of testing and research in high temperature corrosion

Prepared by the Working Party on Corrosion by Hot Gases and Combustion Products

15 Microbial corrosion (Proc. 3rd Int. EFC Workshop)

Prepared by the Working Party on Microbial Corrosion

16 Guidelines on materials requirements for carbon and low alloy steels for H₂S-containing environments in oil and gas production

Prepared by the Working Party on Corrosion in Oil and Gas Production

17 Corrosion resistant alloys for oil and gas production: guidance on general requirements and test methods for H₂ S Service

Prepared by the Working Party on Corrosion in Oil and Gas Production

18 Stainless steel in concrete: state of the art report

Prepared by the Working Party on Corrosion of Reinforcement in Concrete

19 Sea water corrosion of stainless steels – mechanisms and experiences

Prepared by the Working Parties on Marine Corrosion and Microbial Corrosion

20 Organic and inorganic coatings for corrosion prevention – research and experiences

Papers from EUROCORR '96

21 Corrosion–deformation interactions

CDI '96 in conjunction with EUROCORR '96

22 Aspects on microbially induced corrosion

Papers from EUROCORR '96 and the EFC Working Party on Microbial Corrosion

23 CO₂ corrosion control in oil and gas production – design considerations

Prepared by the Working Party on Corrosion in Oil and Gas Production

- 24 **Electrochemical rehabilitation methods for reinforced concrete structures – a state of the art report**
Prepared by the Working Party on Corrosion of Reinforcement in Concrete
- 25 **Corrosion of reinforcement in concrete – monitoring, prevention and rehabilitation**
Papers from EUROCORR '97
- 26 **Advances in corrosion control and materials in oil and gas production**
Papers from EUROCORR '97 and EUROCORR '98
- 27 **Cyclic oxidation of high temperature materials**
Proceedings of an EFC Workshop, Frankfurt/Main, 1999
- 28 **Electrochemical approach to selected corrosion and corrosion control**
Papers from 50th ISE Meeting, Pavia, 1999
- 29 **Microbial corrosion (Proc. 4th Int. EFC Workshop)**
Prepared by the Working Party on Microbial Corrosion
- 30 **Survey of literature on crevice corrosion (1979–1998): mechanisms, test methods and results, practical experience, protective measures and monitoring**
Prepared by F. P. Ijsseling and the Working Party on Marine Corrosion
- 31 **Corrosion of reinforcement in concrete: corrosion mechanisms and corrosion protection**
Papers from EUROCORR '99 and the Working Party on Corrosion of Reinforcement in Concrete
- 32 **Guidelines for the compilation of corrosion cost data and for the calculation of the life cycle cost of corrosion – a working party report**
Prepared by the Working Party on Corrosion in Oil and Gas Production
- 33 **Marine corrosion of stainless steels: testing, selection, experience, protection and monitoring**
Edited by D Féron
- 34 **Lifetime modelling of high temperature corrosion processes**
Proceedings of an EFC Workshop 2001, edited by M. Schütze, W. J. Quadackers and J. R. Nicholls
- 35 **Corrosion inhibitors for steel in concrete**
Prepared by B. Elsener with support from a Task Group of Working Party 11 on Corrosion of Reinforcement in Concrete

- 36 **Prediction of long term corrosion behaviour in nuclear waste systems**
Edited by D. Féron and Digby D. Macdonald of Working Party 4 on Nuclear Corrosion
- 37 **Test methods for assessing the susceptibility of prestressing steels to hydrogen induced stress corrosion cracking**
Prepared by B. Isecke on behalf of Working Party 11 on Corrosion of Steel in Concrete
- 38 **Corrosion of reinforcement in concrete: mechanisms, monitoring, inhibitors and rehabilitation techniques**
Edited by M. Raupach, B. Elsener, R. Polder and J. Mietz on behalf of Working Party 11 on Corrosion of Steel in Concrete
- 39 **The use of corrosion inhibitors in oil and gas production**
Edited by J. W. Palmer, W. Hedges and J. L. Dawson
- 40 **Control of corrosion in cooling waters**
Edited by J. D. Harston and F. Ropital
- 41 **Corrosion by carbon and nitrogen: metal dusting, carburisation and nitridation**
Edited by H. J. Grabke and M. Schütze
- 42 **Corrosion in refineries**
Edited by J. Harston
- 43 **The electrochemistry and characteristics of embeddable reference electrodes for concrete**
Prepared by R. Myrdal on behalf of Working Party 11 on Corrosion of Steel in Concrete
- 44 **The use of electrochemical scanning tunnelling microscopy (EC-STM) in corrosion analysis: reference material and procedural guidelines**
Prepared by R. Lindström, V. Maurice, L. H. Klein and P. Marcus on behalf of Working Party 6 on Surface Science
- 45 **Local probe techniques for corrosion research**
Edited by R. Oltra on behalf of Working Party 8 on Physico-Chemical Methods of Corrosion Testing
- 46 **Amine unit corrosion survey**
Edited by F. Ropital on behalf of Working Party 15 on Corrosion in the Refinery Industry

- 47 **Novel approaches to the improvement of high temperature corrosion resistance**
Edited by M. Schütze and W. Quadackers on behalf of Working Party 3 on Corrosion in Hot Gases and Combustion Products
- 48 **Corrosion of metallic heritage artefacts: investigation, conservation and prediction of longterm behaviour**
Edited by P. Dillmann, G. Béranger, P. Piccardo and H. Matthiesén on behalf of Working Party 4 on Nuclear Corrosion
- 49 **Electrochemistry in light water reactors: reference electrodes, measurements, corrosion and tribocorrosion**
Edited by R. W. Bosch, D. Féron and J. P. Celis on behalf of Working Party 4 on Nuclear Corrosion
- 50 **Corrosion behaviour and protection of copper and aluminium alloys in seawater**
Edited by D. Féron on behalf of Working Party 9 on Marine Corrosion
- 51 **Corrosion issues in light water reactors: stress corrosion cracking**
Edited by D. Féron and J.-M. Olive on behalf of Working Party 4 on Nuclear Corrosion

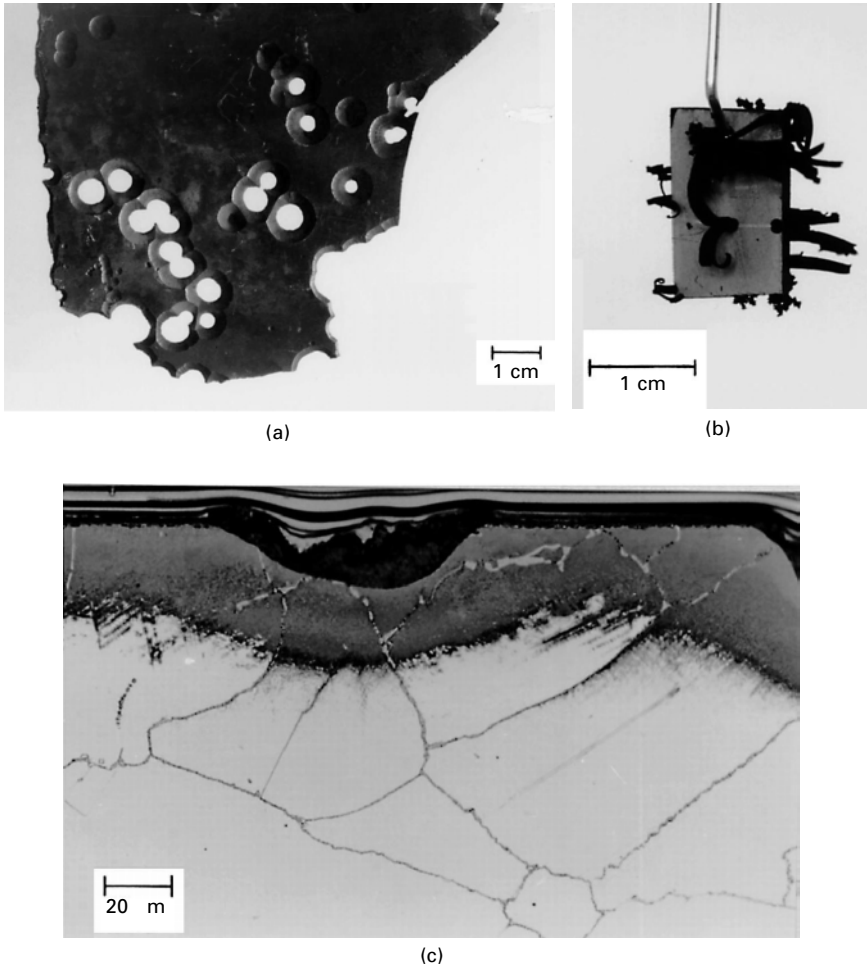
1.1 Definition of metal dusting

Metal dusting is the disintegration of metallic materials into a dust of fine metal particles and graphitic carbon. In the case of chromium steels and Ni-based alloys the corrosion product (coke) may also contain carbides and oxides. This corrosion phenomenon occurs in carburizing atmospheres, containing CO and/or hydrocarbons, at carbon activities $a_C > 1$ which means that a tendency for graphite formation prevails (in equilibrium with graphite $a_C = 1$). Materials susceptible are metals and alloys which dissolve carbon, i.e. Fe, Ni and Co and their alloys. The carbon is transferred from the atmosphere and dissolved into the metal phase, at $a_C > 1$ to oversaturation, leading to growth of graphite which destroys the materials. In the case of iron and steels, cementite is formed as an intermediate into which the graphite grows [1–5]. Nickel and Ni-based alloys are disintegrated by direct inward growth of graphite [6–9].

Fe and Ni and low-alloy materials are attacked uniformly. In the most critical temperature range 400–800 °C mostly chromia-forming steels and Ni-based alloys are used: on these materials metal dusting starts locally, where the oxide scale fails, and leads to pitting and hole formation [3, 8–12]. see Fig. 1.1a. The corrosion product ‘coke’ grows out from the pits and holes, and is mostly carried away in the fast-flowing process gases, but is observed in laboratory studies as outgrowing protrusions (Fig. 1.1b). Typical for Cr steels and alloys is the zone with internal carbides (Fig. 1.1c) formed in a process preceding the metal dusting attack. In the etched metallographic cross-section this zone appears grey or black, since the tiny particles formed at relatively low temperatures are not discernable by optical microscopy.

1.2 Thermodynamics and kinetics of gas–metal reactions

Metal dusting is caused by the tendency to form graphite. The Gibbs free energy for the process is



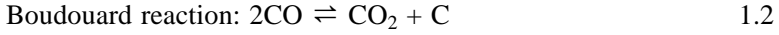
1.1 Metal dusting of Cr-Ni steels: (a) failure case, sheet of Alloy 800 (20Cr-32Ni steel) after use in synthesis gas at 550 °C, pits and holes; (b) Sample of 20Cr-12Ni steel after laboratory exposure in flowing H₂-24% CO-2% H₂O, outgrowing coke protrusions; (c) metallographic cross-section of a sample after laboratory exposure (etched), carburized zone with internal carbides and pit with some coke.

$$G = -RT \ln a_C$$

which is zero in equilibrium with graphite ($a_C = 1$). The main reactions for carbon transfer from the atmosphere are CO reduction:

$$(a_C)_1 = K_1 \frac{P_{CO} \cdot P_{H_2}}{P_{H_2O}} \log K_1 = \frac{7100}{T} - 7.496$$





$$(a_{\text{C}})_2 = K_2 \frac{(p_{\text{CO}})^2}{p_{\text{CO}_2}} \log K_2 = \frac{8817}{T} - 9.071$$

and dissociation of hydrocarbons [13], which is not discussed here in detail.

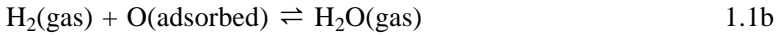
Metal dusting is mainly a problem in gas for synthesis of ammonia, methanol, etc., or gas for reduction of iron ores, produced by conversion or oxidation of natural gas (CH_4). Such process gas or reduction gas is obtained at high temperatures and is not in equilibrium in the critical temperature range for metal dusting. For a non-equilibrium atmosphere generally the values $(a_{\text{C}})_1$ and $(a_{\text{C}})_2$ are different and may be very high, both values are rising with decreasing temperature. On a catalytically active surface, i.e. free metal surface, a steady state a_{C} is established which is nearer to the value $(a_{\text{C}})_1$ because of the faster kinetics of reaction (1.1) [14–16]. Reaction (1.1) transfers carbon into solid solution in Fe according to the rate equation [15]:

$$v_1 = \frac{dn_{\text{C}}}{A dt} = k_1 \cdot p_{\text{CO}} \cdot \frac{1}{1 + K_{\text{O}} \cdot p_{\text{H}_2\text{O}}/p_{\text{H}_2}} \frac{1 - a_{\text{C}}}{(a_{\text{C}})_1} \quad 1.3$$

where v is the rate (mol carbon per area A and time), k_1 a rate constant and K_{O} the adsorption constant of reaction (1.1b), see below. The rate-equation indicates that the CO dissociation on iron is rate-determining:



and that the adsorbed oxygen is rapidly removed by reaction with hydrogen:



so that the equilibrium for the second reaction step is virtually established. The first step (1.1a) is proportional to p_{CO} and the part of surface free of oxygen, which is given by a Langmuir term:

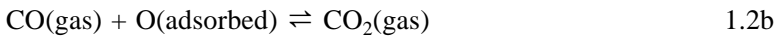
$$1 - \theta_{\text{O}} = \frac{1}{1 + K_{\text{O}} \cdot p_{\text{H}_2\text{O}}/p_{\text{H}_2}}$$

where θ_{O} is the degree of coverage with oxygen adsorbed on the metal surface.

The Boudouard reaction is composed of the steps



and



so the first step is the same as in reaction (1.1), but the second step (1.2b) is much slower than (1.1b) and becomes rate determining. Therefore the Boudouard reaction plays a minor role in kinetics and thermodynamics of

non-equilibrium gas mixtures, compared with CO reduction (1.1), and the latter reaction is decisive for the steady state a_C .

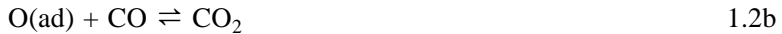
Another thermodynamic value is the oxygen pressure, which is important for the formation of oxides. Again, two reactions deliver oxygen, the H_2O dissociation



and the CO_2 dissociation



In non-equilibrium atmospheres, reaction (1.4) is generally decisive for the p_{O_2} again according to its more rapid kinetics. In fact, these reactions take place on catalytically active surfaces at the temperatures of interest 400–800 °C and a steady state activity of atomic oxygen is established, by the reaction steps of the water-gas shift reaction [17, 18]:



which is generally not in equilibrium in process and reduction gases.

Another reaction to be considered is the oxidation of methane [19]:



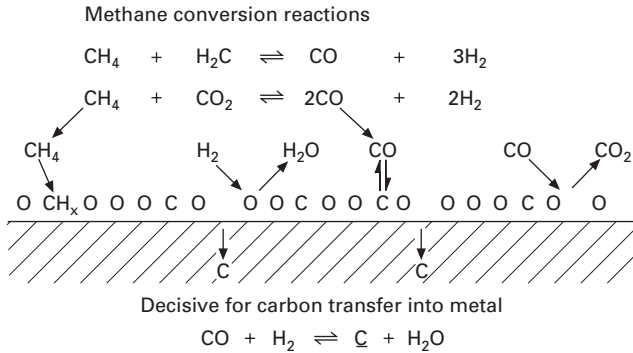
by which the synthesis and reduction gas is produced. This reaction needs catalytic acceleration and is performed generally on Ni catalysts at temperatures > 700 °C. Its back reaction, the methanation of CO, may occur when metal dusting has produced fine metal particles, catalysing the methanation already at rather low temperatures. The methane formation can indicate the occurrence of metal dusting.

So, the elementary reactions in a $CO-H_2-H_2O-CO_2-CH_4$ gas mixture, i.e. synthesis or reduction gas on a metal surface, can be illustrated by the schematic Fig. 1.2, where the strong arrows designate fast reaction steps, leading to the predominance of reactions (1.1) and (1.4).

1.3 Mechanisms of metal dusting

1.3.1 Metal dusting on iron and low-alloy steels

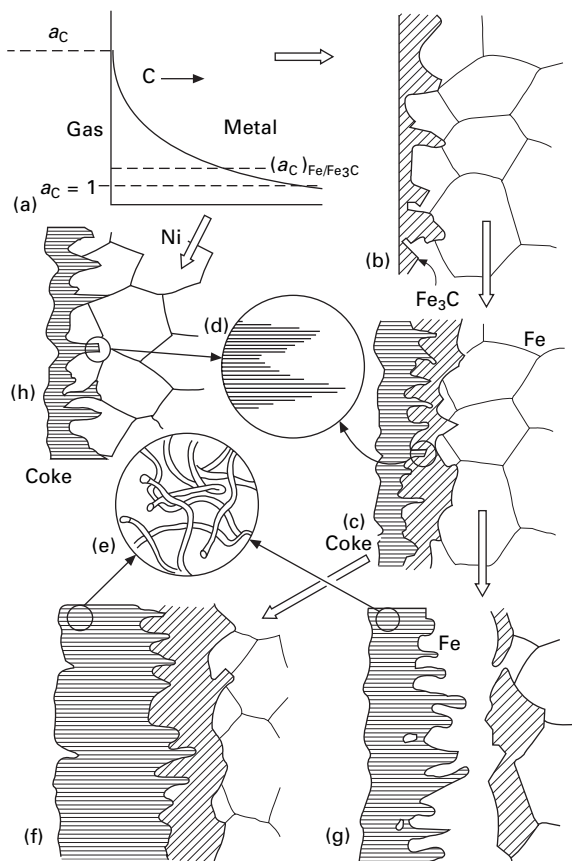
The following mechanism was proven by thermogravimetric studies, optical and electron microscopy on metallographic cross-sections and high-resolution transmission electron microscopy [1–5, 20]. The following reaction sequence occurs on iron and low-alloy steels in the temperature range 400–650 °C in an H_2-CO-H_2O mixture:



1.2 Schematic representation of the partial surface reactions in carburization and metal dusting in a $\text{CO-CO}_2\text{-H}_2\text{-H}_2\text{O}$ atmosphere. The thickness of the arrows characterizes the rates of the respective reactions.

1. Carbon is transferred by reaction (1.1) into solid solution, up to oversaturation, concerning equilibrium with graphite ($a_{\text{C}} = 1$) and cementite ($(a_{\text{C}})_{\text{Fe-Fe}_3\text{C}}$, i.e. somewhat higher than 1, see Fig. 1.3a. Relatively high oversaturations have been observed by electron microprobe.
2. Cementite nucleates and grows, mainly at the surface but also at grain boundaries. A rather irregular layer of cementite crystals grows with characteristic protrusions into the bulk metal phase; Fig. 1.3b. Owing to the low carbon diffusivity in cementite [21–23] this is a barrier against further carbon ingress, therefore the carbon activity at the surface rises.
3. Graphite nucleates locally. This means a decrease of carbon activity to $a_{\text{C}} = 1$ and thus cementite becomes instable.
4. Cementite decomposes to graphite and iron, according to $\text{Fe}_3\text{C} = 3\text{Fe} + \text{C}$, in fact by growth of graphite into the cementite; Fig. 1.3c. Carbon atoms from Fe_3C attach to graphite planes, growing more or less vertically into the cementite [4]. High-resolution transmission electron microscopy (HRTEM) shows graphite tongues or roots invading the cementite; Fig. 1.3d. The iron diffuses outward through the graphite; concentrations of 3–4% Fe have been detected in the graphite. The iron atoms agglomerate under formation of fine particles, of about 20 nm average diameter. Carbon is transferred into these particles, again by reaction (1.1) from the atmosphere with $a_{\text{C}} > 1$.

The carbon diffuses through the particles to some site where graphite nucleation is easy. Here graphite growth starts, and often growth of graphitic carbon filaments is observed; Fig. 1.3e and 1.3f. The rate of carbon transfer into the particles determines that the growth of the filaments, and thus of coke growth, therefore should be governed by the rate law (1.3) for carbon transfer given above [15].



1.3 Schematic illustration of the processes in metal dusting of iron, low-alloy steels and nickel: (a) carbon transfer from the gas phase and oversaturation of the metal phase; (b) nucleation and growth of cementite, Fe_3C , at the surface of Fe and low-alloy steels; (c) nucleation and growth of graphite into the Fe_3C , by; (d) C atoms attaching to the lattice planes of graphite, growing more or less perpendicular into Fe_3C , Ni and high Ni alloys (from TEM studies); (e) carbon filaments grown behind particles detached from the metal phase by the graphite growth (SEM); (f) steady state of metal dusting on Fe and low alloy steels at temperatures $< 600^\circ C$, inward growth of Fe_3C , which disintegrates outward under coke formation; (g) steady state of metal dusting on Fe and low alloy steels at temperatures $> 700^\circ C$, formation of an iron layer between Fe_3C and coke, carbon diffusion through this layer and final disappearance of Fe_3C .

This mechanism can be retarded and altered by the presence of sulphur [24, 25]. Adsorption of sulphur on the metal surface hinders the transfer of carbon into solid solution, i.e. step (1), and also the carbon deposition is retarded. But, more important, the nucleation of graphite is impeded and

reaction step (3) may not take place at all or is delayed for a long time. In this way, cementite is stabilized and its properties concerning thermodynamics, diffusion and stoichiometry could be studied [22, 23]. Suppression of metal dusting depends on carbon and sulphur activity in the atmosphere, carburizing gas CO or CH₄, temperature and time [22–25]; see Section 1.7.1.

At higher temperatures > 700 °C the morphology of the reaction products changes. The iron from the Fe₃C decomposition does not form fine particles but agglomerates to an iron layer through which the carbon must diffuse, to attach to the outer graphite layer; Fig. 1.3g. Thereby the processes are slowed down and metal dusting becomes controlled by carbon diffusion in ferrite, or at higher temperature in austenite. In the system: outer graphite layer, metal layer, cementite layer, metal phase, the phase boundary graphite/metal is instable, since the diffusion control causes that graphite intrusions into the metal layer grow faster, until that layer is disrupted and perturbed [26].

At even higher temperatures, 900 and 1000 °C, in CH₄–H₂ mixtures at $a_C > 1$ no cementite formation occurred [27], but from the oversaturated metal phase, carbon diffuses through an austenite layer to the graphite growing on the surface. Again the strong growth of graphite protrusions indicates carbon diffusion control and instable phase boundaries. After a longer duration metal disintegration is also to be expected, which means that metal dusting occurs at 1000 °C, but not via cementite formation.

These processes are illustrated in Fig. 1.3d and 1.3h, which is valid also for metal dusting of nickel.

1.3.2 Metal dusting of nickel and Ni-based alloys

The latter mechanism, just described for iron at high temperatures > 900 °C is valid also for Ni and Ni-based alloys. Such materials are destroyed by direct inward growth of graphite into the oversaturated solid solution (Fig. 1.3h) as shown by HRTEM [7, 28]. The roots and filaments of graphite growing into the metal phase separate particles from the material, which are considerably bigger than in the mechanism via cementite. Therefore, the catalytic surface area generated is less and coke formation is minor compared with iron and steels [29, 30].

The attack on nickel and its alloys is dependent on the crystal orientation on the surface, due to orientation dependent graphite nucleation and growth. On (111) and some other planes of nickel graphite grows epitaxially, its layers parallel to the metal surface [31], and on these planes no direct metal dusting attack occurs. On other planes such as Ni(100), graphite nucleates more or less vertically and here its layers grow into the metal phase, which leads to destruction of materials.

1.4 Kinetics of metal wastage and coking on iron and low-alloy steels

The rate of metal wastage was determined on iron and low-alloy steels in discontinuous exposures in H_2 -24%CO-2% H_2O at 400–600°C. After exposures for 1–2 days the coke was removed and its metal content was determined by chemical analysis. The rates of metal wastage (in $mg/cm^2 h$) were constant and independent of time from the start. At 475°C experiments in various gas mixtures were conducted and the rate of metal wastage was shown to be independent of carbon and oxygen activity [2]. Thus the rate law results:

$$r_M = \frac{dm_M}{A dt} = k_M \quad 1.8$$

for metal wastage (m_M) per unit area A and time.



i.e. the cementite decomposition occurs by inward growth of graphite [4]. Studies on various steels yield one line in the Arrhenius plot $\log r_M$ vs. $1/T$ (Fig. 1.4a), up to about 540°C which indicates that for these ferritic and austenitic 1–20% Cr steels the cementite decomposition is the rate-determining step in metal dusting, with an activation energy of about 40 kcal/mol. Protection by oxide scales is not considered here; the data in Fig. 1.4a and 1.4b are for samples, attacked on their whole surface.

The cementite decomposition leads to a great number of fine metal particles of about the same size, their mass increases with time according to the expression, obtained by integration of the rate law (1.8)

$$\frac{m_M}{A} = k_M \cdot t \quad 1.10$$

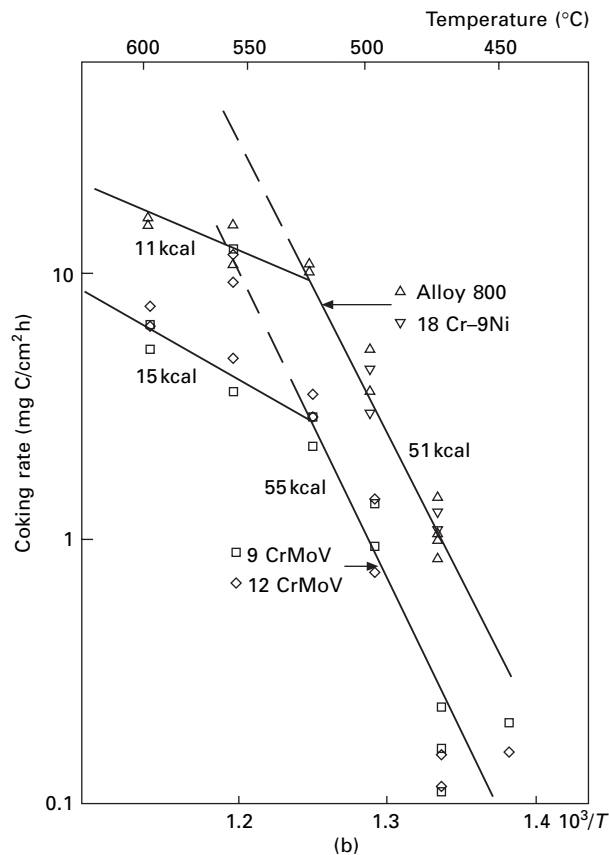
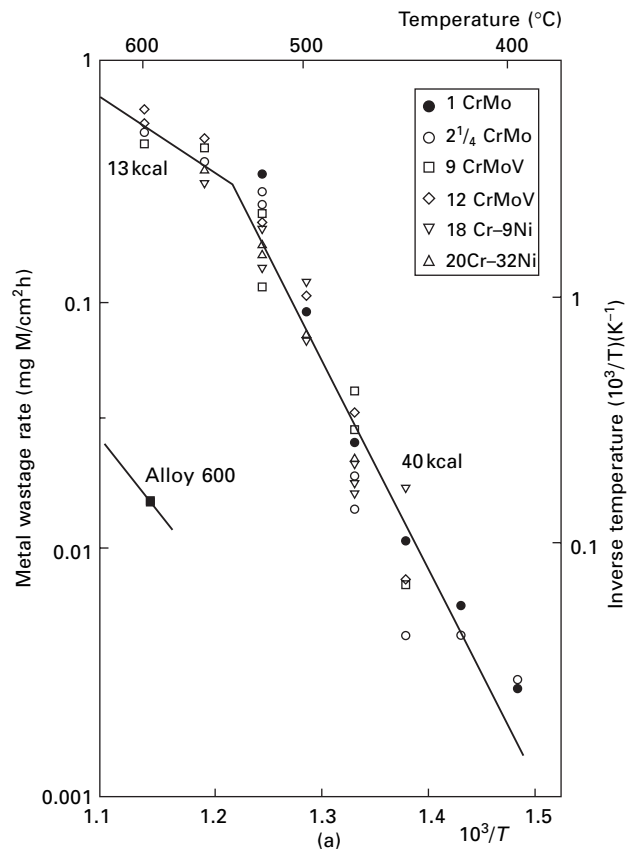
Carbon deposition is catalysed by those fine metal particles and one may assume that the rate of carbon deposition is proportional to their mass:

$$\begin{aligned} r_C \frac{dm_M}{A dt} &= k_C \cdot \frac{m_M}{A} \cdot f(p_i) \\ &= k_C \cdot k_M \cdot f(p_i) \cdot t \end{aligned} \quad 1.11$$

where k_C and k_M are the rate constants of carbon deposition and metal wastage and $f(p_i)$ a function of the partial pressures. Integration yields the result

$$2 \frac{m_C}{A} = k_C \cdot k_M \cdot f(p_i) \cdot t^2 \quad 1.12$$

i.e. the rate of carbon deposition should increase with t^2 , which in fact was proven for coking on steels in experiments up to 10–15 h [2].



1.4 Arrhenius diagrams, from repeated exposures of various steel samples, attacked on their whole surface (no oxide left): (a) metal wastage rates, determined from the coke analysis for its metal content; (b) coking rates, determined by weighing the removable coke.

The Arrhenius plot for coking rates shows differences for ferrites and austenites, on the austenitic steels coking is more severe. The activation energy of coking contains two energy values, since a product of rate constants $k_C \cdot k_M$ is contained in equation (1.12). Therefore it is the sum of the value for metal wastage, 40 kcal/mol, plus the value for carbon transfer, yielding 55 kcal/mol for ferritic steels and 51 kcal/mol for austenitic steels. The dependence on partial pressures $f(p_i)$ was investigated at 475 °C [2] and it was shown that the coking rate is proportional to p_{CO} , it increases with p_{H_2} and decreases with p_{H_2O} . These dependencies are in agreement with the kinetic equation (1.3) for carbon transfer.

The above statements are true for the temperature range below about 550 °C, but at higher temperatures the kinetics changes. The activation energies for metal wastage and coking are lower and the metal wastage rate becomes dependent on the product $p_{CO} \cdot p_{H_2}$ [29] which indicates that carbon transfer is rate determining. More detailed studies of the dependencies of metal wastage and coking on temperature, time and partial pressures are needed for a full description of the very complex mechanisms and kinetics of metal dusting on iron and steels in the temperature range 550–750 °C [26]. At even higher temperatures > 750 °C the kinetics changes again and carbon diffusion in austenite appears to be rate determining for the coke growth.

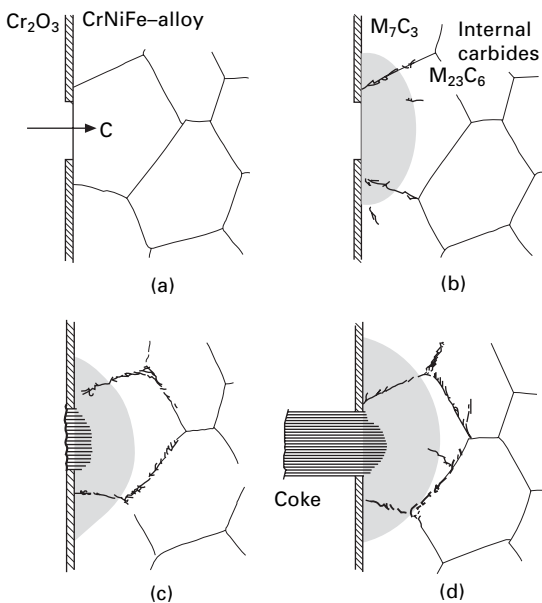
1.5 Metal dusting of high-alloy steels

1.5.1 Joint mechanism of carburization, metal dusting and oxidation

In the temperature range 400–800 °C, which is critical concerning occurrence of metal dusting, generally chromium steels are applied in process industry. Low-alloy steels such as 1% CrMo, 2 $\frac{1}{4}$ % CrMo, etc., are heat resistant and oxidation-resistant up to about 600 °C but in metal dusting conditions ($a_C > 1$) they may be used only in atmospheres with high enough H_2O and/or CO_2 content, so that magnetite can be formed. However, mostly the process conditions are more severe, and metal dusting starts on these steels immediately and uniformly, so that after a few hours the metal wastage rate is constant [2]. Cr-rich oxide scales are necessary for protection against metal dusting which are formed on ferritic steels with >11% Cr and austenitic steels with >17% Cr [3, 32], the difference in chromium needed, is caused by the higher Cr diffusivity in the ferritic lattice. A rapid Cr supply to the surface is necessary to form the protective scale which is composed of an outer layer of the spinel (Mn,Fe)Cr₂O₄ and an inner layer of chromia Cr₂O₃, and it was found advantageous to enhance the Cr diffusion by providing fast-diffusion paths, grain boundaries and dislocations, by a fine-grain microstructure and/or surface working [33–36].

Even high-alloy steels with sufficient Cr-content have shown attack by metal dusting after more or less long periods of exposure under metal dusting conditions. In principle, the same mechanism applies for high-alloy steels as for iron or nickel, but some additional steps must be considered; see Fig. 1.5.

1. The protective oxide scale fails at some weak point in the surface (the character of such weak points will be discussed later).
2. Carbon is transferred into the metal phase at this spot where the gas has access to the bare metal surface (Fig. 1.5a).
3. Carbon diffuses inward and at first reacts with the alloying elements which form stable carbides, $M_{23}C_6$ and M_7C_3 with Cr as main component and MC with $M = \text{Ti, Zr, V, Nb, W and Mo}_2\text{C}$. A zone with internal carbide precipitates is formed (Fig. 1.5b), which are very fine in the temperature range of metal dusting. Then this zone is oversaturated with dissolved carbon.
4. After oversaturation, the remaining Fe or Fe–Ni matrix disintegrates by one of the mechanisms described in Sections 1.3.1 and 1.3.2 (Fig. 1.3) and fine metal particles are formed.



1.5 Schematic illustration of processes in metal dusting of chromia-forming high-alloy steels and Ni-based alloys: (a) defect in the scale, allowing carbon ingress; (b) internal carbide formation, inward moving zones with $M_{23}C_6$ and M_7C_3 ($M = \text{Cr, Fe, Ni}$); (c) after oversaturation with C (dissolved) graphite nucleation and inward growth; (d) outward growth of a coke-protrusion, composed of graphite carbon filaments, metal, carbide and oxide particles.

5. The fine metal particles cause vast carbon deposition and outgrowth of coke from the pit which is starting to grow from the 'weak point' (Fig. 1.5c). If the oxide scale is rather weak, wide and flat pits arise, and in the case of a rather stable oxide scale the pits may be nearly hemispherical. In practice the coke is carried away by the gas flow, in the laboratory experiment different coke and pit morphologies were observed [32].
6. When the metal matrix is subjected to disintegration by metal dusting, simultaneously the carbides $M_{23}C_6$, M_7C_3 and MC are oxidized under formation of spinels and other oxides, ending up in the coke.

So, in metal dusting of high-alloy steels and Ni-based alloys, in the presence of oxidizing gas components, chromia and spinel formation is observed. However, this is not a process that is characteristic and general in metal dusting, and the Cr in the steels and alloys will end up in oxides, since the oxygen pressure needed for Cr_2O_3 formation is very low. No new metal dusting mechanism, other than those described in Sections 1.3.1 and 1.3.2, is required to describe metal dusting of high-alloy materials, in contrast to a recent publication [37].

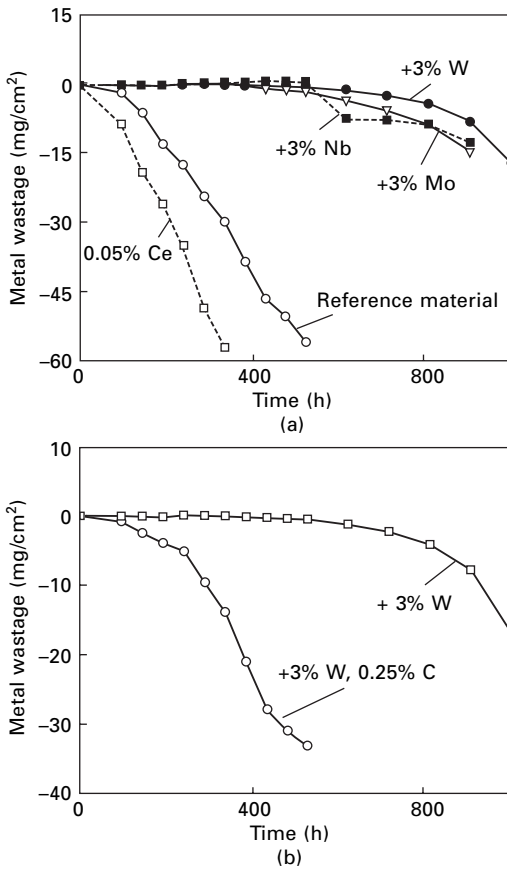
1.5.2 Role of alloying elements in high-alloy steels

Certainly a high Cr content is important for the metal dusting resistance of any alloys, and ferritic steels with 12%Cr–28%Cr have proven to be rather resistant [3, 32]. In contrast, austenitic steels with similar Cr contents are less resistant, as mentioned already, owing to the lower Cr-diffusivity in the austenitic matrix [3, 32]. In particular, the widely used Alloy 800 proved to be very susceptible and many failure cases were reported of this alloy. In a series of exposures with model alloys on the base of Alloy 800, i.e. Fe–20%Cr–32%Ni, the role of several alloying elements was tested, concerning metal dusting resistance [9]. The base alloy showed strong attack and severe mass loss after short time (Fig. 1.6a). The presence of the carbide-forming elements Nb, W and Mo delayed the start of metal dusting up to > 500h. This effect does not clearly enhance the metal dusting resistance, and it easily can be explained by the formation of the stable carbides of these elements which somewhat delays the oversaturation of the matrix.

The kinetics of internal carbide formation is described by the equation for the penetration depth, x , of internal carbide formation [38]:

$$x^2 = 2 \cdot \frac{D_C \cdot c_C}{v \cdot c_M} \cdot t \quad 1.13$$

where D_C and c_C are the diffusivity and solubility of carbon (in the Fe–Ni matrix after carbide precipitation), c_M the concentration of carbide-forming elements, and v an average stoichiometric number for all precipitated carbides



1.6 Mass losses by metal dusting of model alloys based on Fe-32Ni-20Cr (Alloy 800) with different alloying additions: (a) Nb, W, Mo, Ce; (b) W and W + C.

MC. So the start of metal dusting is delayed with increasing concentration c_M of elements forming stable carbides. This interpretation for the role of Nb, W, Mo, etc., was confirmed by exposures of model alloys in which the carbide-forming element was tied up with carbon, e.g. the model alloy with 3% W plus 0.25% C (Fig. 1.6b), for such alloys metal dusting started much earlier, compared with the C-free alloy.

Precipitates of the carbides and nitrides of Ti, Zr, Nb, Mo and W may play a deleterious role in initiating metal dusting. If such precipitate lies at the surface and is oxidized, the growth of the voluminous oxides of these elements disturbs the formation and growth of a protective scale [39]. The negative effect of Ce shown in Fig. 1.6a may be caused by a similar effect, by oxidation of intermetallic phases precipitated in the alloy with 0.05% Ce. The beneficial effects of Ce on chromia formation and adherence are exerted only at higher

temperatures and generally at lower Ce concentration. It may be noted that the 27%Cr–32%Ni–steel AC 66 with 0.05% Ce also proved to be very susceptible to metal dusting [32].

Clearly beneficial effects of Si and Al additions were observed [9]. The samples with 2.5% Si and 4.5% Al showed no mass loss by metal dusting up to 1500h, but small spots of attack were detected. At the low temperature no protective SiO_2 and Al_2O_3 layers are formed. But Si and Al are selectively oxidized in the very first hours of exposure, forming nuclei and islands of oxide which inhibit carbon ingress and allow time for Cr diffusion to the surface and formation of a Cr-rich protective oxide.

This was observed in *in situ* studies [33, 40] by Auger electron spectroscopy (AES) and was seen also from AES sputter profiles taken on the Si- and Al-doped 20Cr–32Ni alloys after 3h exposure [9]. These profiles indicate SiO_2 and Al_2O_3 on top of a Cr-rich oxide scale, obviously formed in the initial ‘transient state’ of oxidation, since in long-term oxidation SiO_2 and Al_2O_3 , should form below Cr_2O_3 , according to thermodynamic rules.

1.6 Metal dusting of Ni-based alloys

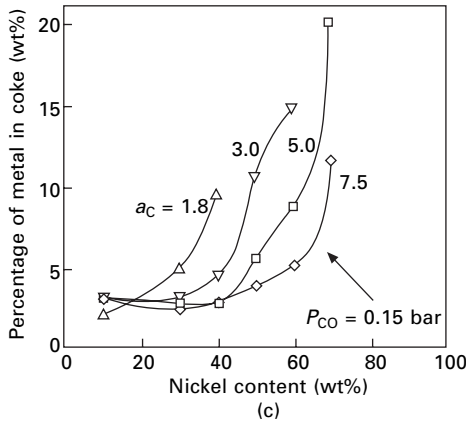
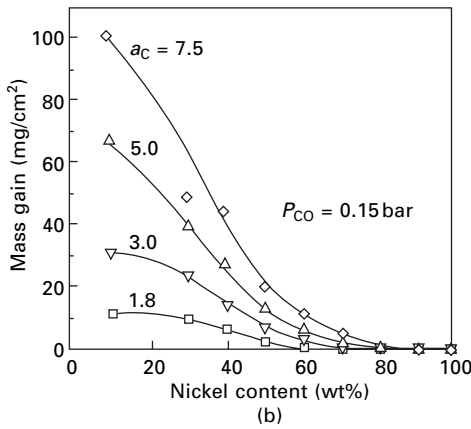
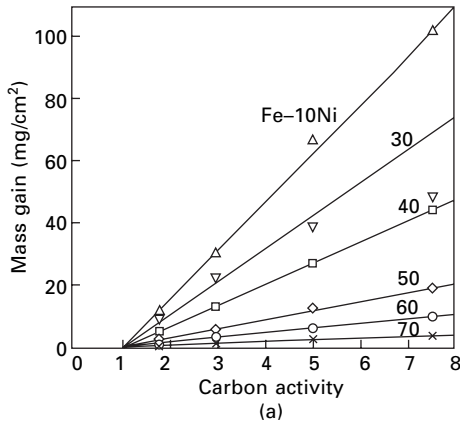
If the mechanism of metal dusting described for Fe and steels applied to Ni-based alloys, $(\text{Ni}, \text{Fe})_3\text{C}$ should be formed as an intermediate. This would need increasing carbon activities with increasing Ni content [1, 41], but in fact metal dusting starts for any Ni–Fe alloy at a carbon activity about $a_{\text{C}} > 1$, as was shown in experiments with binary alloys at 650°C and carbon activities $a_{\text{C}} = 1.8, 3.0, 5.0, 7.5$; see Fig. 1.7a.

The results suggested a change of mechanism for Ni–Fe alloys with more than 40% Ni, on which no M_3C was found after metal dusting exposures [1, 6]. New TEM results [42] indicate that the mechanism has already changed at >10% Ni. The alloys with a higher Ni content are destroyed by the mechanism valid for pure Ni, i.e. direct ingress of graphite. This change in mechanism also results in a decrease of carbon dissolved and deposited on the alloys and an increase in the metal content in the coke with the Ni content in the alloys (Figs 1.7b, 1.7c). The relatively big metal particles, released by metal dusting from Ni-based alloys are less catalytically active for carbon deposition [30] than the fine particles ($\sim 20\text{nm}$) from metal dusting of steels.

So in principle, resistance against metal dusting is better for Ni-based alloys [6, 8, 11, 12] than for steels, since

- the mechanism is different and much slower;
- coke formation is considerably less;
- carbon solubility and diffusivity are lower.

The latter point is important for decreasing the risk of metal dusting initiation on Ni–Cr alloys. As in the case of high-alloy steels there will be a run of C

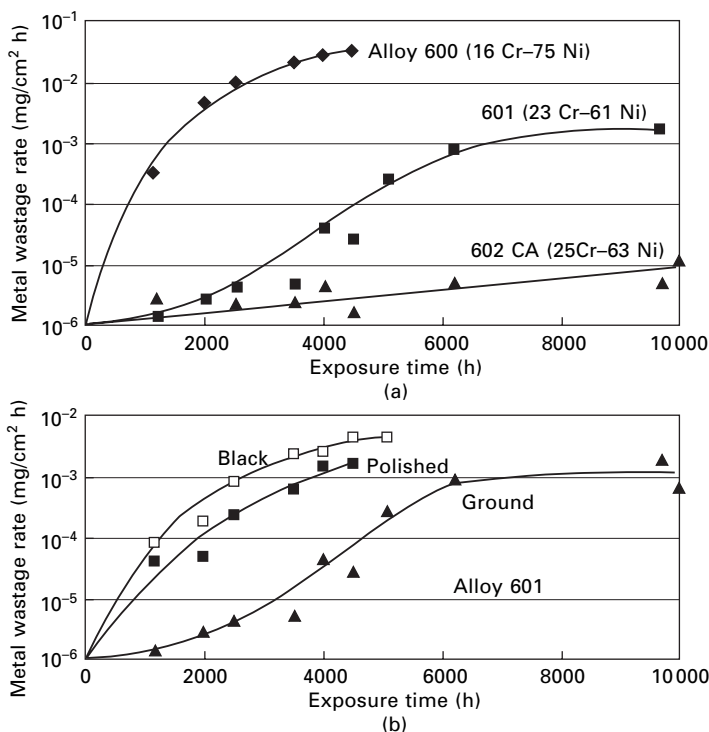


1.7 Metal dusting exposures of Fe-Ni alloys in flowing H_2 -CO- H_2O mixtures at 650°C and different carbon activities: (a) total mass gain by carburization and coking vs. carbon activity of the atmosphere; (b) total mass gain vs. Ni content of the alloys; (c) metal content of the coke vs. Ni content of the alloys.

diffusion inward and Cr diffusion outward, to start either metal dusting or protective scale formation. Cr diffusion is relatively fast and increases with the Ni content of the alloys.

However, the widely used Alloy 600 with only 15–16% Cr is not resistant, and many failure cases have been reported. On Alloy 600 sometimes general attack was observed, but mostly relatively flat pits spread gradually over the surface. In laboratory exposures at 650 °C (Fig. 1.8a) the whole surface was affected after about 3000 h and a wastage rate was observed of 0.033 mg/cm²h corresponding to 0.36 mm/year; this rate is nearly two orders of magnitude slower than that of steels.

Alloy 602, with about 23% Cr and 1.4% Al is more resistant, but this alloy is susceptible to local pitting. In several laboratory exposures some pits started to grow on Alloy 601 from the beginning [8, 43], and grew to nice hemispherical shape and about same depth. Since the wastage rate of 0.7 mm/year calculated from the depth of the pits is even higher than that determined for Alloy 600, perforation of tube or sheet walls would occur even earlier for this material. But the metal dusting behaviour of Alloy 601



1.8 Exposures of Ni-based alloys in CO–H₂–H₂O at 650 °C, increase of metal wastage rate with time: (a) for three different alloys; (b) for Alloy 601 in three different surface states.

can be improved by surface working, as shown by exposures of as-delivered (black), polished and ground samples (Fig. 1.8b). The ground surface state proved to be most resistant, after 10000 h the metal wastage rate was $5.8 \cdot 10^{-4} \text{ mg/cm}^2 \text{ h}$ [40].

Similar and lower wastage rates were observed for the alloys 160 with 28% Cr and 2.8% Si, 45-TM with 27% Cr and 2.7% Si, 617 with 22% Cr and 1% Al, 602 CA with 25% Cr and 2.3% Al, and 690 with 28% Cr [6, 8, 41]. So the important roles of Cr, Si and Al for resistance against metal dusting were confirmed for Ni-based alloys. For these most resistant alloys the formation of a protective scale is strongly favoured, compared with initiation of metal dusting and, in fact, after the exposures the metallographic cross-sections generally showed thin oxide scales. Traces of local carburization were detected, but overgrown by the oxide scale so that metal dusting did not start. Later series of exposures with Alloys 600, 601 and 602CA confirmed the superior resistance of 602CA [43]. This material was recommended for the construction of several plants with severe metal dusting conditions, and after 2–3 years no failures had been reported [44].

Certainly NiCr 50 50 is also very resistant to metal dusting, as shown by application as a coating for components strongly endangered by metal dusting [45] and laboratory tests up to 10000 h [46]. In the latter series of exposures some high-Cr alloys were also tested: Cr–44Fe–5Al–0.3Ti–0.5Y₂O₃, Cr–5Fe–Y₂O₃ and pure Cr, and proved to be resistant. For such alloys the chromia formation is strongly favoured and carbon ingress is nearly impossible since dissolved carbon is tied up by internal carbide formation.

1.7 Protection against metal dusting

To protect metals and alloys against metal dusting their surfaces must be blocked by adsorbed sulphur or sealed by a protective oxide scale. On a sulphur-covered surface or on the surface of oxides such as Cr₂O₃, Al₂O₃ and spinels the adsorption and dissociation of CO, CH₄ and other hydrocarbons generally does not take place. Such surface reaction is necessary for carbon transfer into the metal, i.e. the first step of the metal dusting mechanism. Sulphur is strongly adsorbed on metal surfaces and retards the surface reactions, and in addition interrupts this mechanism. Oxides are impermeable for carbon, if they have no pores or cracks. How to achieve the protection by sulphur and/or oxides is described here.

1.7.1 Protection by sulphur

The effect of sulphur on occurrence of metal dusting was studied in detail in CO–H₂–H₂O–H₂S mixtures on iron. The samples were exposed for about 200 h in the gas mixtures and examined afterwards for occurrence of metal

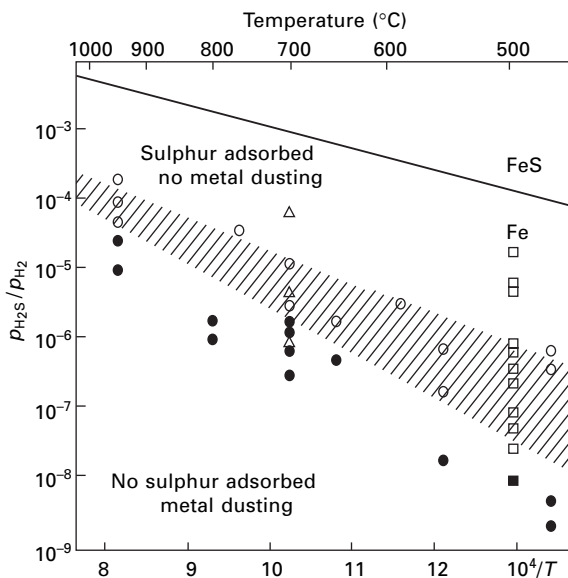
dusting. This study [24, 25, 47] yielded dots for attack (black) or no attack (open) in a diagram $\log p_{\text{H}_2\text{S}}/p_{\text{H}_2}$ vs. $1/T$ (Fig. 1.9).

These data could be well correlated to knowledge about sulphur adsorption on iron from previous studies. The adsorption isotherm for the reaction



had been derived from measurements of the kinetics of nitrogenation in N_2 and carburization in $\text{CH}_4\text{--H}_2$ on iron foils [48, 49]. These reactions are retarded with increasing coverage of adsorbed sulphur and the degree of sulphur coverage depending on $p_{\text{H}_2\text{S}}/p_{\text{H}_2}$ was derived from the dependence of reaction rates on $p_{\text{H}_2\text{S}}/p_{\text{H}_2}$.

The hatched area in Fig. 1.9 corresponds to the approach of sulphur coverage from $\theta_s \sim 0.9$ to a monolayer, and divides the regions of metal dusting attack and no attack. At low temperatures, fairly low values of $p_{\text{H}_2\text{S}}/p_{\text{H}_2}$ are sufficient to provide protection, but at higher temperatures this value increases. It may be noted that the data correspond well to values known from studies of the carburization of high-temperature alloys at 900

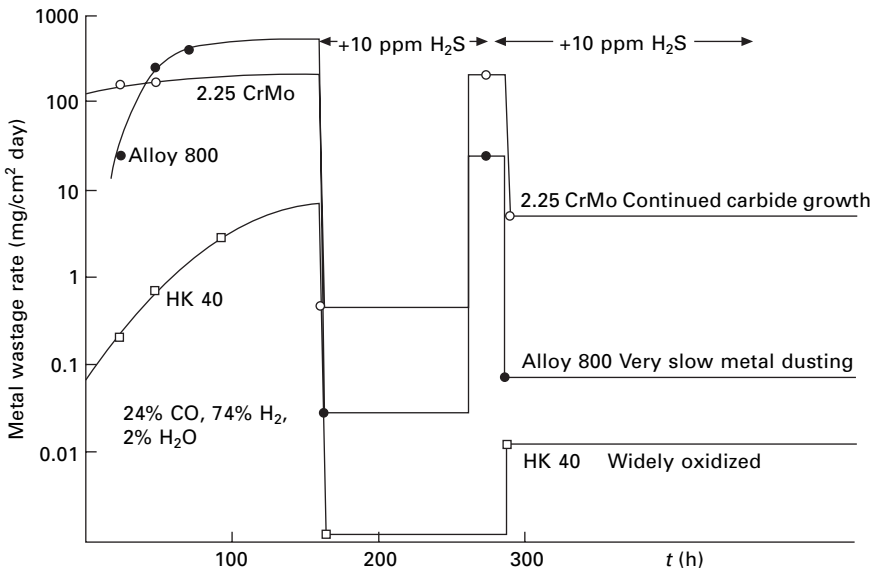


1.9 Effect of sulphur activity in the atmosphere on sulphur adsorption on iron and metal dusting of iron. In the plot of $\log p_{\text{H}_2\text{S}}/p_{\text{H}_2}$ vs. $1/T$ regions are indicated where no sulphur adsorbs and metal dusting occurs after short time (black dots), where sulphur coverage approaches saturation and metal dusting is more and more suppressed (hatched area), and region where a sulphur monolayer suppresses metal dusting (open dots), uppermost region of sulphidation.

and 1000 °C, for ratios $p_{\text{H}_2\text{S}}/p_{\text{H}_2}$ necessary for suppressing internal carbide formation [50].

Adsorbed sulphur blocks the surface for the adsorption of CO or CH₄ and other hydrocarbons, the molecules cannot adsorb and dissociate if their adsorption sites are occupied by sulphur. But even at high $p_{\text{H}_2\text{S}}/p_{\text{H}_2}$ some sites will be free in an adsorption equilibrium such as reaction (1.14) at high temperatures. So carbon can be transferred through such vacancies and the carbon transfer is not suppressed completely but retarded. So after oversaturation, cementite nucleation and growth will occur at the iron surface, beneath the adsorbed sulphur. Now the sulphur has an additional effect, it hinders the nucleation of graphite which would initiate the cementite decomposition. So cementite is stabilized and, in fact, cementite could be grown in CO–H₂–H₂O–H₂S mixtures to considerable thickness [22–25]. On such layers, thermodynamics, disorder and carbon diffusion in cementite could be studied and data obtained that are not currently available for this instable compound.

The action of sulphur on the metal dusting of three steels 2¹/₄% Cr, Alloy 800 and HK 40 was demonstrated in an exposure at 600 °C in H₂–24% CO–2% H₂O. The samples were exposed at first without H₂S addition, until after some days they showed nearly constant metal wastage rate (Fig. 1.10). Then 10 volume ppm H₂S was added and immediately the corrosion was retarded.



1.10 Changes of metal dusting rate without and with H₂S additions – logarithmic plot of metal wastage rates vs. time in metal dusting exposures at 600 °C, of a low-alloy 2.25Cr–Mo steel, a high-alloy 20Cr–32Ni steel (Alloy 800) and a cast 25Cr–20Ni steel (HK 40).

Interruption of H_2S addition resulted in acceleration of attack, and a new addition of H_2S in retardation. So metal dusting can be switched off and on very abruptly by the presence or absence of H_2S in the atmosphere; the adsorption equilibrium (1.14) is established rapidly. But, for the three alloys, the sulphur effect is different. As described for iron on the low-alloy steel, continued cementite growth is observed. On Alloy 800 metal dusting continues, but is strongly retarded in the presence of H_2S . For HK40 (cast 25% Cr–20% Ni steel) during the periods with H_2S , oxide growth is possible as indicated by the metallographic cross-section, and the metal dusting attack is reduced effectively. One may conclude that for low-alloy steels the protection is limited, and corrosion by cementite growth continues. On the very susceptible Alloy 800 the metal dusting is not fully suppressed. Only through the joint effect of sulphur and oxide formation on HK40 is sufficient protection achieved.

1.7.2 Protection by an oxide scale

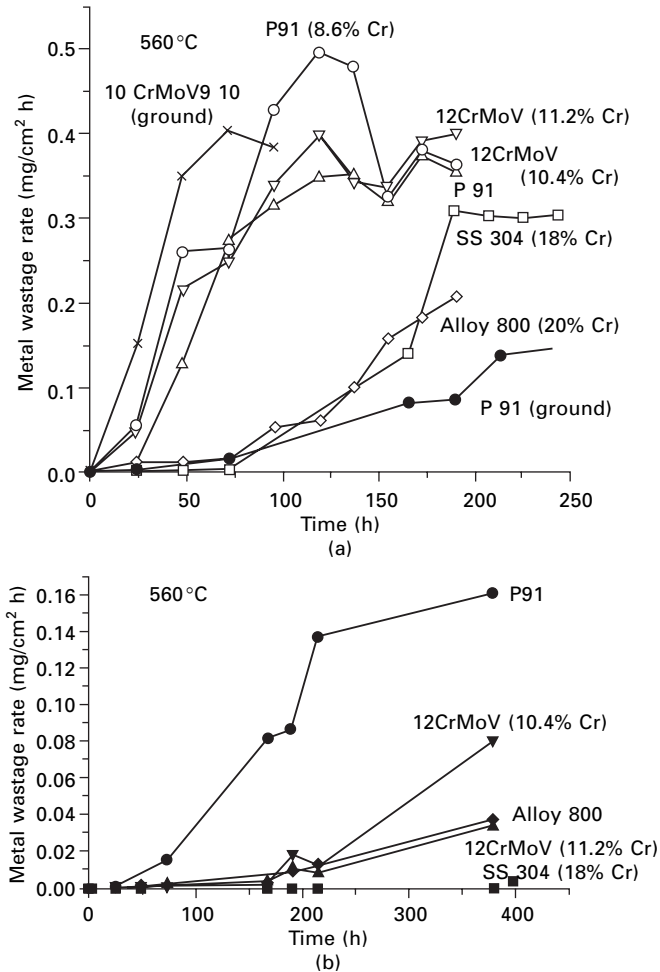
The protection by a dense uniform oxide scale is more effective than by the monoatomic sulphur adsorption layer. But the scale must be composed of chromium-rich oxides, i.e. on Ni-based chromia alloys Cr_2O_3 and on steels generally an outer spinel $(\text{Mn}, \text{Fe})\text{Cr}_2\text{O}_4$ and inner chromia layer. Such Cr-rich scales are not easily formed in the temperature range most critical concerning metal dusting, about 600°C , since Cr diffusivities are low. The Cr supply to the surface upon exposure to the corrosive atmosphere must be rapid, so that the protective oxide is dense, before too much carbon enters the metal phase and ties up the Cr by formation of stable carbides M_{23}C_6 and M_7C_3 . Therefore fast diffusion paths must be supplied for Cr transport to the surface, which is possible by application of fine-grained steels and alloys, and/or surface working by grinding, sandblasting, shot-peening, etc. Certainly a high Cr content is also useful, and possibly the use of ferritic steels, in which Cr diffusion is faster by about two orders of magnitude compared with austenitic steels [33–36].

The effect of fine grain size was clearly demonstrated by a failure case, of a heat exchanger made of Alloy 800 which served for cooling syngas from 575 to 350°C [34]. In the same regions where Alloy 800 was wasted from 10mm to zero, some sheets made of stainless steel 304 were not attacked at all. Surface analysis of the fine-grained steel 304 showed the presence of a thin protective Cr- and Si-rich oxide film. Obviously, the stainless steel had a good chance of forming such film, whereas on the large-grained Alloy 800, Cr-rich oxide grows only above the grain boundaries, and on the wide grain surfaces Fe-rich unprotective oxide is formed [34]. So the Alloy 800 most probably was attacked from the start of operation.

The positive effect of cold rolling and of fine grain size was further confirmed by exposure of the steels 304, 310 and 800 to different states, but

for the same exposure grinding proved to be even more favourable in prolonging protection [34].

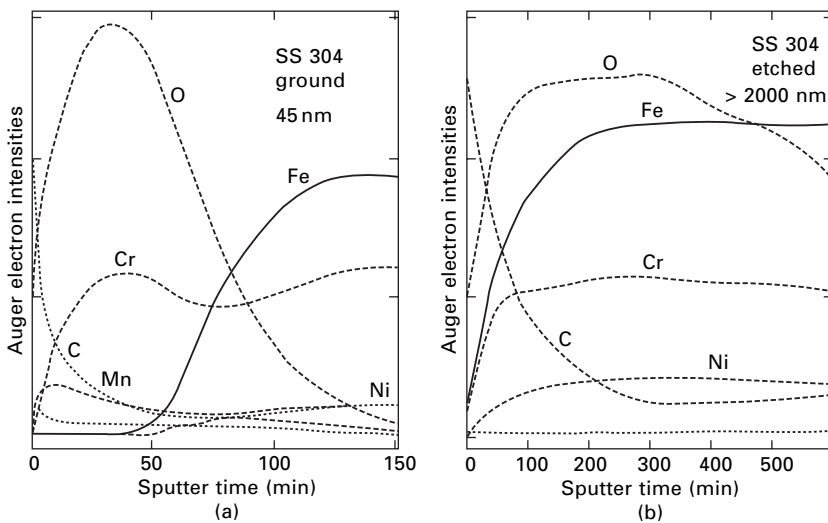
In exposures of four ferritic steels and two austenitic steels the effects of grinding and of etching (in $\text{H}_3\text{PO}_4\text{--H}_2\text{SO}_4$) were studied, by determining the metal mass transferred into the coke after each period. Such studies were performed at 500, 525, 560 and 600 °C [33, 34], the increase of wastage rate with time is shown for the exposures at 560 °C in Fig. 1.11. In the etched state the 2 $\frac{1}{4}$ % Cr steel, 9% Cr steel, and 12CrMoV steel(low) with 10.4% Cr were attacked by metal dusting all over their surface and more or less constant



1.11 Increase of metal wastage rates with time in metal dusting exposures of various steels at 560 °C: (a) etched steels; (b) ground steels.

wastage rates were observed after a short time. This is also valid for the austenitic steels 304 and 800, for which the wastage rate attained is somewhat lower. Only the 12CrMoV steel(high) with 11.2% Cr is more resistant. In the ground state all steels show better resistance, except the 2 $\frac{1}{4}$ % Cr steel which would not form an oxide in both states. In the ground state the steels 12CrMoV(high) and 304 proved to be rather resistant, better than the Alloy 800 with its higher Cr content. Similar results were obtained at the other temperatures.

The effect of grinding on the oxide composition was clearly demonstrated by Auger sputter profiles, taken after 240h exposure at 600 °C (Fig. 1.12). On the most resistant steels relatively thin scales had grown: 110nm on the 12CrMoV steel and 45 nm on steel 304, composed of Mn and Cr oxide, nearly free of iron. This kind of scale is impermeable for carbon, the carbon signal decreases to zero from the surface into the oxide. For the etched specimens the oxide scale is thicker and is composed of Fe and Cr oxide in the case of steel 304, even Ni is in the oxide, which is most probably a (Fe,Cr,Ni)₃O₄ spinel. Such spinel appears to be permeable for carbon since the carbon signal stays high throughout the oxide into the metal phase. Such spinel is also permeable for sulphur [51] as shown by tracer studies, probably due to pores and channels.



1.12 Auger sputter profiles of stainless steel 304 after metal dusting exposures at 600 °C for 300 h: (a) thin protective Mn- and Cr-rich scale on the ground sample; (b) thick non-protective Fe-rich scale on the etched sample.

1.7.3 Conclusions on protection

Protection against metal dusting is possible by preventing ingress of carbon into the metal phase by adsorbed sulphur and/or dense oxide scales. Adsorption of sulphur from H_2S in the atmosphere can protect low-alloy steels up to limited temperatures $< 600^\circ\text{C}$, the content of H_2S necessary is rather low but it must always be present. Only at high $\text{H}_2\text{O}/\text{H}_2$ and CO_2/CO ratios are protective scales (magnetite) formed on low-alloy steels.

High-alloy steels can form protective Cr-rich scales, but for their formation Cr diffusion in the steels should be enhanced by a fine-grained microstructure and/or a surface near deformation by grinding, sandblasting, etc. Additional presence of sulphur from the atmosphere is very advantageous for mending spots where the scale has cracked or spalled – the sulphur adsorption on the bare metal surface impedes carbon ingress and start of metal dusting, until the oxide layer heals again. So, for high-alloy steels one should aim at protection by controlled sulphur in the atmosphere and generation of a protective Cr-rich scale.

If process conditions do not allow the presence of sulphur, Ni-based alloys with high Cr- and Al- or Si-addition are the only choice to attain resistance against metal dusting.

1.8 References

1. Grabke, H.J.; R. Krajak and J.C. Nava Paz: *Corrosion Sci.* **35** (1993) 1141–1150.
2. Grabke, H.J.; C.B. Bracho-Troconis and E.M. Müller-Lorenz: *Werkst. und Korr.* **45** (1994) 215–221.
3. Grabke, H.J.: *Corrosion NACE* **51** (1995) 711–720.
4. Pippel, E.; J. Woltersdorf; H.J. Grabke and S. Strauss: *Steel Research* **66** (1995) 217–221.
5. Grabke, H.J.: *Mat. Corr.* **49** (1998) 303–308.
6. Grabke, H.J.; R. Krajak; E.M. Müller-Lorenz and S. Strauss: *Werkst. u. Korr.* **47** (1996) 495–504.
7. Schneider, R.; E. Pippel; J. Woltersdorf; S. Strauss and H.J. Grabke: *Steel Research* **68** (1997) 326–332.
8. Grabke, H.J.; E. Müller-Lorenz; J. Klöwer and D.C. Agarwal: *Mat. Performance* **37** (1998) 58.
9. Strauss, S. and H.J. Grabke: *Mat. Corr.* **49** (1998) 321–327.
10. Grabke, H.J. and E.M. Müller-Lorenz: *Mat. Corr.* **49** (1998) 317–320.
11. Klöwer, J.; H.J. Grabke and E.M. Müller-Lorenz: *Mat. Corr.* **49** (1998) 328–329.
12. Grabke, H.J.: *Corrosion* **56** No. 8 (2000) 801–808.
13. Grabke, H.J.: *Proceed. Intern. Conference Corrosion in Refinery Petrochemical and Power Generation Plants*, Venice, 18–19 May 2000, Ass. Italiana di Metallurgia, Milano.
14. Turkdogan, E.T. and J.V. Vinters: *Metallurg. Trans.* **5** (1974) 11–19.
15. Grabke H.J. and G. Tauber: *Archiv Eisenhüttenwes.* **45** (1974) 215–222.
16. Shatynski, S.R. and H.J. Grabke: *Archiv Eisenhüttenwes.* **49** (1978) 129–133.

17. Meschter, P. and H.J. Grabke: *Metallurg. Trans.* **10B** (1979) 323–329.
18. Münster, P. and H.J. Grabke: *Berichte Bunsenges. Phys. Chem.* **84** (1980) 1068–1071.
19. Münster, P. and H.J. Grabke: *Archiv Eisenhüttenwes.* **51** (1980) 319–324.
20. Chun, C.M.; J.D. Mumford and T.A. Ramanarayanan: *Mat. Corr.* **50** (1999) 634–639.
21. Ozturk, B.; V.L. Fearing; J. A. Ruth and G. Simkovich: *Solid State Ionics* **12** (1984) 145–151.
22. Schneider, A.; G. Inden; H.J. Grabke; Q. Wei; E. Pippel and J. Woltersdorf: *Steel Research* **71** (2000) No. 5 179–184.
23. Schneider, A.; G. Inden; H.J. Grabke: *Interface Controlled Materials* Vol. 9 (2000) EUROMAT 99, M. Rühle; H. Gleiter (Eds), Wiley-VCH 30–37.
24. Grabke, H.J. and E.M. Müller-Lorenz: *Steel Res.* **66** (1995) 252–258.
25. Grabke, H.J.; E.M. Müller-Lorenz; A. Schneider: *ISIJ Int.* **41** (2001) Supplement S1–S8.
26. Schneider, A.; J. Zhang and G. Inden: *Corrosion Sci.* **44** (2002) 2353, **45** (2003) 281.
27. Forseth, S. and H.J. Grabke: unpublished.
28. Chun, C.M.; J.D. Mumford and T.A. Ramanarayanan: *J. Electrochem. Soc.* **147** (2000) 3680–3686.
29. Müller-Lorenz, E.M. and H.J. Grabke: *Mat. Corr.* **50** (1999) 614–621.
30. Strauss, S.; R. Krajak and H.J. Grabke: *Mat. Corr.* **50** (1999) 622–627.
31. Blakely, J.M.: *CRC Crit. Rev. Solid State Mater. Sci.* (1978) 333–355.
32. Grabke, H.J.; R. Krajak and E.M. Müller-Lorenz: *Werkst. und Korros.* **44** (1993) 89–97.
33. Grabke, H.J.; E.M. Müller-Lorenz; B. Eltester; M. Lucas and D. Monceau: *Steel Res.* **68** (1997) 179–185.
34. Grabke, H.J.; E.M. Müller-Lorenz; S. Strauß; E. Pippel and J. Woltersdorf: *Oxid. Metals* **50** (1998) 2241–2254.
35. Grabke, H.J. and E.M. Müller-Lorenz: *Mat. Corr.* **49** (1998) 317–320.
36. Grabke, H.J.; E.M. Müller-Lorenz; B. Eltester and M. Lucas: *Proceedings Microscopy of Oxidation 4*, Cambridge 1999 and *Mat. at High Temp.* **17** (2000) 339–346.
37. Szakalos, P.; R. Petterson and S. Hertzman: *Corrosion Sci.* **44** (2002) 2253.
38. Schnaas, A. and H.J. Grabke: *Oxid. Metals* **12** (1978) 387–404.
39. Litz, J.; A. Rahmel and M. Schorr: *Oxid. Metals* **30** (1988) 95.
40. Tökei, Zs.: H. Viefhaus and H.J. Grabke: *Appl Surface Sci.* **165** (2000) 23–33.
41. Klarström, D.L.; L.D. Paul and H.J. Grabke: *Corrosion NACE 2001* paper 1379.
42. Pippel, E.; J. Woltersdorf and H.J. Grabke: *Mat. Corr.* **54** (2003) 747.
43. Grabke, H.J.; E.M. Müller-Lorenz and M. Zinke: *Mat. Corr.* **54** (2003) 783.
44. Agarwal, D.C. and U. Brill, J. Wilson: *Corrosion NACE 2002* paper 02372.
45. Holland, M.: *Corrosion NACE 2001* (2001) 1379.
46. Grabke, H.J.; H.P. Martienz and E.M. Müller-Lorenz: *Mat. Corr.*, **54** (2003) 860.
47. Schneider, A.; H. Viefhaus; G. Inden; H.J. Grabke and E.M. Müller-Lorenz: *Mat. Corr.* **49** (1998) 330–335.
48. Grabke, H.J.; E. M. Petersen and S.R. Srinivasan: *Surface Sci.* **67** (1977) 501–516.
49. Grabke, H.J.: *Materials Sci. Eng.* **42** (1980) 91–99.
50. Grabke, H.J.; R. Möller and A. Schnaas: *Werkst. Korros.* **30** (1979) 794–799.
51. Lobnig, R.; H.J. Grabke and E.M. Müller-Lorenz: *Corrosion Sci.* **30** (1990) 1045–1071.

The metal dusting corrosion of steels with varying concentrations of chromium

C M CHUN* ExxonMobil Research and Engineering
Company, USA and T A RAMANARAYANAN,
Princeton University, USA

2.1 Introduction

Metal dusting involves the disintegration of bulk metals and alloys into metal particles at high temperatures in environments that are supersaturated with carbon. It is generally believed that the phenomenon is most widespread in the temperature range 400–700 °C. Such corrosion has been observed in processes in chemical and petrochemical industries where hydrocarbons or other strongly carburizing atmospheres are encountered. Hochman [1–3] did early research on metal dusting. More recently, Grabke and coworkers [4–10] have carried out some detailed studies on the subject. Pippel *et al.* [11] and Chun *et al.* [12–15] have significantly extended the understanding of the micro-mechanistic aspects of metal dusting of pure metals by transmission electron microscopy (TEM).

The Hochman proposal for the metal dusting corrosion of iron, which has been further refined by Grabke and coworkers, involves the initial formation of a metastable Fe_3C carbide layer on the iron surface in the carbon-supersaturated environment. The carbide subsequently dissociates into carbon and metal particles when it is destabilized by carbon deposition, leading to the formation of ‘dust’. Our investigations are in agreement with this mechanism in an overall sense. However, studying the corrosion interface at the nano level using cross-sectional TEM provides additional insights. For instance, the crystalline nature of deposited carbon and its orientation play a key role in determining the severity of corrosion. Graphitic carbon deposit with the graphite planes oriented perpendicular to the Fe_3C surface accelerates the corrosion process since the carbon atoms resulting from Fe_3C dissociation attach themselves to graphite [14]. At the same time iron atoms arising from Fe_3C dissociation can intercalate into graphite and diffuse outward via the space between adjacent graphite planes from the Fe_3C /graphite interface to the carbon-supersaturated environment where they coalesce and catalyze filamentous carbon formation.

Grabke and coworkers [16] have also done some studies on the metal

dusting of low-chromium steels, which are widely used for pressure vessels and heat exchangers in the industry. If the low-chromium steels are not protected by an oxide layer, the corrosion is general, the metal is wasted uniformly and coke forms as a thick coat. By contrast, if the steels are capable of forming protective oxide films, the corrosion is local and leads to the formation of hemispherical pits and holes, from which the coke grows in various forms such as cones, worms and leeches, etc. The following sequence of steps has been proposed by Grabke [10, 17]:

1. Carbon is transferred from the carbon-supersaturated environment to the steel surface and dissolves in the steel through local defects and failure in the oxide film.
2. The dissolved carbon diffuses inward and causes internal precipitation of stable carbides.
3. Upon further carbon transfer, metastable M_3C carbide forms on the internal carbide.
4. Metastable M_3C carbide subsequently decomposes into carbon and metal upon carbon deposition.
5. Metal particles generated by the disintegration of the steel act as catalyst for the formation of coke arising from the growing pit.

This transition from general corrosion to localized attack as the Cr content is increased is the subject of the investigations reported here. A mechanistic picture is presented which attempts to explain the influence of temperature, internal carbide formation and forms of carbon on the corrosion process.

2.2 Experimental procedure

The steel compositions used in the investigations are listed in Table 2.1. Coupons having a thickness of ~1.5 mm were obtained from Metal Samples Co. The specimens had rectangular geometry with approximate dimensions of ~6.5 mm 25.5 mm; the faces were polished using Linde B (Extex Co.,

Table 2.1 List of chromium steels used in the experiments

Grade	UNS designation	ASTM identification symbol	Composition (wt%)
$1\frac{1}{4}Cr-1\frac{1}{2}Mo$	K11572	A182 F11	Bal Fe : 1.01Cr : 0.49Mo : 0.38Mn : 0.72Si : 0.11C
$5Cr-1\frac{1}{2}Mo$	K42544	A182 F5a	Bal Fe : 4.81Cr : 0.50Mo : 0.44Mn : 0.38Si : 0.08C
9Cr-1Mo	K90941	A182 F9	Bal Fe : 8.90Cr : 0.98Mo : 0.48Mn : 0.31Si : 0.10C
13Cr	S41000	A182 F6a	Bal Fe : 12.7Cr : 0.40Mn : 0.29Si : 0.11Ni : 0.17C
20Cr			Bal Fe : 20.2Cr

0.05 m Al_2O_3 powder) and cleaned ultrasonically in acetone. Fe-20Cr steel was prepared by arc melting. The arc-melted steel was rolled into a thin sheet of ~1.5 mm thickness. The sheet was annealed at 1100 °C overnight in inert argon atmosphere and furnace-cooled to room temperature. Rectangular samples of ~6.5 mm × 25.5 mm were cut from the sheets. The sample faces were polished and cleaned.

The gas mixture used for metal dusting studies had a 50CO:50H₂ composition. Carbon monoxide is the most potent metal dusting molecule and the presence of H₂ in CO tends to accelerate metal dusting corrosion. Our previous research showed the maximum rate of carbon transfer from CO-H₂ mixtures to occur at the 50CO:50H₂ composition [14]. Corrosion kinetics were investigated thermogravimetrically using a Cahn 1000 electrobalance and also by timed exposure to the gas mixture in a tubular reactor followed by microscopic measurement of the recession of the metal surface from its initial location. The temperature of corrosion ranged from 650 °F (343 °C) to 1100 °F (593 °C). In the thermogravimetric measurements, the carbon pick-up by the metal sample is used as a measure of metal dusting corrosion while the microscopic approach involves a direct measurement of metal loss. The latter is thus considered more accurate.

After corrosion, selected samples were mounted vertically in an EpoFix embedding medium. The cross-sectional morphology of the corrosion interface was examined by JEOL 840A SEM. Cross-sectional TEM combined with microdiffraction and microchemical analysis was used to investigate the reaction interfaces at the nano level. A sandwich structure with the specimen in the middle was created using Gatan G1 epoxy glue and dummy glass pieces. Discs of 100 m thickness were then cut and polished from the sandwich. These were dimpled and ion-milled to generate electron transparent areas. Micrographs were taken using a Philips CM200/FEG TEM. In order to identify various elements and their approximate proportions, quantitative energy dispersive X-ray spectroscopy (EDXS) was performed using a Princeton Gamma Tech (PGT) system attached to the TEM. A probe of approximately 5 nm in diameter was used for chemical analysis. Some corroded samples were examined by the FEI Strata DB235 focused ion beam (FIB) system, which comprises both focused ion beam column and scanning electron beam platform. The selected area of the corroded surface was initially coated with platinum and milled by a focussed gallium ion beam accelerated at 30 keV. The cross-section so generated was then examined using an electron beam accelerated at 5 keV by field emission. The combined nano-scale milling and high-resolution imaging capabilities enabled detailed investigation of the corrosion interface without mechanical damage that is caused by conventional metallographic sample preparation procedure.

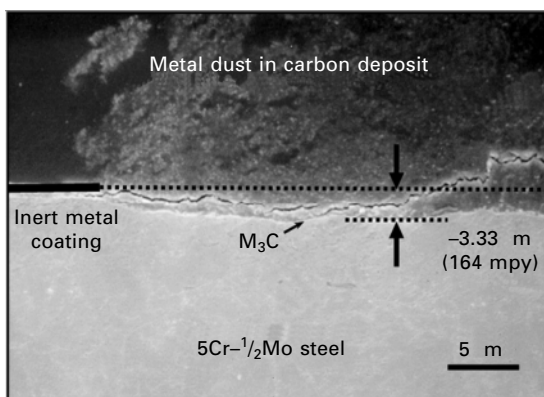
2.3 Results

2.3.1 Methodology for accurate corrosion quantification

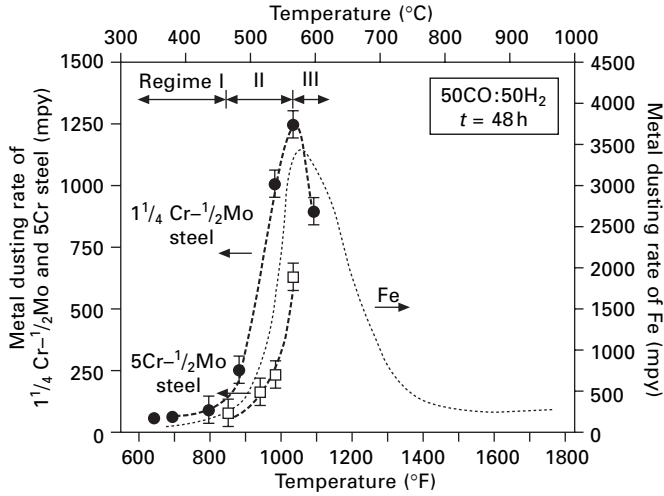
Since metal dusting is accompanied by carbon deposition, thermogravimetric analysis (TGA) provides some measure of the corrosion intensity based on the mass gain due to carbon dissolution and deposition. However, the actual quantification of metal loss cannot be done by TGA. In order to measure the metal dusting rate more accurately, the low-chromium steel samples used in the corrosion studies were first sputter-deposited with a thin strip of an inert metal. The metal recession with respect to the inert metal coating was then measured by cross-sectional SEM, and the corresponding corrosion rate was calculated. For example, after reaction at 950°F (510°C) for 7 h at the 50CO:50H₂ composition, the cross-sectional microstructure in Fig. 2.1 reveals the regions of general corrosion of 5Cr-¹/₂Mo steel: the arrows indicate the recession of the metal surface with respect to a coated region free of metal dusting. The measured recession is about 3.33 m, therefore the general metal dusting rate is 164 mils per year (mpy). Figure 2.1 also shows the typical microstructure after metal dusting. An M₃C surface layer and a carbon deposit consisting of dust particles can be readily observed in the regions of corrosion.

2.3.2 Effect of temperature on metal dusting corrosion of 1¹/₄Cr-¹/₂Mo and 5Cr-¹/₂Mo steels

The temperature dependence of the general corrosion rate of 1¹/₄Cr-¹/₂Mo and 5Cr-¹/₂Mo steels measured after 48 h of reaction in a 50CO:50H₂ gas



2.1 Cross-sectional SEM image showing a region of general corrosion of 5Cr-¹/₂Mo steel after reaction at 950°F (510°C) for 7 h in 50CO:50H₂.

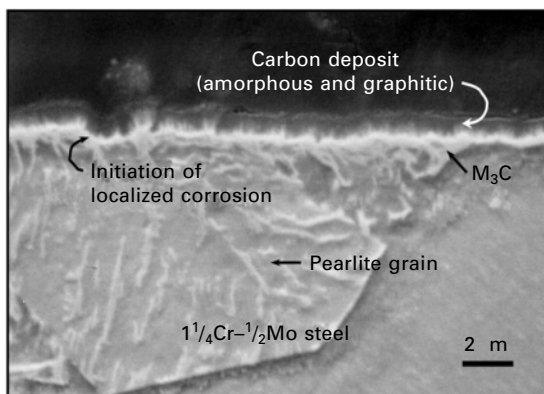


2.2 Temperature dependence of the metal dusting corrosion rate of $1\frac{1}{4}\text{Cr}-\frac{1}{2}\text{Mo}$ and $5\text{Cr}-\frac{1}{2}\text{Mo}$ steels in $50\text{CO}:50\text{H}_2$.

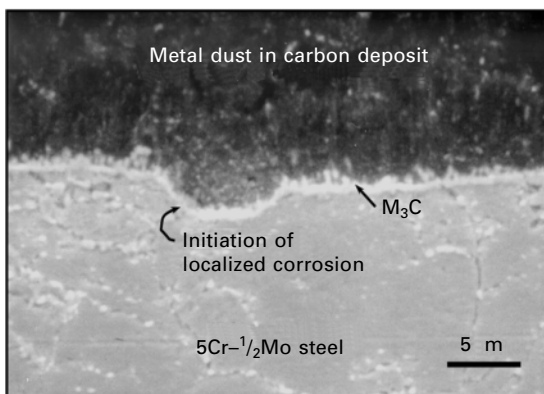
mixture is shown in Fig. 2.2. Also plotted is the general corrosion rate of pure Fe measured under the same conditions for comparison. A detailed discussion of the temperature dependence of the metal dusting of Fe has been published previously [14]. Similar to the behavior of Fe, the effect of temperature on the metal dusting rate can be divided into three regimes – these regimes are marked in Fig. 2.1. In regime I, which extends from 650°F (343°C) to 850°F (454°C), there is a gradual increase in corrosion rate with temperature with a very small slope. Between 850°F (454°C) and 1050°F (566°C), regime II, the corrosion rate undergoes a rapid rise, reaching a maximum at 1050°F (566°C). In regime III, which extends above 1050°F (566°C), the corrosion rate decreases with temperature. Each of these regimes is described below.

Regime I [$650\sim 850^\circ\text{F}$ ($343\sim 454^\circ\text{C}$)]

The rate of general corrosion in regime I is rather low (Fig. 2.2), increasing slowly with temperature. This regime is characterized by the formation of a surface M_3C layer on steel and deposited carbon on the surface. The cross-sectional SEM micrograph in Fig. 2.3 shows the typical microstructure of the general corrosion region of $1\frac{1}{4}\text{Cr}-\frac{1}{2}\text{Mo}$ steel after reaction at 700°F (371°C) for 48h in a $50\text{CO}:50\text{H}_2$ gas mixture. Also shown is a pre-existing pearlite grain composed of ferrite and cementite. Most surfaces of M_3C grains at the interface with carbon deposit are serrated. A few regions show the initiation of localized corrosion with the characteristic appearance of pitting. Above a critical stress level, the surface M_3C layer could break up,



2.3 Cross-sectional SEM image of $1\frac{1}{4}\text{Cr}-\frac{1}{2}\text{Mo}$ steel after reaction at 700°F (371°C) for 48h in $50\text{CO}:50\text{H}_2$.

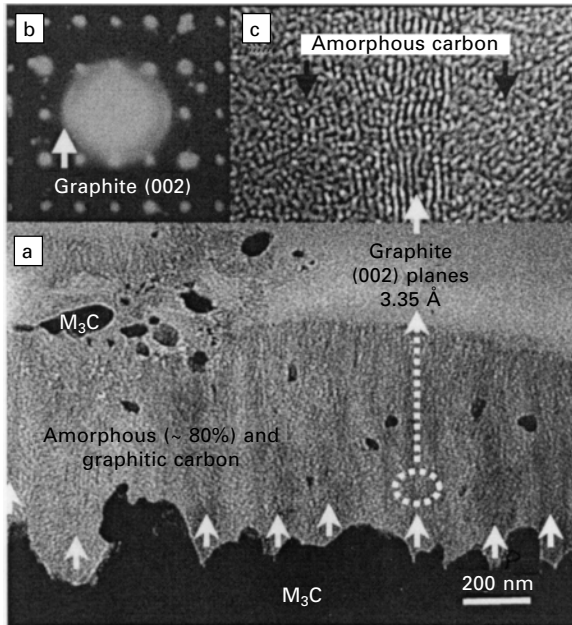


2.4 Cross-sectional SEM image of $5\text{Cr}-\frac{1}{2}\text{Mo}$ steel after reaction at 850°F (454°C) for 48h in $50\text{CO}:50\text{H}_2$.

resulting in debris of fractured M_3C that erupts upward through the carbon deposit. Thus stresses generated during the formation and growth of M_3C appear to be rather large in regime I. A similar observation has been made for the $5\text{Cr}-\frac{1}{2}\text{Mo}$ steel.

The cross-sectional SEM micrograph in Fig. 2.4 shows the microstructure of the general corrosion region after reaction at 850°F (454°C) for 48h in a $50\text{CO}:50\text{H}_2$ gas mixture. Serrated M_3C grains are readily observed at the interface with carbon deposit consisting of dust particles. Some regions also show the initiation of localized corrosion.

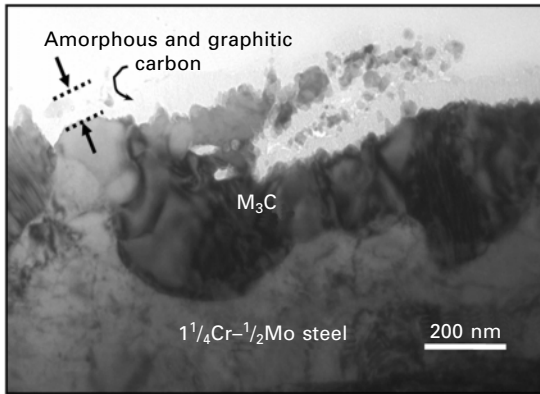
The bright field (BF) TEM image in Fig. 2.5a is a cross-section of the same sample of $1\frac{1}{4}\text{Cr}-\frac{1}{2}\text{Mo}$ steel (Fig. 2.3) showing a surface layer of M_3C and carbon deposit on M_3C . Relatively large particles within the carbon deposit are M_3C , which are probably dislocated from the surface M_3C layer



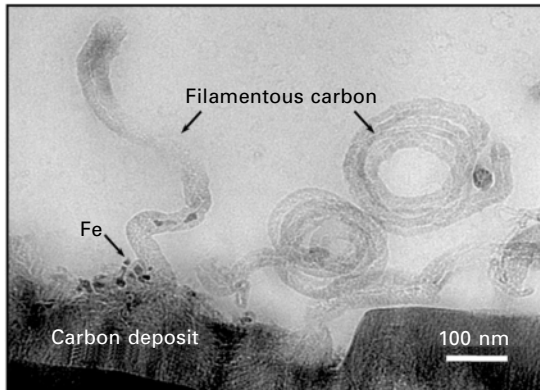
2.5 (a) Cross-sectional BF TEM image showing M_3C /carbon interface of $1\frac{1}{4}Cr-1\frac{1}{2}Mo$ steel subjected to metal dusting at $700^\circ F$ ($371^\circ C$) for 48 h in $50CO:50H_2$. (b) SAED pattern from the M_3C /carbon interface. (c) High-resolution TEM image showing graphite fringes.

and undergo further disintegration with continued carbon transfer. A selected area electron diffraction (SAED) pattern, taken in the M_3C /carbon interfacial area at a beam orientation of $B = [011] Fe_3C$, Fig. 2.5b, confirms that the carbon deposit is a mixture of amorphous and graphitic carbon. The reflection from graphite (002) plane is highly diffused, indicating amorphous carbon. Figure 2.5c, a high-resolution TEM image of the carbon deposit, confirms that the nature of the carbon deposit on the surface of M_3C is predominantly amorphous (~80%), the rest being graphitic. Amorphous carbon does not provide a pathway for iron atoms from dissociated M_3C to escape. Therefore, stress relief by fracturing of M_3C is characteristic of regime I.

The BF TEM image in Fig. 2.6 is another example which reveals the fracturing of M_3C carbide. In general, the proportion of amorphous carbon increases with decrease of temperature, being about 95% at $650^\circ F$ ($343^\circ C$). Figure 2.7 shows the cross-sectional TEM image of filamentous carbon at the outermost surface after corrosion of $1\frac{1}{4}Cr-1\frac{1}{2}Mo$ steel at $700^\circ F$ ($371^\circ C$) for 48 h in a $50CO:50H_2$ gas mixture. The outer surface of the carbon deposit, which is in contact with the gas phase, is profuse with filamentous carbon, whose growth has been catalyzed by metal particles located on the top of carbon deposit.



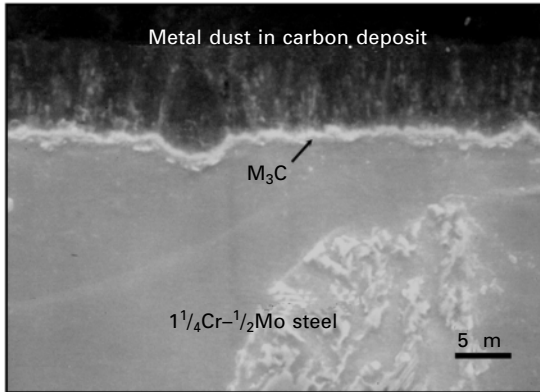
2.6 Cross-sectional BF TEM image showing steel/ M_3C /carbon interface of $1\frac{1}{4}Cr-\frac{1}{2}Mo$ steel subjected to metal dusting at $650^\circ F$ ($343^\circ C$) for 48 h in $50CO:50H_2$.



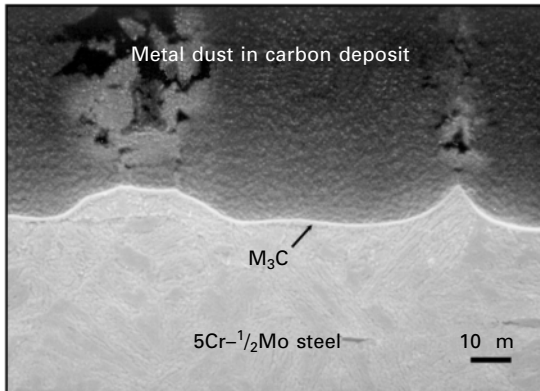
2.7 Cross-sectional BF TEM image showing filamentous carbon at the outer surface of carbon deposit after reacting $1\frac{1}{4}Cr-\frac{1}{2}Mo$ steel at $700^\circ F$ ($371^\circ C$) for 48 h in $50CO:50H_2$.

Regime II [850~1050 °F (454~566 °C)]

The cross-sectional SEM micrograph in Fig. 2.8 shows the microstructure characteristic of the general corrosion region of $1\frac{1}{4}Cr-\frac{1}{2}Mo$ steel after reaction at $900^\circ F$ ($482^\circ C$) for 48 h in a $50CO:50H_2$ gas mixture. Both general corrosion, characterized by the growth and dissociation of M_3C , and localized corrosion resulting from the rupture of M_3C , occur in regime II. The cross-sectional SEM micrograph in Fig. 2.9 shows the microstructure of the general corrosion region of $5Cr-\frac{1}{2}Mo$ steel after reaction at $1000^\circ F$ ($538^\circ C$) for 48 h in a $50CO:50H_2$ gas mixture. An M_3C surface layer and a carbon deposit consisting of dust particles can be observed in the regions of



2.8 Cross-sectional SEM image of $1\frac{1}{4}\text{Cr}-\frac{1}{2}\text{Mo}$ steel after reaction at 900°F (482°C) for 48 h in $50\text{CO}:50\text{H}_2$.

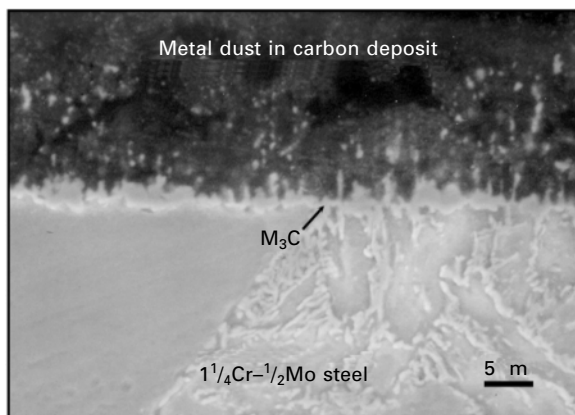


2.9 Cross-sectional SEM image of $5\text{Cr}-\frac{1}{2}\text{Mo}$ steel after reaction at 1000°F (538°C) for 48 h in $50\text{CO}:50\text{H}_2$.

corrosion. The competition between M_3C growth and M_3C dissociation at the carbide/carbon deposit interface characterizes general corrosion. The carbon deposit next to M_3C has a substantial amount of graphite in addition to amorphous carbon; the proportion of graphitic carbon increases with temperature. At the same time, general corrosion is favored since graphitic carbon offers a pathway for the migration of metal atoms arising from M_3C dissociation.

Regime III [$>1050^\circ\text{F}$ ($>566^\circ\text{C}$)]

The typical microstructure in the falling part of the curve (Fig. 2.2) is shown in Fig 2.10. A cross-sectional SEM micrograph of the corroded region of



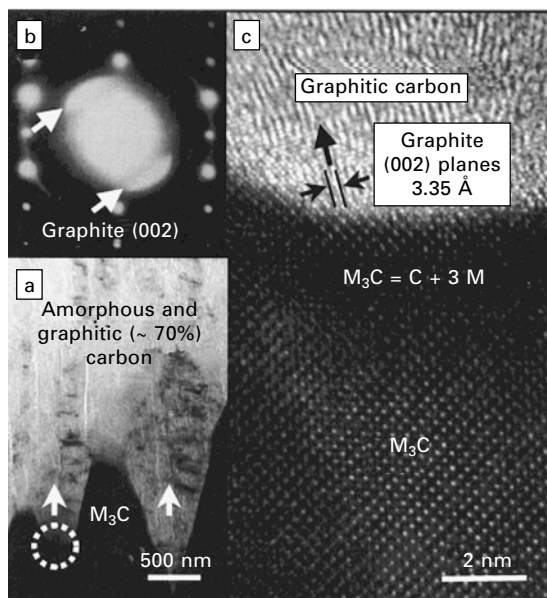
2.10 Cross-sectional SEM image of $1\frac{1}{4}\text{Cr}-\frac{1}{2}\text{Mo}$ steel after reaction at 1100°F (593°C) for 48 h in $50\text{CO}:50\text{H}_2$.

$1\frac{1}{4}\text{Cr}-\frac{1}{2}\text{Mo}$ steel was taken after reaction at 1100°F (593°C) for 48 h in a $50\text{CO}:50\text{H}_2$ gas mixture. M_3C growth and its dissociation are the principal corrosion processes in this regime. The average M_3C layer thickness is about two times larger as compared with the 900°F (482°C) case (Fig. 2.8). This suggests a slowing down in the M_3C dissociation rate, which is the principal rate-limiting step in this region.

The BF TEM image in Fig. 2.11a is a cross-section of the same sample of $1\frac{1}{4}\text{Cr}-\frac{1}{2}\text{Mo}$ steel (Fig. 2.10) showing a surface layer of M_3C and carbon deposit on M_3C . The M_3C at the interface is seen to be highly serrated. The carbon deposit is a mixture of amorphous and graphitic carbon. The nature of carbon layer next to M_3C is predominantly graphitic ($\sim 70\%$), the rest being amorphous. An SAED pattern, taken in the $\text{M}_3\text{C}/\text{carbon}$ interfacial area at a beam orientation of $B = [112] \text{Fe}_3\text{C}$, Fig. 2.11b, confirms that the carbon in this region is predominantly graphitic. The reflection from graphite (002) plane is highly oriented, indicating a preferred alignment of graphite. A high-resolution TEM image at the graphite/ M_3C interface, Fig. 2.11c, reveals graphite fringes throughout the interface. Graphitic carbon deposits on the M_3C layer in more or less perpendicular orientation to M_3C . The distance between basal planes in graphite is $\sim 3.35 \text{ \AA}$. On the other hand, the atomic diameter of Fe is 2.52 \AA . Thus it is not unreasonable to expect that the interplanar space of graphite provides a pathway for iron atoms from dissociated M_3C to escape to the outer surface of the graphite.

2.3.3 Metal dusting corrosion of 9Cr-1Mo and 13Cr steels

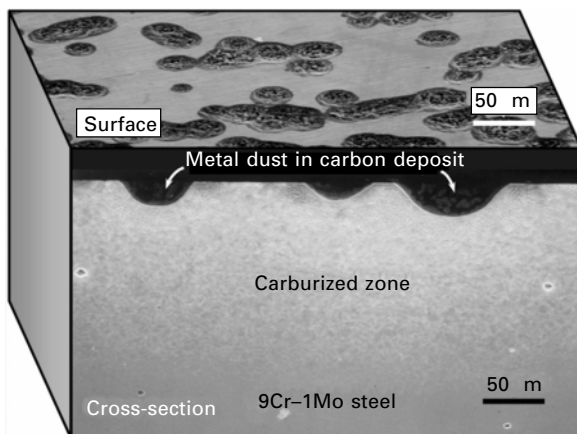
Low-chromium steels with higher levels of chromium added for corrosion resistance were tested in the temperature range, $900\text{--}1100^\circ\text{F}$ ($482\text{--}593^\circ\text{C}$).



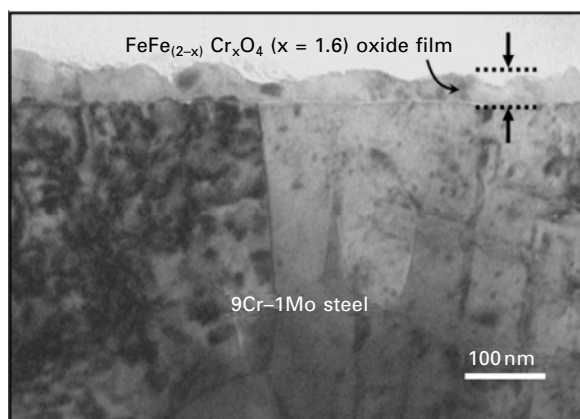
2.11 (a) Cross-sectional BF TEM image showing M_3C /carbon interface of $1\frac{1}{4}Cr-1\frac{1}{2}Mo$ steel subjected to metal dusting at $1100^\circ F$ ($593^\circ C$) for 48 h in $50CO:50H_2$. (b) SAED pattern from the M_3C /carbon interface. (c) High-resolution TEM image at M_3C /graphite interface.

Regardless of temperature, the steels after metal dusting displayed local outgrowths of carbon emerging through small pits that broaden with time. Figure 2.12 shows the characteristic appearance of such pitting on 9Cr–1Mo steel surface after reaction at $1000^\circ F$ ($538^\circ C$) for 48 h in a $50CO:50H_2$ gas mixture. Before taking this micrograph, a profuse amount of carbon that had grown preferentially from the pit area was removed. Pits of 50 μm average diameter are observed on the entire steel surface. Also shown is a cross-sectional SEM micrograph of the same sample. Carbon deposit within semi-spherical pits is revealed. Close to the steel surface, which was in contact with the corrosive gas environment, an internally carburized zone is also observed. The BF TEM image in Fig. 2.13 is a cross-section of the 9Cr–1Mo steel subjected to metal dusting at $1000^\circ F$ ($538^\circ C$) for 48 h in a $50CO:50H_2$ gas mixture showing a surface layer of spinel oxide film free of carbon deposit. This micrograph was taken from an area where pits were absent. The 50 nm thick continuous oxide layer has the chemical composition $Fe_{1.4}Cr_{1.6}O_4$.

The SEM micrographs in Fig. 2.14 show the microstructure of the localized corrosion region of 13Cr steel after reaction at $1000^\circ F$ ($538^\circ C$) for 48 h in a $50CO:50H_2$ gas mixture. The surface after removing the carbon deposit shows pits with an average diameter of about 100 μm . The cross-section

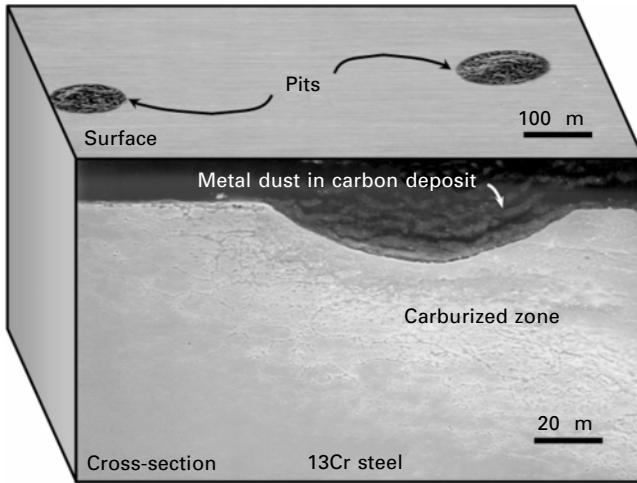


2.12 Surface and cross-sectional SEM images showing regions of localized corrosion of 9Cr-1Mo steel after reaction at 1000°F (538°C) for 48 h in 50CO:50H₂.

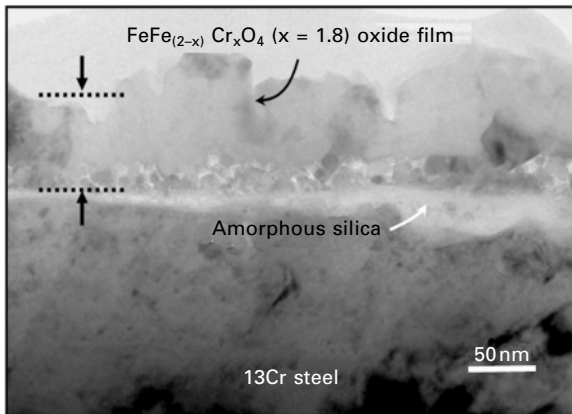


2.13 Cross-sectional BF TEM image showing a spinel oxide film layer of 9Cr-1Mo steel after reaction at 1000°F (538°C) for 48 h in 50CO:50H₂.

reveals the semi-spherical nature of a pit, internally carburized zone and carbon deposit with metal dust particles. The BF TEM image in Fig. 2.15 is a cross-section of the 13Cr steel subjected to metal dusting at 1000°F (538 °C) for 48 h in a 50CO:50H₂ gas mixture, showing a surface layer of spinel oxide film, free of carbon deposit. This micrograph was taken from the area where pits were absent. A roughly 80 nm thick continuous oxide layer with chemical composition of Fe_{1.2}Cr_{1.8}O₄ is observed on an amorphous silica sublayer. The presence of silicon in a steel with a sufficient amount of Cr can promote silica sublayer formation. The chromium content beneath the surface

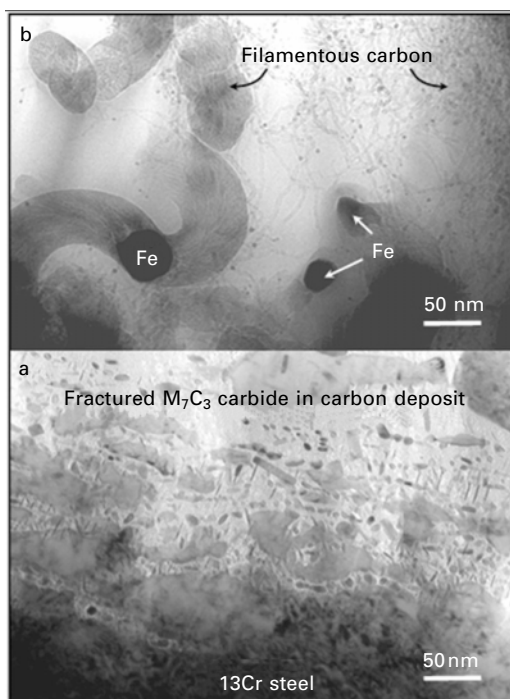


2.14 Surface and cross-sectional SEM images showing regions of localized corrosion of 13Cr steel after reaction at 1000°F (538°C) for 48 h in 50CO:50H₂.



2.15 Cross-sectional BF TEM image showing oxide film layers of 13Cr steel after reaction at 1000°F (538°C) for 48 h in 50CO:50H₂.

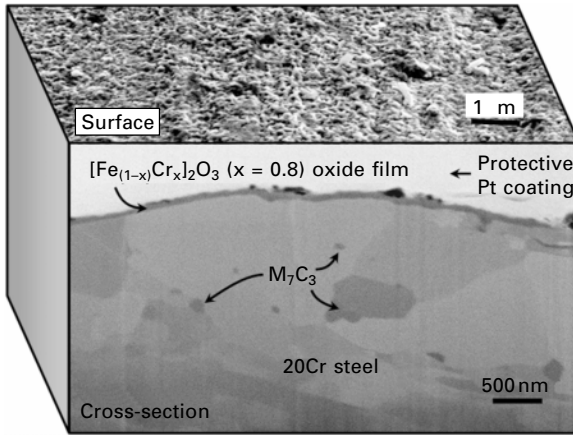
oxide film is depleted. Based on EDXS analysis, the Cr concentration is seen to be about 9.2 wt% compared with a bulk concentration of 12.7 wt%. The BF TEM image in Fig. 2.16a is a cross-section of the 13Cr steel taken from an area where a pit was present. Fractured M₇C₃ type carbides in carbon deposit were observed at the 13Cr steel surface. These carbides are stable and enriched in Cr with at least about 25 wt% Cr. The BF TEM image in Fig. 2.16b is taken from the outer surface of the carbon deposit which is in contact with the gas phase. Profuse amounts of filamentous carbon, whose growth has been catalyzed by metal particles, are observed.



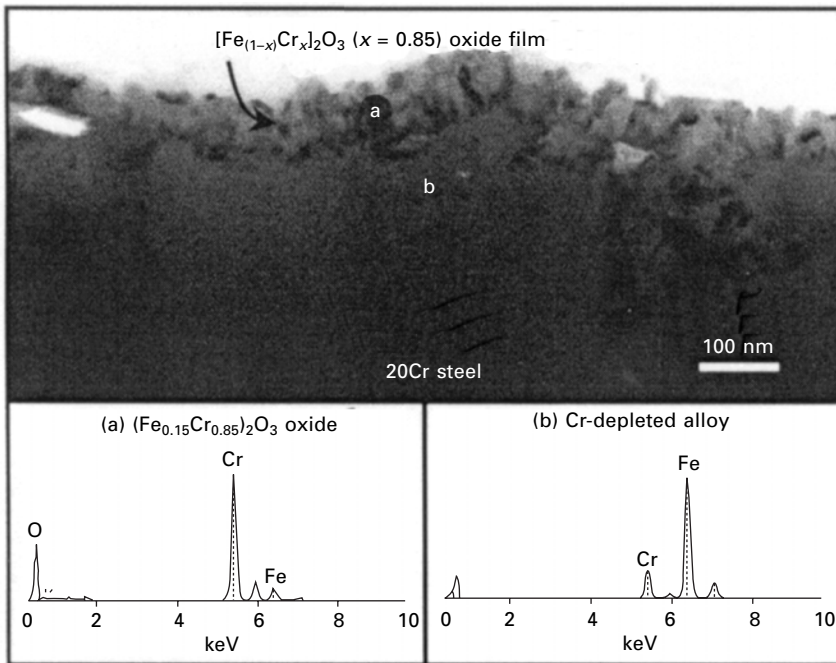
2.16 Cross-sectional BF TEM images of 13Cr steel taken from the pit area after reaction at 1000°F (538°C) for 48 h in 50CO:50H₂ showing (a) fracturing of M_7C_3 carbides at steel/carbon interface and (b) filamentous carbon at the outer surface of carbon deposit.

2.3.4 Metal dusting corrosion of 20Cr steel

Coupons of arc melted 20Cr steel were tested in the temperature range 900–1100°F (482–593°C). Coupons subjected to 50CO:50H₂ gas mixtures at 900°F (482°C) for 48 h showed regions of localized corrosion and regions of a Cr-rich surface oxide film similar to observations on the 13Cr steel. At a higher temperature of 1100°F (593°C), however, only a small amount of carbon was found on the surface and no pits were observed. The secondary electron images obtained by the FIB system in Fig. 2.17 show both the surface and cross-section of the 20Cr steel after metal dusting at 1100°F (593°C) for 48 h in a 50CO:50H₂ gas mixture. A surface layer about 90 nm thick of a continuous chromium-rich oxide film was observed. The chemical composition of the oxide film was analyzed as $(Fe_{0.2}Cr_{0.8})_2O_3$. Also shown are internally precipitated M_7C_3 -type stable carbides in the steel sub-surface region. The BF TEM image and EDXS patterns of both Cr-rich oxide and the steel shown in Fig. 2.18 were taken from a cross-section of the 20Cr steel subjected to metal dusting at 1100°F (593°C) for 48 h in a 50CO:50H₂ gas



2.17 Surface and cross-sectional secondary electron images obtained by FIB system showing an oxide film of 20Cr steel after metal dusting at 1100°F (593°C) for 48 h in 50CO:50H₂.



2.18 Cross-sectional BF TEM image showing an oxide film of 20Cr steel after reaction at 1100°F (593°C) for 48 h in 50CO:50H₂ and EDXS patterns taken from both chromia and the steel.

mixture. The BF TEM image reveals a surface layer of chromium-rich oxide film free of carbon deposit. The continuous oxide layer of about 100 nm thickness has the chemical composition $(\text{Fe}_{0.15}\text{Cr}_{0.85})_2\text{O}_3$. The chromium content beneath the surface oxide film was depleted. Based on EDXS analysis, the Cr concentration was found to be about 15.9 wt% compared with a bulk concentration of 20.2 wt%. Thus a rapidly formed Cr-rich oxide film on the ferritic steel surface is believed to provide initial protection against metal dusting. Based on results using other higher Cr steels we believe that the 20Cr steel will begin to metal dust at 1100 °F (593 °C) in about 200 h or so.

2.4 Discussion

2.4.1 Temperature dependence of metal dusting rate of $1\frac{1}{4}\text{Cr}-\frac{1}{2}\text{Mo}$ and $5\text{Cr}-\frac{1}{2}\text{Mo}$ steels

The temperature dependence of the general corrosion rate of $1\frac{1}{4}\text{Cr}-\frac{1}{2}\text{Mo}$ and $5\text{Cr}-\frac{1}{2}\text{Mo}$ steels can be correlated with the nature of carbon on the corroding surface. The rate of general corrosion in regime I was rather low (Fig. 2.2), increasing slowly with temperature. High-resolution TEM images of the M_3C /carbon interface at temperatures from 800 °F (427 °C) to 850 °F (454 °C) are very similar to the one at 700 °F (371 °C) (Fig. 2.5). The nature of the carbon layer next to M_3C was substantially amorphous. The proportion of graphitic carbon increased slightly with temperature in regime I. Since metal atoms from dissociated M_3C cannot migrate away through amorphous carbon, the corrosion rate was suppressed, leading to fracturing of surface M_3C . However, there was a very rapid increase in the rate of corrosion in regime II. This is due to a substantial increase in the content of graphitic carbon in the carbon deposit with temperature, which leads to a rapid rise in corrosion rate as a function of temperature in this regime.

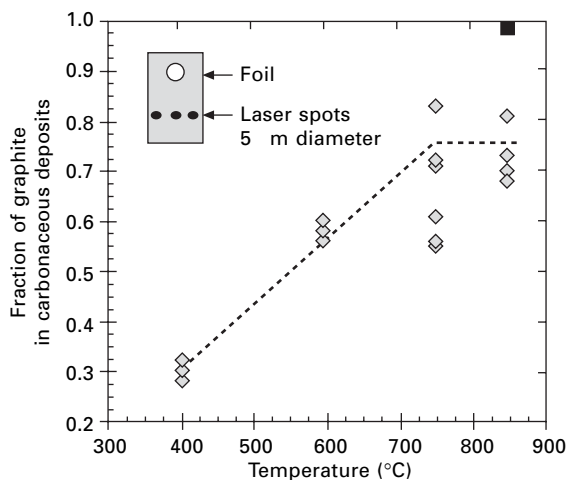
Graphitic carbon perpendicularly aligned to the M_3C surface provides a pathway for the intercalation and outward migration of metal atoms from the dissociation of M_3C . The carbon atoms that are generated attach to the graphite. The decrease in corrosion rate in regime III can be explained by considering the carbon activity profile at various interfaces, as previously reported in the case of pure Fe corrosion [14]. The decomposition of cementite is triggered by carbon deposition whereby the carbon activity at the M_3C /carbon interface becomes unity. The activity of carbon within M_3C decreases with increasing temperature. The nucleation rate of metal particles by cementite decomposition should correlate with the chemical potential difference of carbon in bulk cementite and graphite. Since this difference decreases with temperature in regime III, it qualitatively provides an explanation for the decrease in corrosion rate with temperature. Because of the slower

decomposition rate of M_3C , one would expect a thicker M_3C layer in this regime as temperature increases. This is confirmed by the cross-sectional SEM micrograph in Fig. 2.10.

2.4.2 Mechanism of metal dusting corrosion of $1^{1/4}Cr-^{1/2}Mo$ and $5Cr-^{1/2}Mo$ steels

Cross-sectional TEM images of the different interfaces and electron diffraction pattern from the carbon deposit revealed that the metal dusting mechanism of $1^{1/4}Cr-^{1/2}Mo$ and $5Cr-^{1/2}Mo$ steels was consistent with recent findings of Fe corrosion [14]. After formation of a M_3C surface layer on $1^{1/4}Cr-^{1/2}Mo$ and $5Cr-^{1/2}Mo$ steels in the carbon supersaturated environment, the carbon deposit on M_3C is essentially a mixture of amorphous carbon and graphitic carbon. If the nature of carbon deposit on the surface of M_3C is mostly graphitic, the graphite planes are oriented more or less perpendicular to the dissociating M_3C . Graphite deposition triggers M_3C dissociation with iron atoms intercalating and diffusing outward through the interspace between adjacent graphite planes. At the outer surface of the graphite, the metal atoms coalesce to metal particles, which catalyze filamentous carbon formation and are carried away.

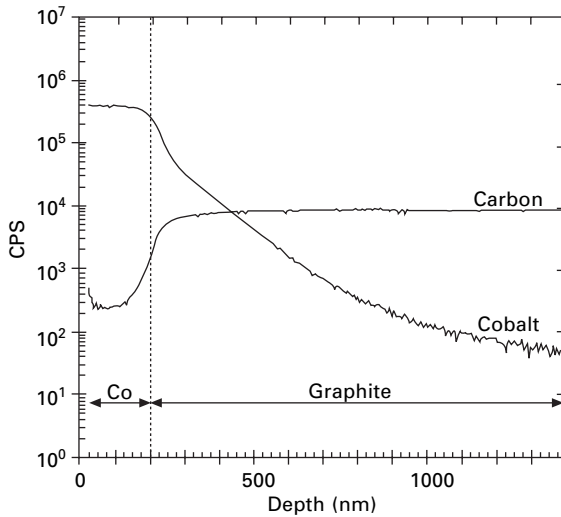
The role of the crystalline nature of deposited carbon in supporting intercalation mechanism was confirmed using Raman spectroscopy [15]. Carbonaceous deposit produced the decomposition of CO and H_2 at 400, 600, 750 and 850 °C on Co foil substrates were studied to investigate the nature of carbon layer adjacent to the Co substrate as a function of temperature. The predominant bands at 1581 cm^{-1} (G band, corresponding to graphite) and 1355 cm^{-1} (D band, corresponding to amorphous carbon) in the first order Raman spectrum excited at 514.5 nm were used to determine the fraction of graphite in carbonaceous deposits. For this study, the ratio of the G band intensity to the total intensity of the (G + D) bands was taken to represent the degree of order (fraction of graphite) in the deposits. Figure 2.19 shows the monotonic increase in this fraction with temperature up to 1320 °F (750 °C). For the 750 and 1110 °F (400 °C and 600 °C) temperatures, the fraction for the three positions (left, center, and right, shown as diamond data points) shows good sample homogeneity. For the 1320 and 1560 °F (750 and 850 °C) samples, additional measurements were made since the samples were found to be structurally more inhomogeneous, due primarily to the growth of highly ordered graphitic grains. The single square data point for the 1560 °F (850 °C) sample is representative of scattering from a single large graphite grain. These results suggest that the amorphous carbon becomes more highly ordered and graphitic as the temperature increases. The gradual increase in corrosion rate with temperature in Fig. 2.2 is consistent with this finding.



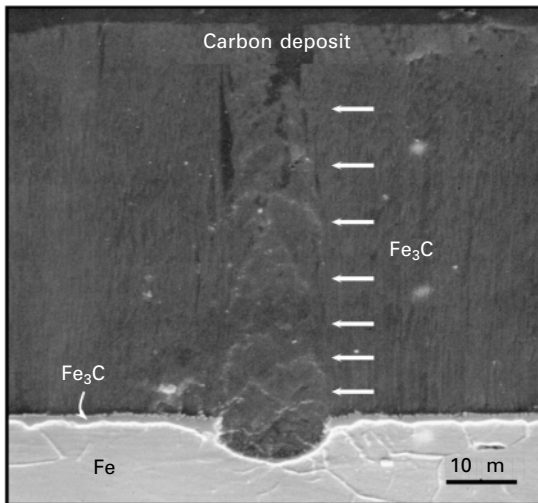
2.19 Fraction of graphite in carbonaceous deposits on the surface of cobalt foils after reaction at various temperatures for 7 h at $\text{CO}/\text{H}_2 = 25$.

In order to confirm the intercalation and diffusion of Co atoms through basal planes of graphite, a diffusion couple experiment was carried out [15]. A thin film of Co having a thickness of about 200 nm was sputter-coated on the face of single crystalline graphite rod in which graphite planes were aligned along the length of the rod. After annealing at 1020 °F (550 °C) for 1 h in an inert atmosphere, the concentration profile of cobalt and carbon in the vicinity of the Co/C interface was examined using a Cameca secondary ion mass spectrometer (SIMS). Sputter depth profiles for Co and C are shown in Fig. 2.20. The area examined was about 50 m^2 . A 15 keV beam of O_2^+ was used to excite positively charged secondary ions of Co and C. It is clearly seen that cobalt from the sputtered layer has diffused through basal planes of graphite.

In addition to the above mechanism, an additional corrosion mechanism is operative which involves the break-up of M_3C and the formation of ‘pits’ on the surface. If the nature of carbon deposit on the surface of M_3C is mostly amorphous, stress-induced fracturing of M_3C could occur in some regions since amorphous carbon does not provide a pathway for metal atoms from dissociated M_3C to escape. During the formation and growth of M_3C , stresses accumulate and lead the break-up of M_3C above a critical stress level. Once initial fracture of M_3C has occurred, corrosion preferentially continues in the same region. Figure 2.21 shows a region where the intensity of Fe_3C fracture is apparent from the way in which broken pieces are forced out, generating a ripple effect.



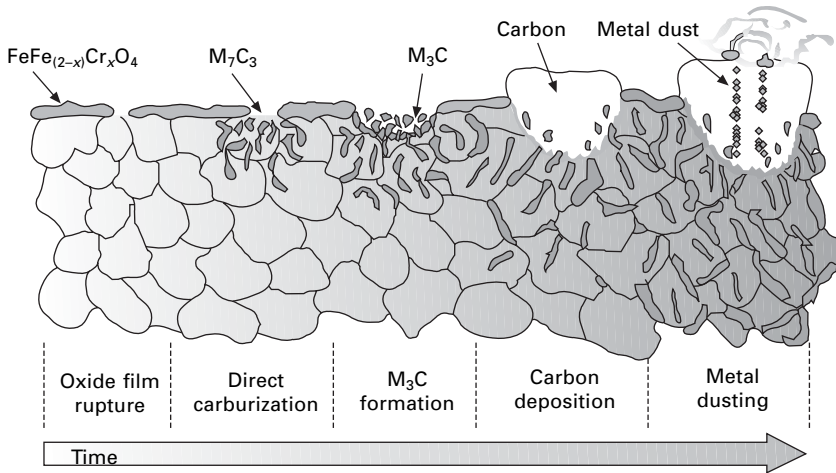
2.20 SIMS depth profile of cobalt and carbon for a Co coated (~200nm) graphite specimen after annealing at 1020°F (550°C) for 1 h in Ar atmosphere.



2.21 Cross-sectional SEM image showing ripples of fractured Fe_3C after metal dusting of iron at 930°F (500°C) for 7 h in 50CO:50H₂.

2.4.3 Mechanism of metal dusting corrosion of 9Cr–1Mo, 13Cr and 20Cr steel

For chromium steels with higher levels of chromium added for corrosion resistance, metal dusting in high carbon activity, low P_{O_2} environments



2.22 Schematic representation of the progression of low-Cr steel degradation.

involves a number of sequential steps leading to the final deterioration of the material. Detailed microscopy of such steels during corrosion has enabled the identification of specific stages in the steel degradation process. Five distinct stages are proposed: oxide film rupture, direct carburization, M_3C formation, carbon deposition and metal dusting. A schematic representation of the progression of steel degradation is shown in Fig. 2.22. The specific details of each stage are discussed below.

Oxide film rupture

Consider chromium steels having >9 pct chromium being brought to the process temperature in a mixed carburizing-oxidizing environment (e.g. $\text{CO}-\text{H}_2$), at temperatures that could range from 700 to 1200 °F (370–650 °C). Under these conditions, surface oxidation of the steel occurs leading to a two-layered oxide morphology. The outer layer is a spinel (M_3O_4), consisting mainly of Fe and Cr in the metallic sublattice. Beneath this is an oxide layer, which is predominantly chromia (Cr_2O_3) as observed in the 20Cr steel. Occasionally beneath this is a more stable oxide layer, which is amorphous silicon oxide, SiO_2 , as observed in the 13Cr steel. The oxygen partial pressure is sufficiently low to keep spinel and/or chromia surface oxide films thermodynamically stable. Figures 2.15, 2.16 and 2.18 are cross-sectional TEM micrographs, typical of this stage. The presence of a surface oxide film is evident. The formation of spinel and/or chromia films provides initial protection against carbon ingress. The steel is protected from carbon ingress in as much as carbon does not migrate through the oxide films. However, the

presence of defects and differential thermal contraction between steels and an oxide during oxide film growth could induce stresses that may result in rupture of the oxide film. Such local rupture of oxide film would lead to carbon migration into the steel.

Direct carburization

The steel is protected from carburization as long as spinel and/or chromia films are present on the surface. The processes of oxide film rupture and its reformation will continue until the chromium content in the steel subsurface reaches a value below which continuous oxide film formation on the surface becomes impossible. Figures 2.15 and 2.18 indicate that the Cr content beneath the surface oxide film is depleted. The observation clearly suggests that continued oxide formation and rupture will lead to continued Cr depletion. When a stage is reached at which the Cr content in the steel subsurface region is inadequate for oxide film formation, both oxygen and carbon from the environment have easy entry into the steel interior. Since the diffusivity of carbon is in general much higher than that of oxygen, carbon rapidly diffuses in, causing the precipitation of the M_7C_3 -type stable carbide in the steel subsurface region. Such direct carbon entry is a prelude to the rapid degradation of the steel. The different specific volumes of the steel and precipitating M_7C_3 -type carbide phase could introduce internal stresses. As an example, the specific volume of a typical low-chromium steel is $0.127 \text{ cm}^3/\text{g}$ and that of Cr_7C_3 is $0.145 \text{ cm}^3/\text{g}$. Therefore, carbide precipitation accompanied by volume expansion could generate internal stresses: above a critical stress level, the carbide breaks up. Fragments of fractured carbide are ejected through the carbon deposit as seen in Fig. 2.16. It is also evident that corrosion preferentially continues in the region where initial fracture of the carbide has occurred. This is probably due to increased stress build-up in the carbide on the concave steel surface resulting from the break-up of the first-formed carbide. The sequence of carbide formation and fracture leads to localized corrosion. Fractured M_7C_3 undergoes further disintegration with continued carbon transfer.

M_3C formation

Internally precipitated stable M_7C_3 carbides are rich in Cr. It is observed that about 25 wt% Cr is partitioned in the M_7C_3 carbide formed at the surface of 13Cr steel. Therefore, the base steel composition becomes further depleted in Cr, initially by Cr-rich spinel oxide film formation and rupture on the steel surface and later by Cr-rich stable carbide precipitation. The chromium concentration in the 13Cr steel immediately adjacent to the fractured carbide is seen to be about 4.5 wt% compared with a bulk concentration of 12.7 wt%

for 13Cr steel as shown in Fig. 2.16a. This Cr-depleted ferritic steel is now vulnerable for metastable surface M_3C formation. In the first step, carbon from the gas phase is transferred to the surface of Cr-depleted steel followed by its dissolution and diffusion into the steel. The steel gets supersaturated with carbon up to a certain thickness, which depends on temperature and the chemistry of the carbon-supersaturated gaseous environment. In the next step in corrosion a surface carbide of M_3C forms on Cr-depleted steel. This carbide is generally stable only in carbon-supersaturated environments, requiring a carbon activity in excess of unity to form.

Carbon deposition

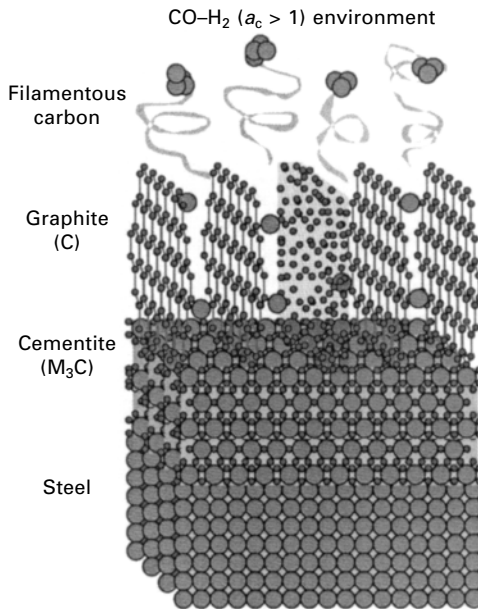
In the next stage in the corrosion sequence, carbon, principally graphite, deposits on the M_3C surface, whereby the carbon activity at the carbide/graphite interface drops to unity. This destabilizes the M_3C carbide and leads to its dissociation into iron particles and graphite. At this stage, metal dusting is in progress.

Metal dusting

One critical question relates to how the metal particles are carried away from the reaction interface in order to sustain corrosion. The above question has been considered by Pippel *et al.* [11], Wei *et al.* [18] and Chun *et al.* [12–15]. These investigators conclude that iron atoms can indeed migrate via intergraphitic planes away from the dissociation interface. Cross-sectional TEM was used to formulate the above conclusions. In a detailed investigation of the metal dusting corrosion of iron in CO–H₂ mixtures, Chun *et al.* [12, 14] found that the carbon deposit on Fe_3C is essentially a mixture of amorphous carbon and graphitic carbon. The proportion of graphitic carbon increases with temperature, accounting for nearly 80% of the carbon next to the Fe_3C . Moreover, the graphite planes are oriented more or less perpendicular to the dissociating Fe_3C , facilitating the intercalation of iron atoms into graphite. At the outer surface of the graphite deposit, filamentous carbon is catalyzed by iron particles. It is thus proposed that metal atoms from the dissociation of Fe_3C intercalate and diffuse out through intergraphitic planes and are ultimately carried away by filamentous carbon whose formation they catalyze. This mechanism is schematically illustrated in Fig. 2.23.

2.5 Summary

Metal dusting corrosion of steels containing about 1.25 to 20 wt% Cr was investigated in CO–H₂ environments at temperatures ranging from 650 °F (343 °C) to 1100 °F (593 °C). With increasing Cr content the corrosion rate



2.23 Schematic illustration of the mechanism of metal dusting corrosion.

decreases and the corrosion becomes more localized. The corrosion process is strongly influenced by the chromium content of the steels. For steels containing lower levels of chromium (e.g. $1\frac{1}{4}\text{Cr}-\frac{1}{2}\text{Mo}$ and $5\text{Cr}-\frac{1}{2}\text{Mo}$), metastable surface M_3C growth and its subsequent decomposition upon carbon deposition is the main corrosion mechanism. If graphitic carbon deposit is predominant on the M_3C surface, the graphite planes are mostly oriented perpendicular to the M_3C surface. In this case, iron atoms arising from M_3C dissociation intercalate into graphite and diffuse outward to the carbon-supersaturated environment where they coalesce and catalyze filamentous carbon formation. By contrast, if amorphous carbon deposit is predominant on the M_3C surface, stress-induced fracture of M_3C leads to surface pitting, since amorphous carbon does not provide a pathway for iron atoms from dissociated M_3C to escape.

Although the presence of a continuous surface layer of M_3C is characteristic of general corrosion, such a layer is absent in chromium steels with significant levels of chromium added for corrosion resistance (e.g. $9\text{Cr}-1\text{Mo}$ and 13Cr). In such steels, the formation of a Cr-rich spinel oxide film provides initial protection from carbon ingress. However, local rupture of the oxide film triggers rapid carbon diffusion into the steel and extensive internal carbide (M_7C_3) precipitation. Carbide precipitation is accompanied by volume expansion and therefore generates stresses, causing the carbides to break up.

Sequential Cr-rich oxide film formation and Cr-rich carbide precipitation lead to rapid depletion of Cr from the steel. At low enough Cr contents, the steel becomes vulnerable to metastable surface M_3C formation. Upon carbon deposition, metastable M_3C carbide subsequently decomposes into carbon and metal as corrosion progresses. Highly chromium alloyed steel (e.g. 20Cr) shows initial protection against metal dusting because of the formation of surface chromia films. However, the presence of defects and growth stresses may result in rupture of the oxide film. In this case, the steel would experience rapid carbon diffusion into the steel: a prelude to metal dusting.

2.6 References

1. R. F. Hochman, in *Proceedings of the 4th International Congress on Metallic Corrosion*, N. E. Hammer, Editor, p. 258, National Association of Corrosion Engineers, Houston, TX (1972).
2. R. F. Hochman, in *Proceedings of the Symposium on Properties of High Temperature Alloys with Emphasis on Environmental Effects*, Z. A. Foroulis and F. S. Pettit, Editors, p. 715, The Electrochemical Society, Pennington, NJ (1977).
3. R. F. Hochman and J. H. Burson, *Proceedings of API Division of Refining*, **46**, 331 (1966).
4. J. C. Nava Paz and H. J. Grabke, *Oxidation of Metals*, **39**, 437 (1993).
5. H. J. Grabke, R. Krajak and J. C. Nava Paz, *Corrosion Science*, **35**, 1141 (1993).
6. H. J. Grabke, R. Krajak and E. M. Muller-Lorenz, *Materials and Corrosion*, **44**, 89 (1993).
7. H. J. Grabke and E. M. Muller-Lorenz, *Materials and Corrosion*, **49**, 317 (1998).
8. S. Strauss and H. J. Grabke, *Materials and Corrosion*, **49**, 321 (1998).
9. J. Klower, H. J. Grabke and E. M. Muller-Lorenz, *Materials and Corrosion*, **49**, 328 (1998).
10. H. J. Grabke, *Materials and Corrosion*, **49**, 303 (1998).
11. E. Pippel, J. Woltersdorf and R. Schneider, *Materials and Corrosion*, **49**, 309 (1998).
12. C. M. Chun, J. D. Mumford and T. A. Ramanarayanan, *Materials and Corrosion*, **50**, 634 (1999).
13. C. M. Chun, J. D. Mumford and T. A. Ramanarayanan, *Journal of the Electrochemical Society*, **147** [10] 3680 (2000).
14. C. M. Chun, J. D. Mumford and T. A. Ramanarayanan, *Journal of the Electrochemical Society*, **149** [7] B348 (2002).
15. C. M. Chun, J. D. Mumford and T. A. Ramanarayanan, *Journal of the Electrochemical Society*, **150** [2] B76 (2003).
16. H. J. Grabke, C. B. Bracho-Troconis and E. M. Muller-Lorenz, *Materials and Corrosion*, **45**, 215 (1994).
17. H. J. Grabke, *Materials and Corrosion*, **54**, 736 (2003).
18. Q. Wei, E. Pippel, J. Woltersdorf and H. J. Grabke, *Materials and Corrosion*, **50**, 628 (1999).

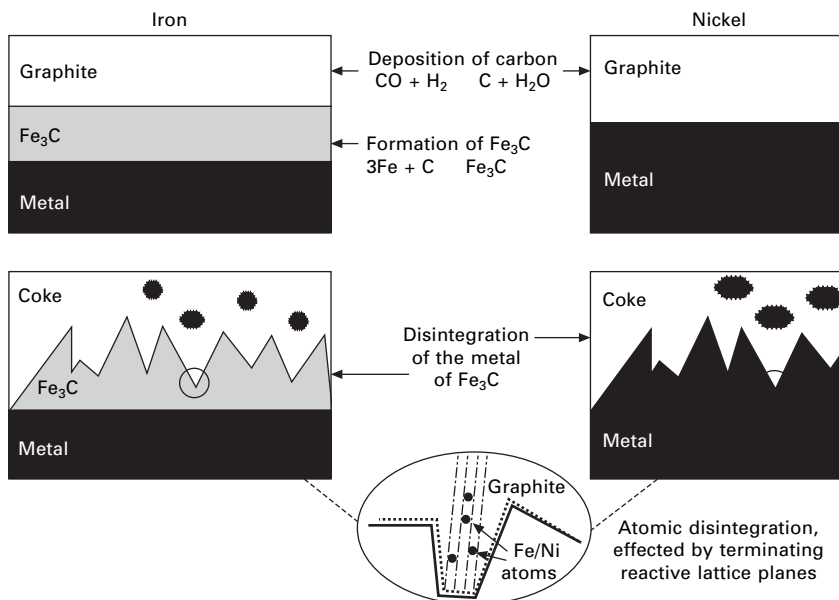
Microprocesses of metal dusting on iron–nickel alloys and their dependence on the alloy composition

E PIPPEL and J WOLTERSDORF, Max-Planck-Institut für Mikrostrukturphysik, Germany and H J GRABKE, Max-Planck-Institut für Eisenforschung, GmbH, Germany

3.1 Introduction

The phenomenon of metal dusting, which is known to be a carbon-induced catastrophic high-temperature corrosion process, leads to the disintegration of iron, steels, nickel and nickel-base alloys into a dust of fine metal particles and carbon. Extended research has been performed where this process was simulated in flowing CO–H₂–H₂O mixtures at temperatures between 400 and 800 °C and at a high carbon activity of the atmosphere, i.e. $a_c > 1$ (cf., for example Grabke *et al.* [1–4]). The morphological and chemical phenomena of the different reaction zones have been characterised using transmission electron microscopy (TEM) and analytical electron microscopy (AEM) techniques down to the nanometre range [5–9], and atomistic mechanisms of the metal dusting could be deduced. In the experiments the actual values of temperature, time and gas composition determine the disintegration state of the materials. For iron and steels, metal dusting proceeds via the formation and disintegration of a metastable carbide, cementite Fe₃C and, at very high carbon activities, additionally Hägg carbide Fe₅C₂. The thermogravimetric measurements revealed a quadratic increase of deposited carbon with time which is due to the catalytic effect of the fine metal particles (some 10 nm) formed in the coke [1, 2]. For nickel the disintegration proceeds by direct inward or internal growth of graphite (graphitisation), not via an instable carbide and leads to larger metal particles (some 100 nm) which are not wrapped by graphitic layers as in case of iron and steels. Thus, the nickel particles are less active catalysts for the carbon deposition than the iron particles, and therefore the mass gain by carbon deposition on nickel is much less than in case of iron and steels, and is linear with time [6].

Our previous results concerning the microprocesses of metal dusting on iron and nickel can be summarised as shown schematically in Fig. 3.1 (cf. Pippel *et al.* [7]): in both cases the process starts with the carbon transfer to the metal surface, delivered from the gas atmosphere and dissolving in the metal. After oversaturation, in case of iron (cf. left part of Fig. 3.1) a solid



3.1 Scheme of the fundamental processes of metal dusting on iron (left) and nickel (right).

state reaction takes place: the formation of cementite from the carbon oversaturated metal. The cementite is a barrier for carbon transfer into the metal, and graphite may nucleate on its surface. This causes a decrease of the carbon activity at the interface between graphite and cementite to $a_c = 1$, the cementite becomes unstable and starts to disintegrate, resulting in (i) the formation of a serrated interface and (ii) an agglomeration of iron atoms within the coke region. In contrast, in the case of nickel (cf. right part of Fig. 3.1), no carbide is formed, and the metal directly disintegrates, again forming a serrated interface to the coke area. In both cases, however, it could be demonstrated by TEM that on the atomic scale the metal dusting process has the same reaction principle, namely the more or less perpendicular deposition of basal planes of graphite on the substrate followed by their directed inward growth. During this process the free ends of the growing graphite lattice planes operate as active centres for the disintegration of the penetrated material (cf. lower encircled part of Fig. 3.1). The 'solved' metal atoms are transported along between the graphite planes, the inward growth of which is somewhat accelerated in iron and steels as the carbon atoms released during the carbide decomposition can be consumed immediately by the graphite lattice.

The different mesoscopic and microscopic phenomena of the disintegration mechanisms for iron and nickel described above exhibit two fundamental reaction paths of metal dusting. Therefore, successive alloying of iron with nickel should lead from one mechanism to the other. In particular, above a

certain nickel concentration or within a range of compositions of iron/nickel alloys the formation of metastable cementite should not occur. In addition, for thermodynamical reasons [10] it follows that a possible mixed carbide $(\text{Fe,Ni})_3\text{C}$ will be stable between 10 and 30 wt% Ni. To elucidate these questions in this chapter the microstructure and nanochemistry of different iron/nickel alloys after metal dusting will be reported, as obtained by both imaging and analytical transmission electron microscopy, particularly using energy-dispersive X-ray spectroscopy (EDXS). A comparison of the observations with those obtained with the pure metals should enable a deeper understanding of the fundamental mechanisms of metal dusting, resulting in further hints at corrosion prevention with special regard to the important Fe–Ni–Cr engineering alloys.

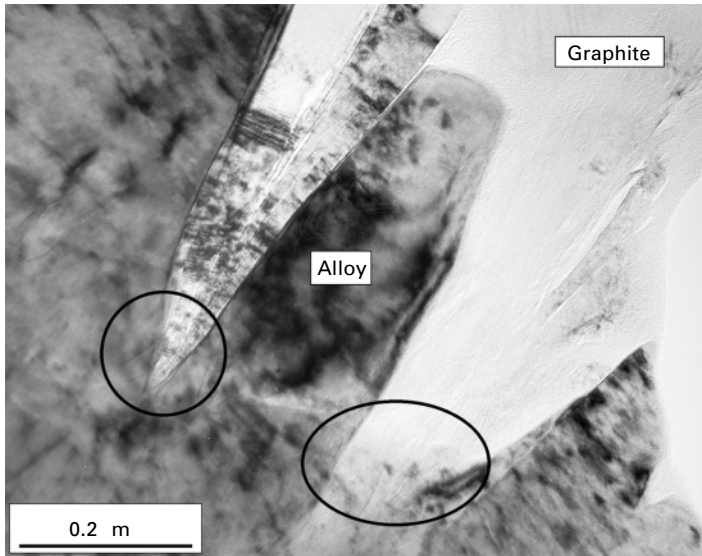
3.2 Experimental procedure

Thin foils of iron alloyed with 5, 10, 15 and 25 wt% nickel, respectively, were exposed to a flowing gas mixture of $\text{CO-H}_2\text{-H}_2\text{O}$ at a carbon activity of $a_c = 13$ at 650°C for 2 h to obtain a well-developed metal dusting attack.

Specimens for TEM were prepared by the standard cross-section technique: thin foils (10 μm) with metal dusting products on both sides were glued between ceramic blocks. Thereafter thin slices were cut with the interfaces of interest in perpendicular orientation to the surface, followed by grinding, dimpling and final Ar-ion thinning down to electron transparency using a segmental method in the PIPS (precision ion polishing system, Gatan 691). High-resolution electron microscope investigations were performed in a Philips CM20 FEG (200 keV) equipped with an X-ray detector (Ge crystal, Voyager system of Tracor) having an ultra-thin window. A cooling holder (Gatan model 636) was used to keep the specimen at liquid nitrogen temperature to reduce the carbon contamination during the nanoprobe analysis at a spatial resolution of about 2 nm in the scanning transmission mode.

3.3 Results

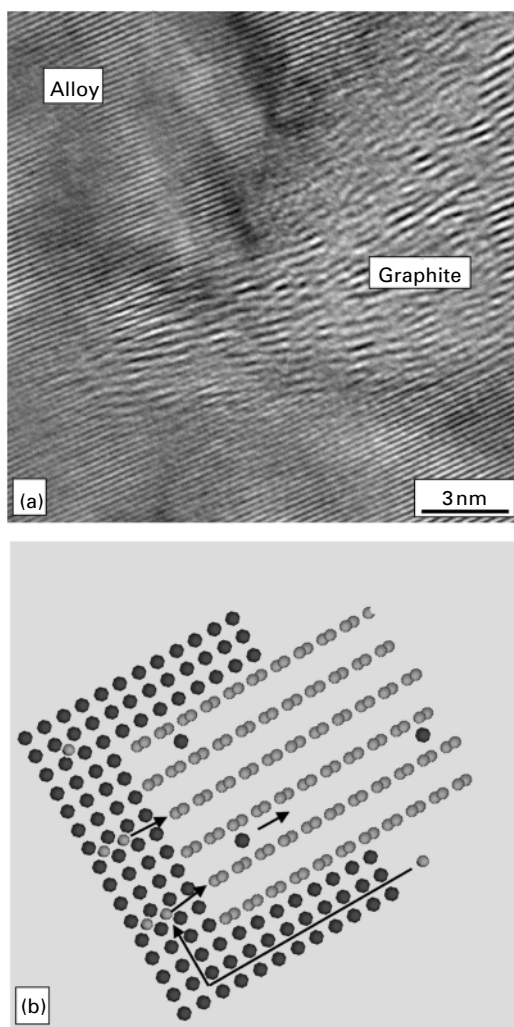
Figure 3.2 shows the typical details of the metal dusting process on the specimen with 25 wt% Ni, the alloy with the highest nickel content investigated. The interlayer region between the metal substrate (lower left of Fig. 3.2) and the carbon deposit (upper right) is presented. The surface of the metal grain appears serrated by tongue-shaped intrusions of graphite which penetrate the metal phase. The composition of the metal relics almost resembles that of the basic alloy (25–30 wt% Ni) with no intermediate carbide being found at the reaction front. Both the irregular, serrated disintegration of the metal and the absence of carbide lead to the conclusion that this alloy disintegrates in the manner of pure nickel as schematically shown in Fig. 3.1, right part. The



3.2 Interfacial region between an Fe/25 wt% Ni alloy and graphite after metal dusting (encircled: initial stages of the decay).

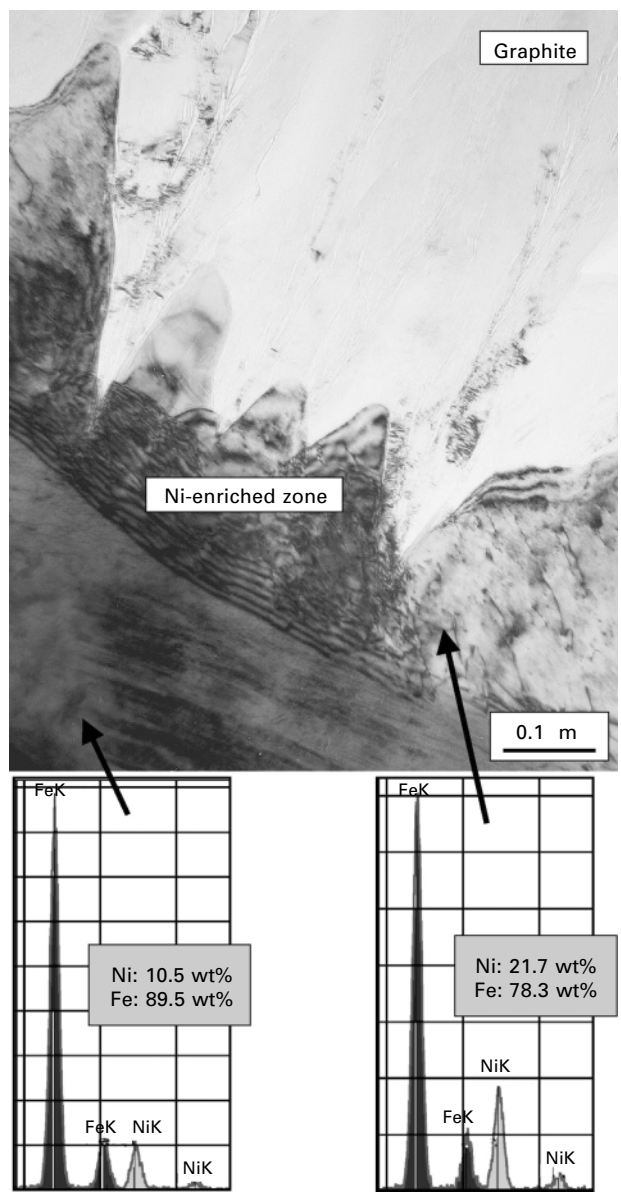
fibrillar structure of the carbon regions observable under diffraction contrast conditions indicates an oriented growth of the atomic basal planes of graphite in perpendicular orientation with respect to the original metal surface. Furthermore, two regions of local decay are marked in Fig. 3.2.

Such a region is shown in the high-resolution image (Fig. 3.3a), which demonstrates both the local metal decay and the oriented growth of the graphite basal lattice planes. The penetration of the graphite planes into the metal (the latter exhibits more close and regular lattice planes) suggests that especially the reactive free ends of the graphite lattice planes cause the disintegration of the metal phase, by fixing the dissolved carbon from the oversaturated alloy. In particular, the immediate front of the graphite growth can be observed in the lower left in Fig. 3.3a, being indicated by an overlap of metal and graphite lattice planes as well. Metal atoms, dissolved during this process, can diffuse between the widely separated graphitic basal planes into the coke region and form particles which further catalyse the carbon deposition (cf. Fig. 3.1). In the case of nickel and high-Ni alloys, however, most metal particles in the coke stem from the fragmentation of the metal phase by the inward growing graphite tongues. The scheme in Fig. 3.3b demonstrates this concept in more detail, using an [100] oriented austenite crystal as an example. At interfaces where the graphite planes are running parallel to the metal surface, the decomposition may be retarded or becomes impossible at all, so that on nickel and high-Ni alloys metal dusting is orientation dependent [11].



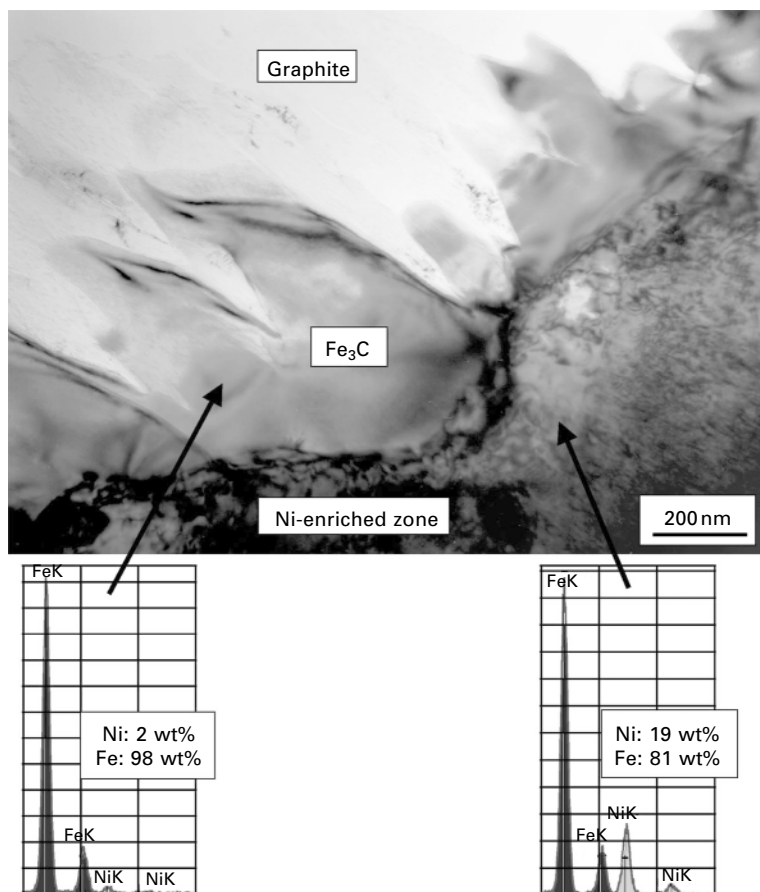
3.3 (a) High-resolution electron microscopy image of the initial stages of the decay of an Fe/25 wt% Ni alloy saturated with carbon. (b) Model of this process (black: metal atoms, grey: carbon atoms).

Even by reducing the nickel content of the alloy down to 10 wt% no intermediate carbide is formed after oversaturation. But, as already implied from alloys with higher Ni contents, a considerable enrichment of nickel near the reacting surface is observed, as shown in Fig. 3.4. Clearly two regions can be distinguished from their different diffraction contrast phenomena in the metal (lower left). The X-ray peaks of Fe and Ni incorporated in the figure demonstrate an increase of the Ni content up to almost 21 wt% in the surface layer (right) with a sharp boundary to the basic alloy (left, 10.5 wt%



3.4 Ni-enriched layer next to the inward growing graphite on an Fe/10 wt% Ni alloy after metal dusting (EDX spectra below).

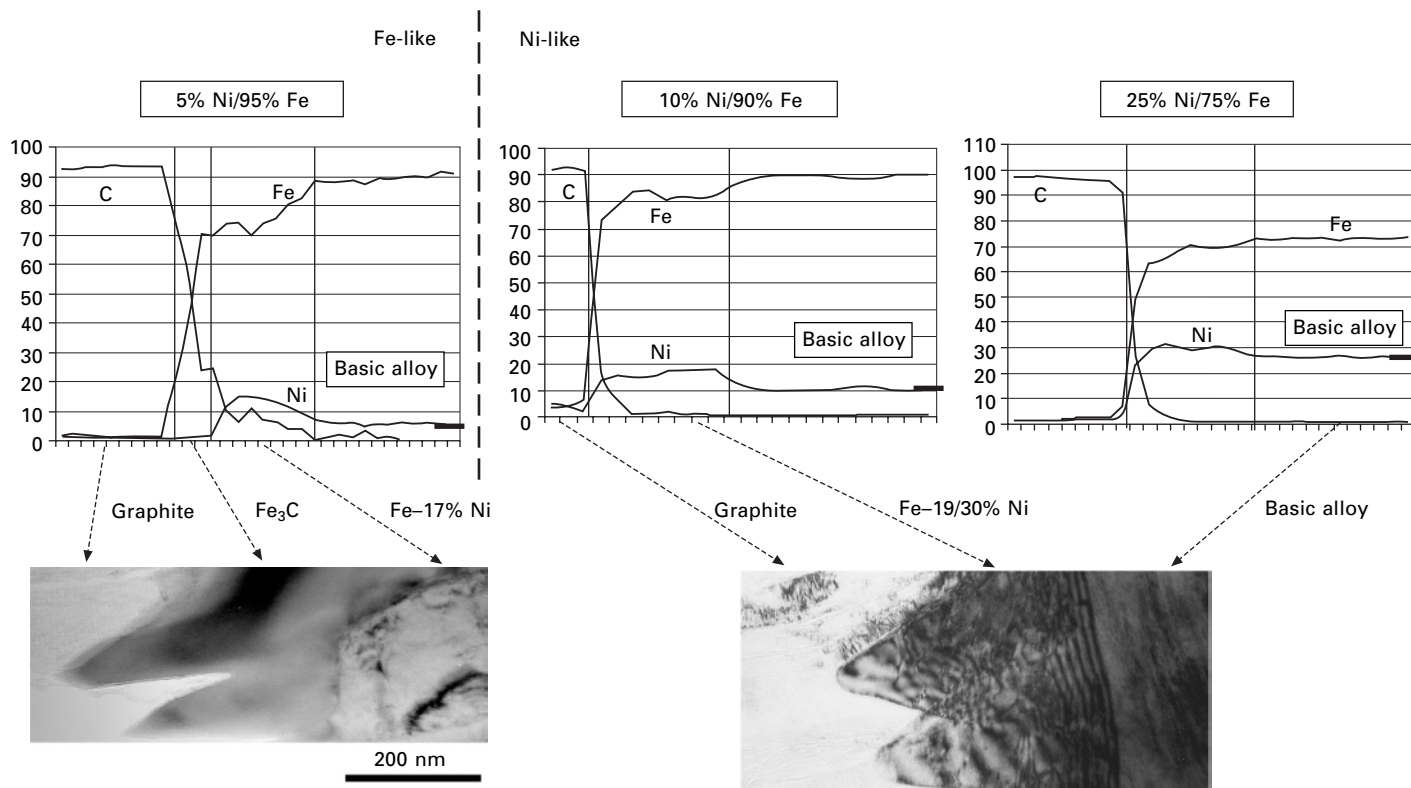
Ni). As will be discussed later, this finding can be understood as a depletion of iron near the metal surface. Nevertheless, the serrated structure of the reaction surface in Fig. 3.4 and the absence of carbide indicate a metal dusting attack similar to that of pure nickel.



3.5 Formation of a steady state carbide layer on an Fe/5 wt% Ni alloy during metal dusting (EDXS spectra below).

In the case of the alloy with only 5 wt% nickel, the metal dusting process has changed in the way that an intermediate carbide (Fe₃C) has formed on the metal surface, as revealed in Fig. 3.5. The EDX analysis indicates a Ni content of only 2 wt% in the carbide (left spectrum in Fig. 3.5; carbon is not shown in the spectrum). Again, an iron-depleted zone follows next to the carbide, but with a higher relative nickel increase (right spectrum in Fig. 3.5). From these findings it can be deduced that at this low Ni content in the basic alloy the metal dusting process has changed from that of pure nickel to that of pure iron.

The results concerning the micromechanisms of metal dusting on iron–nickel alloys are summarised in Fig. 3.6, together with additionally performed and quantified EDX analyses along lines across the observed reaction areas. The diagrams reflect the chemical composition (in wt%, accumulated to



3.6 Line profiles of the composition (EDXS) of the near-surface areas of different Fe/Ni alloys after metal dusting (bottom: examples of related TEM images).

100%) of the individual disintegration products near the substrate surface. Two important features are worth noting:

1. In all investigated materials a depletion of iron (or an increase in Ni content, respectively) has developed in a near-surface zone a few hundred nanometres in thickness. The relative iron depletion increases with the Ni content decreasing, up to a value of about 13% in case of the Fe 5 wt% Ni alloy.
2. No intermediate surface carbide has formed upon metal dusting of the alloys, down to a Ni content of 10 wt%. Only on the alloy with 5 wt% Ni was a thin layer of cementite observed. Thus, at this composition the metal dusting mechanism has changed from that typical for pure nickel to that valid for iron.

3.4 Discussion

Unfortunately, to understand the above behaviour, the Fe/Ni phase diagram seems to be rather unsuitable. This is because the equilibrium adjusts very sluggishly at the relatively low temperatures (650°C) and the high iron content used here. On the other hand, the α -transition in this system comprises a relatively high hysteresis, preventing an exact definition of the phase situation [12]. Further on, the metal dusting process is generally a non-equilibrium one, and arguing in terms of equilibrium phases is of limited value.

From our point of view the depletion of iron observed near the surface during the metal dusting attack of Fe–Ni alloys should be caused by a selective corrosion effect similar to that found in oxidation of these alloys [13]. Such a selective corrosion will be caused by the lower chemical interaction of C and Ni, compared with the interaction of C and Fe, as known from the solid solution and carbide thermodynamics for these systems [14]. The observed dissolution of iron in the graphite may also explain the enhanced coke formation of Fe–Ni alloys in the range of some 10% of Ni as described in [15], resulting from the catalytic effect of small iron particles in the coke. Otherwise, the formation of $(\text{Fe, Ni})_3\text{C}$ was not observed in the present study although it should be possible for thermodynamic reasons [10] as already mentioned. Of course, metal dusting processes have a pronounced non-equilibrium character, in particular if the special kinetics of selective corrosion mechanisms change the alloy composition continuously with time. Following this basic idea also the interesting result can be interpreted that the existence of cementite (Fe_3C) is restricted to a nickel content of about 5 wt% at maximum. Obviously at such low nickel content the formation of a thin layer of Fe_3C is in steady state with its simultaneously occurring decay at the interface to the graphite ($a_c = 1$). Then, at higher Ni concentrations (>10 wt%) the formation of the carbide becomes slower than its decay. Such kinetics can occur if the carbide

formation does not proceed within the bulk metal (as in the case of pure iron); but, rather, as a consequence of a selective outward diffusion of the iron from the alloy (as in the present case). This special kind of diffusion kinetics appears to be the reason for the slowing down of the carbide formation below the critical amount for its decomposition, in accordance with the results of our present investigations that no carbide layer is established at nickel contents > 5 wt%.

Overall, it turns out that the system iron/nickel favours the disintegration mechanism characteristic for pure nickel, even at very low nickel content. The diffusion kinetics described above locally enables the necessary stoichiometric shifts: If the amount of the selectively removed iron exceeds the decay of the formed carbide, then cementite will be observed.

3.5 Acknowledgement

Support of this study by the Deutsche Forschungsgemeinschaft is gratefully acknowledged.

3.6 References

1. H.J. Grabke, R. Krajak, E.M. Müller-Lorenz, S. Strauß: *Werkstoffe und Korr.* **47** (1996) 495.
2. H.J. Grabke, C.B. Bracho-Troconis, E.M. Müller-Lorenz: *Werkstoffe und Korr.* **45** (1994) 215.
3. H.J. Grabke, R. Krajak, E.M. Müller-Lorenz: *Werkstoffe und Korr.* **44** (1993) 89.
4. H.J. Grabke: *Solid State Phenomena* **41** (1995) 3.
5. E. Pippel, J. Woltersdorf, H.J. Grabke, S. Strauß: *Steel Research* **66** (1995) 217.
6. R. Schneider, E. Pippel, J. Woltersdorf, S. Strauß, H.J. Grabke: *Steel Research* **68** (1997) 326.
7. E. Pippel, J. Woltersdorf, R. Schneider: *Materials and Corrosion* **49** (1998) 309.
8. Q. Wei, E. Pippel, J. Woltersdorf, H.J. Grabke: *Materials and Corrosion* **50** (1999) 628.
9. C.M. Chun, J.D. Mumford, T.A. Ramanarayanan: *Materials and Corrosion* **50** (1999) 634.
10. H.J. Grabke, R. Krajak, J.C. Nava Paz: *Corrosion Science* **35** (1993) 1141.11
11. Q. Wie, L. Pippel, J. Woltersdorf, S. Strauß, H.J. Grabke: *Materials and Corrosion* **51** (2000) 652.
12. W. Bergmann: *Werkstofftechnik*, Carl Hauser Verlag, München/Wien 2002.
13. A. Rahmel, W. Schwenk: *Korrosion und Korrosionsschutz von Stählen*, Verlag Chemie, Weinheim/New York 1977.
14. O. Kubaschewski, C.B. Alcock: *Metallurgical Thermochemistry*, Pergamon Int. Library, Oxford 1979.
15. S. Strauß, R. Krajyk, H.J. Grabke: *Materials and Corrosion* **50** (1999) 622.

Metal dusting behaviour of welded Ni–base alloys with different surface finishes

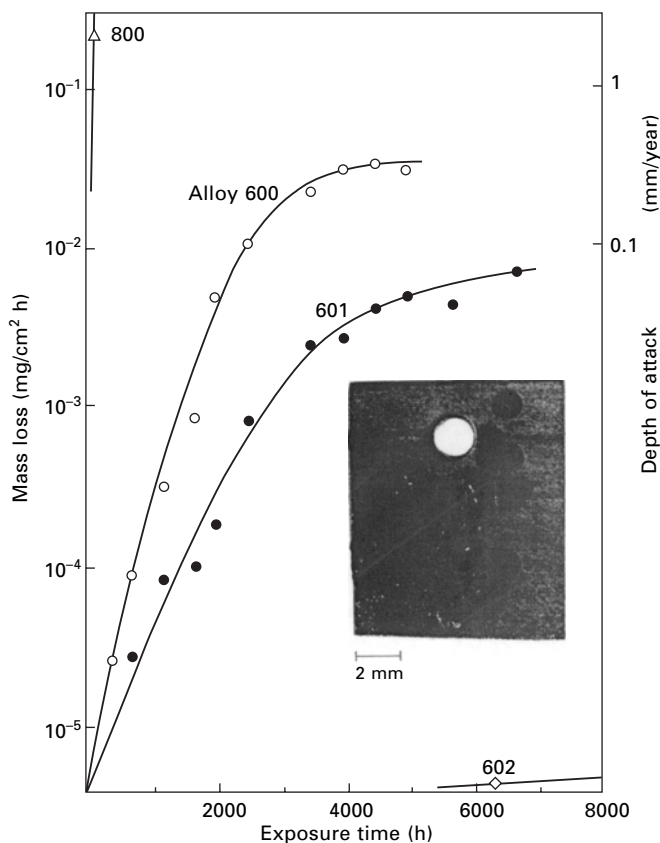
HJ GRABKE and EM MÜLLER-LORENZ,
Max-Planck-Institut für Eisenforschung GmbH, Germany and
M ZINKE, Institut für Füge- und Strahltechnik, Germany

4.1 Introduction

The aim of this study was to investigate the metal dusting resistance of welded specimens made of the alloys 800H, 600H, 601H and 602CA. These materials had been tested before, in discontinuous exposures at 650 °C in flowing H_2 –CO– H_2O mixtures [1–5]. In these tests Alloy 800H was attacked strongly after a few hours, the metal dusting attack on Alloys 600 and 601 spread gradually over the surface and led to relatively low metal wastage rates, whereas alloy 602CA was nearly not attacked at all up to 10000h, see Fig. 4.1. Accordingly, Alloy 602CA (and also Alloy 690 which behaves similarly [2, 3]) were considered as most resistant against metal dusting and recommended for applications under strongly carburizing conditions all over the world – and as yet no failures are known [6]. However, for welded materials one may expect a more susceptible behaviour of the weldment and of the heat-affected zone (HAZ), therefore the present study was conducted in cooperation between Max-Planck-Institut für Eisenforschung (MPI) and Institut für Füge- und Strahltechnik, Univ. Magdeburg (IFST).

4.2 Experimental procedure

At the IFST welded specimens were prepared in 10 different versions concerning base and weld metal, welding process and/or surface finish; see Table 4.1. Two samples of each version were exposed in two horizontal tube furnaces at 600 and 650 °C in a flowing H_2 –24% CO–2% H_2O atmosphere. The first exposures were only for 24h, but the samples with Alloy 800 as a base material already showed vast coking because of a strong metal dusting attack; see Table 4.2. Therefore these samples had to be excluded from further exposures after 72h or 552h. They were replaced by two other specimens (6/3 and 6/4) based on Alloy 600 but with special surface treatments: sand blasting and pickling. The exposures were interrupted after different periods, to remove the corrosion product, i.e. the coke which was scratched



4.1 Increase of metal wastage rates with time, determined for Alloys 800, 600, 601 and 602 in discontinuous exposures at 650°C in a flowing H₂-CO-H₂O mixture [1 – 5], photo of the Alloy 601 H sample after 6700 h.

from the samples, collected and weighed; see Table 4.3. Generally, the formation of coke indicates the start and extent of metal dusting, but in the first exposures some coking may be due to fine metal particles, stemming from the welding and brushing.

Table 4.4 gives the data for the later exposures 7–11, and it must be noted that here formation rates of coke are given, related to surface area and time. In addition Table 4.4 lists the Ni content of the coke formed in exposure 11, and the metal wastage rate, calculated from the amount of coke and its metal content. This metal wastage rate, reached in the final exposure, gives no evidence of the metal wastage in mm/year or pit growth rate, since generally not all the surface was affected by metal dusting, and the behaviour of base and weld material was different. More information on the metal dusting

Table 4.1 Tested samples: materials, surface finish and welding process (TIG = Tungsten Inert Gas Welding, MMAW = manual metal arc welding, SMAW = shielded metal arc welding)

Number	Base metal	Welding process		Consumable	Surface
3	Alloy 602CA	Root layer	TIG	Nicrofer S 6025	Brushed
		Filling layer	MMAW	UTP 6225 Al	
		Cap layer	MMAW	UTP 6225 Al	
4	Alloy 601H	Root layer	TIG	Nicrofer S 6025	Brushed
		Filling layer	MMAW	UTP 6225 Al	
		Cap layer	MMAW	UTP 6225 Al	
5	Alloy 800H	Root layer	TIG	Nicrofer S 7020	Brushed
		Filling layer	MMAW	UTP 068 HH	
		Cap layer	MMAW	UTP 068 HH	
6/1	Alloy 600H	Root layer	TIG	Nicrofer S 7020	Brushed
		Filling layer	MMAW	UTP 068 HH	
		Cap layer	MMAW	UTP 068 HH	
6/2	Alloy 600H	Root layer	TIG	Nicrofer S 7020	Ground
		Filling layer	MMAW	UTP 068 HH	
		Cap layer	MMAW	UTP 068 HH	
6/3	Alloy 600H	Root layer	TIG	Nicrofer S 7020	Sandblasted
		Filling layer	MMAW	UTP 068 HH	
		Cap layer	MMAW	UTP 068 HH	
6/4	Alloy 600H	Root layer	TIG	Nicrofer S 7020	Pickled
		Filling layer	MMAW	UTP 068 HH	
		Cap layer		UTP 068 HH	
7	Alloy 602 CA	Root layer	TIG	Nicrofer S 6025	Brushed
		Filling layer	TIG	Nicrofer S 6025	
		Cap layer	TIG	Nicrofer S 6025	

Table 4.1 Continued

Number	Base metal	Welding process		Consumable	Surface
8	Alloy 800H	Root layer	TIG	Nicrofer S 7020	Brushed
		Filling layer	TIG	Nicrofer S 7020	
		Cap layer	TIG	Nicrofer S 7020	
9	Alloy 600H	Root layer	TIG	Nicrofer S 7020	Brushed
		Filling layer	TIG	Nicrofer S 7020	
		Cap layer	TIG	Nicrofer S 7020	
10	Alloy 601H	Root layer	TIG	Nicrofer S 6025	Brushed
		Filling layer	TIG	Nicrofer S 6025	
		Cap layer	TIG	Nicrofer S 6025	
11	Alloy 800H Alloy 602CA	Root layer	TIG	Nicrofer 7020	Brushed
		Filling layer	SMAW	UTP 068 HH	
		Cap layer	SMAW	UTP 6225 AI	

Table 4.2 Amount of corrosion product (coke) after each exposure (mg/sample)

	Base alloy weldment	Welding process surface finish	t (°C) t (°C)	24h 24h	24h 48h	24h 72h	480h 552h
5	Alloy 800 UTP 068HH	TIG/MMAW brushed	600 650	556.4 35.4	681.4 37.7	170.5 121.4	* *
8	Alloy 800H S 7020	TIG/ brushed	600 650	106.4 22.4	188.6 24.5	37 943.8	8925.6 *
11	Alloy 602 CA Alloy 800H/ UTP 068HH UTP 6225 Al	TIG/MMAW brushed	600 650	172.5 25.1	221.9 43.9	39.7 58.5	2707.0 314.1

* Not continued.

attack could be derived from metallographic cross-sections which were taken after the exposures 1–6 at 2604.5 h, and after the exposures 7–11 at 6025 h.

4.3 Results

4.3.1 Alloy 800 – samples 5, 8 and 11 (with 602CA)

The samples made of Alloy 800 were attacked severely already in the first exposures for only 24 h. Owing to the vast coke formation the exposures of these samples were stopped after 72 or 552 h (see Table 4.2). The part of sample 11 consisting of Alloy 602 was not attacked, but on the other samples the attack of Alloy 800 started from the zone beside the weld (see Fig. 4.2 a,b,c). Obviously this HAZ is the starting area of metal dusting, as can also be seen from the metallographic cross-sections. Here the material is carburized and corroded widely, whereas far from the weldment the attack is still local. In the HAZ the material is recrystallized and relatively large grained, while at some distance from the HAZ glide-lines can be seen, which indicate some deformation. These observations again confirm the positive role of fast diffusion paths in the deformed region for Cr diffusion and protective scale formation [7, 8]. Also the higher temperature 650 °C favours oxide formation, since points of attack are fewer than on the samples exposed at 600 °C.

4.3.2 Alloy 600H – samples 6/1, 6/2, 6/3, 6/4, 9

At 600 °C all samples made of Alloy 600 showed metal dusting attack, widespread pitting or nearly general attack, already after exposures 1–6 (2604 h; 1625.5 h for samples 6/3 and 6/4). But it can still be seen (Figs 4.3a–d) that the attack probably started from the border region weld/base material (HAZ). Obviously

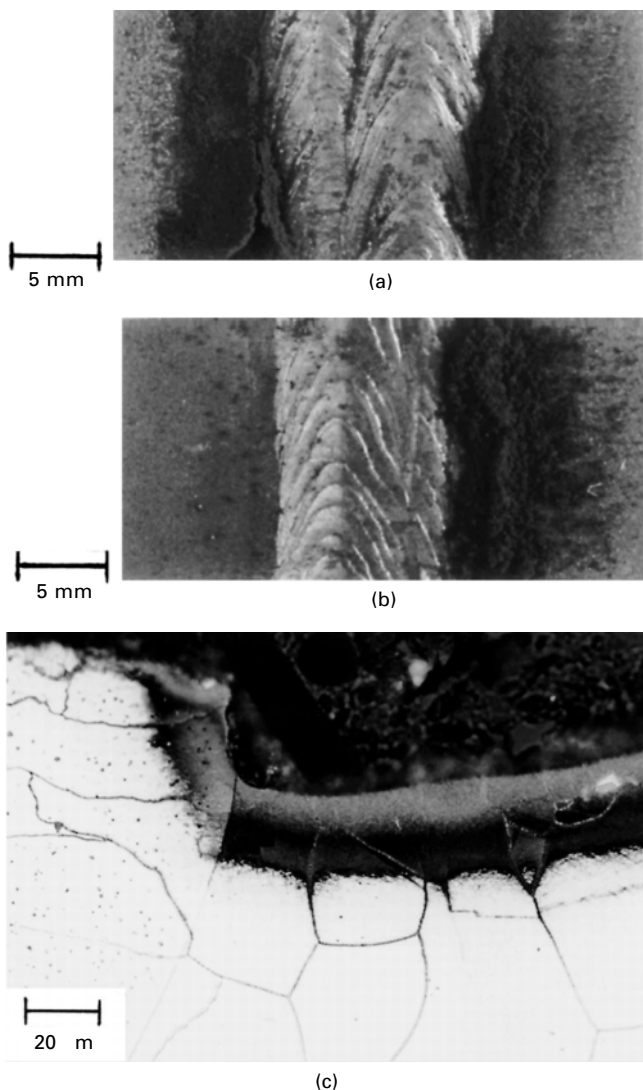
Table 4.3 Amount of corrosion product (coke) after each exposure (mg/sample)

Base material											
Number of exposure period	Alloy	Welding process/ surface finish	t°C t°C	1. 24h 24h	2. 24h 48h	3. 452h 500h	4. 480h 980h	5. 814h 1794h	6. 810.5 h 1794 h	7. 670.5 h 3275 h	8. 500 h 3275h
6/1	600H	TIG/MMAW brushed	600	1.0	0.8	14.2	23.7	22.3	70.6	98.0	289.8
			650	2.9	1.3	6.6	3.0	17.5	34.8	33.8	525.5
6/2	600H	TIG/MMAW ground	600	—	0.3	1.3	0.2	5.0	15.2	30.1	113.0
			650	—	—	0.8	0.1	1.7	5.9	14.3	380.7
6/3	600H	TIG/MMAW sandblasted	600	*	*	*	*	69.6	57.3	110.9	319.1
			650	*	*	*	*	42.6	24.5	43.1	469.6
6/4	600H	TIG/MMAW pickled	600	*	*	*	*	6.55	14.8	54.9	203.8
			650	*	*	*	*	112.3	61.4	40.5	655.0
9	601H	TIG brushed	600	52.6	0.8	9.3	3.3	13.6	44.7	76.1	231.1
			650	2.5	1.3	3.5	1.4	8.8	20.0	26.4	547.4
4	601H	TIG/MMAW brushed	600	2.1	0.8	12.9	1.1	9.2	16.0	18.0	50.7
			650	1.1	1.3	15.7	12.5	24.6	54.3	55.5	129.1
10	601H	TIG brushed	600	4.3	1.1	8.5	0.8	5.8	7.6	22.5	27.9
			650	4.1	3.3	5.9	2.0	7.8	19.4	22.8	30.9
3	602CA	TIG/MMAW brushed	600	2.2	0.7	3.8	0.6	1.4	1.4	9.1	5.6
			650	0.8	0.9	10.6	5.1	3.7	30.4	34.9	37.8
7	602CA	TIG brushed	600	14.3	31.8	287.2	20.8	59.4	49.3	107.2	40.5
			650	11.3	40.1	93.7	2.2	7.0	9.3	19.6	17.3

*Start with the 5. exposure.

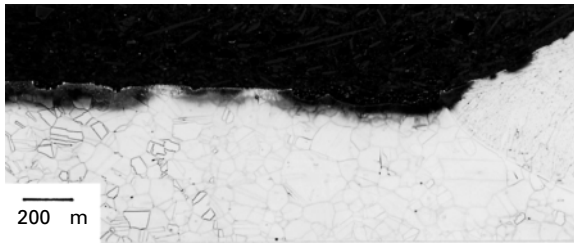
Table 4.4 Rates of coke formation (g/coke/cm²h) in the exposure periods 7–11 and of metal wastage (g metal/cm²h) in period 11

Alloy consumable	Welding process surface treatment	<i>t</i> (°C) <i>t</i> (°C)	7. 670.5h 3275h	8. 500h 3775h	9. 980h 4755h	10. 571.25h 5326.25h	11. 698.75h 6025h	ad 11. % Ni	g metal/ cm ² h
6/1 Alloy 600H UTP 068HH	MMAW brushed	600 650	17.7 6.11	70.2 127.4	101.0 170.5	137.5 210.0	102.3 107.8	12.2 5.41	16.6 7.77
6/2 Alloy 600H UTP 068HH	MMAW ground	600 650	5.44 2.59	27.4 92.3	20.2 220.0	72.3 123.8	53.1 26.1	13.2 6.42	9.34 2.23
6/3 Alloy 600H UTP 068HH	MMAW sand- blasted	600 650	20.0 7.79	77.4 113.8	89.3 164.9	159.8 144.0	106.4 31.5	12.5 6.91	17.7 2.90
6/4 Alloy 600H UTP 068HH	MMAW pickled	600 650	9.92 7.32	49.4 158.8	63.8 277.5	93.5 154.1	62.1 76.8	14.2 6.46	11.75 6.61
9 Alloy 600 S 7020	TIG brushed	600 650	13.76 4.77	56.0 132.7	67.1 113.2	115.0 181.3	84.3 42.0	13.0 5.92	14.6 3.31
4 Alloy 601H UTP 6225 Al	MMAW brushed	600 650	3.25 10.0	12.3 31.3	32.1 67.1	38.6 28.8	46.2 27.9	8.91 2.72	6.68 1.23
10 Alloy 601H S 6025	TIG brushed	600 650	4.07 4.12	6.76 7.49	19.3 19.1	47.2 8.63	43.8 15.5	6.97 3.17	4.95 0.80
3 Alloy 602CA UTP 6225Al	MMAW brushed	600 650	1.65 6.31	1.35 9.16	11.7 1.46	3.18 20.2	1.21 9.65	11.4 4.02	0.22 0.64
7 Alloy 602CA S 6025	TIG brushed	600 650	19.3 3.54	9.82 4.19	7.06 86.4 (?)	7.87 5.07	11.2 3.67	10.1 4.52	1.79 0.26

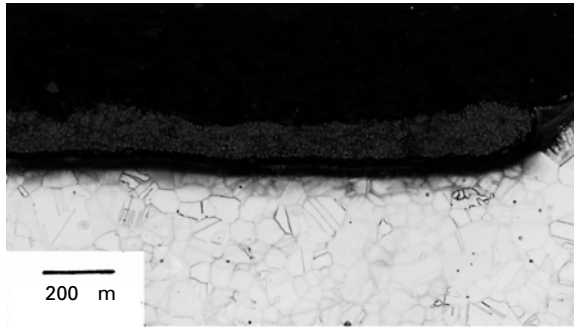


4.2 Metal dusting attack on Alloy 800 and weld material after 72 h exposure at 600°C: (a) topview of sample 5, Alloy 800 attacked starting from the HAZ; (b) topview of sample 11, Alloy 800 attacked, Alloy 602 with only few coke flakes; (c) metallographic cross-section of sample 5, showing attack of weld and base material (Alloy 800).

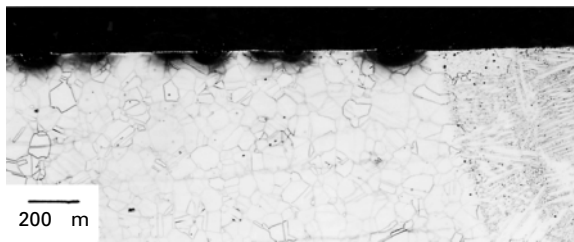
the metal dusting of the weld material is less than on the base material, because of the higher Cr content (~ 19%) of the weld material. The surface treatment by grinding proved to be most favourable, concerning metal dusting resistance, since after 2604h at 600°C (Fig. 4.4a) the pits had not grown together on the ground sample. Even after 6025h the attack is not uniform on this sample, in



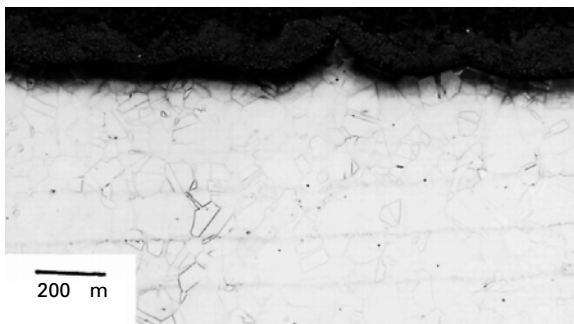
(a)



(b)

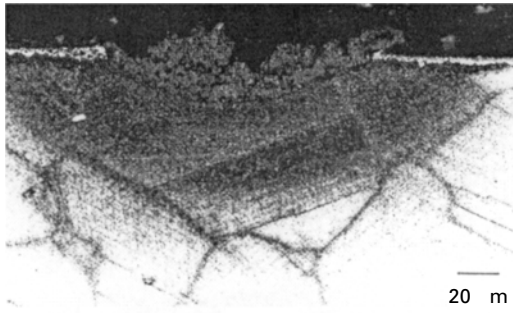


(c)

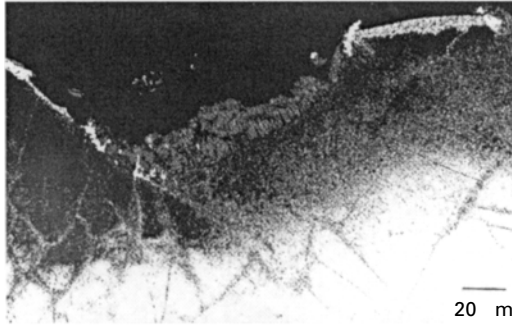


(d)

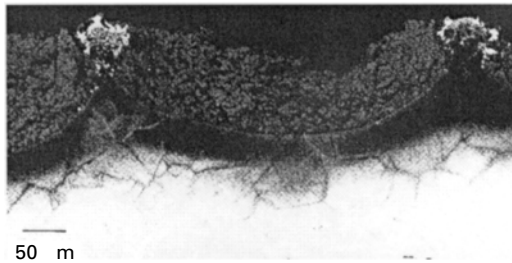
4.3 Metallographic cross-sections of Alloy 600 with weldment (at the right), brushed sample (6/1) after (a) 2605 hours and (b) 6025 hours and ground sample (6/2) after (c) 2605 hours and (d) 6025 hours.



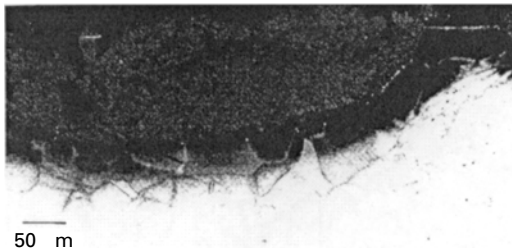
(a)



(b)



(c)



(d)

4.4 Typical metal dusting pits on Alloy 600 after exposure at 600°C:
(a) single pit on ground sample (6/2) after 2605h with carburized zone and filled with coke, edges oxidized, as indicated by the white, Cr – and carbide depleted surface region; (b) deep pit grown at the border weld/base material (sample 6/1) from the start of exposures for 2605h; (c) pits grown together on sample 6/1 after 6025h; (d) deep pit at the border base material/weld on sample 6/2 after 6025h.

contrast to the other surface treatments: brushing, sandblasting and pickling. The latter treatment is most unfavourable for metal dusting resistance. The deepest pits formed after 2604 h at 600°C, had a depth of 65–70 μm (Fig. 4.4b) which corresponds to a growth rate of 0.23 mm/year. Obviously the deepest pits have started to grow from the beginning of the exposures, and often the starting point was apparently situated in the borderline weld/base material.

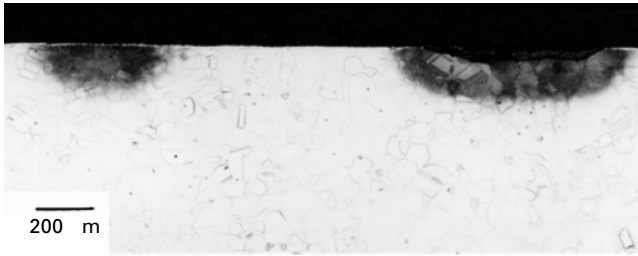
After the very last exposure after 6025 h at 600°C (for 700 h) all samples are covered with coke, only on the weld is there less coke, especially on samples 6/2 and 9. After removal of the coke the base material appears black and roughened, due to overall attack by metal dusting. The metallographic cross-sections confirm this appearance, i.e. after 6025 h exposure at 600°C the attack is uniform, except on the ground sample, where the pits have not grown together totally. The deepest pits are in the range $\sim 150 \mu\text{m}$ (Fig. 4.4c, d) which corresponds to the growth rate 0.22 mm/year, well in agreement with the value for 2605 hours.

At 650°C metal dusting attack is generally less than at 600°C. This means it has started from fewer points, and the pits have not joined together even after 6025 h. This is true especially for the ground sample (Fig. 4.5a, b, c) and here, and also on other samples, there are carburized spots where acute metal dusting has not started. Carburization is of a hemispherical volume, obviously starting from one defect in the surface. But the surface was passivated by oxidation, indicated by the white carbide-depleted zone (see Fig. 4.5b) before the start of metal dusting, which also leads to the attack spreading (see Fig. 4.5c).

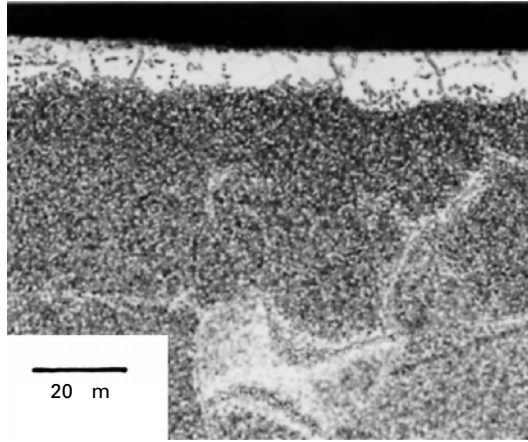
The appearance of the samples after the final (11) exposure confirms that the extent of metal dusting is less at 650°C than at 600°C, since the samples were not covered by a continuous coke layer as in the case of 600°C, but with local coke flakes, especially in the HAZ region. However, the pits are deeper in the samples exposed at 650°C, and the growth rate calculated from pit depths after 2605 h corresponds to 0.4 mm/year, whereas from pit depths after 6025 h the value is 0.29 mm/year, which indicates a decrease of pit growth rate with time, perhaps because of the presence of rather tight and dense coke.

4.3.3 Alloy 601H – samples 4 and 10

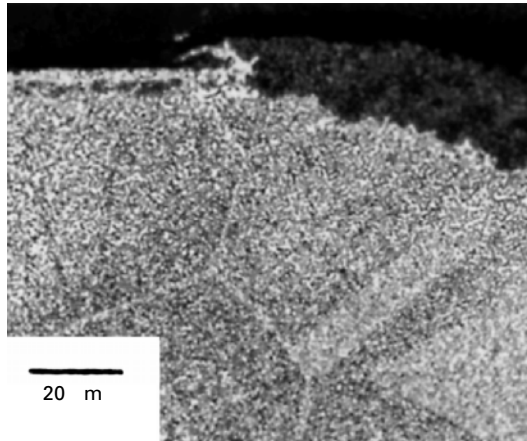
At 600°C all samples already showed metal dusting attack after 2605 h. The appearance of attack is different from Alloy 600, being less widely spread and rather localized. Pits have grown that are nicely hemispherical in many cases and have often apparently started to grow at the borderline weld/base material. The appearance after the final (11) exposure also differs from that of Alloy 600: loose coke is lying on the base material 601 and it appears tarnished grey-black. Much coke is sitting on the weldments and there are



(a)



(b)



(c)

4.5 Metallographic cross-section of Alloy 600, ground sample (6/2) after 6025 h exposure at 650 °C: (a) at low magnification (50x), left: carburized region – passivated by oxidation, and right carburized region with active metal dusting attack; (b) and (c) both regions at a higher magnification (500x).

many pits. Also the metallographic cross-sections taken after 6025 h confirmed that the attack on the weldments is severe, and even more severe for the hand-welded specimen than for the TIG-weld.

The deepest pits after 2604 h at 600 °C were 120 and 130 μm deep, corresponding to a growth rate of 0.42 mm/year; the deepest pit after 6025 h was 200 μm deep corresponding to 0.29 mm/year. So the pit growth rate appears to be higher for Alloy 601 than for Alloy 600 and possibly decreases with time.

One especially symmetric pit was observed after 2605 h at 650 °C. This obviously started from the borderline weld/base material (Fig. 4.6a), 150 μm deep, corresponding to a growth rate of 0.5 mm/year, but there are also carburized spots that have been passivated by oxidation as indicated by the carbide-depleted zone (Figs. 4.6b, c). The metal dusting attack at 650 °C is again severe on the weldments and especially on the hand-welded sample No. 4 (Fig. 4.7a).

4.3.4 Alloy 602CA – samples 3 and 7

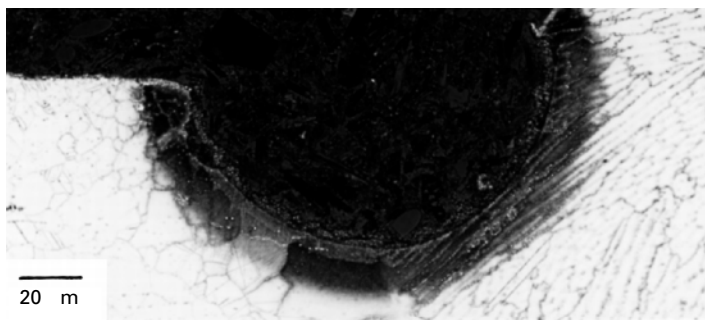
Neither sample shows a typical metal dusting attack of the base material, after 2605 h exposure at 600 and 650 °C. But the weldment of sample 7 is already somewhat corroded after 2605 h, and after 6025 h at 600 °C the attack on the weldments is severe on both samples (Fig. 4.7b).

After 6025 h in addition to the frequent pits on the weldment, sample 7 had some little pits (50–80 μm) in the base material, (Fig. 4.8a, b), in contrast to the previous studies [2, 3] in which Alloy 602 remained unattacked up to 10000 h. The pits have rather different depths so that they have started to grow after different exposure times and the pit growth rate cannot be derived. The rather high coke formation on sample 7 during the first exposures is astonishing, and decreases only gradually.

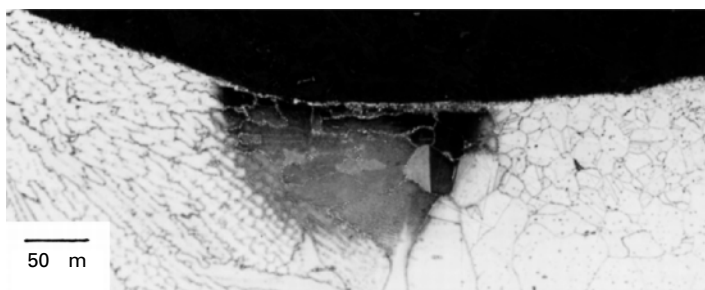
A clear conclusion may be drawn from this study, i.e. Alloy 602CA is also susceptible to metal dusting, especially the weldments, although made of the weld material with the same composition as Alloy 602. The most severe attack was observed on the weld of the hand-welded specimen after 6025 h at 650 °C, (Fig. 4.7b), where numerous rather deep, wrinkled pits have been formed, but there was also considerable attack on the TIG weld.

4.4 Conclusions

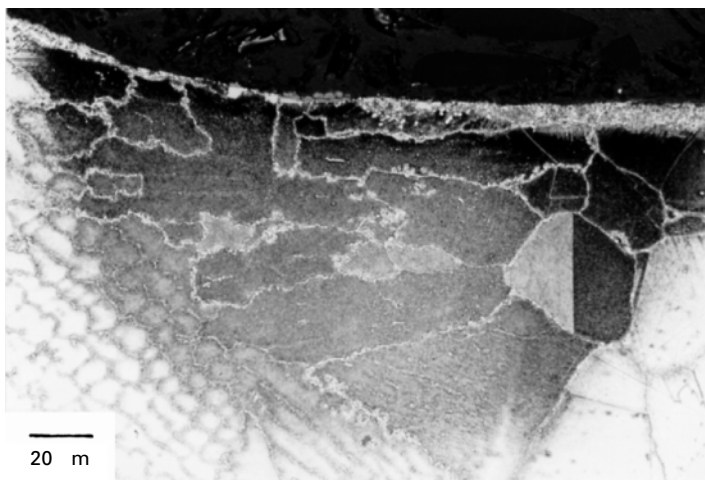
Welded specimens made of Alloys 800H, 600H, 601H and 602CA were exposed under metal dusting conditions in H_2 –24% CO –2% H_2O at 600 and 650 °C. Owing to strong dusting, the samples with Alloy 800H had to be excluded from the exposures after some days, but the other samples were



(a)

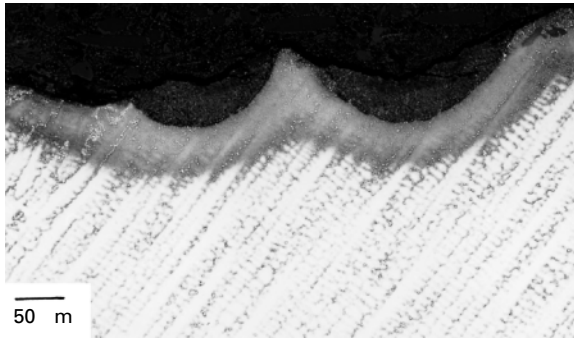


(b)

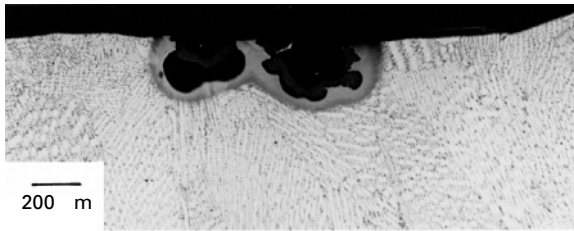


(c)

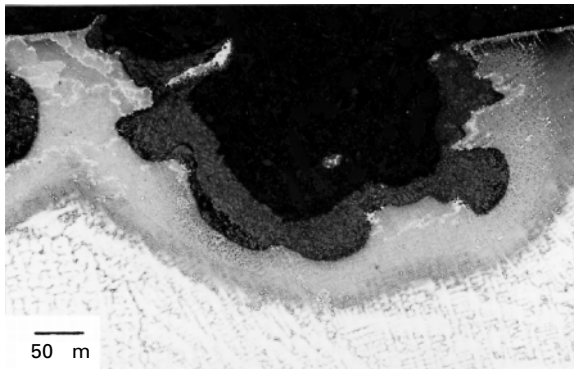
4.6 Metallographic cross-section of Alloy 601H (sample 4) after exposures at 650°C for 2605 hours: (a) pit obviously grown from one point defect at the border weld/base material; (b) and (c) carburized region, passivated by oxidation as indicated by the white, carbide- and Cr-depleted regions.



(a)



(b)

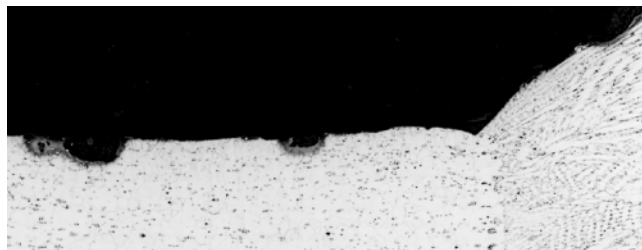


(c)

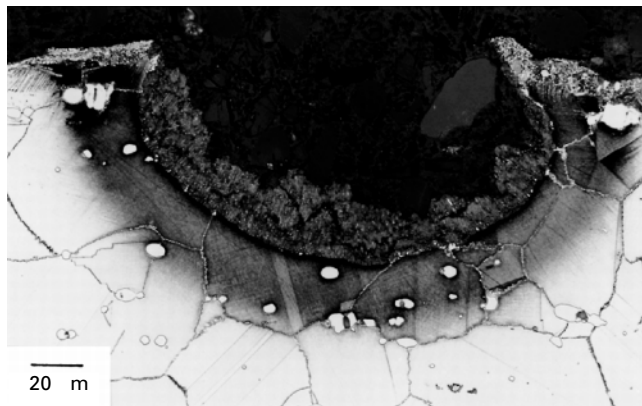
4.7 Severe pitting on the weldments of the hand-welded specimens made of (a) Alloy 601 (sample 4) and of (b) Alloy 602 (sample 3), both after 6025 hours at 650°C.

exposed up to 6025 h. Metallographic cross-sections were examined after 2604 h and at the end after 6025 h.

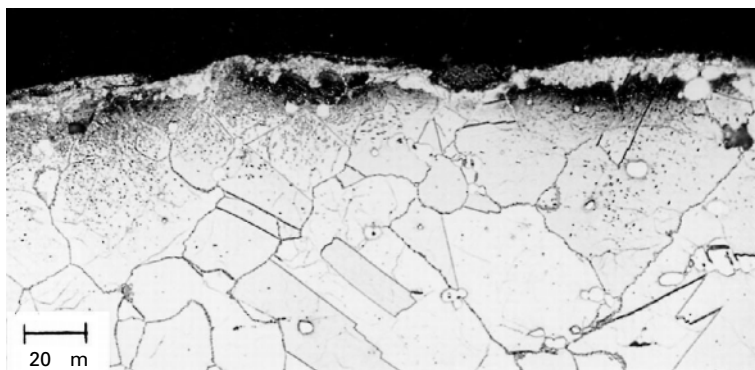
The metal dusting attack started on alloys 800 and 600 mainly in the HAZ and spread fast on the base material but more slowly on the weld material. On Alloy 601 the attack started locally and caused pit formation, especially at the borderline base material/weld. Even on Alloy 602 some local pitting attack was observed after a long incubation period. From the penetration



(a)



(b)



(c)

4.8 Metallographic cross-section of Alloy 602 CA after (a) 6025 hours and (b) exposure at 600°C, pits on the base material (sample 7).

depth of pits, which had probably been growing from the start of the exposure, a metal wastage rate can be derived for Alloy 600 of about 0.2 mm/year at 600°C and about 0.3 mm/year at 650°C. Generally the attack at 600°C started from more points and spread more widely than at 650°C; this is valid for all materials.

On Alloy 600 several surface treatments were applied – brushing, grinding, sandblasting and pickling – but the material remained more or less susceptible to metal dusting. Grinding proved to be best for retardation, and pickling was worst, strongly accelerating the metal dusting attack.

For the samples with Alloy 600 and 800 the weld material was better resistant to metal dusting than the base material. For the samples made of Alloys 601 and 602 the attack on the weld material was clearly stronger than on the base material, although the chemical composition is almost the same. The welds were attacked more severely in the case of manual welding than in automatic TIG welding. Continued exposure after grinding of the welds showed no attack after 2300h.

4.5 Acknowledgement

This study was supported by funds from the ‘Kultusministerium des Landes Sachsen-Anhalt’.

4.6 References

1. H.J. Grabke, R. Krajak, E.M. Müller-Lorenz, S. Strauß: *Werkst. u. Korros.* **47** (1996) 495–504.
2. H.J. Grabke, E.M. Müller-Lorenz, J. Klöwer, D.C. Agarwal: *Mat. Performance (NACE)* **37** (1998) 58.
3. J. Klöwer, H.J. Grabke, E.M. Müller-Lorenz: *Mat. Corr.* **49** (1998) 328–329.
4. S. Strauß, R. Krajak, H.J. Grabke: *Mat. Corr.* **50** (1999), 622–627.
5. H.J. Grabke: *Corrosion* **56**, No. 8 (2000) 801–808.
6. D.C. Agarwal, J. Klöwer, U. Brill: *Corrosion NACE Conference*, Houston 2001, paper 01382.
7. H.J. Grabke, E.M. Müller-Lorenz, B. Eltester, M. Lucas, D. Monceau: *Steel Res.* **68** (1997) 179–185.
8. H.J. Grabke, E.M. Müller-Lorenz, S. Strauß, E. Pippel, J. Woltersdorf: *Oxid. Metals* **50** (1998) 2241–2254.

A SCHNEIDER and HJ GRABKE, Max-Planck-Institut
für Eisenforschung GmbH, Germany

5.1 Introduction

Metal dusting is a high-temperature corrosion process, a disintegration of metals into a dust of fine metal particles and graphite, which occurs in strongly carburising atmospheres at carbon activities $a_{\text{C}} \gg 1$ in the temperature range 400–1000 °C [1–3]. Metal dusting attacks iron, low- and high-alloy steels, nickel and cobalt-based alloys. In the case of iron and steels, during metal dusting, cementite (Fe_3C) forms as an intermediate phase, which decomposes into graphite and iron, whereas nickel disintegrates by direct inward growth of graphite [4].

The thermodynamics, mechanisms and kinetics of metal dusting of iron have been studied by Grabke and coworkers using $\text{CO-H}_2\text{-H}_2\text{O}$ and $\text{CH}_4\text{-H}_2$ gas mixtures [5–9]; the reaction sequence is (i) rapid supersaturation of iron with dissolved carbon, (ii) growth of a cementite layer at the surface, (iii) graphite deposition, (iv) subsequent cementite decomposition into graphite and fine metal particles, which (v) act as catalysts for coke deposition. These particles catalyse the growth of carbon filaments. Catalytic coke deposition is observed in thermogravimetric experiments as a drastic acceleration of the mass gain kinetics.

Transmission electron microscopy (TEM) investigations of carburised iron samples showed a coke layer on the cementite surface which consists of graphite, often as filaments, and finely dispersed iron particles [9] or carbide particles [10, 11].

The presence of H_2S leads to sulphur adsorption, which retards the carbon transfer and coke deposition. The adsorbed sulphur also suppresses graphite nucleation, thus preventing step (iii) and stopping the reaction sequence of metal dusting. In fact, continued growth of Fe_3C on Fe has been observed in $\text{CO-H}_2\text{-H}_2\text{O-H}_2\text{S}$ atmospheres [12–15]. Using the advantage of the sulphur effect, not only can metal dusting be prevented, but also fundamental studies on metastable iron carbides can be performed. The system Fe–C is of great technical importance and high complexity, considering the existence of a

stable system Fe–graphite and a metastable system Fe–Fe₃C, and the many different microstructures arising from cementite formation in the iron matrix.

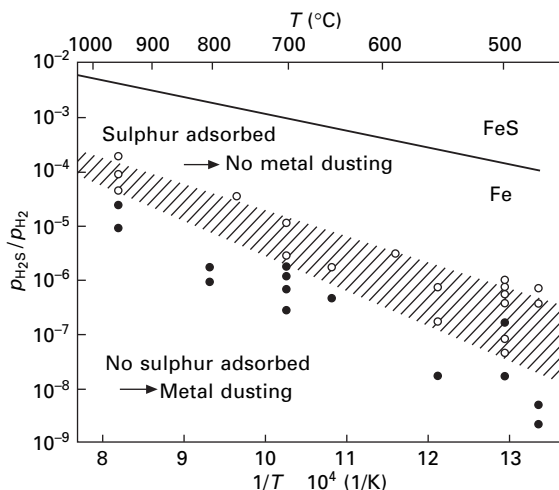
5.2 Effect of H₂S on carburisation kinetics and graphite formation

Sulphur is a very surface-active element. It tends to adsorb or segregate at surfaces or interfaces. In this study adsorption of sulphur is established by the equilibrium $\text{H}_2\text{S} \rightleftharpoons \text{H}_2 + \text{S}_{\text{ads}}$. The enthalpy of adsorption is $H = -200 \text{ kJ/mol}$ for sulphur on polycrystalline iron [16, 17]. Sulphur on iron surfaces retards gas carburising and nitriding processes by site blocking [18, 19]. The influence of sulphur activity a_s on the carburisation kinetics in a CH₄–H₂–H₂S atmosphere has been studied at carbon activities $a_C < 1$ by Grabke *et al.* [18, 19]. By increasing the H₂S content in the carburising atmosphere, the reaction velocity decreases. From such experiments the coverage with sulphur was derived. In principle, carbon transfer should be prevented by a monolayer S on an iron surface, but vacancies in the monolayer lead to a slow, continued carburisation.

Metal dusting of iron occurs at carbon activities $a_C > a_C(\text{Fe}/\text{Fe}_3\text{C})$; under this condition carburisation is followed by cementite formation. It was observed that sulphur also prevents graphite from nucleating on a Fe₃C surface [20]. By preventing graphite nucleation, metal dusting can also be prevented.

Since there are no quantitative results on sulphur adsorption on cementite, in Fig. 5.1 the effect of H₂S on metal dusting of iron is shown in a simplified diagram. This diagram presents the stability ranges of Fe and FeS depending on the ratio $p(\text{H}_2\text{S})/p(\text{H}_2)$ versus temperature [12, 13]. Open symbols represent experiments where the onset of metal dusting was retarded for more than 48 h, and filled symbols correspond to an earlier onset of metal dusting. The hatched region represents the transition to an iron surface saturated with sulphur. The upper boundary of this hatched region corresponds to saturation with adsorbed sulphur ($\theta_s = 1$) and the lower to approximately $\theta_s = 0.9$. This diagram includes data of a study by Ando *et al.* [21], who investigated the influence of H₂S on the growth of carbon filaments, i.e. on metal dusting, at 950 °C.

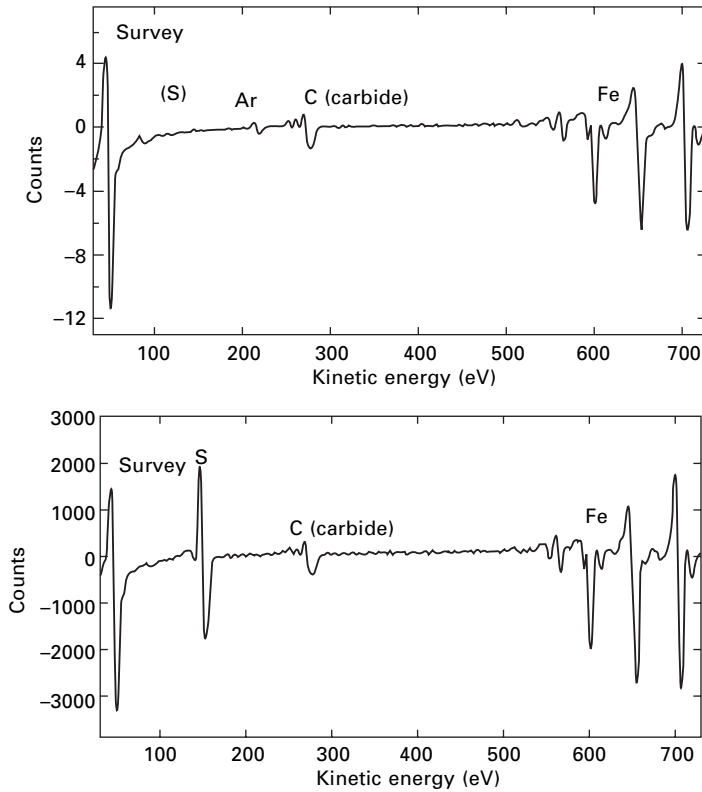
In order to ensure that the diagram shown in Fig. 5.1 can also be applied to the complex processes during metal dusting of iron, surface analytical studies on sulphur segregation on Fe₃C surfaces have been performed in an *in situ* experiment with a hot stage in an Auger apparatus [15]. At first an iron foil was carburised at 700 °C for 340 h in a CH₄–H₂–H₂S gas mixture with $a_C = 100$ and 1 ppm H₂S to obtain Fe₃C on the surface. The sample was then introduced into the Auger apparatus and cleaned by sputtering with Ar ions. The spectra from Auger electron spectroscopy (AES) recorded at the iron and carbide surfaces showed that after cleaning there was no sulphur



5.1 Influence of H_2S on metal dusting of iron as a function of temperature and the ratio $p_{\text{H}_2\text{S}}/p_{\text{H}_2}$. Open symbols represent experiments where the onset of metal dusting was retarded for more than 48 h, filled symbols correspond to an earlier onset of metal dusting. The hatched region represents the transition to an iron surface saturated with sulphur [3, 13].

present on either of these surfaces, as can be seen in the case of cementite in the upper part of Fig. 5.2. Then, the specimen was heated to 700°C for 0.5 h. After this treatment, sulphur was clearly detected on both iron and cementite surfaces. The lower part of Fig. 5.2 shows the AES spectrum of cementite with segregated sulphur.

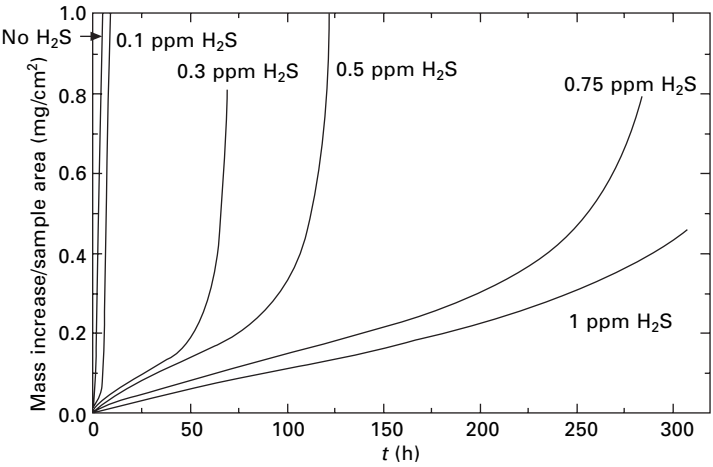
The effect of H_2S on the carburisation kinetics under metal dusting conditions was investigated by thermogravimetric experiments [13]. Generally, the iron samples are at first supersaturated with carbon and then Fe_3C formation occurs. Later on, the accelerating mass gain indicates the onset of metal dusting, as described above. It was observed that at high carbon activities $a_{\text{C}} > 150$, a second carbide forms in addition to cementite. With X-ray diffraction (XRD) analysis of the carburised samples this carbide was identified as Hägg carbide Fe_5C_2 [22]. In Fig. 5.3, thermal gravimetric analysis (TGA) mass gain curves are shown for pure iron carburised at 500°C in $\text{CO-H}_2\text{-H}_2\text{O-H}_2\text{S}$ atmospheres with $a_{\text{C}}=1000$ for different H_2S additions. The metal dusting kinetics slows down with increasing H_2S content. Additions of 0.3 and 0.5 ppm H_2S retard graphite nucleation for a period of 30–60 h. Upon adding 0.75 or 1 ppm H_2S , the mass gain is almost linear over a long period. During this period layers of cementite and Hägg carbide are growing. Then graphite nucleation starts and initiates the metal dusting process. The onset of metal dusting can be retarded for up to 300 h by 1 ppm H_2S addition.



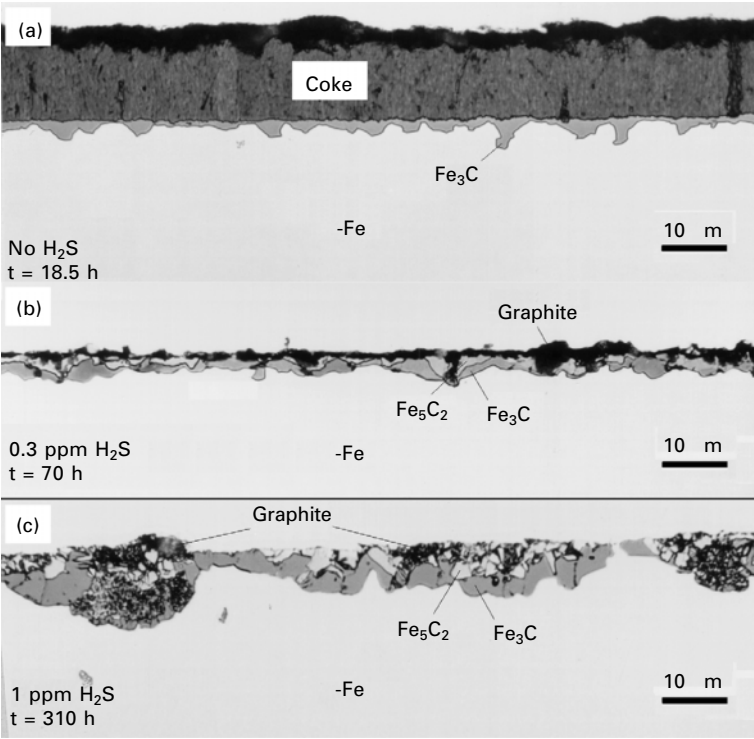
5.2 Auger electron spectra of a sputter cleaned (Ar⁺) cementite surface of a carburised iron foil (700 °C, CH₄-H₂-H₂S, $a_C = 100$, 1 ppm H₂S, $t = 340$ h) (upper part) and of a cementite surface after annealing within the Auger system at 700 °C for 0.5 h (lower part). The presence of segregated sulphur is observed [15].

In Fig. 5.4 metallographic cross-sections of three of these samples are shown [13]. Figure 5.4(c) indicates decomposition of cementite and Hägg carbide. It is striking that the cross-section of the sample carburised without H₂S addition has no Fe₅C₂, as confirmed by XRD. Only a very small amount of Fe₅C₂ was detected in the sample exposed to 0.1 ppm H₂S. This observation indicates that, after supersaturation of iron with dissolved carbon, cementite forms first and, after its saturation, Hägg carbide starts to form. Consequently, without H₂S addition cementite starts to decompose before Hägg carbide nucleation sets on.

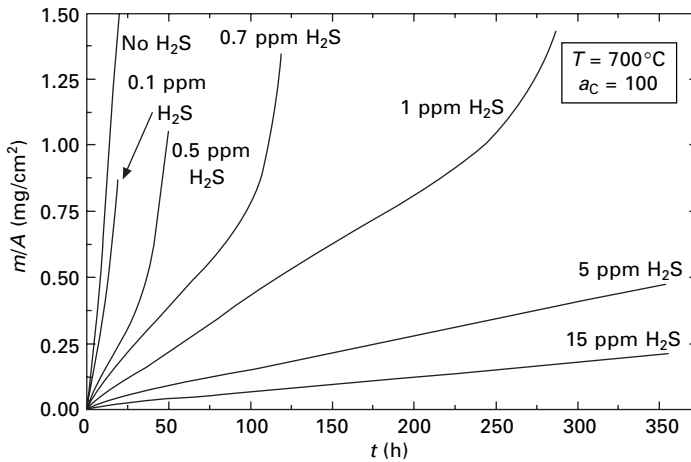
The effect of sulphur on metal dusting was also studied using CH₄-H₂-H₂S gas mixtures [15]. The TGA curves in Fig. 5.5 represent the influence of H₂S on the carburisation kinetics in CH₄-H₂-H₂S gas mixtures at 700 °C and $a_C = 100$. With increasing H₂S content the mass gain is reduced in the



5.3 Influence of H₂S on the carburisation and metal dusting kinetics in CO–H₂–H₂O–H₂S mixtures at 500°C and at $a_c = 1000$ [13].



5.4 Metallographic cross-sections of iron samples carburised in CO–H₂–H₂O–H₂S gas mixtures at 500°C and at $a_c = 1000$: (a) without H₂S; (b) 0.3 ppm H₂S; and (c) 1 ppm H₂S [13].



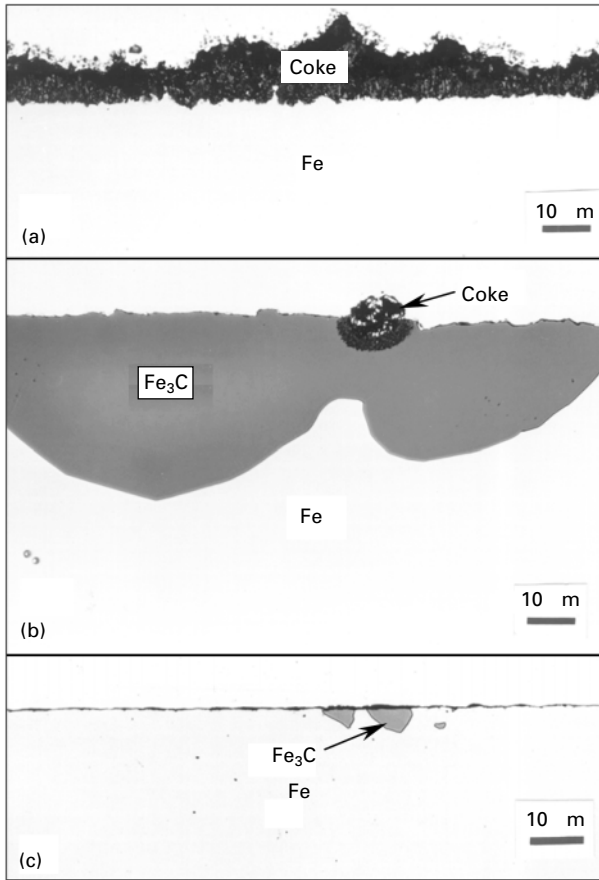
5.5 Thermogravimetric measurements of iron samples carburised at 700°C in $\text{CH}_4\text{-H}_2\text{-H}_2\text{S}$ gas mixtures at $a_{\text{C}} = 100$ [15].

same way as observed for carburisation at 500°C in $\text{CO-H}_2\text{-H}_2\text{O-H}_2\text{S}$ mixtures (see Fig. 5.3). Again, the beginning of the metal dusting process can be seen from the drastic increase of the mass gain. Without H_2S this process starts immediately (see Fig. 5.5). With different amounts of H_2S the onset of metal dusting is retarded or even suppressed for 350h for 5 and 15 ppm H_2S . In the case of 1 ppm H_2S addition the different steps of the process are explained as follows: during the first 10h ferrite is carburised until the carbon activity is raised above $a_{\text{C}} = a_{\text{C}}(\text{Fe}/\text{Fe}_3\text{C})$, followed by a decreased carburisation rate during cementite formation (for about 200h) and eventually the onset of metal dusting after about 270h.

Metallographic cross-sections of specimens selected out of those in Fig. 5.5 are shown in Fig. 5.6. Without H_2S the metal dusting reaction is so fast that only a coke layer, and no carbide, remains after 26h of carburisation (Fig. 5.6 (a)). Energy-dispersive X-ray (EDX) analyses of the coke layer confirmed the presence of iron within the coke. After 288h carburisation in a $\text{CH}_4\text{-H}_2\text{-H}_2\text{S}$ atmosphere with 1 ppm H_2S addition, large isolated carbide particles form at the surface (Fig. 5.6 (b)), and also in the bulk. The particles are irregularly distributed over the surface, reaching sizes up to 100 μm . The local onset of metal dusting can be seen in Fig. 5.6 (b). The effect of 15 ppm H_2S is shown in Fig. 5.6 (c). After 360h of carburisation only a few carbide particles are observed and metal dusting has not yet started.

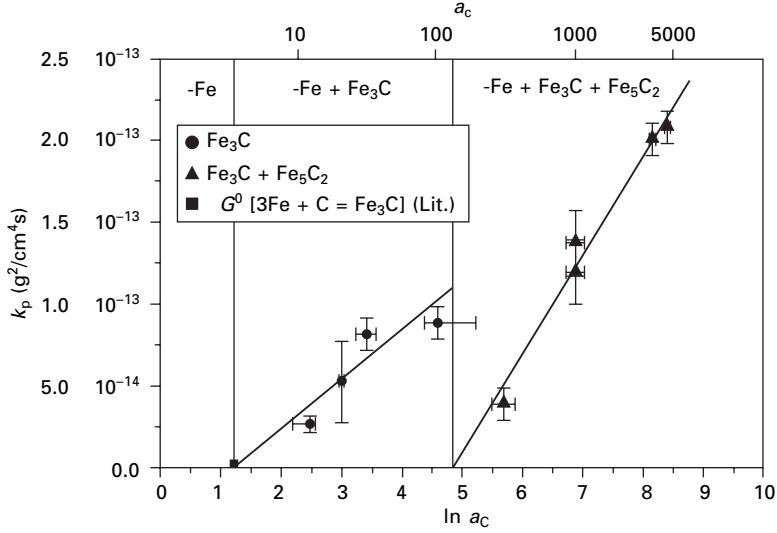
5.3 Carbon diffusion in cementite and Hägg carbide

Owing to the suppression of metal dusting it was possible to determine parabolic rate constants for the growth of cementite and of Hägg carbide



5.6 Metallographic cross-sections of iron samples carburised at 700°C in $\text{CH}_4\text{-H}_2\text{-H}_2\text{S}$ gas mixtures at $a_{\text{C}} = 100$ with different H_2S additions: (a) no H_2S , $t = 26\text{h}$; (b) 1 ppm H_2S , $t = 288\text{h}$; (c) 15 ppm H_2S , $t = 360\text{h}$ [15].

during carburisation of pure iron at 500°C in $\text{CO-H}_2\text{-H}_2\text{O-H}_2\text{S}$ gas mixtures at various carbon activities in the range $12 < a_{\text{C}} < 4600$ [23]. For each carbon activity several experiments were conducted to find a suitable H_2S content in order to observe parabolic mass gain with time, corresponding to diffusion-controlled carbide layer growth. From the dependence of the parabolic rate constants, obtained from the carburisation experiments, on carbon activity, the self-diffusion coefficient D_{C}^* for carbon in both carbides was derived. The results are plotted in Fig. 5.7 versus the natural logarithm of carbon activity in the gas phase. The data can be represented by two straight lines, one for cementite growth and a second for growth of Hägg carbide. From the slopes of these lines the coefficients D_{C}^* for carbon self-diffusion in cementite and in Hägg carbide have been calculated using the equation [23]



5.7 The parabolic rate constants for the growth of cementite and Hägg carbide at 500°C are plotted versus the natural logarithm of the carbon activity of the gas phase [23].

$$D_C^* = \frac{1}{2} \frac{dk_p}{d \ln a_C^{\text{gas}}}$$

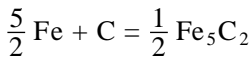
and taking into account the different densities and weight fractions of carbon in Fe₃C and Fe₅C₂. The obtained self-diffusion coefficients of carbon at 500°C in these carbides are as follows:

$$D_C^* (\text{Fe}_3\text{C}) = 5.57 \cdot 10^{-14} \text{ cm}^2/\text{s}$$

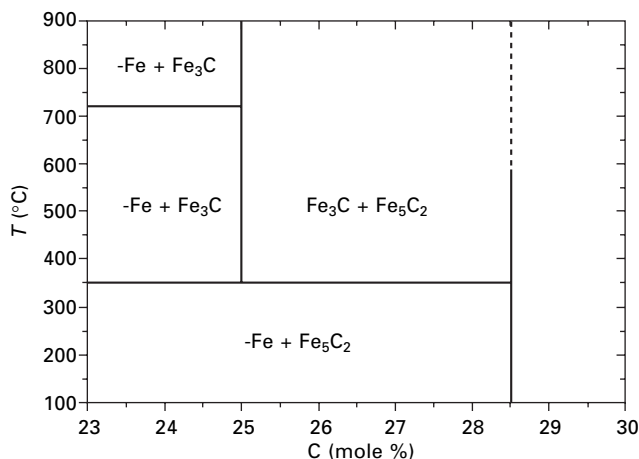
$$D_C^* (\text{Fe}_5\text{C}_2) = 8.22 \cdot 10^{-14} \text{ cm}^2/\text{s}$$

5.4 Thermodynamics of Hägg carbide formation

In order to determine the enthalpy of formation of Hägg carbide (Fe₅C₂), carburisation experiments were performed on iron samples at 500°C in CO–H₂–H₂O–H₂S gas mixtures with different carbon activities. Additions of H₂S to the carburising atmosphere suppressed early onset of metal dusting and made possible to observe Hägg carbide formation. It was found that at 500 °C the Hägg carbide forms on top of cementite at carbon activities $a_C \geq a_C(\text{Fe}_3\text{C}/\text{Fe}_5\text{C}_2) \approx 150$. The enthalpy of formation for the reaction



was calculated with respect to 1 mol of carbon atoms. Plotting this value



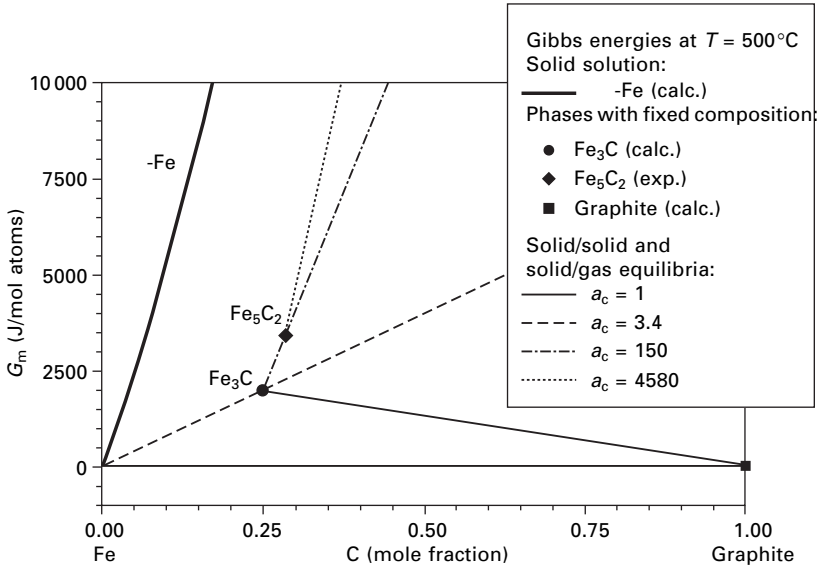
5.8 Part of the metastable phase diagram of the iron carbon system. The temperature for the three-phase equilibrium $\alpha\text{-Fe}/\text{Fe}_3\text{C}/\text{Fe}_5\text{C}_2$ was estimated at 350°C [25].

together with results of Browning *et al.* [24] for Hägg carbide and cementite formation, it can be concluded that a triple point of the phases $\alpha\text{-Fe}$, Fe_3C and Fe_5C_2 exists at approximately 350°C [25]. Thus the binary phase diagram of the metastable Fe–C system is to be changed as shown in Fig. 5.8. At temperatures below 350°C there is a drive to the transformations $\alpha\text{-Fe}/\text{Fe}_3\text{C}$, $\alpha\text{-Fe}/\text{Fe}_5\text{C}_2$ and $\text{Fe}_3\text{C}/\text{Fe}_5\text{C}_2$.

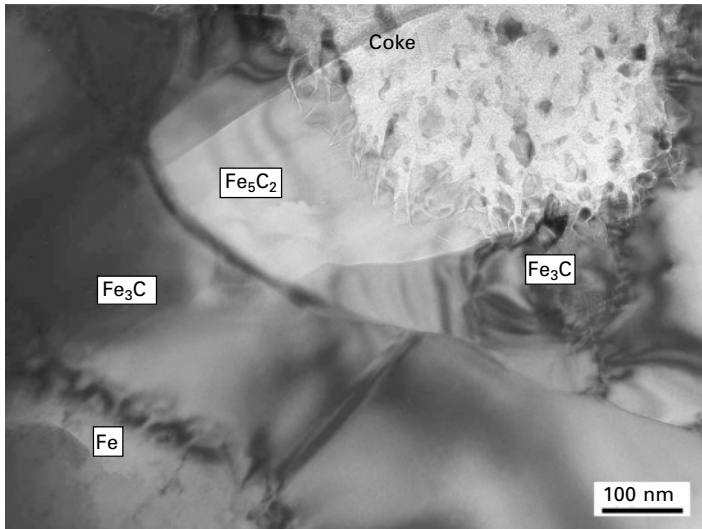
5.5 Decomposition of Fe_3C and Fe_5C_2

From the finding that a second iron carbide, the Hägg carbide, plays a role during metal dusting at very high carbon activities, the question arose as to whether the metastable Hägg carbide decomposes after its formation. The Gibbs energies calculated for the various phases are given in Fig. 5.9. The calculations were performed using the software Thermo-Calc and the database SSOL [26–28]. From the Gibbs energies of both carbides, Fe_3C and Fe_5C_2 , it can be seen that these are metastable phases in the Fe–C system.

Thin iron foils were carburised and quenched for the electron microscopic investigations of the decomposition processes. The carbon activity was set to $a_{\text{C}} = 4580$. At this activity Fe_5C_2 forms even without H_2S additions [13]. In Fig. 5.10 a TEM image is shown of layers in the sequence $\alpha\text{-Fe}/\text{Fe}_3\text{C}/\text{Fe}_5\text{C}_2/\text{coke}$, which demonstrates the microstructural peculiarities of the main steps of the metal dusting attack on iron in a carburising atmosphere with high carbon activity. After supersaturation of the metal with carbon, Fe_3C and Fe_5C_2 carbides are formed on the surface of the metal. The decay of both carbide layers starts after nucleation of graphite and its inward growth into



5.9 Molar Gibbs energy of ferrite, cementite and Hägg carbide at 500°C . The Gibbs energy of the Hägg carbide was determined from carburisation experiments reported in [25].



5.10 TEM-image of a layer sequence $\text{-Fe/Fe}_3\text{C/Fe}_5\text{C}_2/\text{coke}$ of an iron foil carburised for 24 h at 500°C in a $\text{CO-H}_2\text{-H}_2\text{O-H}_2\text{S}$ mixture at $a_c = 4580$ with 0.5 ppm H_2S [10].

the carbides as reported earlier by Woltersdorf and coworkers [9, 29, 30] and is followed by the formation of an outer coke region. Performing high-resolution electron microscopy it was found that Fe_5C_2 converts to graphite and iron directly and not via formation of the intermediate decomposition products cementite and graphite [10]. In this study it was also shown that graphite intrusions grow into the carbides by branching out. At a later stage of the process, the carbide particles become isolated from each other and are distributed in the coke layer with different sizes. Because of the high carbon activity in the atmosphere, after disintegration the carbide particles are preserved in the coke.

5.6 Iron sulphide formation in atmospheres containing H_2S

In some experiments, the formation of iron sulphides was unexpectedly observed for conditions where FeS formation is thermodynamically not stable [14]:

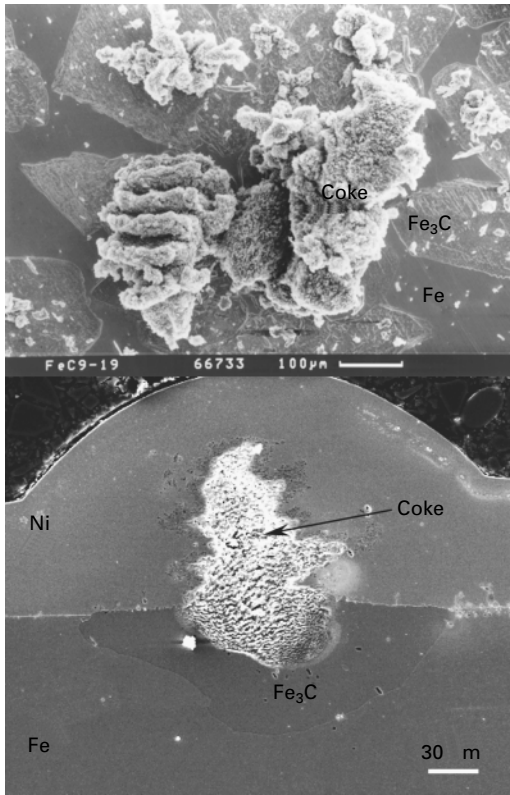
$$\frac{p_{\text{H}_2\text{S}}}{p_{\text{H}_2}} < \frac{p_{\text{H}_2\text{S}}}{p_{\text{H}_2}}_{\text{Fe/FeS}}$$

This observation could only be explained for experiments where metal dusting was already in progress. In such cases there are small iron particles stemming from the metal dusting process which can transform to FeS even for low H_2S contents according to the Gibbs–Thomson effect [31, 32]. Iron sulphide formation was also observed in experiments without coke formation. The reason for this is still unknown and remains to be investigated. Hochman assumed a possible formation of a carbo-sulphide [33] which could not be proved by AES investigations [14].

5.7 Practical aspects of sulphur adsorption

The retarding effect of sulphur adsorbed from the atmosphere is used in practice, e.g. in petrochemical processes such as steam-cracking of hydrocarbons for the production of ethylene. It is well known that dosing of sulphur-bearing compounds suppresses the carburisation of the cracking tubes. These tubes are made of high Cr–Ni-steels by centrifugal casting and their carburisation leads to internal carbide formation, embrittling the material and causing loss of oxidation resistance.

From industrial practice it was known that addition of sulphur compounds (H_2S , CS_2 , $(\text{CH}_3)_2\text{S}_2$, etc.) to the atmosphere inhibits metal dusting and this effect was used to protect plants. The diagram in Fig. 5.11 is of great interest: it shows that at low temperatures very low H_2S contents are sufficient for



5.11 SEM image of the surface (upper part) and of the cross-section (lower part) of an iron sample carburised at 700 °C in a $\text{CH}_4\text{-H}_2\text{-H}_2\text{S}$ mixture with 1 ppm H_2S at $a_c = 100$ for 288 h [15].

protection. In fact, for continuous catalytic reformer (CCR) units of refineries one can conclude that plants are protected at about 600 °C by < 1 ppm H_2S [34, 35]. For heaters of direct reduction plants, operating up to 900 °C, 25 ppm H_2S have been proven to be sufficient for protection.

It is questionable whether, even using relatively high H_2S quantities, protection against metal dusting can be reached over very long time periods under service conditions by adsorbed sulphur on its own. Therefore a combination of different concepts yields a successful protection of Cr-containing steels. Here, sulphur adsorption at the sites of local defects of a chromia layer will retard the onset of metal dusting until self-healing has finished.

5.8 Acknowledgement

Support of this study by the Deutsche Forschungsgemeinschaft is gratefully acknowledged.

5.9 References

1. H. J. Grabke: Mechanisms of carburisation, metal dusting and coking – ways and means for protection, in: E. Bardal (Ed.), *Proceedings of EUROCORR '97*, Vol. II, European Federation of Corrosion, Trondheim (1997) 1.
2. H. J. Grabke: *Mater. Corros.* **49** (1998) 303.
3. H. J. Grabke, E. M. Müller-Lorenz, A. Schneider: *ISIJ Int.* **41** (Suppl. S1) (2001) 1–8.
4. R. Schneider, E. Pippel, J. Woltersdorf, S. Strau, H. J. Grabke: *Steel Res.* **68** (1997) 326.
5. H. J. Grabke, R. Krajak: *Härterei-Tech. Mitt.* **49** (1994) 150.
6. H. J. Grabke: *Solid State Phen.* **41** (1995) 3.
7. H. J. Grabke, R. Krajak, J. C. Nava Paz: *Corros. Sci.* **35** (1993) 1141.
8. J. C. Nava Paz, H. J. Grabke: *Oxid. Met.* **39** (1993) 437.
9. E. Pippel, J. Woltersdorf, H. J. Grabke, S. Strau: *Steel Res.* **66** (1995) 217.
10. A. Schneider, G. Inden, H. J. Grabke, Q. Wei, E. Pippel, J. Woltersdorf: *Steel Res.* **71** (2000) 179.
11. J. Zhang, A. Schneider, G. Inden: *Corros. Sci.* **45** (2003) 1329.
12. H. J. Grabke, E. M. Müller-Lorenz: *Steel Res.* **66** (1995) 254.
13. A. Schneider, H. Viehhaus, G. Inden, H. J. Grabke, E. M. Müller-Lorenz: *Mater. Corros.* **49** (1998) 336.
14. A. Schneider: Einfluß von H₂S auf die Bildung und den Zerfall von Eisenkarbiden beim Metal Dusting, Dr. thesis, VDI-Verlag, Düsseldorf (1999).
15. A. Schneider, H. Viehhaus, G. Inden: *Mater. Corros.* **51** (2000) 338.
16. J. Benard, J. Oudar, N. Barbouth, E. Margot, Y. Berthier: *Surface Sci.* **88** (1979) L35.
17. J. Oudar: *Materials Sci. Engg.* **42** (1980) 101.
18. H. J. Grabke: *Materials Sci. Engg.* **42** (1980) 91.
19. H. J. Grabke, E. M. Petersen, S. R. Srinivasan: *Surface Sci.* **67** (1977) 501.
20. S. R. Kelemen, A. Kaldor: *J. Chem. Phys.* **75** (1981) 1530.
21. S. Ando, N. Kurose, H. Kimura: *Transactions of the Japan Institute of Metals* **29** (1988) 820.
22. G. Hägg: *Z. Kristall.* **89** (1934) 92.
23. A. Schneider, G. Inden, H. J. Grabke, Growth kinetics of iron carbide layers during gas carburisation, in: M. Rühle, H. Gleiter, *Interface controlled materials (EUROMAT 99)* (Eds.), Vol. 9, Wiley-VCH, Weinheim (2000) 30.
24. L. C. Browning, T. W. DeWitt, P. H. Emmett: *J. Amer. Chem. Soc.* **72** (1950) 4211.
25. A. Schneider, G. Inden: *Steel Res.* **72** (2001) 503.
26. B. Jansson, M. Schalin, B. Sundman: *J. Phase Equilibria* **14** (1993) 557.
27. Thermo-Calc SSOL (Solid Solution Data Base) Foundation of Computational Thermodynamics, Royal Institute of Technology – Stockholm, Sweden.
28. P. Gustafson: *Scand. J. Metallurgy* **14** (1985) 259.
29. E. Pippel, J. Woltersdorf, R. Schneider: *Mater. Corros.* **49** (1998) 309.
30. E. Pippel, S. Strau, J. Woltersdorf: In: *Proc. of EUROCORR '98*, European Federation of Corrosion, Utrecht (1998).
31. J. M. Blakely: *Introduction to the properties of crystal surfaces*, Pergamon Press, Oxford (1973).
32. P. G. Shewmon: *Transformations in metals*, McGraw-Hill Book Company, New York, (1969).
33. R. F. Hochman: Catastrophic deterioration of high temperature alloys in carbonaceous

- atmospheres, in: Z. A. Foroulis, F. S. Pettit (Eds.), *Proc. of the Symposium on Properties of High Temperature Alloys*, The Electrochemical Society, (1976), 715.
34. H. J. Grabke, C. Gerk: In: *Proc. of EUROCORR '99*, European Federation of Corrosion, Aachen (1999).
 35. H. J. Grabke: In: *Proc. of Corrosion in Refinery, Petrochemical and Power Generation Plants*, NACE, Italy (2000).

Occurrence of metal dusting – referring to failure cases

H J GRABKE and M SPIEGEL, Max-Planck-Institut für Eisenforschung GmbH, Germany

6.1 Metal dusting – present knowledge

In carburizing atmospheres with carbon activities $a_C > 1$, carbon transfer into iron and nickel and their alloys leads to oversaturation and disintegration into fine metal particles and graphite. This metal dusting is caused by the high thermodynamic tendency for graphite formation and, in fact, graphite growth into the materials causes their destruction [1–6]. Two mechanisms have been observed [7, 8]:

1. Direct inward or internal growth of graphite occurs on Ni and Ni–base alloys. Carbon atoms from the oversaturated solution attach to the graphite basal planes which grow into the metal matrix.
2. On iron and steels the unstable carbide Fe_3C is formed, which, after graphite nucleation on its surface, decomposes by inward growth of graphite.

In these processes metal particles are created, very fine particles in mechanism 2, coarser particles by mechanism 1 which act as catalysts for carbon deposition from the atmosphere, i.e. ‘coking’ [9, 10].

The kinetics and mechanism of metal dusting and coking have been studied in detail in H_2 –CO– H_2O atmospheres on iron and low-alloy steels. At temperatures up to 540°C the rate of metal wastage is controlled by the continuous decomposition of a cementite layer:



which is described by a linear time law. The decomposition reaction is independent of a_C and partial pressures; its activation energy is about 170 kJ/mol. The metal dusting attack on iron and steels reaches a maximum at about 600°C . For iron the rate decreases, since a dense Fe-layer is formed by the decomposition reaction, through which the carbon must diffuse outwards, so carbon diffusion becomes rate determining in the higher temperature range.

Metal dusting can be inhibited or even prevented by the presence of sulphur. The *sulphur inhibition* is caused by three effects of sulphur: (i) the carbon transfer from the atmosphere is retarded, since adsorbed sulphur blocks the surface reaction in the carburization, (ii) adsorbed sulphur restricts the nucleation of graphite, and thus the start of cementite decomposition (6.1) is retarded, and (iii) sulphur inhibits the graphite growth, so reaction (6.1) is slowed [11, 12]. Also the coking is reduced by the presence of sulphur. The adsorption of sulphur on the metal phase and on the cementite occurs by the reaction



This means a certain amount of H_2S must be present in the atmosphere (and also formed from additions such as CS_2 , $(\text{CH}_3)_2\text{S}_2$). It has been shown that only relatively small sulphur activities $a_{\text{S}} = K_{\text{S}} \cdot p_{\text{H}_2\text{S}} / p_{\text{H}_2}$ are needed for formation of a monolayer S(adsorbed) on iron [13, 14] and thus for protection of iron and steels, e.g. about $p_{\text{H}_2\text{S}} / p_{\text{H}_2} = 10^{-6}$ is sufficient at 600°C – but with increasing temperature this value increases, which must be considered in operation (see Section 6.2.3).

Besides sulphur inhibition, the other more important way of protection is by *oxide scales*. In the temperature range in question, a protective scale generally consists of two layers: an outer spinel MnCr_2O_4 and an inner chromia Cr_2O_3 layer. Such layer can be formed on ferritic steels with $>11\%$ Cr and on austenitic steels with $>17\%$ Cr, the latter steels need more Cr since the Cr diffusivity is lower in the austenitic lattice. Even at a low p_{O_2} , as established in process gases by the presence of some CO_2 and/or H_2O , these oxides are stable. But such scales may have defects, where carbon ingress and metal dusting can start and will lead to the well-known appearance of pits and holes in high-alloy steels. The defects can be caused by heterogeneities in the surface, inclusions and precipitates (TiN, WC, NbC, etc.), scratches or edges [15]. Defects may also arise from oxide cracking and spalling, due to creep, fatigue and thermal cycling. The first step in the metal dusting of high-alloy materials is the precipitation of internal carbides (MC, M_7C_3 , M_{23}C_6). Oversaturation follows and then material disintegration by one of the mechanisms described above. Pits are formed which grow together in the case of very susceptible alloys (P91, Alloy 800 and 600), so that attack becomes uniform. The chromium ends up in oxides, chromia and/or spinels.

At temperatures $<650^\circ\text{C}$ a protective Cr-rich scale may not be formed, owing to slow Cr diffusion; Fe-rich oxides may form which are less protective [16–18]. The growth of the Cr-rich scale must be fostered by fast diffusion paths, i.e. grain boundaries, sub-boundaries and dislocations. Therefore a fine-grain microstructure is advantageous as is near-surface deformation by surface working: grinding, sandblasting, shot-peening, etc. The positive effect of a fine-grain microstructure and of grinding has been proven by metal

dusting exposures of various steels at 500–600 °C [16]. In contrast, pickling or electropolishing have negative effects on metal dusting resistance of steels, since any surface deformation is removed. Near-surface deformation clearly enhances the Cr diffusivity in steels as shown by tracer diffusion studies and by taking SNMS profiles of the Cr depletion beneath the oxide scale after different surface treatments and oxidation at 600 °C.

Alloying additions of Al, Si and Mn can be helpful to increase the metal dusting resistance [15]. Since generally no more than a few wt% can be added to the usual high-temperature materials, no continuous scales of these elements are formed, but they help in the formation of protective scales.

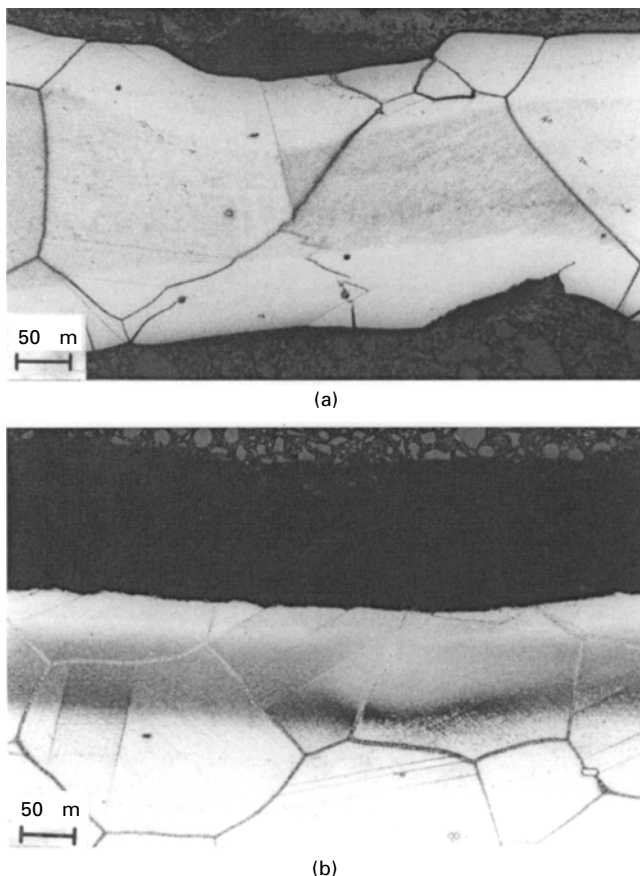
High Ni contents are favourable since the carbon solubility and diffusivity decrease with increasing Ni content, so the carbon ingress is retarded. In fact, some Ni-base alloys have proven to be rather resistant against metal dusting [19, 20]: Alloy 600 is still rather susceptible, owing to its low Cr content of about 15% Cr; Alloy 601 is much better with 23% Cr but it shows a tendency to form a small number of solitary pits; and Alloy 602 with 25% Cr and 2.3% Al and Alloy 690 with 30% Cr are very resistant. But even Alloy 602 is attacked by metal dusting, after pickling or electropolishing, and at the weldments although made of the same material.

6.2 Failure cases

6.2.1 Metal dusting in a heat exchanger

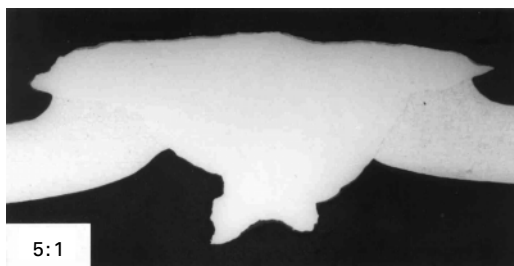
The heat exchanger, built mainly of Alloy 800, failed after 23 000 h thorough localized wastage of the 10 mm thick sheet. The hole was closed by welding a patch of Alloy 601 on the wall, but after 31 000 h the heat exchanger was taken out of service. Metallographic cross-sections of the wall material indicate nearly uniform metal wastage all over the surface. Figure 6.1a shows a piece of Alloy 800 which was found to have been attacked from both sides: it was still covered with some coke but did not have the typical carburized zone. On Fig. 6.1b, a wall section from another place, both carburized zone and coke were visible and the grain boundaries were marked by carbon ingress. A weldment in the wall attacked from both sides showed metal dusting of the base material Alloy 800 and a somewhat slower attack of the Ni-base weld material (~ Alloy 600), see Fig. 6.2a, b.

Since the wall of Alloy 800 was wasted from 10 mm to 3–0 mm in different places, a metal wastage rate results of 2–3 mm/year. Such rates were measured in laboratory tests on Alloy 800 and other steels in the temperature range 525–550 °C [21, 22]. Since the heat exchanger operated in the temperature range 575–350 °C, one can conclude that the walls made of Alloy 800 were attacked from the start of the operation. The large-grained material is very susceptible to metal dusting and has no chance to form a Cr-rich protective



6.1 Metal dusting attack on the wall of a heat exchanger, made of large grained Alloy 800, metallographic cross sections: (a) wall segment, thinned from both sides from 10 mm to 2–3 mm; (b) uniformly attacked wall surface, typical appearance of metal dusting: coke layer, carburized zone.

scale at the relatively low temperatures, owing to insufficient Cr diffusion and supply to the surface [16–18]. In contrast, some small metal parts which had been in the same heat exchanger, exposed to the same atmosphere and temperature range, showed no sign of metal dusting attack, see Fig. 6.3a, b. Both were made of fine-grained steels with about the same Cr content, a nut made of a 21Cr–12Ni–0.7Si–steel, and a stainless steel sheet of 17Cr–9Ni–0.5Si–0.33Ti steel. Both materials had formed a protective oxide scale, the stainless steel in the temperature range 460–550°C. For both steels the fine-grained microstructure was of importance for the oxide formation, providing many fast diffusion paths for transport of Cr and Si to the surface. The analysis of the oxide scales showed a high content of Si at the outer surface,



(a)



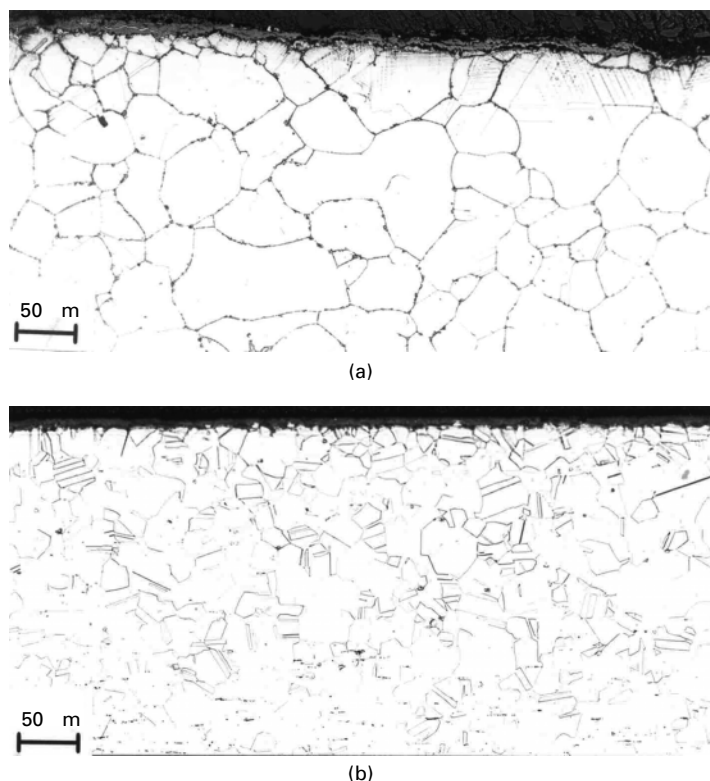
(b)

6.2 Metal dusting attack on a weldment in the wall of the same heat exchanger, metallographic cross-sections: (a) total view, weld material less attacked than the base material (unetched); (b) corner of the weldment, showing carburized zone in the weld and base material.

so presumably the relatively high Si content of the steels led to an initial SiO_2 formation and was helpful in formation of a protective dense scale which prohibited carbon ingress and start of metal dusting.

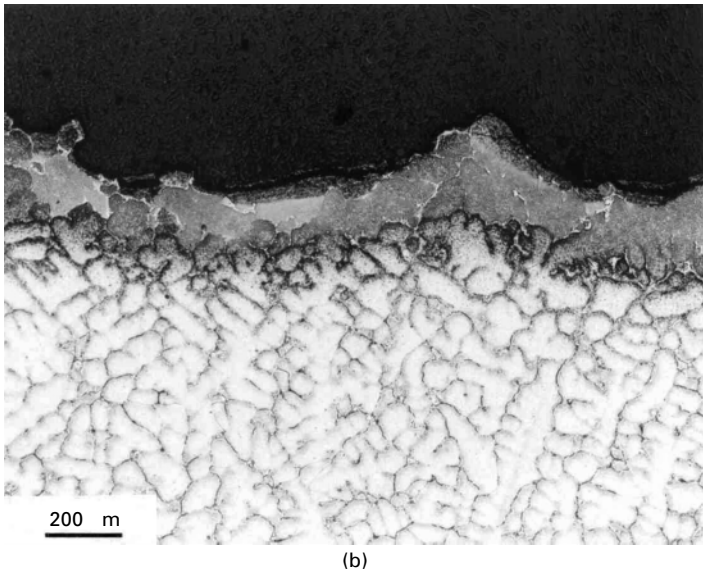
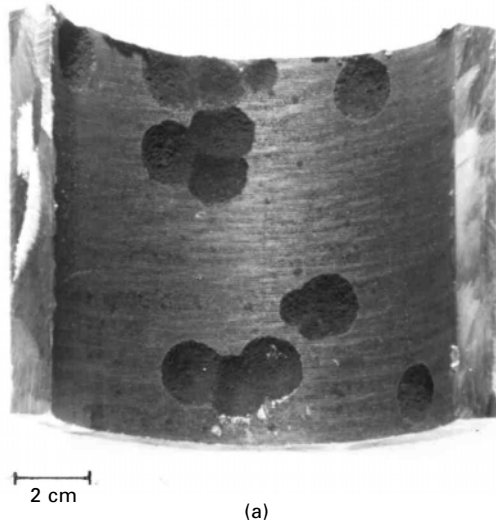
6.2.2 Metal dusting in the gas heaters of a direct reduction plant

A strong attack by metal dusting was investigated in detail [23] which had occurred in the gas heaters of a direct reduction plant, where a $\text{H}_2\text{--CO--CO}_2\text{--H}_2\text{O}$ mixture is heated from ambient temperature to reduction temperature, about 950°C . The heater coils had been produced from centrifugally cast tubes of the steel HK 40. This steel has the nominal composition 25Cr–20Ni–1–2Si, but in the case described the Cr content was at the lower level 22–23% Cr which was one reason of the failure. The material has a coarse dendritic microstructure with large carbide precipitates (M_{23}C_6). At elevated temperature the steel tends to ageing by precipitation of fine secondary carbides and γ' -phase. The inner walls of the straight tube segments are machined, the cast surface with its pores is removed and additionally a



6.3 Metallographic cross-sections of parts from the same heat exchanger (see Figs 6.1 and 6.2), not attacked by metal dusting but covered with a protective scale, parts made of fine-grained materials: (a) 21Cr–12Ni–0.7 Si steel; (b) 17Cr–9Ni–0.5Si–0.33Ti steel.

certain near-surface deformation is introduced. The heaters are operated usually under introduction of sulphur, by dosing DMDS, $(\text{CH}_3)_2\text{S}_2$, which should decompose at process temperature, yielding a sufficient level of H_2S for protection. A constructional error in the plant that for some time one of the heaters was not supplied with DMDS. Shortly after, leaks occurred and a strong metal dusting attack was detected in wide regions of the coils. Depending on the temperature pits of varying depth were found in the inner wall of the tubes, see Fig. 6.4a, b. The welds or the heat-affected zones near the weld were attacked even more strongly than the straight machined sections. Since heaters of this type have been used without severe failures for many years (with continuous supply of sulphur), the lack of H_2S in the atmosphere was obviously the main reason for this failure. Additionally, the low Cr content of the steel was a weakness and the microstructure and composition of the welded joints caused enhanced attack.



6.4 Metal dusting attack in the heater tube of a direct reduction plant at about 600 °C: (a) tube section of HK40 (cast 25%Cr–20%Ni steel) with deep pits; (b) metallographic cross-section, showing pits and carburized zone.

6.2.3 Failure of a platformer unit in a refinery

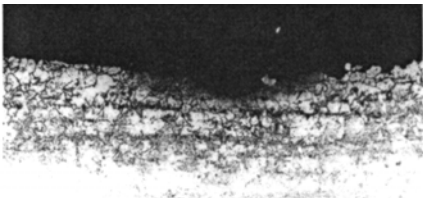
In continuous catalyst regeneration (CCR) units there are heaters for heating naphtha or other feedstock to the critical temperature range about 600 °C. The tubes are made of 2 $\frac{1}{4}$ Cr–, 5Cr– or 9Cr steels, depending on the temperature

range. Two failure cases by metal dusting have been reported [24, 25], both most probably because of an increase of operating temperature and insufficient supply of sulphur at the higher temperature. One of these cases happened in a plant where the unit had been operated with 5%Cr steel tubes for 25 years without failure. Some changes preceded the failure: (i) in the heater concerned, new steels made of 9%Cr steel had been installed, (ii) the amount of sulphur in the feedstock had been reduced, owing to the introduction of a new catalyst, and (iii) the operating temperature was raised up to about 675 °C. The new 9%Cr tube failed after a short time: because of metal dusting, coke deposits had formed in certain regions, which led to overheating and crack formation. The overheating could be induced from changes in the steel microstructure and the formation of a ‘red scale’ on the outer tube wall.

By analyses of intact old tubes from the same CCR unit, hints were found to explain why the pipes installed earlier did not fail. The metallographic cross-section showed an internally carburized zone and a scarred surface (see Fig. 6.5a, b), i.e. indications of metal dusting. Auger spectra taken on the surface showed graphitic deposits or metallic areas covered with adsorbed sulphur (see Fig. 6.5c, d). Obviously the material had been largely protected by adsorbed sulphur and a coke layer, and only very slow metal dusting had taken place. In contrast, the new tube had no chance to obtain such a protective coating, owing to the enhanced operation temperature and the insufficient level of sulphur in the atmosphere.

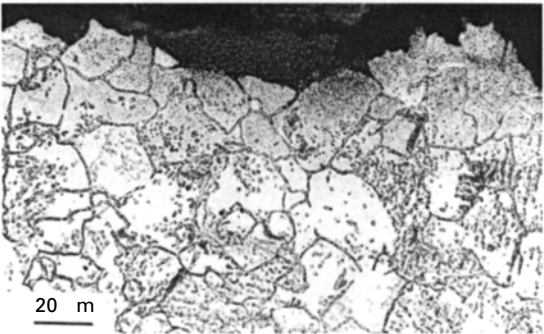
6.2.4 Metal dusting in a direct reduction furnace

In this case, sheets of Alloy 800 suffered a very strong attack (see Fig. 6.6a, b, c) within about six months, after 20 years of operation with only minor attack. These sheets guide the cooling gas from the lower part of the shaft furnace into the upper part, where the reduction gas enters. The ore is reduced on its way from the top of the furnace and leaves as iron sponge at the bottom. In the region in question the temperature is 400–500 °C and the H_2 –CO–CO₂–H₂O atmosphere has carbon activities between $a_C = 2000$ to 100. The material Alloy 800 is fairly susceptible, but the sulphur content ~ 10–12 ppm H₂S should effectively retard the metal dusting attack so that the 20–25 mm thick sheet could serve for many years. Some additional attack must have caused the acceleration. Energy dispersive spectroscopy (EDS) analysis of the corrosion products indicated presence of chlorides, and it was known that chlorine had been introduced in the process line for controlling the growth of algae in a cooling unit. Obviously the presence of chlorine and the formation of chlorides hindered the formation of protective oxide scale and the very severe attack is due to the combined action of chloridation and metal dusting.



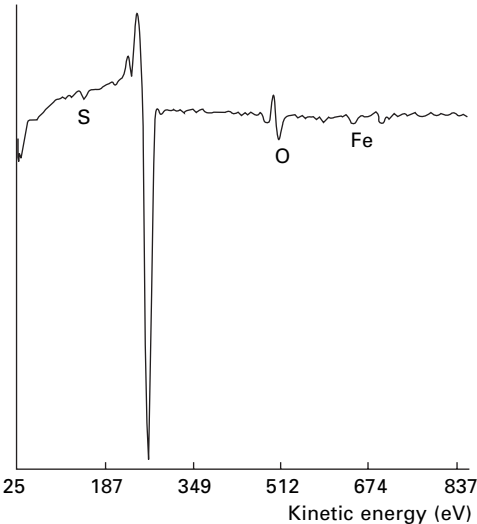
100 m

(a)



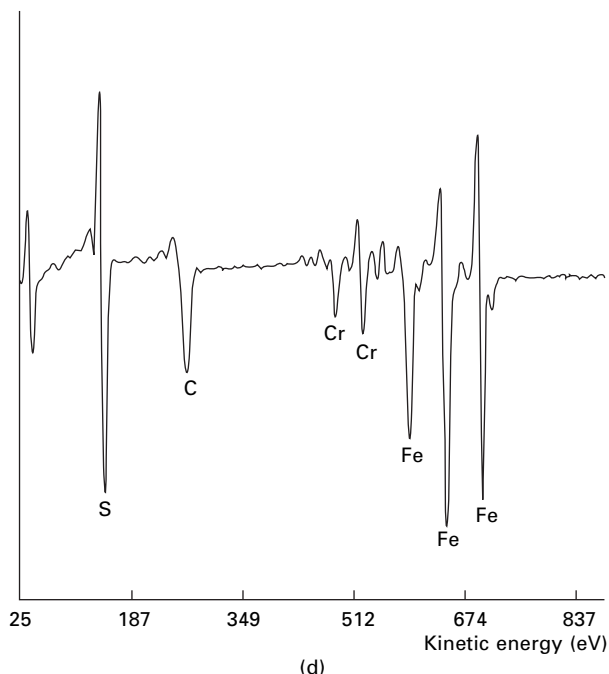
20 m

(b)



(c)

6.5 Metal dusting of the inner tube wall in a refinery heater (CCR unit): (a) and (b) metallographic cross-sections, showing only moderate attack of the 5%Cr-steel; (c) and (d) Auger spectra demonstrating the protecting carbon and sulphur layer on the surface.



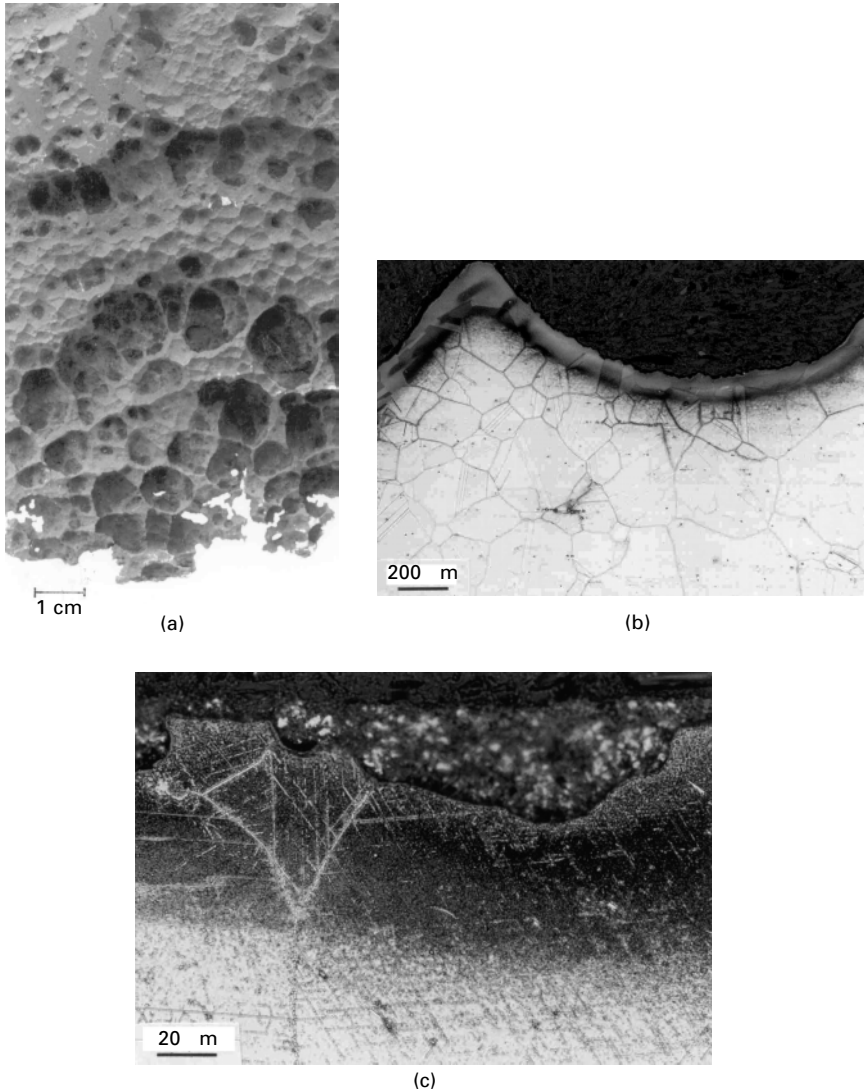
6.5 Continued

6.2.5 Metal dusting in a heat exchanger of an ammonia plant

A tube section which had been in service for $2\frac{1}{4}$ years was received for failure analysis, it showed severe attack by metal dusting on the outer surface (Fig. 6.7a, b) and locally some greenish spots. These spots were deposits of mineral salts, as shown by EDS and Auger electron spectroscopy (AES) analysis and most probably stemmed from an ingress of steam at the gas side, six months before the failure and inspection. In addition to the alloying elements, the analyses detected K, Na, Mg, Ca, Cl and S, which should not be carried by the process gas and should not be present on the tube. It may be concluded that deposition of mineral salts from the impure steam on the tube has locally destroyed the protective oxide layer on the Alloy 601. Preliminary tests on the effect of salt deposits, chlorides, sulphates and carbonates have shown accelerated start and enhanced attack by metal dusting on several materials.

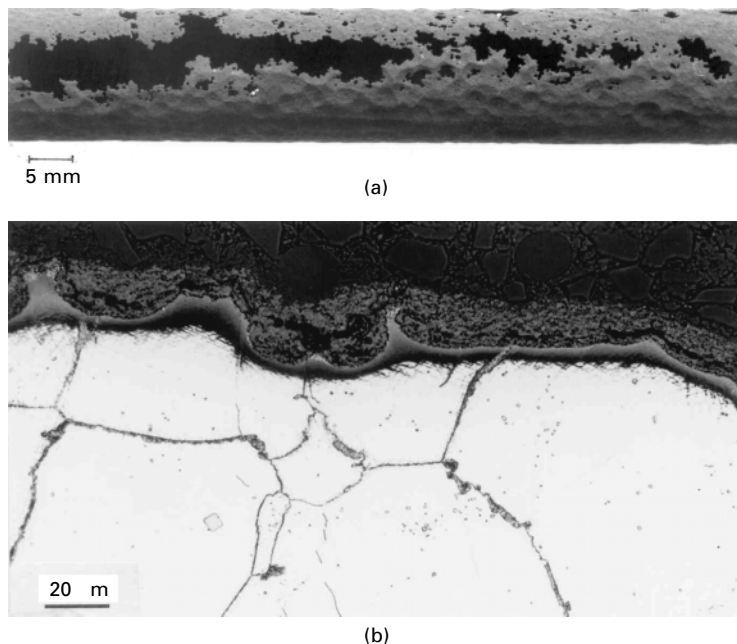
6.3 Conclusions

Metal dusting is a corrosion phenomenon that may start immediately on susceptible materials such as low-alloy steels, Alloy 800 and 600, sometimes



6.6 Severe metal dusting attack on a steel sheet (Alloy 800) from a direct reduction furnace: (a) piece of the steel sheet with vast erratic pitting; (b) and (c) metallographic cross-sections, showing pits with carburized zone and coke.

unexpectedly, but mostly after some change in the operation conditions, repairs or changes of material and sudden ingress of impurities. On the base of current knowledge the occurrence of metal dusting can generally be explained. Some failed cases and reasons for their failure have been presented.



6.7 Severe metal dusting attack on a heat exchanger tube made of Alloy 601: (a) part of the corroded tube; (b) metallographic cross-section, showing general metal dusting – quite unusual for Alloy 601 on which otherwise single hemispherical pits occur.

One way of protecting steels is the presence of an appropriate partial pressure of H_2S in the atmosphere, and the concentrations necessary for suppressing metal dusting have been determined. A failure case has been described of the heater in a direct reduction plant, where metal dusting of HK40 started, because of the lack of a supply of sulphur. In the second case, of a CCR unit in a refinery, the sulphur content was lowered and the temperature increased, so that newly installed tubes suffered immediate metal dusting, owing to a $p_{\text{H}_2\text{S}}$ value that was too low at the raised operation temperature.

In two other cases, the start of metal dusting was caused by ingress of impurities, chlorine in the case of a reduction furnace, and mineral salts in the case of a heat exchanger. Both impurities obviously destroyed protective oxide scales, so that metal dusting attack started at numerous points and caused erratic attack.

6.4 References

1. H.J. Grabke, R. Krajak, J.C. Nava Paz: *Corrosion Sci.* **35**, 1141–1150 (1993).
2. H.J. Grabke, R. Krajak, E.M. Müller-Lorenz: *Werkst. u. Korros.* **44** (1993) 89–97.
3. H.J. Grabke, C.B. Bracho-Troconis, E.M. Müller-Lorenz: *Werkst. u. Korros.* **45** (1994) 215–221.

4. H.J. Grabke: *Corrosion NACE* **51** (1995), 711–720.
5. H.J. Grabke, R. Krajak, E.M. Müller-Lorenz, S. Strauss: *Werkst. u. Korros.* **47** (1996) 495–504.
6. H.J. Grabke: *Mat. Corr.* **49** (1998) 303–308.
7. E. Pippel, J. Woltersdorf, H.J. Grabke, S. Strauss: *Steel Res.* **66** (1995) 217–221.
8. R. Schneider, E. Pippel, J. Woltersdorf, S. Strauss, H.J. Grabke: *Steel Res.* **68** (1997) 326–332.
9. E. M. Müller-Lorenz, H.J. Grabke: *Mat. Corr.* **50** (1999) 614–621.
10. S. Strauss, R. Krajak, H.J. Grabke: *Mat. Corr.* **50** (1999) 622–627.
11. H.J. Grabke, E.M. Müller-Lorenz: *Steel Res.* **66** (1995) 252–258.
12. A. Schneider, H. Viefhaus, G. Inden, H.J. Grabke, E.M. Müller-Lorenz: *Mat. Corr.* **49** (1998) 330–335.
13. H.J. Grabke, E.M. Petersen, S. R. Srinivasan: *Surf. Sci.* **67** (1977) 501.
14. H.J. Grabke: *Mat. Sci. Engg.* **42** (1980) 91.
15. S. Strauss, H.J. Grabke: *Mat. Corr.* **49** (1998) 321–327.
16. H.J. Grabke, E.M. Müller-Lorenz, B. Eltester, M. Lucas, D. Monceau: *Steel Res.* **68** (1997) 179–185.
17. H.J. Grabke, E.M. Müller-Lorenz: *Mat. Corr.* **49** (1998) 317–320.
18. H.J. Grabke, E.M. Müller-Lorenz, S. Strauss, E. Pippel, J. Woltersdorf: *Oxid. Metals* **50** (1998) 241–254.
19. J. Klöwer, H.J. Grabke, E.M. Müller-Lorenz: *Proc. EUROCORR '97*. 22–25 Sept. 1997, Trondheim, Norway.
20. H.J. Grabke: *Corrosion* **56** (2000) 801–807.
21. E.M. Müller, H.J. Grabke: *Mat. Corr.* **50** (1999) 614.
22. H.J. Grabke: *Mater. High Tempe.* **17** (2000) 483.
23. H.J. Grabke, D. Gläser: *Prakt. Metallogr.* **33** (1996) 540–548.
24. M.H. Ravesteyn: Corrosion 97, paper No. 496, *NACE Int.*, Houston, Texas 1997.
25. H.J. Grabke, C.H. Gerk: *EUROCORR '99*, Aachen, CD-ROM.

Protective behaviour of newly developed coatings against metal dusting

C ROSADO and M SCHÜTZE, Karl-Winnacker-Institut der DECHEMA e.V., Germany

7.1 Introduction

Whether a material is resistant to metal dusting or not depends on the ability of the material to develop a protective oxide scale. Most of the conventional low-cost steels widely used in plant technology do not possess a sufficient potential for protective oxide scale formation. However, in order to prevent corrosion of the materials, protective coatings rich in Al, Cr, Ti and Si can be applied, which can form protective oxide scales and, thus, protect the underlying substrate from corrosive attack. In the present work, Al, Cr, Si and Ti have been chosen to produce diffusion and overlay coatings for reasons of their ability to form very stable protective oxide layers.

The specific features of these elements in a coating system are:

- *Al*: Formation of protective thermodynamically very stable Al_2O_3 or with chromium (Al,Cr)-oxide.
- *Si*: Formation of protective thermodynamically very stable SiO_2 . Si furthermore can improve ductility of coatings [1].
- *Ti*: Promotes (in combination with Al) the formation of $\text{-Al}_2\text{O}_3$ at low temperatures. Formation of protective thermodynamically very stable Ti oxides.
- *Cr*: Acts as inter-diffusion barrier for Al and forms Cr_2O_3 .

In the past, several coatings have been applied to different materials in order to protect them against metal dusting attack [2–4]. It is known from the literature [5] that carbon can penetrate oxide scales through pores and defects, producing internal carburization. Thus, the oxide scale formed on such coatings must be homogeneous, adherent and free from pores and defects.

In this chapter, several newly developed coatings will be presented and the influence of temperature on oxide formation and behaviour of the different coatings will be discussed. The first type of coatings was applied by the pack cementation method [6, 7], leading to a diffusion coating on the base material.

These coatings are based on stable oxide formers such as Al, Ti, Si and Cr. The material to be coated is placed in a 'pack' which consists of a powder mixture of the master alloy (element/s to be diffused), the activator (NH_4Cl), and an inert filler material (Al_2O_3). The retort is then heated to a certain temperature and time and components of the master alloy diffuse into the material forming a diffusion coating. Diffusion coatings were applied to the ferritic steels 10CrMo9 10 (2.25%Cr), Alloy P91 (9%Cr), X18CrAl18 (18%Cr), X18CrN28 (28%Cr) and to the austenitic steel Alloy 800. The composition of these alloys is shown in Table 7.1. The second type of coating was a HVOF (high-velocity oxyfuel) spray coating based on the intermetallic - TiAl phase [8].

The coatings were tested under metal dusting conditions at three temperatures, 400, 620 and 700°C. Under these conditions the coatings could develop an oxide scale; but not in all cases (in particular, not for the single element coatings) was this oxide homogeneous and adherent. Therefore, a combination of various elements was also used in order to optimize the coating properties and to improve protection by the oxide scale formed.

7.2 Experimental procedure

7.2.1 Substrates

As mentioned above, in the present investigation, five different substrates were chosen (Table 7.1). Four of them were ferritic steels with differences in the chromium content ranging from 2.25%Cr to 28%Cr. The other substrate was the austenitic steel Alloy 800, containing about 20%Cr.

Before application of the coatings, the samples were ground up to 500 grit by a SiC grinding paper and ultrasonically cleaned in acetone and ethanol before inserting them into the pack.

7.2.2 Coatings

The coatings applied to the samples were based on strong oxide formers. The different one-step diffusion coatings were:

- *Single element diffusion coatings:*
 - Al diffusion coating
 - Si diffusion coating
 - Cr diffusion coating
- *Multi-element co-diffusion coatings:*
 - Si–Al co-diffusion coating
 - Ti–Al co-diffusion coating
 - Ti–Si–Al co-diffusion coating

Table 7.1 Composition of the alloys investigated

Alloy	%C	%Si	%Cr	%Al	%Ni	%Mn max.	%Mo max.	%P max.	%S max.	Other
10CrMo9 10	0.08–0.15	0.5	2–2.5	–	–	0.40–0.70	0.90–1.20	0.030	0.025	Cu 0.30
Alloy P91	0.08–0.12	0.20–0.50	8.0–9.5	<0.040	<0.40	0.30–0.60	0.85–1.05	0.02	0.01	V 0.20 – Nb 0.08
X10CrAl18	0.12	0.70–1.40	17–19	0.70–1.20	–	1	–	0.04	0.03	–
X18CrN28	0.15–0.20	1	26–29	–	–	1	–	0.045	0.03	N 0.15–0.20
Alloy 800	0.12	1.00	19–23	0.15–0.60	30.0– 34.0	2	–	0.03	0.02	Ti 0.15–0.60

Sometimes the combination of more than one element in the diffusion coating can improve the properties of the coating, such as adherence, ductility, and even the corrosion resistance. In order to study the different effects that these elements have on the coatings, the above-mentioned co-diffusion coatings of two and three elements were produced and tested.

The metallic oxide formers contained in the pack form chlorides that are volatile and are transported via the gas phase to the surface of the material to be coated. In order to adjust the activity of the pack, thermodynamic data have been taken into account to characterize the stability and the amount of the chlorides formed. Using the data, the optimum experimental parameters such as temperature and time of the diffusion process can be defined. The thickness of the coating must be sufficient to provide protection to the material but it must not be too high, since the mechanical properties would suffer and the different thermal expansion coefficients of substrate and coating can lead to cracks and defects in the coating during cooling. The thickness is normally between 50 and 200 μm . In order to achieve this thickness as well as a good adherence on the base metal, it is necessary to adjust the different variables of the diffusion process, such as diffusion process temperature, pack composition, material composition, time of the diffusion process, etc. Several pre-screening tests had to be performed before the optimum experimental parameters were found.

For the application of the coatings, the samples were introduced in the powder pack. The system was then heated to a temperature that varied between 700 and 1200 °C. At such temperatures the master alloy reacts with the activator and forms a halide, which is transported via the gas phase to the surface of the material to be coated. This metal halide decomposes in contact with the surface. The metal is absorbed in the material surface and diffuses into the material, and depending on time and temperature, different coating thicknesses are achieved. The thickness and the phases of the coating depend on the substrate material composition since the diffusion rate, for example of aluminium, is different for different substrates.

For alloy 10CrMo9 10, a Cr–Al-2 step diffusion coating was also applied. Chromium acts as a diffusion barrier against the inward diffusion of aluminium. The alloy 10CrMo9 10 has a chromium content of 2.25%. With this small amount of chromium, if an Al diffusion coating were applied, there would be further inward diffusion of aluminium into the material during plant operation. This would provoke the loss of aluminium at the surface, which is needed to form the oxide scale, owing to interdiffusion. In order to avoid this, a chromizing step was performed first by the pack cementation method. Thus, an enrichment of chromium is achieved. After this process, the aluminizing step is performed. Contrary to the other diffusion coatings this was not a co-diffusion coating since the elements (Cr and Al) were not diffused simultaneously but in two different processes. The Cr–Al 2-step diffusion coating was only applied to Alloy 10CrMo9 10.

The chromizing process has three different effects:

1. It prevents further inward diffusion of aluminium (which is diffused in the second step by aluminizing) into the substrate, thus keeping the level of aluminium high, which is needed for scale defect repair and protective oxide formation.
2. It is also beneficial for the adherence of the aluminizing coating, leading to a more homogeneous and regular interface between coating and substrate with only a small amount of or no pores.
3. Chromium may help for additional protection against metal dusting since chromium is able to develop a protective stable oxide scale as well.

The application of the HVOF spray coating was performed by ATZ EVUS. This coating was applied to the ferritic steel X10CrAl18 and to the austenitic steel Alloy 800. Under working conditions, the coating is able to develop Ti and Al oxide which is protective and thermodynamically stable, providing protection against metal dusting.

7.2.3 Metal dusting tests

In the metal dusting tests, samples with and without coatings were investigated. The samples were isothermally tested under the metal dusting conditions (for gas composition see next section) at the three different temperatures, 400, 620 and 700 °C.

The coated and uncoated samples were ultrasonically cleaned in ethanol and acetone and weighed before being inserted into the furnace. After different time intervals, which varied between 24 and 336 h, depending on the overall testing time, the samples were taken out of the furnace, brushed for coke removal if necessary and weighed again to register the mass change. Measurements of the thickness of the specimens were also carried out. After this procedure the specimens were inserted again into the furnace continuing the test. At the end of each test the samples were cross-sectioned for metallographic examination.

7.2.4 Test atmospheres

Two different atmospheres were selected with the following compositions:

- Standard atmosphere: 25%CO–73% H_2 –2% H_2O
- Industrial atmosphere: CH_4 – CO_2 –CO– H_2 – H_2O – N_2 –HCl– H_2S

The standard atmosphere was used for all temperatures while the industrial atmosphere was used only for 620 °C. This temperature was chosen for the experiments under the industrial atmosphere since it is assumed to be the most critical metal dusting temperature for most of the steels. The water

Table 7.2 Carbon activities and oxygen partial pressures of the test atmospheres calculated for different temperatures

Atmosphere		400 °C		620 °C		700 °C	
Standard	a_c	9904		25.63		5.68	
	p_{O_2} (bar)	1.7478	10^{-36}	4.5437	10^{-27}	1.0883	10^{-24}
Industrial	a_c	20073		23.3		8.75	
	p_{O_2} (bar)	2.025	10^{-36}	3.0355	10^{-26}	3.068	10^{-24}

vapour content of the atmosphere was added by passing the dry gas through a water bath held at a constant temperature by a thermostat. The gas flow rates were controlled using digital flow meters. Argon was used during heating and cooling of the furnace.

The potential uptake of carbon by the substrate can be described by three different reactions depending on the gas atmosphere [9–11]:



The kinetics of reactions (7.1) and (7.3) are not favourable under the experimental conditions and the carbon activity of the gas mixture in the present investigations was calculated assuming that formation of carbon takes place by reaction (7.2):

$$a_c = \frac{p_{CO} \cdot p_{H_2}}{K \cdot p_{H_2O}} \quad 7.4$$

The carbon activities calculated for the test atmospheres by equation (7.4) are shown in Table 7.2. When the carbon activity is greater than 1 (non-equilibrium atmosphere; $a_c = 1$ corresponds to equilibrium with graphite), carbon deposition, graphite growth and metal dusting can take place.

7.2.5 Metallographic examination

After the different time intervals during each test, photographs of the surface appearance of the samples were taken. At the end of the whole metal dusting exposure for each test the samples were hot embedded and cross-sectioned for metallographic investigation. Before embedding, a Ni plating was applied by electrodeposition in order to enhance the contrast between the embedding material and the surface of the sample which, in most of the cases, shows the formation of an oxide scale or coke deposition.

Some samples were etched in order to allow a better interpretation of the different microstructures and to assess the depth of attack in the samples.

The etching procedure was performed with different reagents such as 20% alcoholic hydrochloric acid, electrolytically etching in oxalic acid (10%), V2A-Pickel and Nital, depending on the substrate material and phases to be seen.

Besides optical microscopy the samples were analysed by SEM (scanning electron microscopy), EDX (energy dispersive X-ray analysis) and EPMA (electron probe micro-analysis).

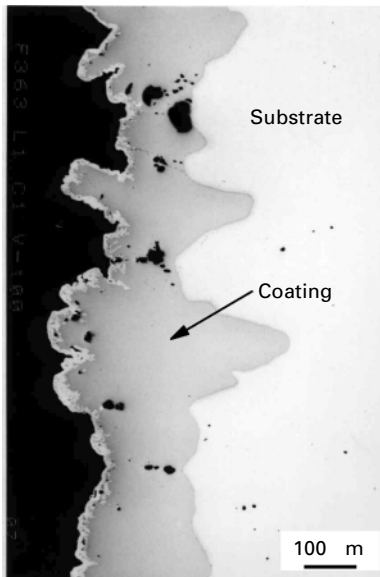
7.3 Results and discussion

7.3.1 Alloy 10CrMo9 10

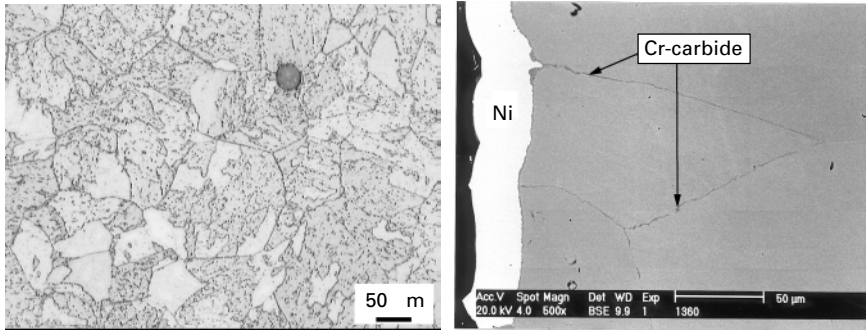
Coating process

The first coating applied to this material was an Al diffusion coating. As can be observed in Fig. 7.1, the coating/substrate interface is very irregular and there are some regions where the diffusion front reaches 400 μm in depth. This is an undesired result and therefore a preceding chromizing step was applied. With this process, chromium is diffused into the steel, leading to an enrichment of chromium in the surface.

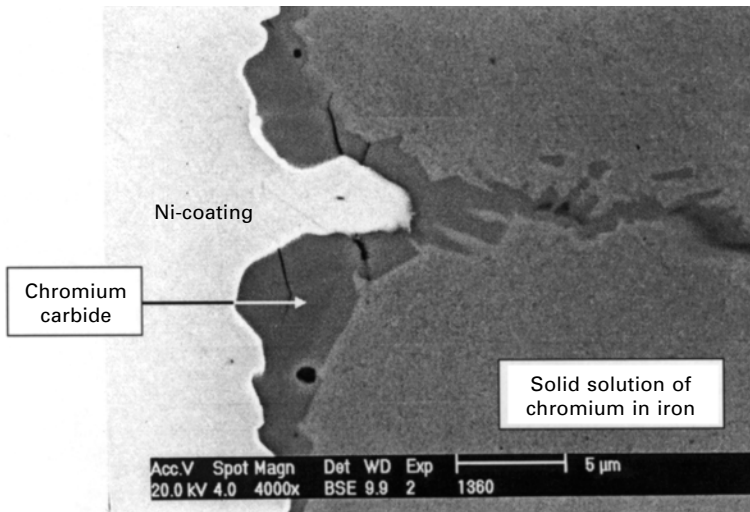
The chromium diffusion step is performed at 1120°C for 24h, and the microstructure of the steel is affected during the process (Fig. 7.2). The change in the microstructure of the alloy is due to the heat treatment during



7.1 Al diffusion coating applied to alloy 10CrMo9 10.



7.2 Left: Microstructure of alloy 10CrMo9 10 in its original condition. Right: Alloy 10CrMo9 10 after the chromizing process. Chromium carbide is formed at the surface and at the grain boundaries.



7.3 Detail of the chromium carbide formation at the surface of the sample and at the grain boundaries of alloy 10CrMo9 10 after the chromizing process.

the coating process. At 1120 °C for a period of time of about 24h chromium carbides in the substrate are dissolved and, since the cooling process is slow enough, carbon can reprecipitate at grain boundaries as chromium carbides. The grains, which are decorated with Cr carbides at the boundaries, have grown during the diffusion process. A detail of this carbide precipitation can be seen in Fig. 7.3.

From the EDX analyses and from the Fe–Cr phase diagram, it is concluded that under the chromium carbide layer at the surface the coating consisted of a solid solution of chromium in iron (–Fe, Cr) with a chromium content that

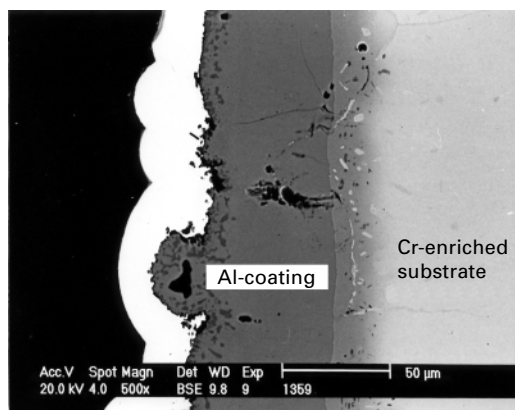
varies from 38.9%Cr at the surface to around 2.25%Cr, which is the original substrate content which is reached at about 250 μm in depth.

After the chromizing process, the aluminium diffusion coating was applied in a second step (Fig. 7.4). A more homogeneous/regular coating is obtained than after the single step aluminizing process shown in Fig. 7.1. In the case of the aluminizing process as a second step of the whole diffusion process, the coating consists of two phases. One is a solid solution of Al in Fe (γ_2) and the other is the intermetallic FeAl_2 (dark precipitates in the outer part of the coating in Fig. 7.4).

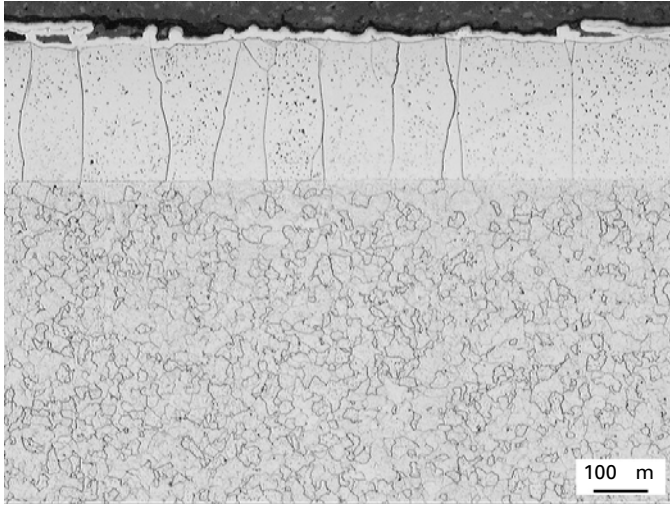
Silicon is a strong oxide former as well, and it can develop a protective SiO_2 scale. It is also known from the literature [1] that silicon may improve the ductility when added as an additional element to an aluminium diffusion coating. For the first reason, an Si diffusion coating was developed as well for this alloy (Figs 7.5 and 7.6). However, it was not possible to diffuse large amounts of silicon into the material. EDX analyses revealed a maximum amount of 1.25% Si in the present investigations. It can be observed that there is a change in the microstructure as in the case of chromizing. Carbides are dissolved and reprecipitated at the grain boundaries.

Since it was difficult to produce a Si diffusion coating and for the second reason mentioned above (i.e. improvement of the physical properties of Al diffusion coatings), an Si–Al co-diffusion coating was developed (Fig. 7.7). A diffusion zone in the substrate is obtained with a maximum concentration of 28.3%Al and 3.5% Si.

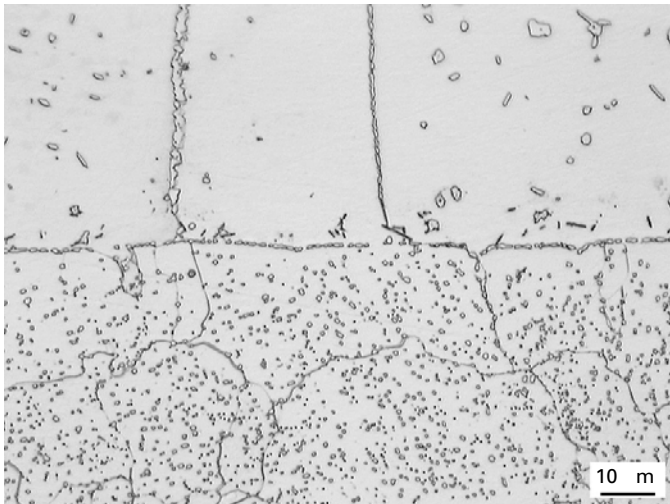
A Ti–Al co-diffusion coating was applied as well. In this case a titanium carbide layer was formed at the surface (Fig. 7.8), which prevented any further inward diffusion of aluminium and/or titanium. In the outer part of this layer, a second phase was formed consisting of Ti–Al intermetallics.



7.4 Cr–Al 2-step diffusion coating on alloy 10CrMo9 10.



7.5 Si diffusion coating applied to Alloy 10CrMo9 10.

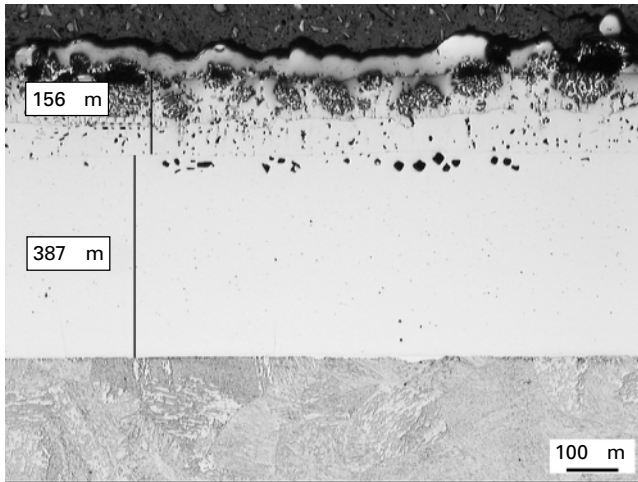


7.6 Detail of the Cr-carbide precipitation in Alloy 10CrMo9 10 coated with a Si diffusion coating.

However, the formation is irregular and discontinuous. A detail of these precipitates is shown in Fig. 7.9.

Metal dusting behaviour

Table 7.3 shows the general behaviour of the coatings applied to alloy 10CrMo9 10 tested under metal dusting conditions at different temperatures. Mass



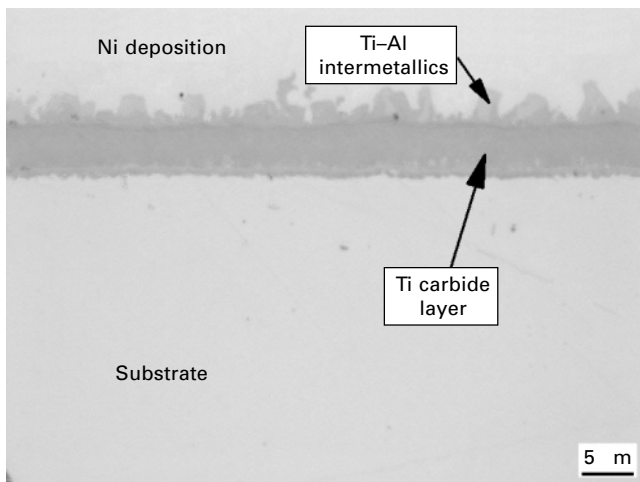
7.7 Si-Al co-diffusion coating applied to Alloy 10CrMo9 10.



7.8 Ti-carbide layer as a result of the Ti-Al co-diffusion coating process on Alloy 10CrMo9 10.

change measurements have been carried out as well at all temperatures (Fig. 7.10).

Although 700°C is the temperature at which the carbon activity is lower, attack of the uncoated material also takes place in the early stages of exposure. At this temperature, diffusion is faster than at lower temperatures. Because of this, stronger attack was found at 700°C than at 400°C although the carbon activity is much higher at the latter temperature. At 620°C the mass loss of the specimen is very high (Fig. 7.10). The attack is homogeneous all



7.9 Ti-Al co-diffusion coating on Alloy 10CrMo9 10.

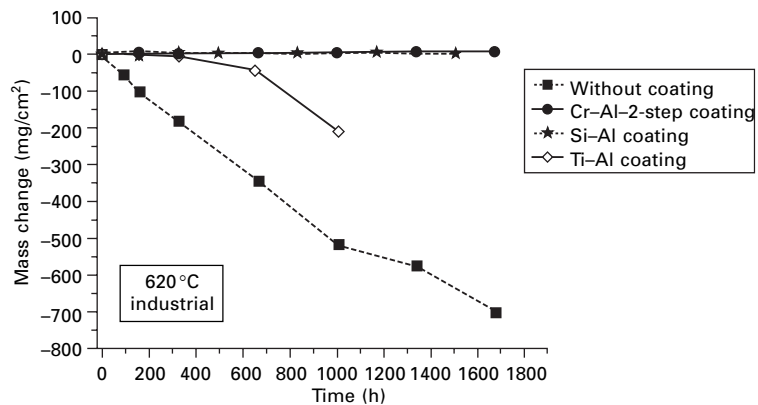
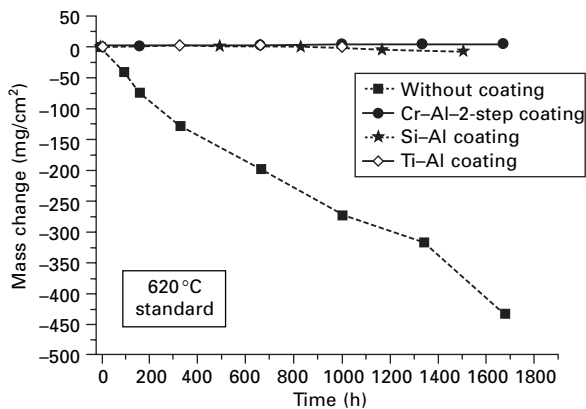
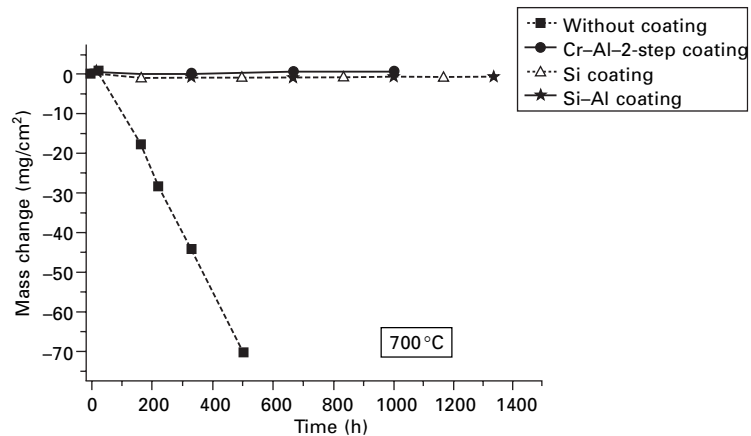
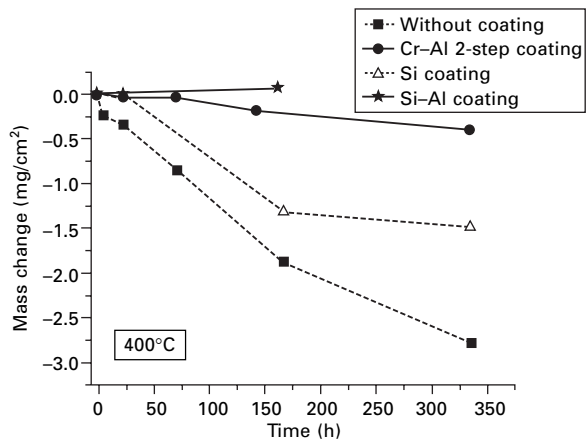
over the surface (Fig. 7.11) and loss of thickness occurs very rapidly. Under the industrial atmosphere there is a higher mass loss than under the standard atmosphere. Figure 7.12 shows the attack at 620 °C for the uncoated alloy. Owing to etching, it is possible to observe the carburization of the substrate.

If we now examine the results for the 2-step aluminized sample (Fig. 7.10), very different results are obtained. Although no attack was observed at any of the temperatures, differences in the mass change are evident. At 400 °C the kinetics of the formation of the oxide scale are very slow. The diagram shows a mass loss of the sample. This is not due to metal dusting attack but to spallation of the oxide scale. During the exposures, some spallation occurred at edges, although this did not affect the protective behaviour of the coating and protection was always provided. At 620 °C there is a larger mass gain than at 700 °C and kinetics of oxide formation are different as well. This is possibly due to the formation of Fe oxides over the Al oxide. After longer testing times, some cracks were observed in the diffusion coating (Fig. 7.13), which grow perpendicular to the sample surface. These cracks within the coating are due to stresses caused by heating and cooling during discontinuous exposure of the samples. The sample tested at 700 °C showed more cracks than the one at lower temperatures. At 700 °C the temperature difference from this temperature to room temperature while cooling is higher than at 620 and 400 °C and, thus, coating stresses increase. Growth of the oxide leads to aluminium consumption [12] and pores in the subsurface of the oxide were observed being more numerous in the sample tested at 700 °C.

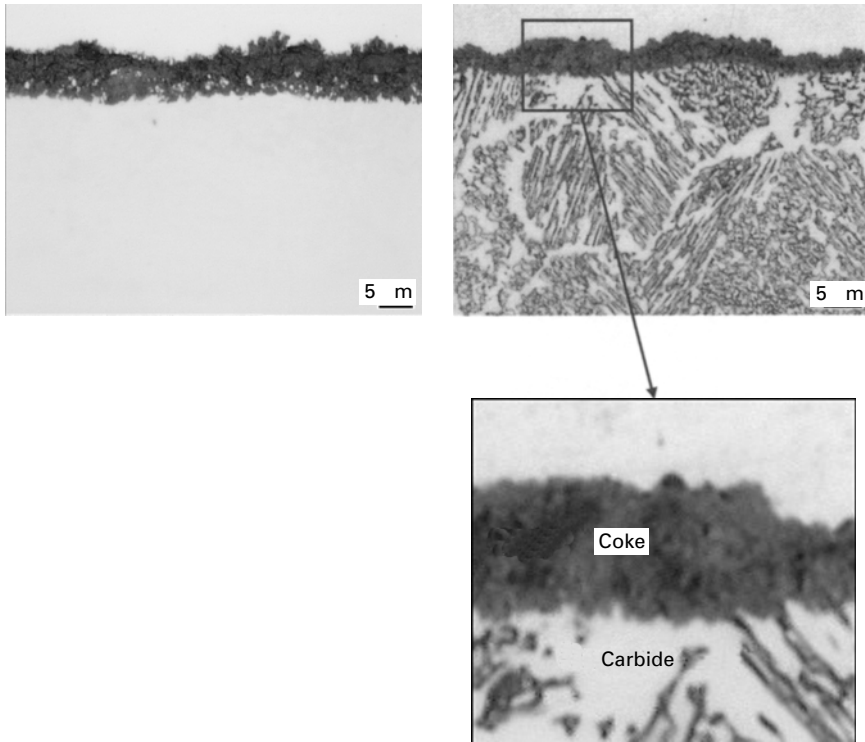
The Si diffusion coating showed very poor metal dusting resistance at 400 and 700 °C. Owing to the poor behaviour, this coating was not tested at 620 °C. The formation of a continuous SiO_2 scale needed to provide protection

Table 7.3 General behaviour of the coatings applied to Alloy 10CrMo9 10 tested under metal dusting conditions

400 °C			620 °C			700 °C		
Coatings	Protective behaviour	Coke deposition	Coatings	Protective behaviour	Coke deposition	Coatings	Protective behaviour	Coke deposition
Uncoated	– –	Yes	st uncoated in uncoated	– –	Yes Yes	Uncoated	– –	Yes
Cr–Al	+ (s)	No	st Cr–Al in Cr–Al	++ ++ (s)	No No	Cr–Al	++	No
Si	– –	Yes				Si	–	Yes (p)
Si–Al	+	No	st Si–Al in Si–Al	– (s) +	Yes Yes	Si–Al	+	Yes
			st Ti–Al in Ti–Al	– –	Yes (p) Yes (p)			
++ very good			(s) spallation					
+ good			(p) pitting					
– poor			st standard atmosphere					
– – very poor			in industrial atmosphere					



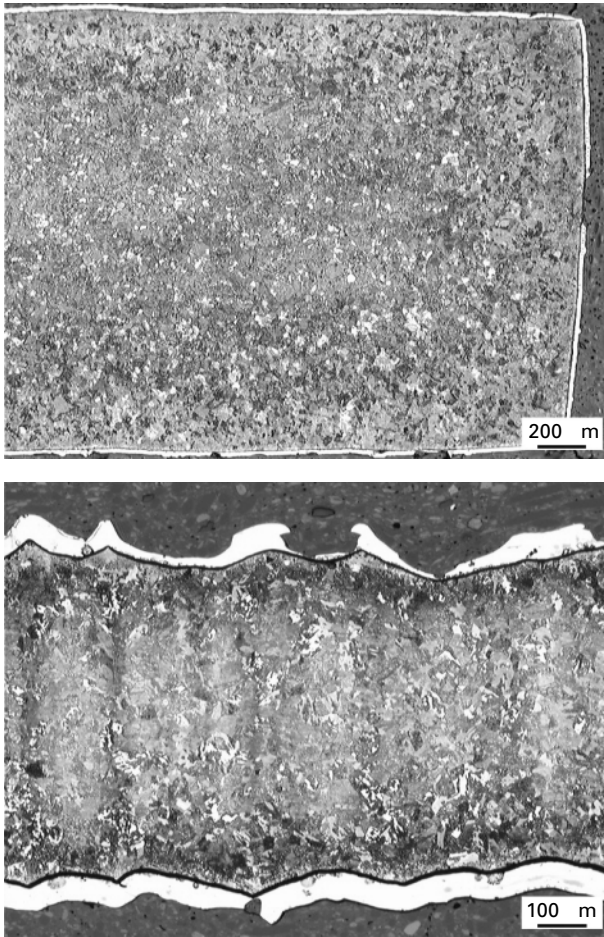
7.10 Mass change measurements of coated and uncoated Alloy 10CrMo9 10 tested under metal dusting conditions at 400, 620 and 700°C.



7.11 Uncoated alloy 10CrMo9 10 tested at 620°C under standard atmosphere for 1681 h. Left: Metal particles within the coke. Right: etched sample showing massive carbide precipitation.

to the material was not possible. As the atmosphere could reach the sample surface through defects in the oxide scale, pitting attack and coke deposition took place in the very early stages of exposure (Fig. 7.14).

The Si-Al co-diffusion coating showed poor behaviour as well. The addition of Si to the Al diffusion coating was detrimental. This effect was observed for all ferritic steels, but not for the austenitic steel Alloy 800 for which this Si-Al co-diffusion coating showed very good results. The oxide scale was a mixture of Al and Si oxide, which had a poor adherence leading to some spallation. Under the oxide scale, a large number of pores were found. In some cases, local coke deposition was observed (Fig. 7.15). There were many defects in the oxide scale and the atmosphere could reach the material through these defects.



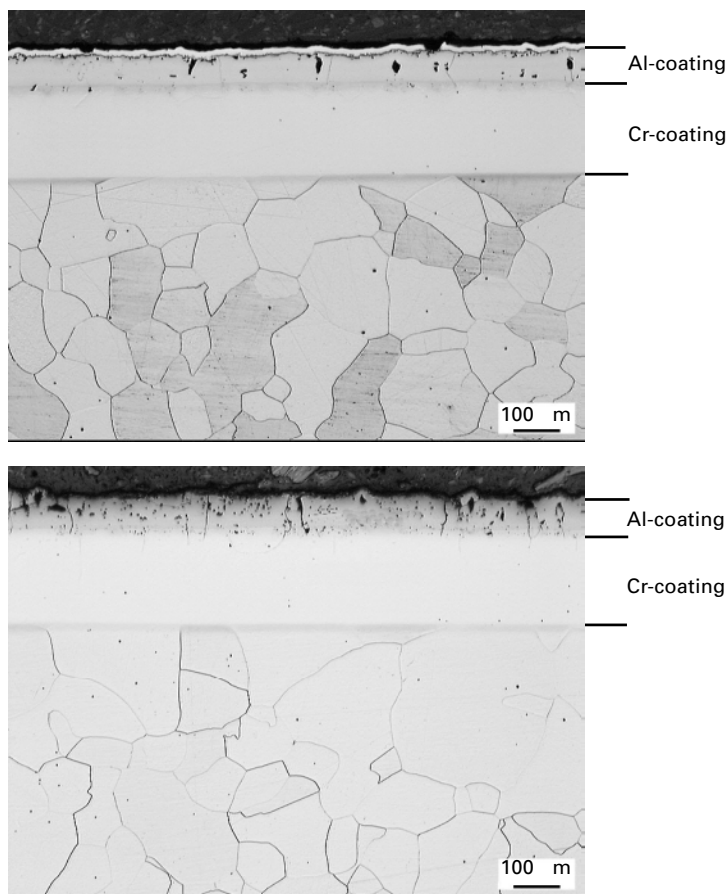
7.12 Uncoated alloy 10CrMo9 10 after etching tested at 620°C under metal dusting conditions for 1681 h. Top standard atmosphere. Bottom industrial atmosphere which was more aggressive.

7.3.2 Alloy P91

Coating process

The Si diffusion process was again very difficult to perform and according to EDX and microprobe analysis, the diffusion zone contained a maximum Si content of 2.5 wt% (Fig. 7.16). Furthermore, diffusion coatings of the type Al, Si-Al, Ti-Al and Si-Ti-Al were also applied. Problems were found in the application of the Si-Al and Ti-Al coatings.

For the case of Si-Al, Si could only be diffused locally, as shown by the microprobe element mapping in Fig. 7.17. For the Ti-Al coating, Ti again



7.13 Cr-Al 2-step diffusion coating on Alloy 10CrMo9 10 tested under standard atmosphere. Top: 400°C. Bottom: 700°C.

formed a Ti-carbide layer as in the case of the low-alloy steel 10CrMo9 10 (Fig. 7.8). This carbide layer prevented any further diffusion of Al and Ti into the base material. The other coatings mentioned above could be produced without problems.

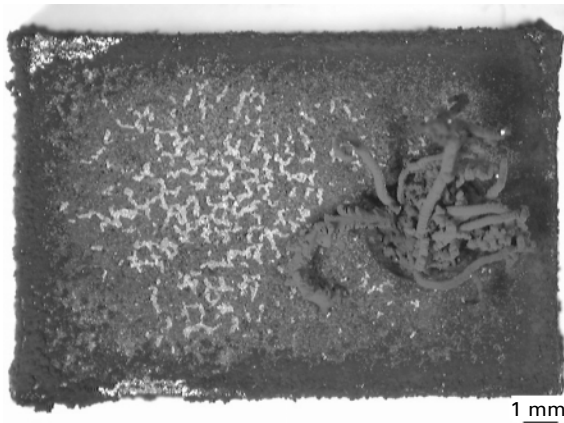
Metal dusting behaviour

Table 7.4 shows the general behaviour of the coatings applied to Alloy P91 tested under metal dusting conditions at different temperatures. Mass change measurements of the specimens are shown in Fig. 7.18.

The uncoated material showed metal dusting and coke deposition at all temperatures. The attack at 400 and at 700°C was less significant than at 620°C. While at 400 and 700°C the type of attack is a general attack, at



7.14 Pitting attack in the siliconized alloy 10CrMo9 10 tested at 700°C under standard atmosphere for 393h.

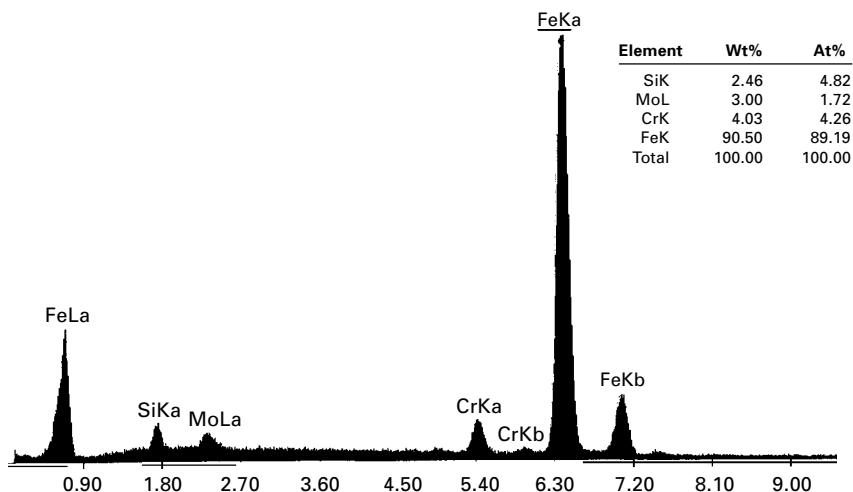


7.15 Local coke deposition on Si-Al coated Alloy 10CrMo9 10 tested at 620°C under standard atmosphere for 393h.

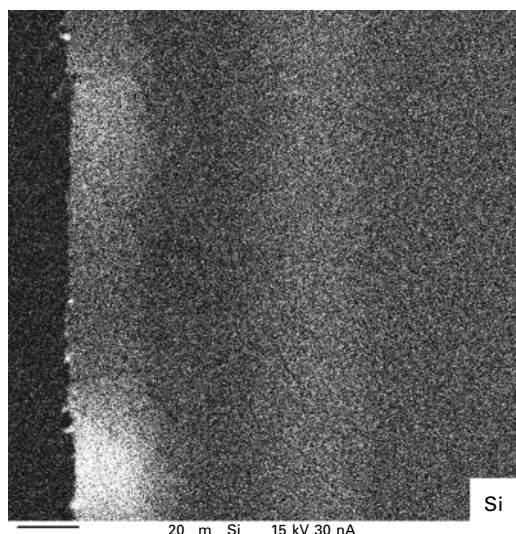
620°C the attack was by pitting under both atmospheres. The mass loss of the sample was more marked at 620°C than at the other temperatures and even more pronounced for the industrial atmosphere (Fig. 7.19).

Although the Al diffusion coating was protective at all temperatures and under both atmospheres, significant spallation occurred. The oxide scale grew preferentially at the edges of the specimen compared with the rest of the sample, leading to high mechanical stresses and spallation (Fig. 7.20). However, no coke deposition occurred during the exposure time.

The Si-Al co-diffusion coating was tested at 620 and 700°C and showed some spallation in all cases. Coke deposition took place only at 620°C under



7.16 EDX analysis of the Si diffusion coating applied to Alloy P91. Outer part of the coating with a Si content of 2.5 wt%.



7.17 Microprobe element mapping for Si of the Si-Al co-diffusion coating on Alloy P91. Local enrichment of Si.

the standard atmosphere, and as for the alloy 10CrMo9 10, the coke deposition was local due to some defects in the oxide scale (Fig. 7.21), mainly at the edges of the specimen.

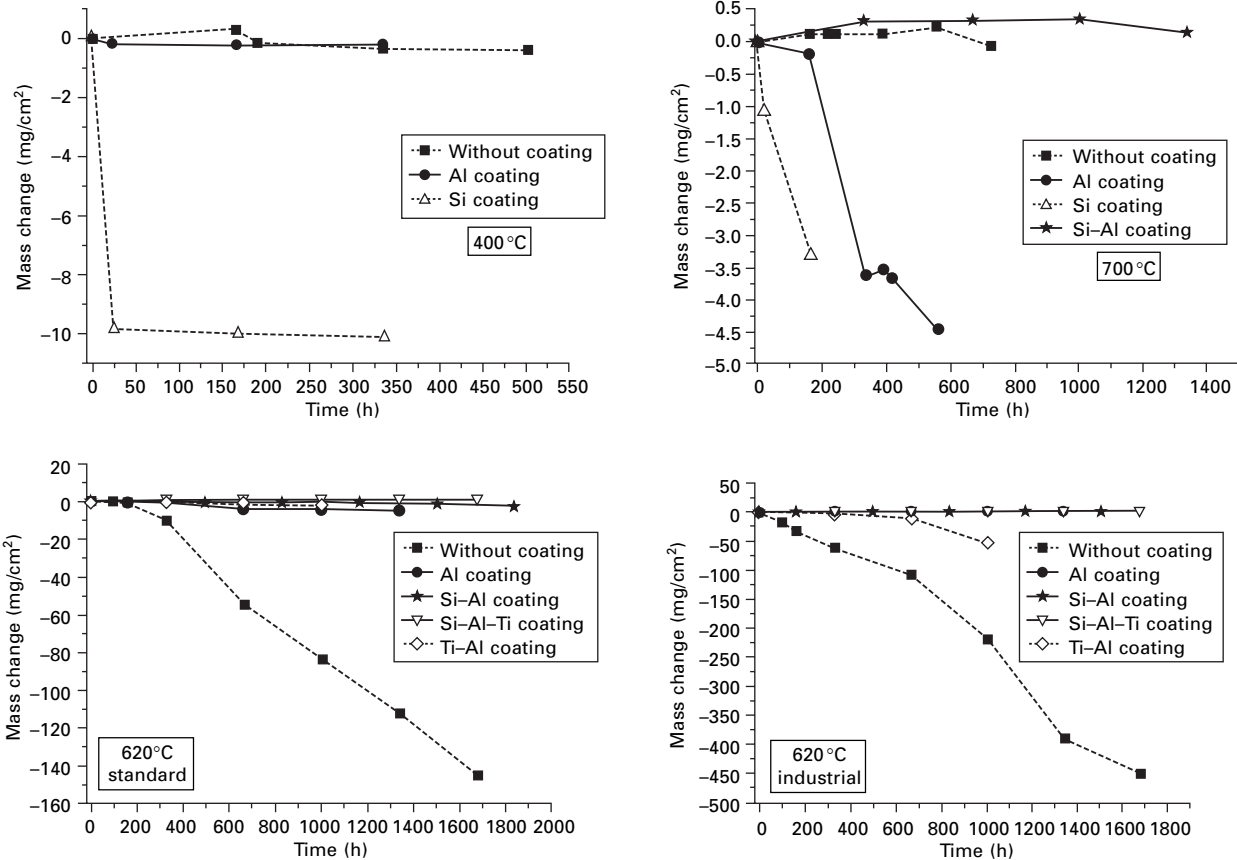
The Ti-Al co-diffusion coating (although by the pack cementation process there was formation of a Ti carbide layer) was tested in order to see whether

Table 7.4 General behaviour of the coatings applied to Alloy P91 tested under metal dusting conditions

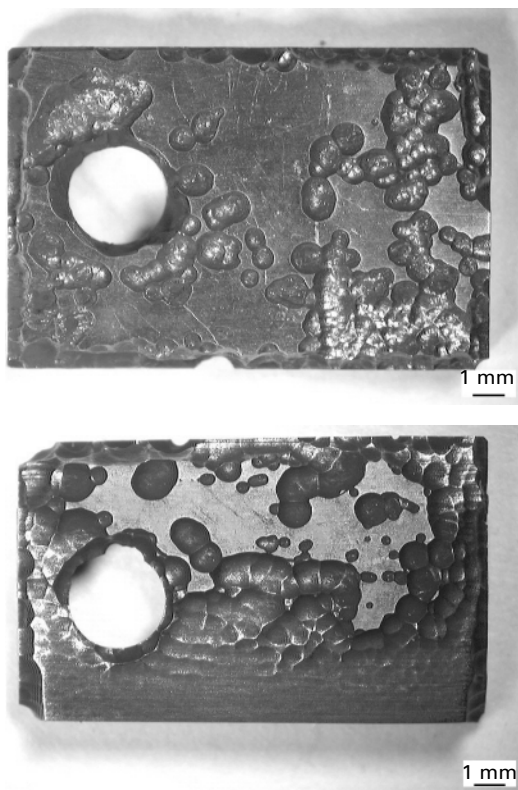
400°C			620°C			700°C		
Coatings	Protective behaviour	Coke deposition	Coatings	Protective behaviour	Coke deposition	Coatings	Protective behaviour	Coke deposition
Uncoated	–	Yes	st uncoated in uncoated	– –	Yes (p) Yes (p)	Uncoated	–	Yes
Al	– (s)	No	st Al in Al	– (s) – (s)	No No	Al	–(s)	No
Si	– – (s)	Yes (p)	st Si–Al in Si–Al	– (s) – (s)	Yes No	Si Si–Al	– – + (s)	Yes (p) No
			st Ti–Al in Ti–Al	– – –	Yes (p) Yes (p)			
			st Ti–Si–Al in Ti–Si–Al	++ ++	No No			

++ very good
+ good
– poor
– – very poor

(s) spallation
(p) pitting
st standard atmosphere
in industrial atmosphere



7.18 Mass change measurements of coated and uncoated Alloy P91 tested under metal dusting conditions at 400, 620 and 700°C.



7.19 Uncoated Alloy P91 tested at 620°C for 1008h. Top tested under standard atmosphere. Bottom tested under industrial atmosphere.

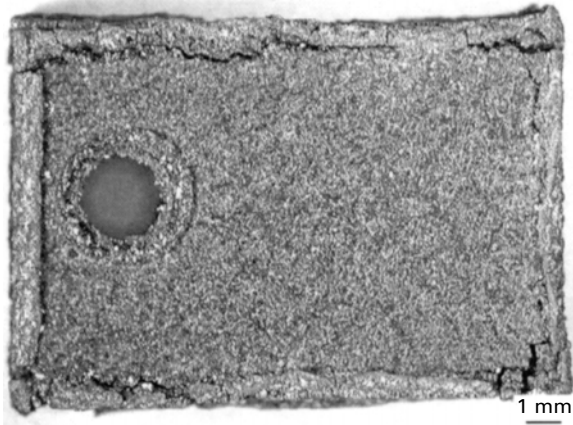
this layer could provide protection to the material. It was only tested at 620°C and pitting attack occurred at the beginning of exposure (Fig. 7.22). Thus, the Ti carbide layer does not seem to provide a significant amount of protection in this case.

The best behaviour was obtained with the Si–Ti–Al co-diffusion coating which was tested only at 620°C under both atmospheres for 1681 h. No metal dusting or coke deposition was observed and a protective oxide scale protected the material from carbon penetration (Fig. 7.23).

7.3.3 Alloy X10CrAl18

Coating process

Not only diffusion coatings were applied to this alloy but also a spray coating based on the γ -TiAl intermetallic phase (Fig. 7.24). This coating was applied



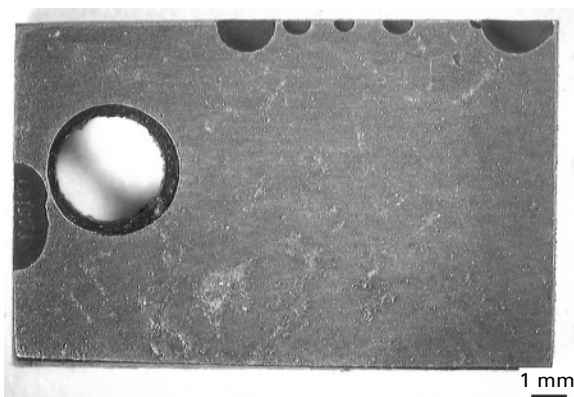
7.20 Aluminized Alloy P91 tested at 620°C under industrial atmosphere for 673h. Oxide formation and spallation at the edges.



7.21 Si-Al co-diffusion coating on Alloy P91 tested at 620°C under standard atmosphere for 336h.

by the HVOF technique. The Al diffusion coating is quite similar to that of alloy X18CrN28 (see Section 7.3.4). The coating is also composed of two different phases (Fig. 7.25). In this case, owing to the high intrinsic Cr content, a Cr diffusion pre-step was not necessary.

The siliconizing process was very difficult to perform on this alloy and significant spallation occurred after the process. The outer layers were completely detached from the surface (Fig. 7.26). Nevertheless, some incorporation of Si was achieved and, despite spallation, the coated material was tested under metal dusting conditions.



7.22 Ti-Al co-diffusion coating on Alloy P91 tested at 620°C under industrial atmosphere for 672 h. Pitting attack started at the edges.

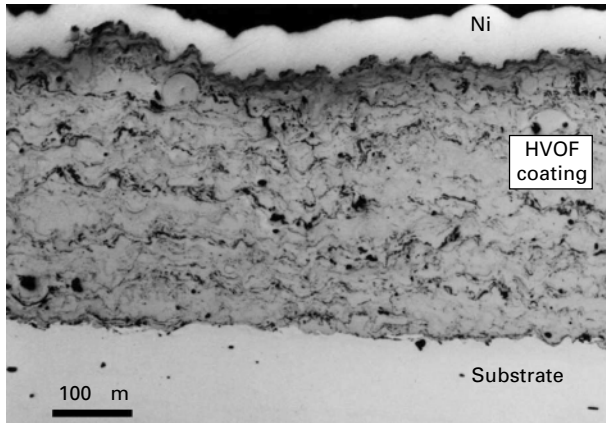


7.23 Alloy P91 coated with a Si-Ti-Al co-diffusion coating tested at 620°C under industrial atmosphere for 1345 h. Formation of a protective oxide scale on the surface.

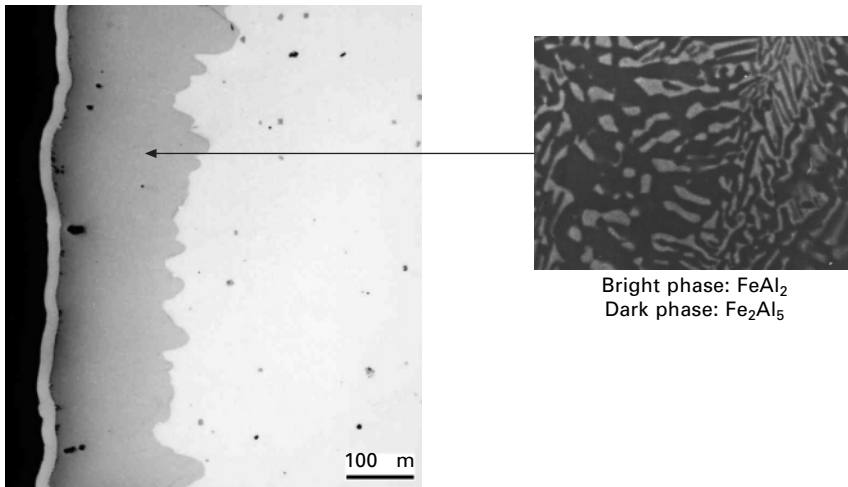
The Si-Al co-diffusion coating appeared to be of the same nature as that on the alloy X18CrN28 (see Section 7.3.4). The same phases were found inside the coating (Fig. 7.27). However, since alloy X10CrAl18 has no nitrogen in its composition, Al nitrides, which were present in the Si-Al co-diffusion coating on alloy X18CrN28, were not formed in this case.

Metal dusting behaviour

Table 7.5 shows the general behaviour of the coatings applied to alloy X10CrAl18 and tested under metal dusting conditions at different temperatures. Mass change measurements of the specimens are shown in Fig. 7.28.

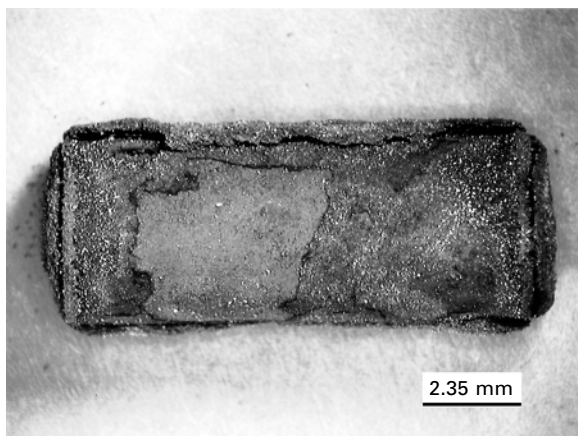


7.24 -TiAl HVOF spray coating on Alloy X10CrAl18. The thickness of the coating is about 300–350 μm .



7.25 Al diffusion coating applied to alloy X10CrAl18 by the pack cementation method.

Although this material has only 18% Cr in its composition, i.e. less than alloy X18CrN28 which has 28% Cr, the behaviour of the uncoated material is much better. While for the alloy X18CrN28 there was coke deposition and mass loss of the specimen, a mass gain is registered for X10CrAl18. However, a very thin coke layer on the surface was found after each exposure. 400 °C is a rather low temperature for a rapid formation of a chromia scale which was the reason why alloy X18CrN28 could not develop a protective oxide scale (see Section 7.3.4). Alloy X10CrAl18 contains, however, 1% Al and it looks as if even small amounts of aluminium help promote the formation of



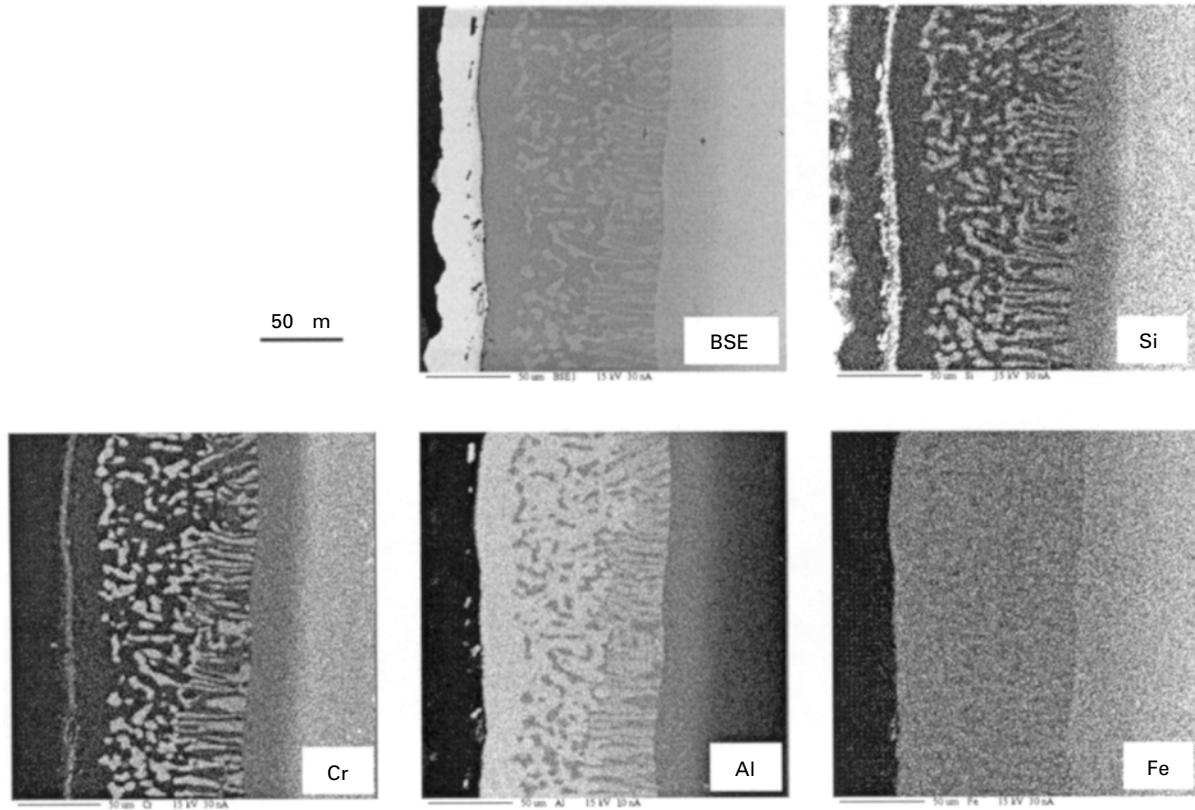
7.26 Si diffusion coating applied to alloy X10CrAl18 by the pack cementation method. Detachment of the outer layers.

the chromia layer. At 400 °C the diffusion of carbon occurs very slowly and there was no carburization in this sample. At 620 and 700 °C, however, the diffusion of carbon is faster and penetration of carbon into the material occurred before the material could develop a protective oxide scale. At 700 °C coke deposition was observed with a slight mass loss of the specimen and at 620 °C, pitting attack occurred under both atmospheres. Under the standard atmosphere a strong decrease in the weight of the sample was observed in the last period of exposure (from 1681 to 2022 h).

For the aluminized sample, although it was resistant at all temperatures, the best behaviour is found at 700 °C. The decrease in weight at 400 and 620 °C in Fig. 7.28 is due to spallation of the oxide scale. However, spallation did not decrease the protective potential of the Al diffusion coating.

For alloy X18CrN28 a large number of pores were found in the Al diffusion coating at 620 °C (see Fig. 7.38 on page 141). However, in the present material only pores below the oxide scale were found and the coating appeared more compact and adherent (Fig. 7.29). The Si diffusion coating was tested only at 400 and 700 °C. At 400 °C no coke deposition or metal dusting occurred. However, the testing time was only 336 h and there was a large amount of spallation even at 700 °C. At this latter temperature, coke deposition and metal dusting were observed.

The Si–Al co-diffusion coating was tested at 620 and 700 °C, showing good behaviour at 700 °C. No spallation, coke deposition or metal dusting took place. At 620 °C a different behaviour was observed depending on the atmosphere. For the standard atmosphere, there was spallation and coke deposition on the surface, while for the industrial atmosphere, no coke deposition was observed. Under the standard atmosphere, a thick Al oxide



7.27 Microprobe element mapping of the Si-Al co-diffusion coating applied to alloy X10CrAl18.

Table 7.5 General behaviour of the coatings applied to alloy X10CrAl18 tested under metal dusting conditions

400 °C			620 °C			700 °C		
Coatings	Protective behaviour	Coke deposition	Coatings	Protective behaviour	Coke deposition	Coatings	Protective behaviour	Coke deposition
Uncoated	+	Yes	st uncoated in uncoated	– –	Yes (p) Yes (p)	Uncoated	–	Yes
Al	+ (s)	No	st Al in Al	+ (s) ++	No No	Al	++	No
Si	+ (s)	No	st Si–Al in Si–Al	– (s) + (s)	Yes No	Si	–	Yes
						Si–Al	++	No
HVOF TiAl	++	No	st HVOF TiAl in HVOF TiAl	++ ++	No No	HVOF TiAl	++	No

++ very good

+ good

– poor

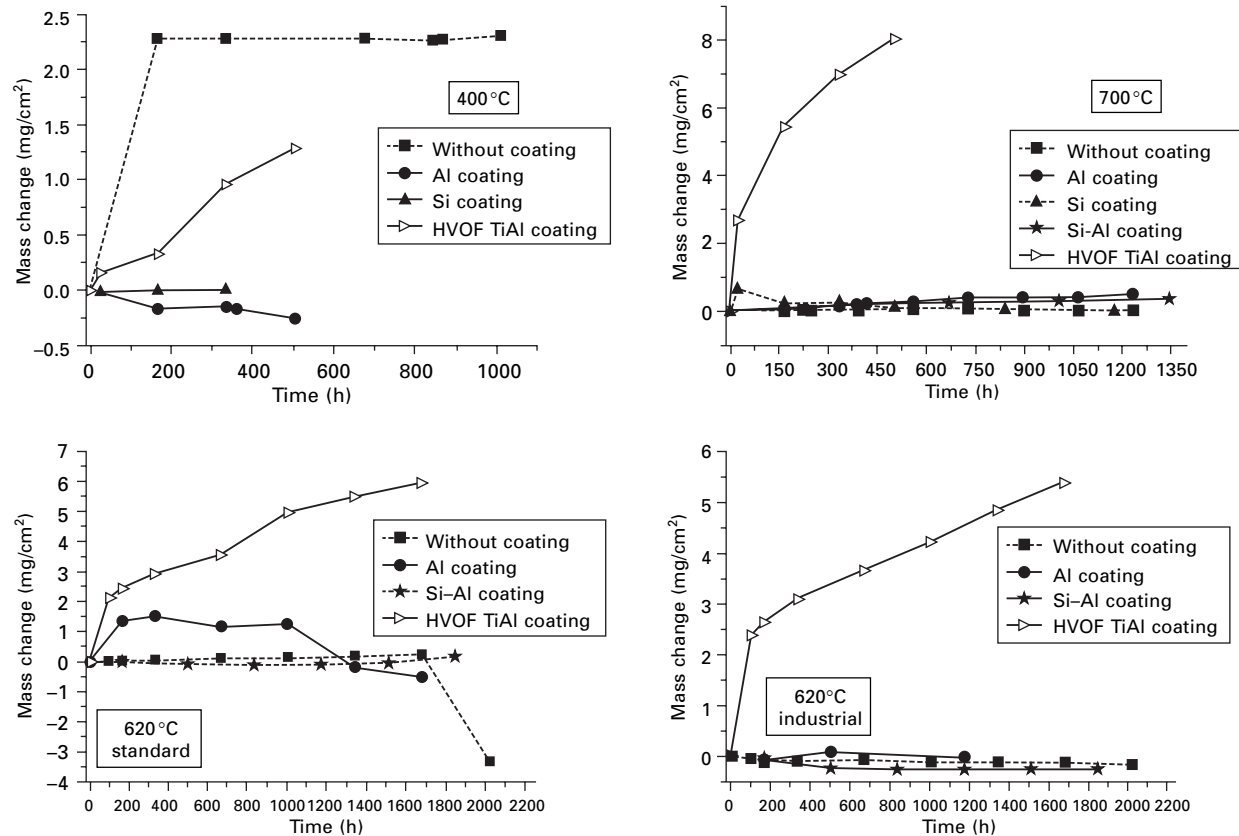
– – very poor

(s) spallation

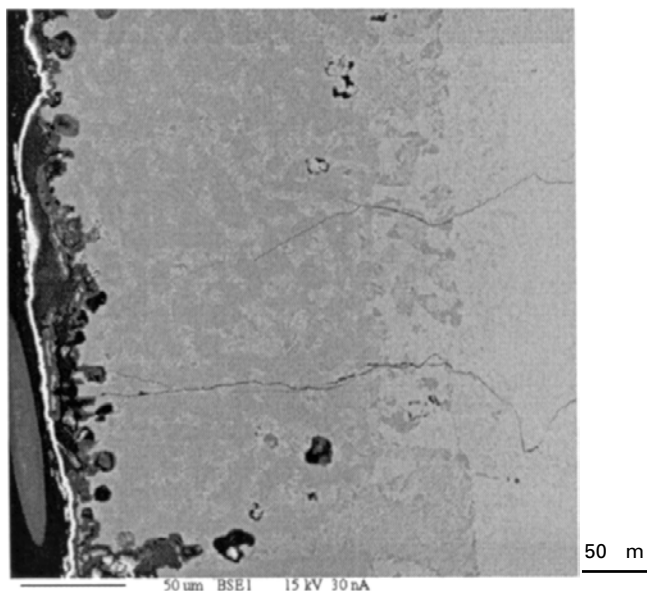
(p) pitting

st standard atmosphere

in industrial atmosphere



7.28 Mass change measurements of coated and uncoated Alloy X10CrAl18 tested under metal dusting conditions at 400, 620 and 700 °C.



7.29 Al diffusion coating on Alloy X10CrAl18 tested at 620°C under standard atmosphere for 1681h. Pores below the oxide scale.

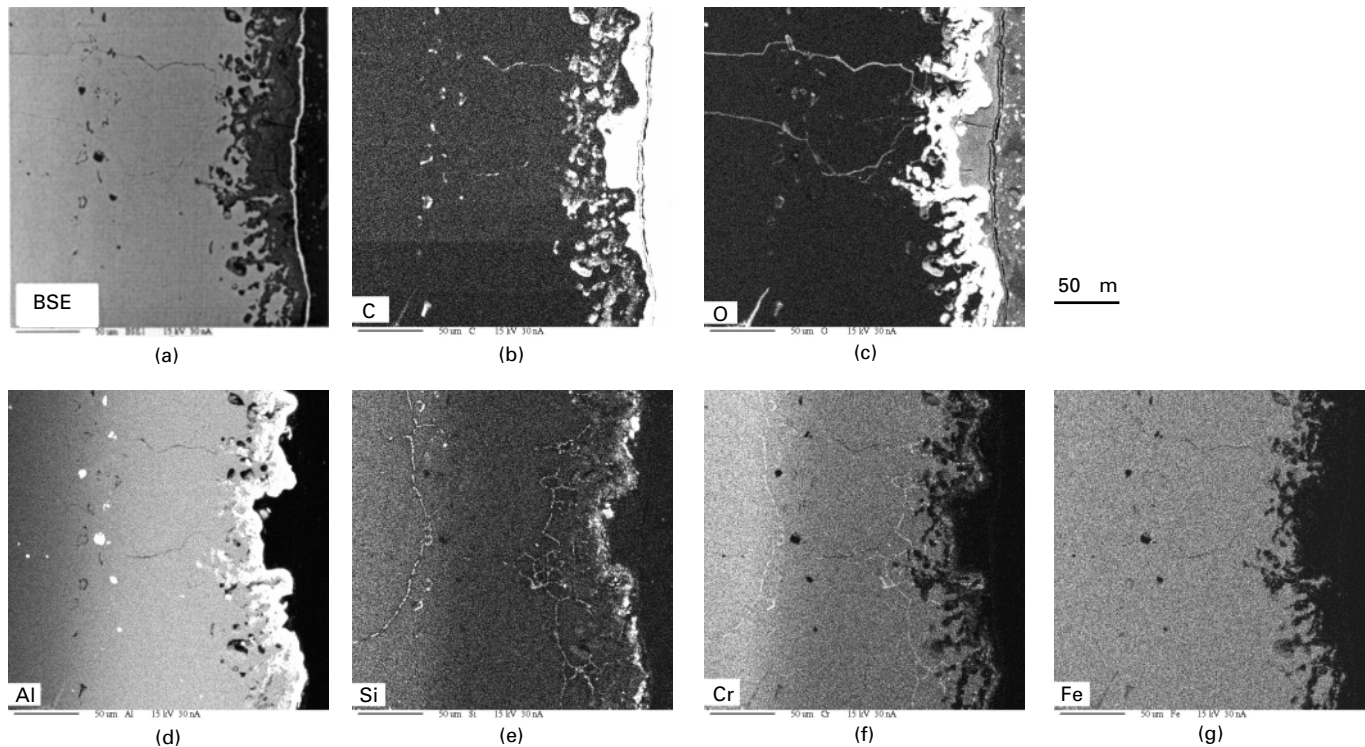
scale was formed which contained Si oxide as well in the outer part of the layer (Fig. 7.30). There is some internal oxidation and coke deposition on top of the oxide scale, although no cracks or defects were observed in the scale. Again in this case, Si (or SiO_2) seems to promote coke deposition. Pores underneath the scale were observed as well as Si–Cr intermetallics precipitated at the grain boundaries.

Finally, the HVOF -TiAl coating, which was tested at all temperatures, showed very good behaviour in all cases by the formation of a protective oxide scale (Fig. 7.31). The scale was a mixed Ti and Al oxide. Although this coating is somewhat porous, the oxide formed is very compact and no metal dusting, coke deposition or spallation occurred. Evidently porosity is sealed by the formation of thermodynamically very stable Ti and/or Al oxides between the splats (Fig. 7.31).

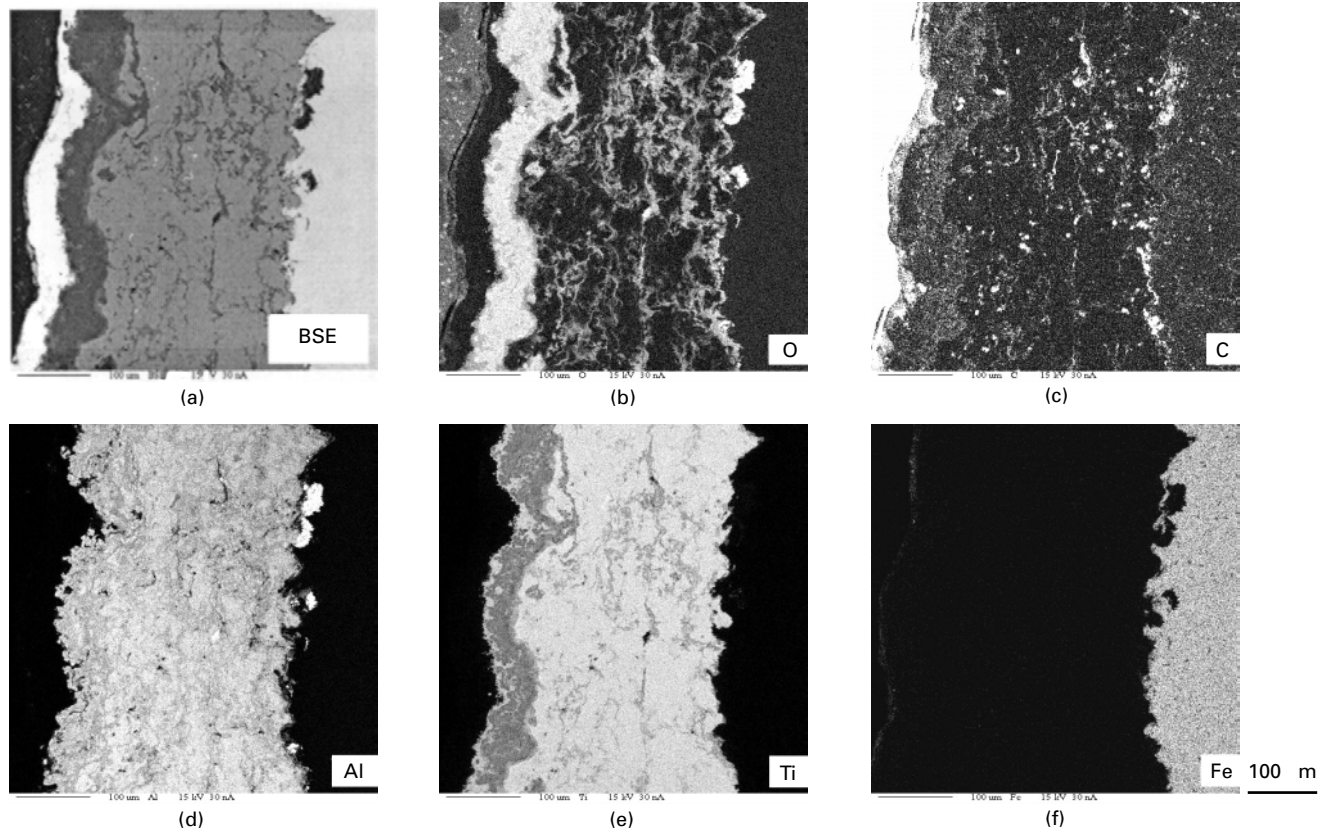
7.3.4 Alloy X18CrN28

Coating process

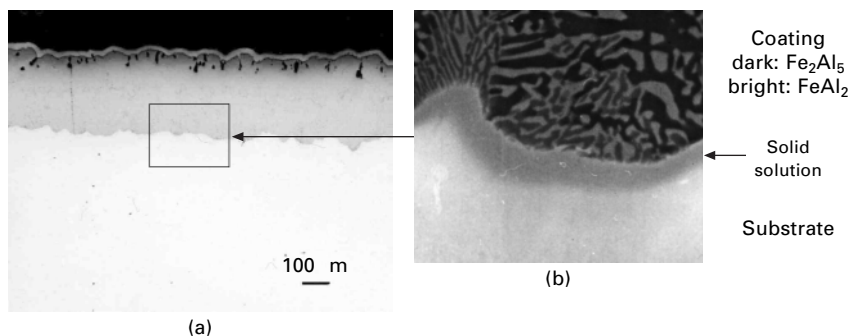
Different diffusion coatings were applied to this material. Since this material contains 28% Cr, Cr diffusion as a pre-step of the aluminizing process is not necessary. Aluminizing of the material led to an aluminium diffusion coating with a two-phase microstructure (Fig. 7.32). The phases in the coating are



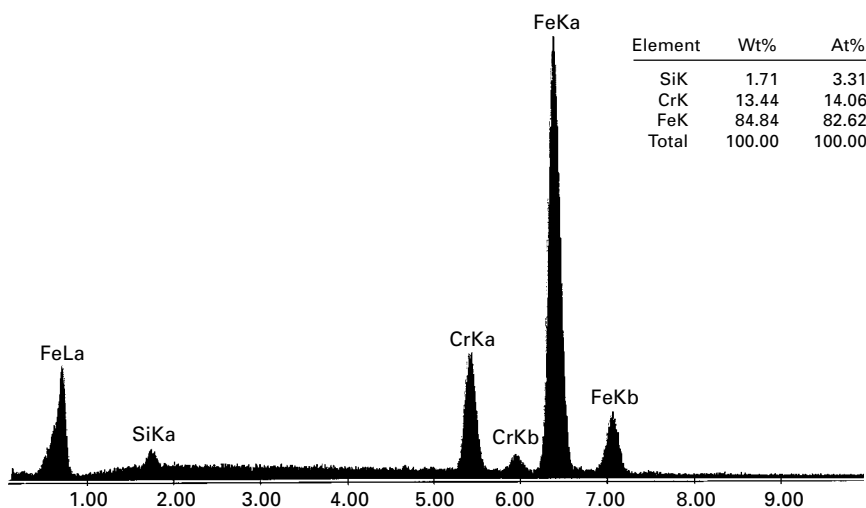
7.30 Si-Al co-diffusion coating applied to alloy X10CrAl18 and tested at 620 °C under standard atmosphere for 1849 h.



7.31 Microprobe element mapping of HVOF -TiAl coating applied to alloy X10CrAl18 tested at 700°C under standard atmosphere for 504 h.



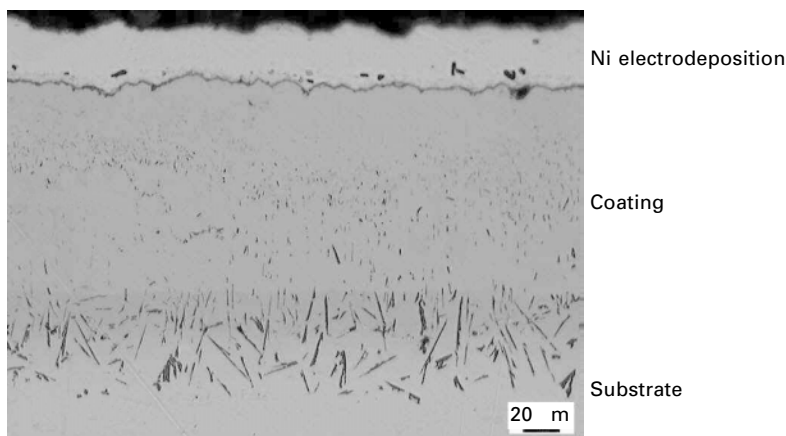
7.32 Aluminium diffusion coating on alloy X18CrN28. The coating is composed of Fe–Al intermetallics.



7.33 EDX analysis for the siliconized alloy X18CrN28. Outer part of the coating. Si content: 1.7 wt% Si. Si content in the matrix: 0.9 wt% Si.

Fe–Al intermetallics, specifically Fe_2Al_5 and FeAl_2 . The Si diffusion coating was also applied to this alloy and similar results were obtained as for the alloy 10CrMo9 10. Only little Si could diffuse into the substrate and only 1.7 wt% Si was obtained at the outer most part of the coating (Fig. 7.33).

Furthermore an Si–Al co-diffusion coating was applied (Fig. 7.34). The coating was free of cracks and pores and different phases were found within the coating. From the microprobe analysis (Fig. 7.35) it can be concluded that at the surface of the coating there is a scale rich in Si and Cr. Although oxygen was not analysed, it is probably a mixed oxide scale. Below is an Al-rich zone and, further down, an Si + Cr-rich zone follows. The concentration



7.34 Si-Al co-diffusion coating on Alloy X18CrN28. Outer zone of the coating rich in Al and Fe, in the middle there is a zone rich in Cr, Si and Fe and in the interdiffusion zone there are Al-nitride precipitates as needles which also appear inside the coating but in a smaller size.

of Fe remains constant within the coating. The formation of Al nitrides is observed more or less all over the coating, which appear in the form of needles being much larger in the interdiffusion zone. Nitrogen was present in the original base material to a significant extent; Table 7.1.

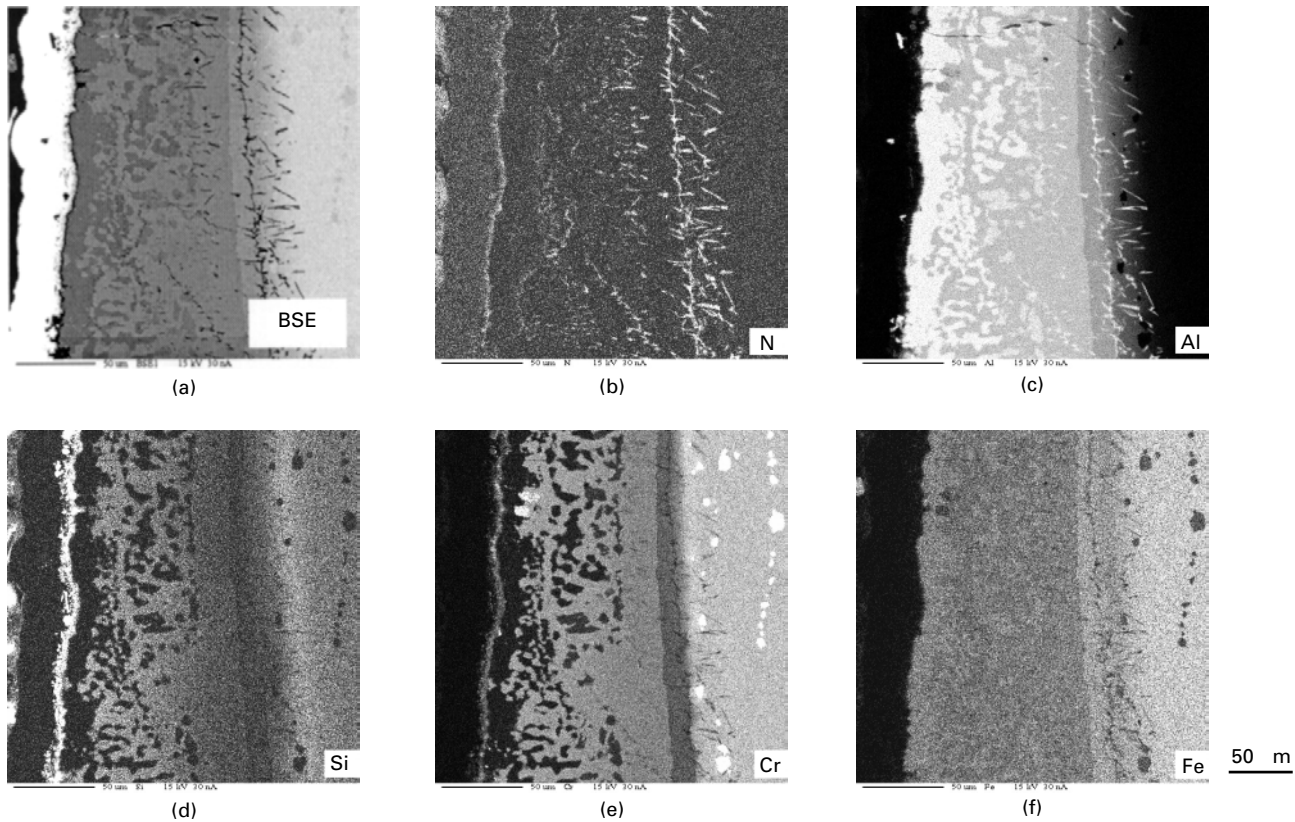
Metal dusting behaviour

Table 7.6 shows the general behaviour of the coatings applied to alloy X18CrN28 tested under metal dusting conditions at different temperatures. Mass change measurements of the specimens are shown in Fig. 7.36.

As the material contains 28%Cr even the uncoated material should be able to develop a protective chromia scale. However, formation of the oxide is dependent on temperature; therefore, resistance of the material against metal dusting depends on temperature as well.

It can be observed that the uncoated material has its worst behaviour at 400°C. The sample was tested for 336h. At this low temperature, the diffusion of Cr to the surface is very slow and the oxide formed is irregular and discontinuous. Under these conditions it is not possible to form an effective barrier against carbon penetration, and coke deposition as well as metal dusting were observed on the sample. At 620 and at 700°C, although there was the formation of an oxide scale, some coke deposition was found but there was no metal dusting in these cases.

This material contains silicon as well. Diffusion of silicon is very slow at low temperatures such as 400 °C but at 620 and 700°C the formation of Si oxide can be observed. Figure 7.37 shows the microprobe analysis of uncoated



7.35 Microprobe element mapping of the Si-Al co-diffusion coating applied to alloy X18CrN28.

Table 7.6 General behaviour of the coatings applied to alloy X18CrN28 tested under metal dusting conditions

400°C			620°C			700°C		
Coatings	Protective behaviour	Coke deposition	Coatings	Protective behaviour	Coke deposition	Coatings	Protective behaviour	Coke deposition
Uncoated	–	Yes	st uncoated in uncoated	– –	Yes Yes	Uncoated	–	Yes
Al	++	No	st Al in Al	+ ++	No No	Al	+	No
Si	– – (s)	Yes	st Si–Al in Si–Al	– –	Yes Yes	Si	– –	Yes
						Si–Al	++	No

++ very good

+ good

– poor

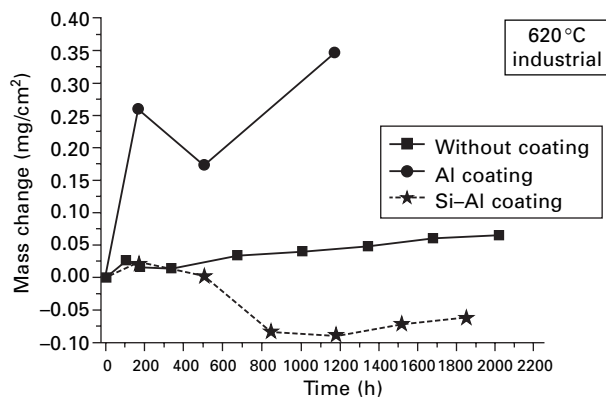
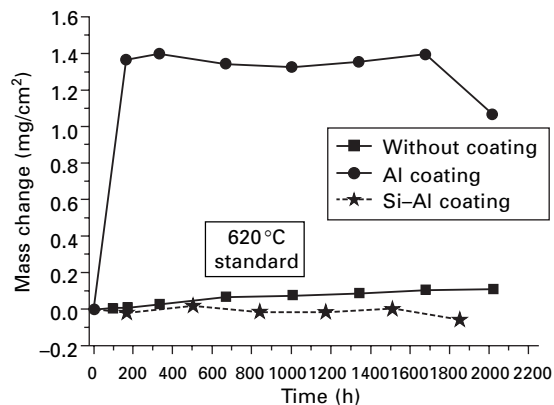
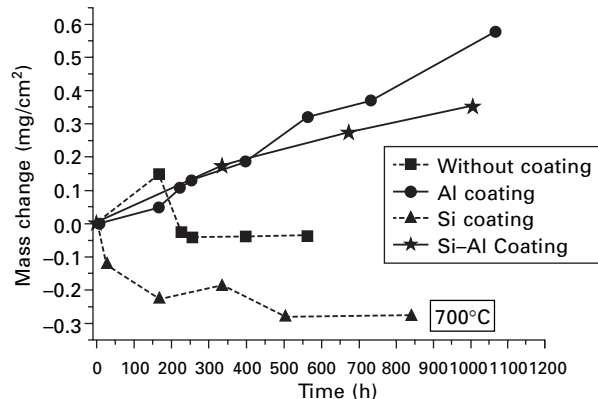
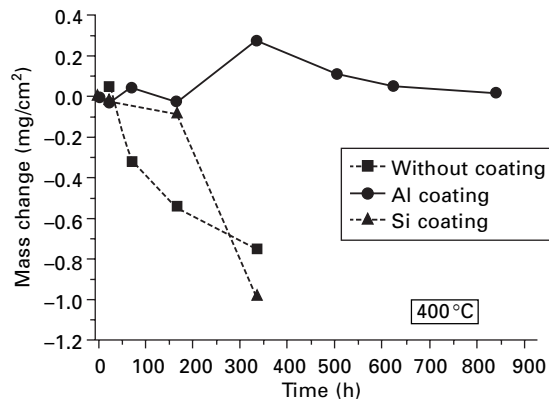
– – very poor

(s) spallation

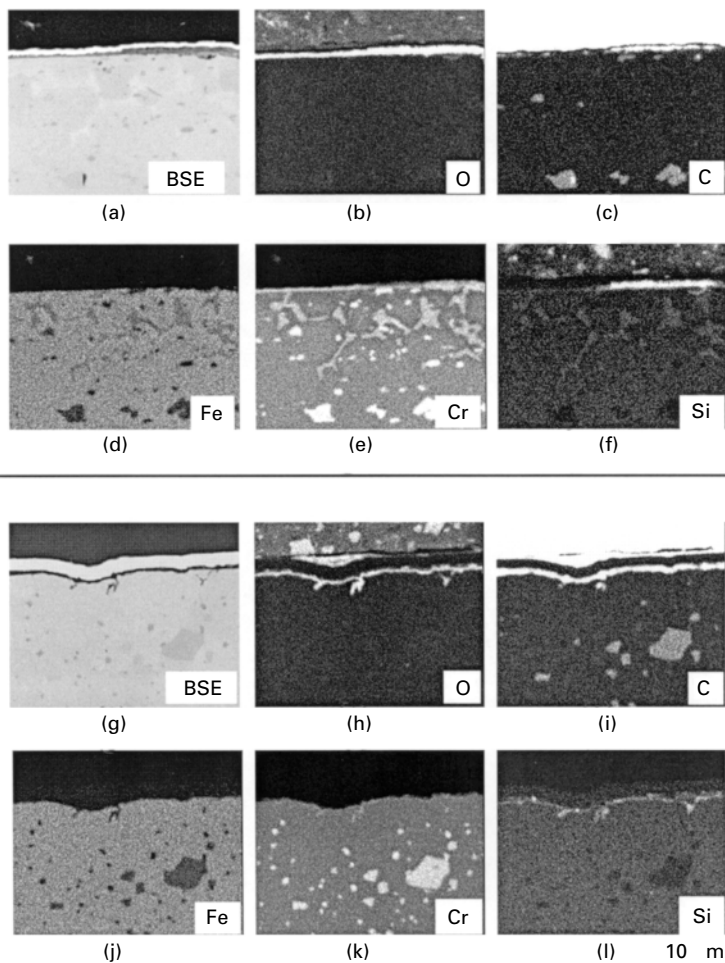
(p) pitting

st standard atmosphere

in industrial atmosphere

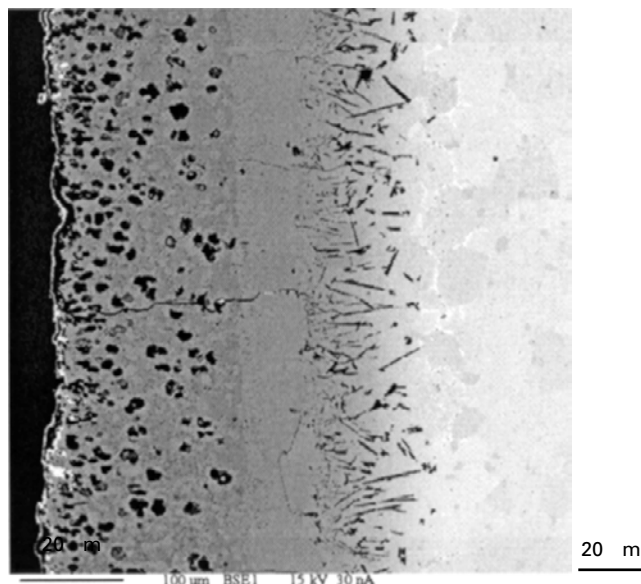


7.36 Mass change measurements of coated and uncoated Alloy X18CrNi28 tested under metal dusting conditions at 400, 620 and 700°C.



7.37 Microprobe element mapping of uncoated alloy X18CrN28: (a)–(f) 620 °C, standard atmosphere, 2022 h; (g)–(l) 700 °C, standard atmosphere, 565 h.

alloy X18CrN28 tested under standard atmosphere at 620 and 700 °C. At 620 °C the diffusion of Si is still slow and the formation of Si oxide occurs only locally. The main oxide consists of chromia. At 700 °C, diffusion of Si is faster and a more continuous Si oxide scale can be observed. Interestingly on top of the Si oxide scale, whether locally at 620 °C or as a continuous scale at 700 °C, there is always coke deposition (Fig. 7.37). It appears as if SiO_2 had a catalytic effect on the coke deposition or graphite formation. In the literature [13–15] it is reported that Si in the microstructure of grey cast iron promotes graphitization. It can, however, not be concluded at this point whether a similar mechanism may be active under metal dusting conditions.

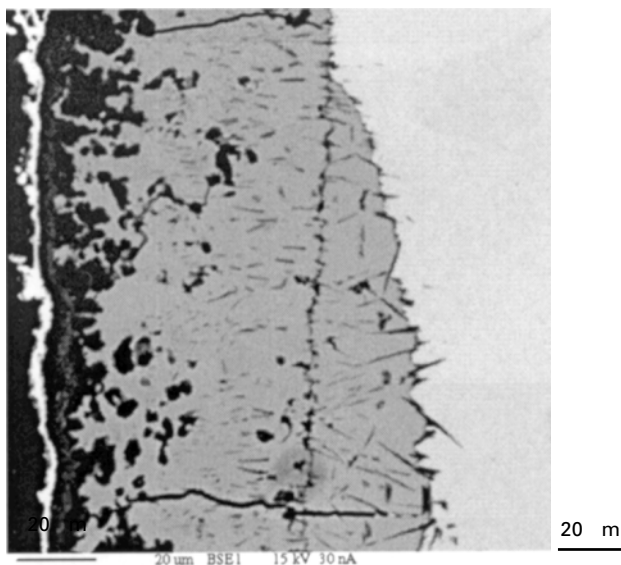


7.38 Al diffusion coating on Alloy X18CrN28 tested at 620°C under standard atmosphere for 2022h. Several pores are in the outer part of the coating.

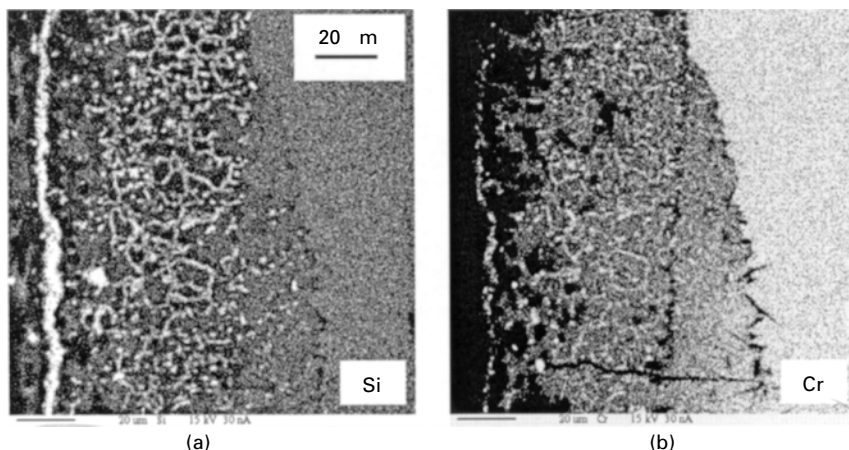
The plain Al diffusion coating showed good protective behaviour at all temperatures. However, after longer exposure times (1400h) several pores appeared under the oxide scale (Fig. 7.38) although no metal dusting attack was observed. These pores can provoke cracking.

The addition of Si to the Al diffusion coating had no beneficial effect on any of the ferritic steels. When the coating was tested under metal dusting conditions, a mixed Si + Al oxide scale formed on top of the sample. The oxide was thicker than that on the sample that was only aluminized. In the case of the Si–Al co-diffusion coating, the oxide scale was non-adherent and several pores and cracks appeared (Fig. 7.39). This led to coke deposition and mass loss of the sample tested at 620°C. However, at 700°C the oxide formed is more compact and adherent and although this coating was tested only up to 1008h, the behaviour was, in this case, better than that of the Al diffusion coating.

It has been reported in the literature [1] that the addition of Si improves the ductility of the Al diffusion coating. However, in the present investigation it was found that Si forms intermetallic compounds with Cr which precipitate at the grain boundaries. This leads to an increase in brittleness of the coating (Fig. 7.40).



7.39 Si-Al co-diffusion coating applied to alloy X18CrN28 and tested at 620°C under industrial atmosphere for 1849h. Formation of a non-adherent oxide scale with a large number of voids underneath.

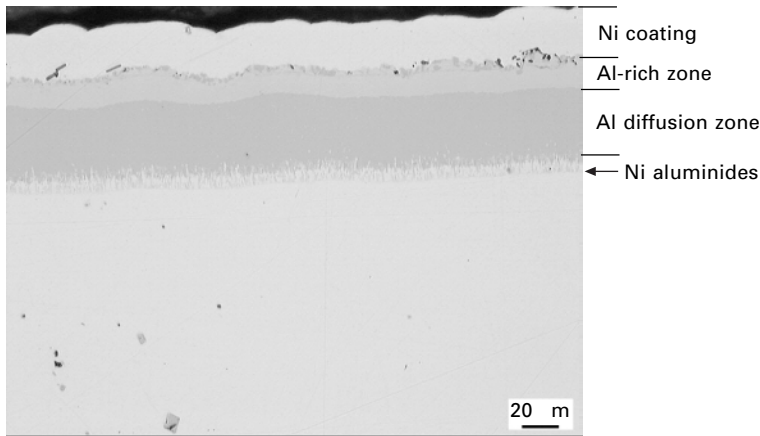


7.40 Microprobe element mapping of the Si-Al co-diffusion coating applied to alloy X18CrN28 tested at 620°C under industrial atmosphere for 2022h. Si-Cr intermetallics at the grain boundaries.

7.3.5 Alloy 800

Coating process

Different diffusion coatings were applied to Alloy 800. The first coating applied was a plain Al diffusion coating of good quality (Fig. 7.41). The



7.41 Al diffusion coating applied to Alloy 800.

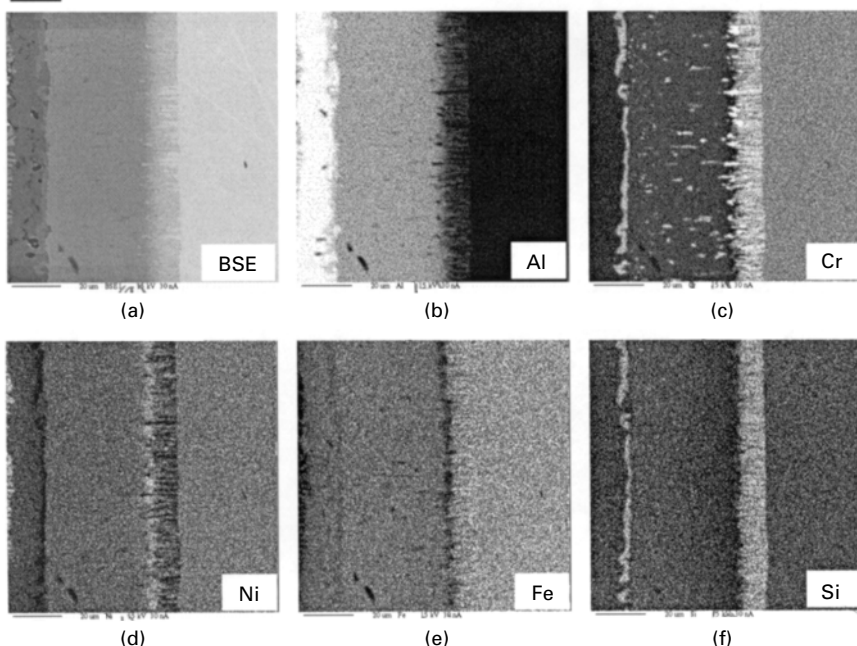
coating consisted of different phases. The outer part of the coating is a diffusion zone rich in aluminium. This is followed by another diffusion zone, which contains less Al but more Cr than the previous one, reaching approximately 60 μm in depth, and, finally, beneath there are some precipitates in the form of needles consisting of the Ni–Al intermetallic phase. The coating is free from pores and cracks.

The Si–Al diffusion coating was very similar in appearance to the Al diffusion coating. There was an outer Al-rich diffusion zone as well but in this case, below this zone a Cr–Si-rich layer had formed. The different phases can be observed in the microprobe analysis (Fig. 7.42).

The Ti–Al diffusion coating had a microstructure totally different from that obtained on alloy 10CrMo9 10. For the low-alloy steel, a Ti carbide layer was formed which avoided any further inward diffusion of Al or Ti. In Alloy 800, different phases are observed in the microprobe analysis (Fig. 7.43). The outer layer is rich in Ti and Al. Below there is a layer rich in Ni. Further down a Ti carbide layer is formed and after it, there are some Al–Ni intermetallic precipitates in the form of needles. Furthermore a Ti–Si–Al co-diffusion coating was applied (Fig. 7.44). In this case, the Al-rich zone is slightly smaller and again Ti-carbide formation occurs. As in the case of the alloy X10CrAl18, a HVOF -TiAl coating was applied to Alloy 800.

Metal dusting behaviour

Table 7.7 shows the general behaviour of the coatings applied to Alloy 800 tested under metal dusting conditions at different temperatures. Mass change measurements of the specimens are shown in Fig. 7.45. At 400 °C no metal dusting attack was observed. The formation of a protective oxide scale is not

20 μ m

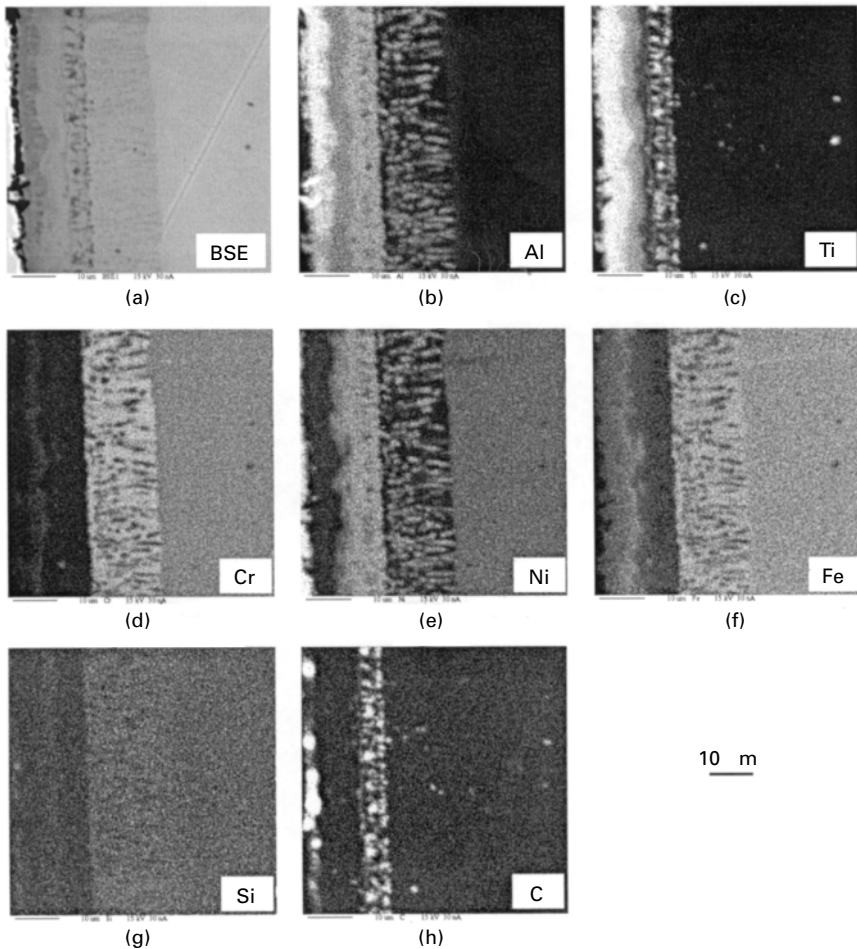
7.42 Microprobe element mapping of the Si-Al co-diffusion coating applied to Alloy 800.

favoured owing to the slow diffusion kinetics at this temperature. However, the penetration of carbon into the material is rather slow as well.

At 620°C the material showed pitting attack. Pits grew in number and size as time increased. There were coke deposits on the surface as well. First, pits appeared at the edges of the sample (Fig. 7.46) and, with longer exposures, the pits also started to nucleate in the middle of the surface. Once the pits were formed, the metal dusting rate increased markedly. The attack was more marked under the standard atmosphere than under the industrial atmosphere.

At 700°C the formation of a protective Cr oxide scale on the uncoated material avoided carbon penetration into the substrate (Fig. 7.47). However, a very thin coke layer, which gave the sample a black appearance, was found at the end of the exposure time (1008 h). For the aluminized material, protection was provided at all temperatures and no metal dusting or coke deposition occurred, owing to the formation of an oxide scale (Fig. 7.48). However, at 620°C some spallation caused a slight decrease in the weight of the specimen.

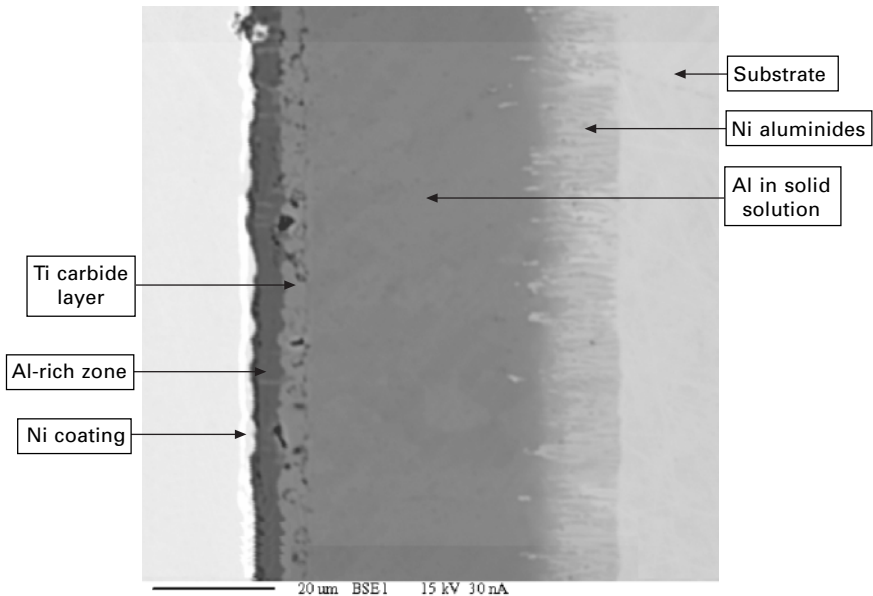
For all the co-diffusion coatings applied to Alloy 800 (Si-Al, Ti-Al and Si-Ti-Al), no metal dusting, coke deposition or spallation occurred owing to the formation of a protective oxide scale like that shown in Fig. 7.49. In this



7.43 Microprobe element mapping of a Ti–Al co-diffusion coating applied to Alloy 800.

case, the addition of Ti and/or Si to the Al diffusion coating clearly has a beneficial effect. The coatings appeared free from pores or cracks, leading to a more compact coating/substrate system.

The HVOF coating was only tested at 400 °C for 336 h. During this time, no attack was visible on the sample and there was no coke formation either. Mass changes were also measured and an increase of weight of the specimen was found during the exposure time. However, the coefficients of thermal expansion of the material and of the coating are quite different, so that after heating and cooling a delamination crack had developed (Fig. 7.50) although no through cracking occurred. Thus, the gas atmosphere could not reach the substrate and any kind of attack of the sample was prevented.



7.44 Ti-Si-Al co-diffusion coating applied to Alloy 800.

Since the coefficient of thermal expansion of ferritic steels is significantly lower and in the range of that for γ -TiAl, the HVOF coating is much better suited for such steels than for austenitic materials.

7.4 Conclusions

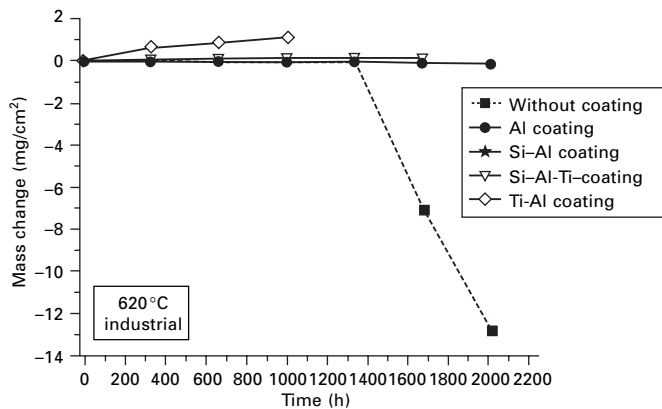
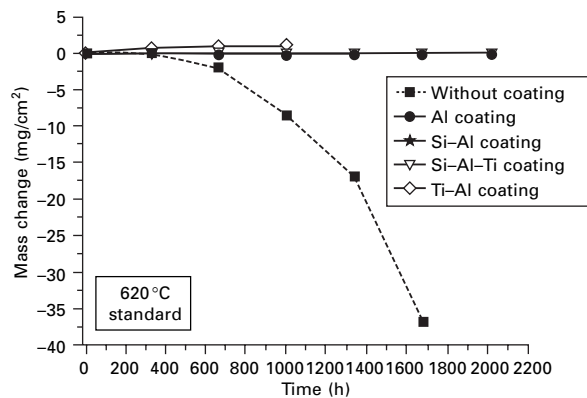
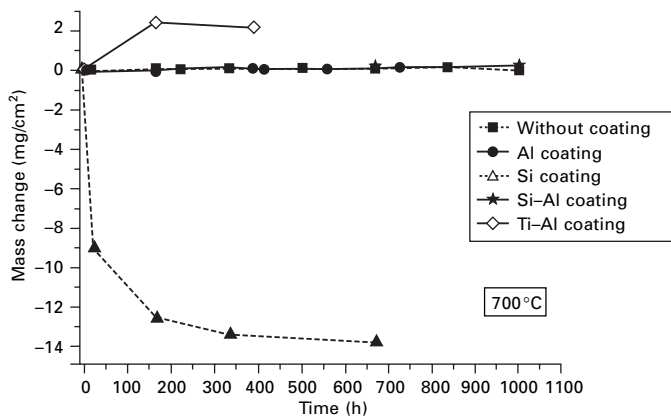
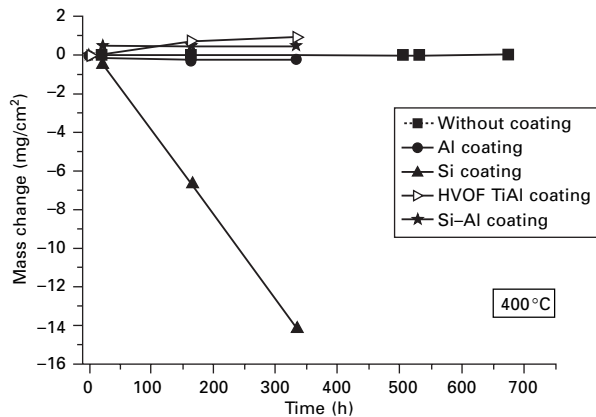
The properties of diffusion coatings to a large extent depend on the structure and chemistry of the substrate materials into which they are diffused. Therefore, no coating can exist which yields the same performance for all types of substrates. Rather, optimum coating/substrate systems have to be developed. In the present investigations these optimum combinations were as follows:

- | | |
|--------------------|---|
| • Alloy 10CrMo9 10 | Cr-Al 2-step diffusion coating |
| • Alloy P91 | Si-Ti-Al co-diffusion coating |
| • Alloy X10CrAl18 | HVOF γ -TiAl coating |
| • Alloy X18CrN28 | plain Al diffusion coating |
| • Alloy 800 | Ti-Al and Si-Ti-Al co-diffusion coating |

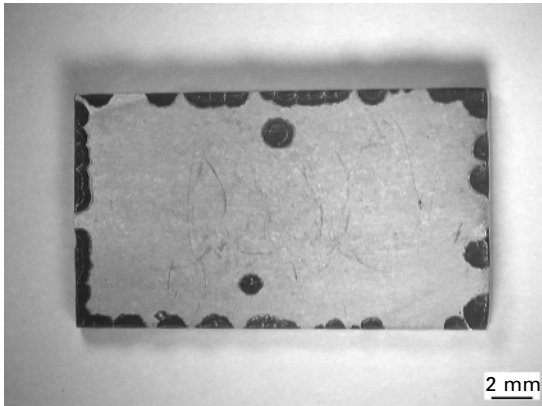
Plain Al-diffusion coatings were protective for all alloys at all temperatures and no coke deposition or metal dusting occurred. However, after long periods of exposure (1400h) pores appeared under the oxide scale which provoke cracking. On Alloy P91 there was spallation as well although no attack was observed.

Table 7.7 General behaviour of the coatings applied to Alloy 800 tested under metal dusting conditions

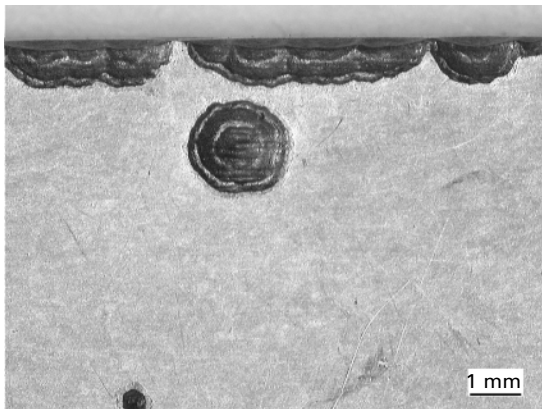
400 °C			620 °C			700 °C		
Coatings	Protective behaviour	Coke deposition	Coatings	Protective behaviour	Coke deposition	Coatings	Protective behaviour	Coke deposition
Uncoated	+	No	st uncoated in uncoated	– – –	Yes (p) Yes (p)	Uncoated	–	Yes
Al	+	No	st Al in Al	+ (s) + (s)	No No	Al	+	No
Si	– (s)	No	st Si–Al in Si–Al	++ ++	No No	Si	– –	Yes
Ti–Al	++	No	st Ti–Al in Ti–Al	++ ++	No No	Si–Al	++	No
			st Ti–Si–Al in Ti–Si–Al	++ ++	No No	Ti–Al	++	No
HVOF TiAl	+ (s)	No						
++ very good			(s) spallation					
+ good			(p) pitting					
– poor			st standard atmosphere					
– – very poor			in industrial atmosphere					



7.45 Mass change measurements of coated and uncoated Alloy 800 tested under metal dusting conditions at 400, 620 and 700°C.

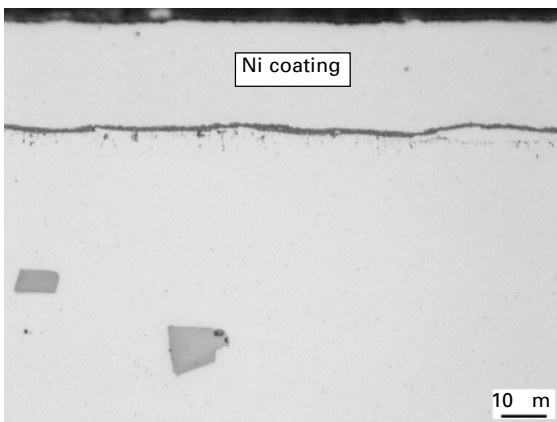


(a)

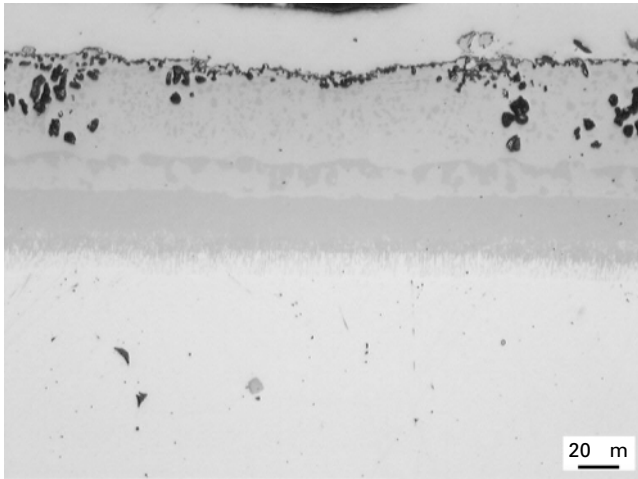


(b)

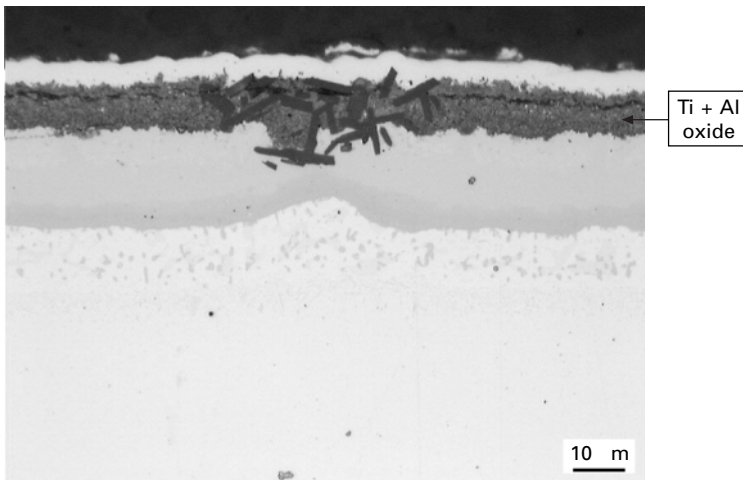
7.46 Pitting attack on Alloy 800 tested at 620°C under standard atmosphere for 1681 h. (a) Most of the pits formed at the edges of the specimen. (b) Higher magnification of the pits.



7.47 Formation of a Cr-oxide scale on Alloy 800 tested at 700°C under standard atmosphere for 1008 h.



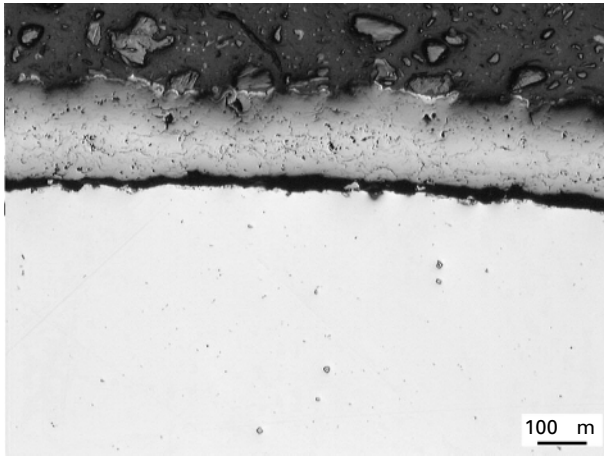
7.48 Oxide formation on top of the aluminized Alloy 800 tested at 700 °C under standard atmosphere for 729 h.



7.49 Formation of a Ti + Al oxide scale on top of Alloy 800 coated with a Ti-Al co-diffusion coating after testing at 700 °C under standard atmosphere for 393 h. The needle precipitates in the middle are Al oxide (residues from the pack cementation powder).

The Si diffusion coatings were only tested at 400 and 700 °C and they revealed poor behaviour. Si could not form a continuous and homogeneous oxide scale and protection was not provided.

The addition of Si to the Al diffusion coating had a beneficial effect at 700 °C for Alloy X10CrAl18, Alloy X18CrN28 and Alloy 800. However at 620 °C there was a detrimental effect for all alloys except for Alloy 800. There were different reasons for the negative behaviour of the coating:



7.50 Delamination crack due to thermal expansion mismatch for Alloy 800 coated with a γ -TiAl intermetallic by the HVOF method and tested at 400°C under standard atmosphere for 336 h.

- The oxide scale formed was a mixed Al + Si oxide, which had a very poor adherence and several pores under the oxide scale were found that could induce cracking.
- Si–Cr intermetallics were precipitated at the grain boundaries, leading to an increase of brittleness of the coating.
- In some cases, it seemed that the presence of Si (or SiO_2) promoted coke deposition on the specimen.

The Ti–Al co-diffusion coating was applied to Alloy 10CrMo9 10, Alloy P91 and Alloy 800. Only for Alloy 800 did the coating show excellent behaviour and neither metal dusting nor coke deposition were observed for this material. However, for Alloy 10CrMo9 10 and Alloy P91 there was the formation of a Ti carbide layer on the surface which prevented the further inward diffusion of Al and Ti into the material. Although the Ti carbide layer was compact and free of pores, it was not really resistant to metal dusting, and pitting attack took place on both materials.

The Ti–Si–Al diffusion coating was applied to Alloy P91 and Alloy 800 and tested at 620°C. The results obtained were positive for both materials and protection was provided in all cases. Spalling did not occur.

The HVOF γ -TiAl coating had only been applied and tested on X10CrAl18 and Alloy 800. In both cases the coating was extremely resistant against metal dusting attack but for the austenitic Alloy 800 coating failure occurred owing to the large thermal mismatch between substrate and overlay coating. Since the thermal mismatch is very small in the case of ferritic substrates, it can be concluded that for all such materials the HVOF γ -TiAl coating would offer excellent protection. This conclusion is of significant importance in the

case of welds or any other joints between components since diffusion coatings can be applied only before joining. After joining HVOF overlays can cover the unprotected parts of diffusion coated components.

Finally, a few general conclusions can be drawn:

- Since chromia is the least stable oxide among the oxide formers of the high-alloy materials, the development of coatings should aim at stabilizing the more stable oxides as a protective scale. The most common will be Al_2O_3 , which, however, will not in all cases easily form as a continuous defect-free scale. Nevertheless, as the present investigations show, already a plain aluminium diffusion coating can offer quite good protection on all the materials tested. A drawback is, however, the significant number of physical defects (e.g. pores) after long-term use. For uncoated materials, Al contents as low as 1% can evidently help with the formation of a continuous protective chromia layer where in the absence of Al even 28% Cr would not be sufficient to form a really protective scale.
- Since diffusion of Al in ferritic materials may become extremely rapid at high temperatures (inter-)diffusion barriers of Cr should be introduced for all materials with less than 9% Cr by a pre-step diffusion treatment before applying the Al diffusion coating. High-Cr materials can build up such a barrier intrinsically when Al is diffused into the material by the coating treatment by piling up the chromium of the alloy in the metal subsurface zone.
- Titanium can evidently help with the formation of a continuous protective alumina scale even in a temperature range where alumina scales are not easily formed. Ti may have a nucleation effect for oxide formation and may seal physical defects by its faster oxide growth. The thermodynamic stability of titanium oxide is not too far away from that of Al_2O_3 so that this effect can work even at the low oxygen partial pressures of metal dusting atmospheres. However, for steels with a relatively low Cr content (in the present investigations 10 wt% and less), i.e. where the amount of a strong carbide former in the form of Cr is relatively low, much of the carbon in the material is available for the formation of a dense Ti carbide layer on the material surface during the co-diffusion process. Thus inward transport and enrichment of the protective elements are suppressed. Therefore the beneficial effect of Ti is limited to low-C or high-Cr materials.
- Si is beneficial only in combination with Al plus Ti by further improving the coating quality (in particular long-term behaviour) in that it suppresses pore formation and leads to a more compact coating/substrate system.

7.5 Acknowledgements

The investigations were financially supported by the German Ministry for Economy and Labour (BMWA) via Arbeitsgemeinschaft industrieller

Forschungsvereinigungen (AiF) (Contract no. 12121N) under the auspices of the German Society for Corrosion Protection (GfKORR) which is gratefully acknowledged by the authors.

Thanks are also due to Mr Aumüller from ATZ-EVUS for supplying the HVOF coatings.

Furthermore the authors appreciate the contributions of Ms Berghof-Hasselbacher and Ms Hasenpflug (metallography), Ms Schorr (microprobe) and Mr Gawenda (SEM).

7.6 References

1. K. A. Wynns, G. T. Bayer: US Patent No: WO9820182 (1998).
2. B. Ganser, K. A. Wynns, A. Kurlekar: *Materials and Corr.* **50** (1999) 700.
3. R. A. Rapp: *Corrosion* **89**, Paper No. 532 (1989).
4. R. Streiff: In: *Elevated Temperature Coatings: Science and Technology II* (Eds. N. B. Dahotre, J. M. Hampikian), The Minerals, Metals & Materials Society 1996, Warrendale pp. 407–416.
5. I. Wolf, H. J. Grabke, P. Schmidt: *Oxid. Metals* **29** (1988) 289.
6. R. L. Wachtell: In: *Science and Technology of Surface Coating* (Eds. B. N. Chapman, J. C. Anderson), Academic Press, London and New York 1974, pp. 105–118.
7. S. C. Kung, R. A. Rapp: *Oxid. Metals* **32** (1989) 89.
8. M. Schütze: German Patent No: DE 197 43 421.5 (1998).
9. H. J. Grabke, E. M. Müller-Lorenz: *Steel Research* **66** (1995) 254.
10. H. J. Grabke: *Carburization: A High Temperature Corrosion Phenomenon*, MIT Publications No. 52, USA, 1998.
11. H. J. Grabke, R. Krajak, E. M. Müller-Lorenz: *Werkstoffe und Korr.* **44** (1993) 89.
12. B. A. Pint: *Oxid. Metals* **48** (1997) 303.
13. E. C. Bain, H. W. Paxton: *Alloying Elements in Steel*, ASM, Washington, DC, 1966.
14. W. G. Moffatt, G. W. Pearsall and J. Wulff, *The Structure and Properties of Materials*, Vol. 1. *Structure*, John Wiley & Sons, New York (1964) 195.
15. C. F. Walton (ed.): *Grey and Ductile Iron Castings Handbook*, Gray and Ductile Founders, Society, Inc., Cleveland (1971).

Metal dusting resistance of high-chromium alloys

HJ GRABKE and EM MÜLLER-LORENZ,
Max-Planck-Institut für Eisenforschung GmbH, Germany and
HP MARTINZ, Plansee AG, Austria

8.1 Introduction

Metal dusting is a catastrophic carburization, leading to disintegration of metals and alloys to a dust of graphite and metal particles. This corrosion phenomenon is caused by a high carbon activity in the environment and the tendency for graphite formation. Carbon is transferred into the metal phase unto high oversaturation, then the graphite growth, either into cementite formed on iron and steels as an intermediate, or directly into the metal phase as in the case of nickel or Ni-base alloys, destroys the materials. Rapid formation of a dense oxide scale suppresses the carbon ingress and Cr-rich scales are most effective [1, 2]. So for high-chromium alloys there is a good chance of avoiding metal dusting, even at very low oxygen pressures, e.g. $p_{\text{H}_2\text{O}}/p_{\text{H}_2} > 1.2 \cdot 10^{-7}$ at 650°C (dew point: -88°C), chromia scales should be formed rapidly.

However, high-Cr alloys are difficult to produce and to form, since Cr imparts brittleness. Such materials were produced at Plansee AG by powder metallurgical processes and strongly deformed to obtain nearly 100% density. PM 2000 with 19% Cr and 5.5% Al is available as tubes or sheets and can be welded. Cr-44%Fe-5%Al is a developmental material and was produced only in small amounts. CrNi50 is available as sheet (but also centrifugally cast tubes) and can be rolled and welded. Plates of Cr-5%Fe-1%Y₂O₃ are produced as sheet, to be applied in high-temperature fuel cells (SOFC), but the material is rather brittle and cannot be welded. Pure Cr was tested as a porous product which is used for filters at high temperature. So the availability, formability and weldability of these materials is limited, but they might be used for small components in critical positions concerning metal dusting imminence.

8.2 Experimental procedure

Two samples of each material (described above) were exposed discontinuously for 10000h in total at 650°C in a flowing gas mixture:

49%CO–49% H_2 –2% H_2O . This environment is characterized by a carbon activity $a_{\text{C}} = 18.9$, as calculated for the carbon transfer reaction $\text{CO} + \text{H}_2 = \text{C} + \text{H}_2\text{O}$, accordingly it is rather strongly carburizing and can cause metal dusting on most steels and Ni–base alloys [1–5]. Before and after each exposure the samples were weighed, the mass increase corresponds to changes by carburization, oxidation and carbon deposition. The mass of coke formed was determined separately by scratching off and weighing this corrosion product, its mass indicates the extent of metal dusting attack. By analysis of the coke for its metal content the metal wastage can be determined for each sample and exposure period; however, this analysis was not conducted since the amount of coke was always rather low.

Metallographic cross-sections of the samples were taken after 4007 and 10000 h exposure, and of the Alloy 601 samples after 1993 h.

8.3 Results

The Ni-base alloy 601 was tested as a reference material but for only two exposure periods (Table 8.1), since the corrosion behaviour of both samples clearly indicated severe metal dusting conditions in the tests. Alloy 601 tends to local attack under formation of nearly hemispherical pits, see Fig. 8.1a, most probably starting from one small defect in the oxide scale. Figure 8.1b shows the typical metal dusting attack is by formation of a zone with internal carbides, which decomposes to flaky coke. The surface around the growing pits is still protected by an oxide layer which, however, is undermined by the spreading of the pits (Fig. 8.1c). Assuming that the pits have grown from the start of the exposure periods, depth penetration rate results of 0.7 to 0.95 mm/year are in good agreement with other data [6]. After both exposure periods of the Alloy 601 samples the metal content was determined in the coke and the metal wastage could be calculated: about $3 \cdot 10^{-4}$ mg/sample

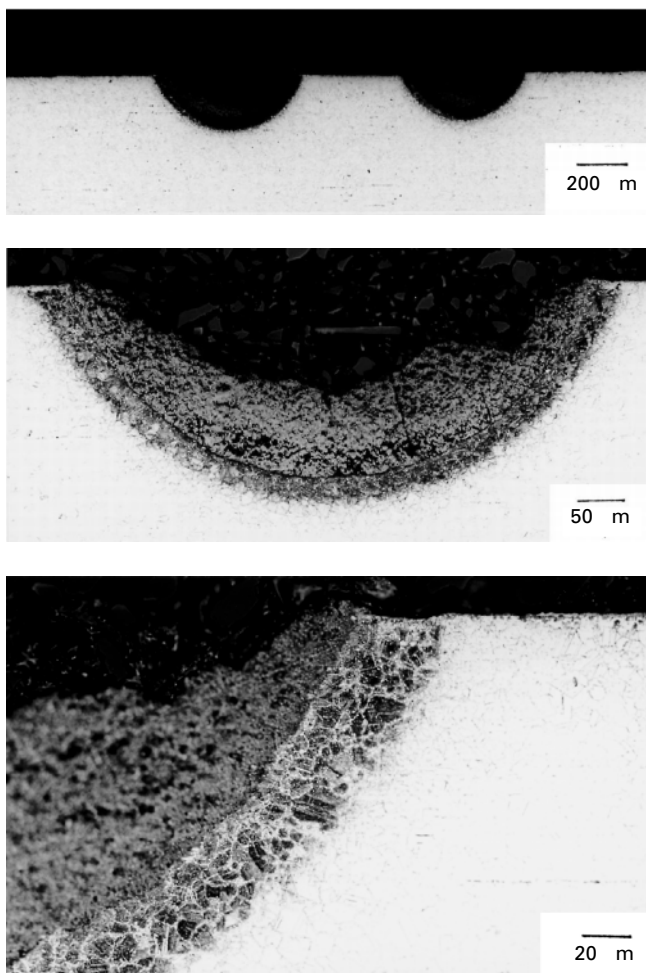
Table 8.1 Mass changes, total, by coke formation and by metal loss of the reference sample after exposures 8 and 9

Exposure duration (h)	m_{total} (mg/cm ²)	m_{coke} (mg/cm ²)	m_{M} (g)
(8) 982	25.25	25.81	0.000 299
	21.07	21.50	0.000 291
(9) 982 + 1011 = 1993	87.40	90.20	0.001 868
	67.05	91.41	0.001 952

m_{total} is the total mass change of the sample by carburization, oxidation and adherent 'coke'.

m_{coke} is the mass of coke formed on the sample, adherent or fallen off.

m_{M} is the metal loss.



8.1 Pit growth on Alloy 601H after 10000h under metal dusting conditions at 650°C, metallographic cross-section at different magnifications.

after 928h and about 19×10^{-4} mg/sample after 1993h; corresponding data have been observed before [3–5].

Indications of slight metal dusting were observed on the samples of the Fe–base alloy PM 2000 with ~ 19%Cr. Coking occurred but the coke amounts decrease with the number of exposures (Table 8.2). The surface of the samples showed tiny pits filled with coke (Fig. 8.2), but the otherwise typical zone with internal carbides is not detectable. Obviously some metal dusting of this material has taken place, but with decreasing rate of metal wastage and coking, as can be concluded from the mass changes. This behaviour is

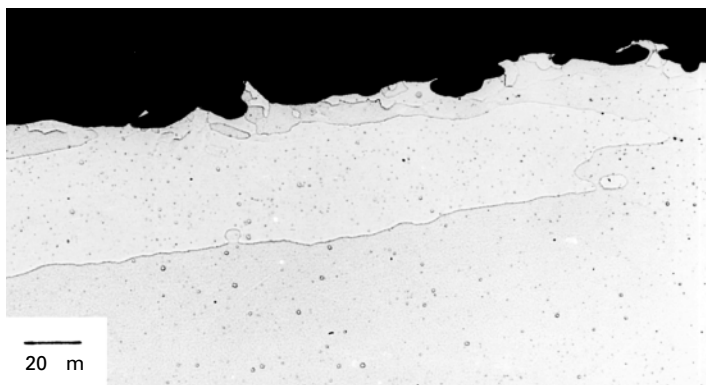
Table 8.2 Mass changes, total and by coke formation, of the high-Cr alloys in exposures 7–11

<i>t/ t</i> (h)	(7) 715/5707		(8) 982/6689		(9) 1011/7700		(10) 1033/8733		(11) 1267/10 000	
	m_{total}	m_{coke}	m_{total}	m_{coke}	m_{total}	m_{coke}	m_{total}	m_{coke}	m_{total}	m_{coke}
1. Chromium	0.2080 0.4310	0.0004 –0.0007	0.3540 0.4980	0.0033 –0.0180	0.1740 0.3080	–0.0240 0.0102	0.166 0.233	–0.0025 0.0120	0.2080 0.2890	–0.0150 0.0090
2. Cr–50 Ni	0.0300 0.0330	0.0065 0.0095	0.0180 0.0130	0.0100 0.0082	0.0290 0.0084	0.0170 0.0088	0.0285 0.026	0.0201 0.0160	0.0220 0.0130	0.0096 0.0090
3. PM 2000	0.0620 0.0130	0.1580 0.1700	0.0440 0.0560	0.0430 0.0960	0.0570 0.0720	0.0540 0.0800	0.105 0.036	0.1090 0.0400	0.0570 0.0220	0.0540 0.0290
4. Cr–5Fe–1Y ₂ O ₃	0.0320 0.0220	0.0047 –0.0053	0.0150 0.0120	0.0066 0.0060	0.0120 0.0120	0.0028 0.0039	0.24 0.013	0.0093 0.0014	0.0026 0.0200	0.0110 0.0080
5*. Cr–44Fe–5Al– 0.3Ti–0.5Y ₂ O ₃	0.2750 0.3970	0.2560 0.3770	0.1100 0.3040	0.0960 0.2310	0.0430 0.0980	0.0450 0.1510	0.034 0.070	0.0260 0.0700	0.0400 0.0430	0.0430 0.0480

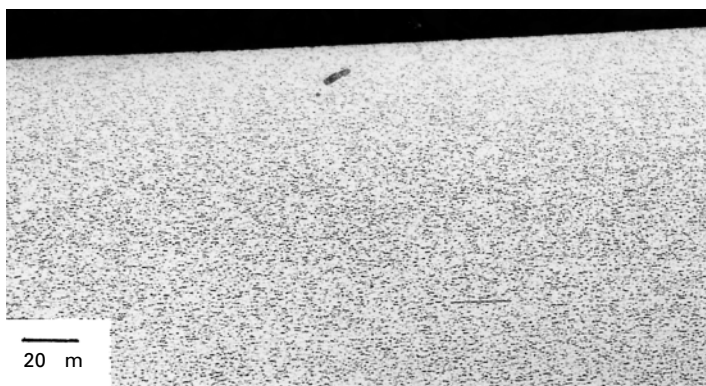
m_{total} is the total mass change of the sample by carburization, oxidation and adherent ‘coke’

m_{coke} is the mass of coke formed on the sample, adherent or fallen off.

* The exposure of these samples (No. 5) was interrupted for periods 4, 5 and 6, therefore the exposure times must be reduced by 3657 h.



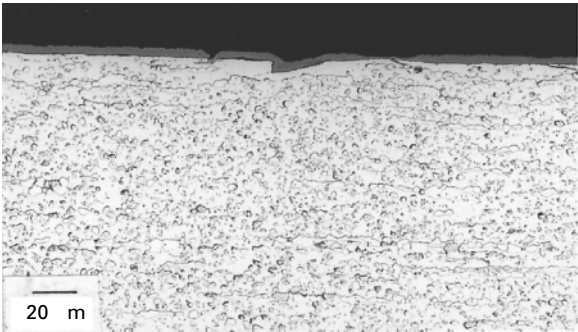
8.2 Tiny pits on PM 2000 after 10000h under metal dusting conditions at 650 °C.



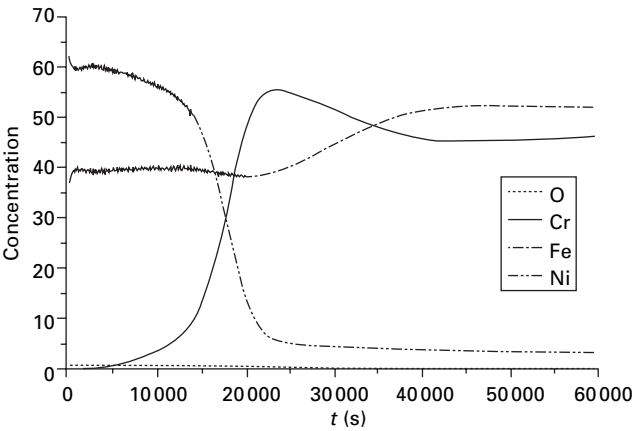
8.3 No attack on Cr-44%Fe-5%Al-0.4%Ti-0.5%Y₂O₃ after 10000 h under metal dusting conditions at 650 °C.

presumably caused by the slow growth of a thin, dense alumina layer, as detected by X-ray diffraction (XRD). The alloy Cr-44Fe-5Al-0.3Ti-0.5Y₂O₃ with about 50%Cr is even more resistant: the metallographic cross-section shows no indication of carburization and pitting (Fig. 8.3) although XRD proves chromia and Cr, Fe carbide as surface phases. Also the nickel alloy with 50%Cr is very resistant against metal dusting. As can be seen from the mass change data, oxidation takes place leading to steady increases of mass and formation of about 3 μm oxide scale (Fig. 8.4). But no carburization occurred and minute amounts of coke were formed (Table 8.2).

Similar observations were made on the Cr-base alloy Cr-5Fe-1Y₂O₃, where the chromia scale is even thinner but protective, since there is no indication of carburization and pitting (Fig. 8.5). The amounts of coke formed are even much lower than on Cr-50Ni (Table 8.2). On the pure porous



(a)

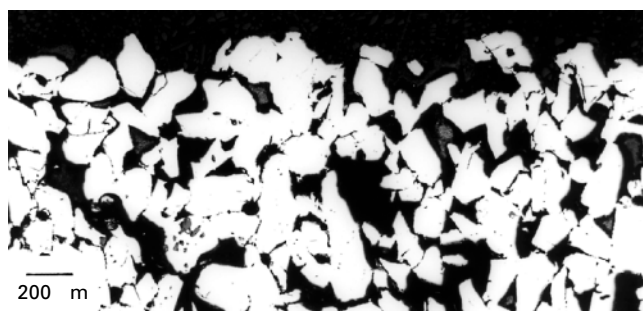


(b)

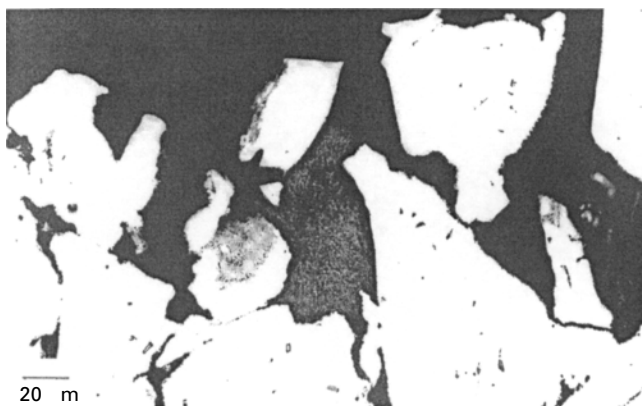
8.4 Cr-50%Ni after 10000h under metal dusting conditions:
(a) metallographic cross-section, showing the chromia layer;
(b) SNMS – sputter profile of the chromia layer.



8.5 Thin chromia scale on Cr-5%Fe-1%Y₂O₃ after 10000h under metal dusting conditions at 650°C.



(a)



(b)

8.6 Porous chromium after 10000h under metal dusting conditions at 650 °C, metallographic cross-section at two magnifications.

chromium no indications of metal dusting were observed. The steady mass increase in the exposures is due to the growth of chromia, in the beginning some carbon deposition may also have taken place but after 10000h the coking is negligible (see Fig. 8.6 and Table 8.2).

8.4 Discussion

That metal dusting is not possible on pure chromium and Cr with 5%Fe is clear, since carbon is virtually insoluble (<3 ppm at 650 °C) in these materials [7], and dissolution of carbon and oversaturation with dissolved C is a precondition for its occurrence. In addition, such high-Cr materials certainly are most apt for rapid chromia formation, suppressing the ingress of carbon.

The alloys with about 50% Cr also strongly tend to oxidation and formation of a protective chromia scale. This was confirmed by the exposures described and by taking a secondary neutral mass spectrometry (SNMS) sputter profile (Fig. 8.4) of the scale on Cr–50Ni, demonstrating a pure, dense chromia

scale. Furthermore, positive experience was reported on the use of 50%Cr–50%Ni as a metal dusting resistant coating. Such coating was applied by thermal spraying on components in a methane reforming plant [8]. On the other hand, carbon can be dissolved in both the ferritic and the austenitic alloy, after precipitation of stable chromium carbides, $M_{23}C_6$ and M_7C_3 . In fact, internal carbide formation has been observed in Cr–50Ni in a certain narrow temperature range [9].

On the materials with very high Cr content ($> 95\%Cr$), metal dusting cannot occur. If oxidizing components are in the gas phase, chromia Cr_2O_3 will grow and in the case of pure hydrocarbons, the chromium carbides Cr_3C_2 , Cr_7C_3 and $Cr_{23}C_6$ will grow on the material's surface [10].

8.5 References

1. Grabke, H.J.; Krajak, R.; Müller-Lorenz, E.M.: *Werkst. und Korros.* **44** (1993) 89–97.
2. Grabke, H.J.: *Corrosion NACE* **51** (1995) 711–720.
3. Grabke, H.J.; Krajak, R.; Müller-Lorenz, E.M.; Strauß, S.: *Werkst. und Korros.* **47** (1996) 495–504.
4. Grabke, H.J.; Müller-Lorenz, E.M.; Klöwer, J.; Agarwal, D.C.: *Mat. Performance (NACE)* **37** (1998) 58.
5. Grabke, H.J.: *Corrosion NACE* **56** (2002) 801–808.
6. Grabke, H.J.; Müller-Lorenz, E.M.; Zinke, M.: *Mat & Corr* **54** (2003) 785–792.
7. Smith, W.H.: *J. Metals* (1957) 47–49.
8. Holland, M.L.: Practical experience with countering metal dusting in a methane reforming unit, *Corrosion NACE*, Houston 2001, paper 01385.
9. Grabke, H.J.; Mersch, H.D.: unpublished.
10. Konev, V.N.: *Fiz. Met. Metallov* **6** (1958) 942.

Study of the metal dusting behaviour of high-temperature alloys

F DI GABRIELE, JR BERNSTEIN,
MM AL-QHATANI, Z LIU, MP JORDAN and
FH STOTT, Corrosion and Protection Centre, UK and
JA RICHARDSON, Anticorrosion Consulting, UK

9.1 Introduction

Metal dusting is defined as catastrophic carburization leading to formation of a dust of graphite, fine metallic and other particles. The phenomenon is observed in carbon-rich environments at temperatures between 450 and 800°C [1]. It is believed that this type of corrosion may occur in any environment with a carbon activity greater than unity [2–6].

The corrosion mechanism has been widely studied in the case of iron and low-alloy steels [3]. On the other hand, understanding of dusting of nickel-based alloys, and their response to highly aggressive carbon-containing environments, still lacks precision and reliability. Also, the large variability in the experimental conditions adopted in previous studies has given rise to a wide range of results, but there are still no coherent conclusions.

Metal dusting has been observed in petrochemical and reforming industries [5] and it is a common problem in industrial process components for the production of syngas [6]. The latter process produces a mixture of CO, H₂, CO₂ and H₂O from natural gas via steam reforming. It is a common route for the production of hydrogen, ammonia, methanol and liquid hydrocarbons. To increase plant efficiency, the trend is to use less steam, thereby increasing the amount of CO in the system [7]. This combination gives rise to a more aggressive environment, with lower oxygen partial pressure and higher carbon activity, giving higher severity in terms of metal dusting attack.

In this preliminary study, the behaviour of several widely used commercial alloys has been investigated as a function of composition, microstructure and experimental set-up. The exposure gas used in the experiments is a mixture of H₂ and CO. For the preliminary experiments, the exposure temperature was 650°C. Corrosion products and areas of reaction in the metals have been examined using optical and electron microscopy techniques and chemically characterised using elemental analyses. Mechanical characterisation of the reacted areas has been carried out using nano-indentation methods.

9.2 Experimental work

The compositions of the alloys exposed to the dusting environment are given in Table 9.1. Specimens were cut from the initial plates provided by the manufacturers; dimensions of the specimens were approximately 10 × 8 mm² and their thicknesses varied, as a function of the thicknesses of the plates, from 3 to 8 mm. A preliminary metallographic study of the alloys was carried out in order to determine basic microstructural characteristics. Different etching solutions were selected for the alloys, to highlight their general microstructures: cast Alloy H46M was electrolytically etched with a solution of 60% HNO₃/40% H₂O; all the other alloys were etched with a solution of 40% HCl/40% H₂O₂/20% H₂O. Before the dusting experiments, each sample was ground to 600 grit finish using SiC paper and its dimensions were measured. In this way, all the surfaces were uniform and the effect of previous surface treatments eliminated. Subsequently, each sample was ultrasonically cleaned, first in water, then in ethanol and, finally, in acetone. The experiments consisted of exposing the samples to a gas mixture of 20 vol.% H₂ and 80% CO, flowing at 100 cm³ min⁻¹, at a temperature of 650 °C. Exposure times varied from 100 to 1000 h. Two variations of the same experiment were carried out. During the first run, specimens of four alloys: H46M, 600, 602CA and 693, were placed in ceramic crucible holders (see composition of the crucible in Table 9.2) and positioned in the reaction tube. In a second set of experiments, five specimens of each of the previous four alloys, plus five other alloys (601, 603XL, 617, 671, 690), were suspended freely from quartz hangers and introduced into the reaction tube.

For both experimental runs, the system was sealed and flushed with argon, before heating. In the first run, the reactive gas mixture was introduced at room temperature and, then, the system was heated to temperature, 650 ± 5 °C. After the required exposure period, the specimens were furnace cooled

Table 9.1 Alloy compositions (wt%)

Alloy	Al	C	Cr	Fe	Mn	Nb	Ni	Si	Ti
H46M		0.4	35	15	1	1	45	1.8	
693	3.3	0.02	28.9	5.8		0.7	60.7		0.4
600	0.3	0.04	16.4	9.5	0.4	0.2	72.1	0.2	0.2
602CA	2.3	0.17	25.2	9.4	0.1		62.5	0.1	0.1

Table 9.2 Composition of the ceramic crucible (wt%)

SiO ₂	Al ₂ O ₃	KOH	Fe ₂ O ₃	C	TiO ₂	MgO	Na ₂ CO ₃	CaO
55.41	39.41	2.02	1.1	1.08	0.43	0.32	0.18	0.12

in the reactive gas. One specimen of each alloy was removed from the furnace for examination, the system was sealed again and the cycle was repeated. Exposure periods were 100, 200, 300, 500 and 1000 h. The second run followed the same sequence, but the specimens were heated to temperature in flowing commercial hydrogen, prior to exposure to the reactive gas; the system was flushed with hydrogen prior to cooling at the end of the exposure period.

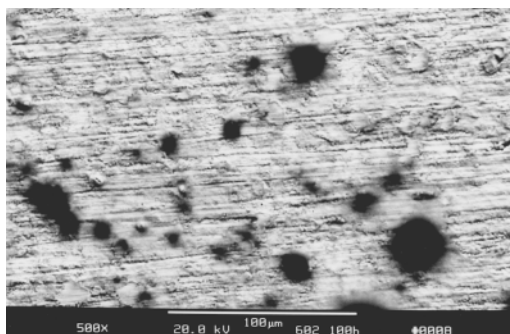
Carbon deposits and corrosion products were mechanically removed from some of the samples after exposure for analysis. The specimens were cleaned of any residual deposit by ultrasonic cleaning in water, then in ethanol and, finally, in acetone. The deposits, containing the corrosion products, were analysed by X-ray diffraction (XRD) and the energy dispersive analysis of X-ray technique (EDX) attached to a transmission electron microscope (TEM). Part of the corrosion products were dissolved in a solution of sulphuric and perchloric acids and analysed by atomic absorption spectrometry (AAS).

Some exposed specimens were mounted in cross-section, sectioned and metallographically polished. The etching solutions were the same as those used for the preliminary metallographic study. The morphologies of the deposits and the underlying damage to the metal surfaces were examined by optical and scanning electron microscopy. Moreover, an EDX attachment in the SEM produced qualitative evaluations of the changes in compositions in the surface reaction zones formed on some of the alloys, while electron probe microanalysis (EPMA) and X-ray photoelectron microscopy (XPS) were used to analyse such zones in more detail.

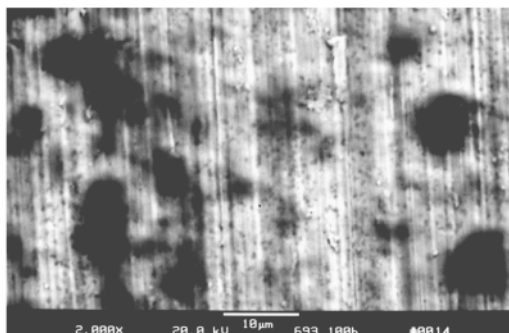
Nano-indentation testing of the alloys from the first experimental run (693, 600, H46M and 602CA) after exposure to the metal dusting environment, was carried out. Sections of the specimens, metallographically polished, were indented along lines from the bulk towards the edge, across the reaction zones. The indents were distributed along five parallel rows, setting a distance of 15 mm between the rows. Each line was composed of 30 indents, distributed at a distance of 5 mm apart.

9.3 Results

A clear difference was observed between the behaviours of the samples exposed to the dusting environment while suspended from the quartz hangers and those located in the ceramic crucible holders. For the samples suspended from the quartz hangers, the incubation time, to the onset of carbon deposition, was much longer than for those placed in the ceramic crucibles. Even after 1000 h, the surfaces of the specimens were only partially covered by thin deposits of carbon, with the appearance of black stains. Most of these stains were superficial (Fig. 9.1); only very occasionally were small areas of more substantial carbon deposit observed on these specimens. Examination in



(a)



(b)

9.1 Alloys (a) 602 CA and (b) 693 exposed in the gaseous environment for 100h at 650 °C, while suspended from a quartz hanger: surface of the sample.

cross-section showed the presence of irregular oxide scales. Even after 1000h exposure, most of the alloys showed little reaction, apart from formation of continuous oxide scales. There were only a few local regions where carbon deposits with embedded metallic particles occurred. The main exception was Alloy 600 where, after periods of 300h and longer, a more conspicuous carbon deposit was apparent, with underlying pits in the metal surface. The specimen of the alloy, exposed for 1000h to the reactive gas, showed significant carbon deposit along all the edges. The damage morphology observed in this case was similar to that observed on specimens from the experiments involving the ceramic crucible holders (Fig. 9.5b).

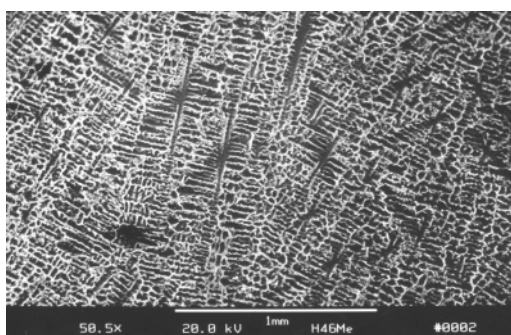
In the case of the specimens located in the ceramic holder during exposure, all alloys reacted with the gas mixture after a short time and showed abundant carbon deposits, even after only 100h. In each case, the presence of carbonaceous deposits corresponded to regions of significant underlying damage in the surfaces of the metal. For all alloys, examinations in cross-section revealed pits in the metal surface, with distinctive reaction zones. These areas were characteristic for each alloy and were always defined by a

chemical/microstructural change in the alloy. The results of this set of experiments are presented in the remainder of this section.

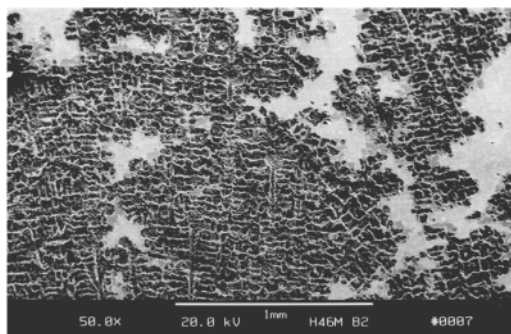
Carbon deposits and incorporated corrosion products, from specimens of all four alloys in the ceramic holder, were examined after 200h exposure. In every case, XRD analyses revealed them to consist of graphite, chromium oxide and metal. EDX analyses revealed that the larger particles were essentially chromium oxide while the smaller ones were combinations of nickel–iron plus other minor alloying elements. Chemical analyses of the solutions into which the deposit had been dissolved by AAS showed that the ratios of the major alloying elements in the metal from the deposits were very similar to those from the original alloy.

9.3.1 Alloy H46M

The cast alloy H46M is characterised by a multi-phase microstructure (Fig. 9.2a). After etching, the base matrix (dark reacted areas), a solid solution



(a)



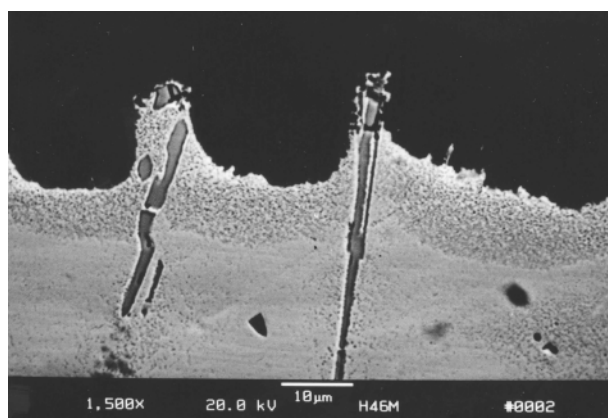
(b)

9.2 Alloy H46M: (a) surface of the non-exposed sample after polishing and electrolytic etching; (b) surface of the sample after 200h exposure in the gaseous environment at 650°C, while located in a ceramic holder, following removal of much of the corrosion products, showing corroded (dark) areas and less damaged (flat/light) areas.

of the alloying elements, surrounds a net-like structure of streaks (white, less attacked areas) of chromium carbide and discrete niobium carbide precipitates.

In the first set of experiments, the specimens, exposed to the dusting environment for 100h, underwent more attack on the side that was in contact with the ceramic holder. The other sides did not show any significant reaction. The graphitic deposit, in between the sample and the crucible, thickened with increasing exposure time and, after 1000h, the specimens were resting on a 7 mm thick stratum of carbon and corrosion products. The surface of the specimens, in contact with the holder, reacted with the environment in strict accordance with the microstructural features. During etching, the alloy matrix reacted preferentially with the etching solution; a similar trend occurred over much of the surface in the dusting environment. Fig. 9.2b shows corroded (dark) areas that were similar in appearance to etched surfaces of the alloy. The carbides in the corroded area stood proud of the base matrix. At high magnification, it was confirmed that there were deep pits in the matrix, separated by less-corroded carbides.

Examination of the samples in cross-section (Fig. 9.3) confirmed that the carbide phase stood proud of the specimen surface without reacting significantly with the aggressive environment, while the surrounding matrix was pitted. The alloy substrate around the pits, with a speckled appearance (about 10 μm thick), is termed the reaction zone and contained numerous small precipitates. The composition of these precipitates could not be determined by EDX analysis, owing to their size, although the technique revealed a change in average elemental composition in this region. The most marked variation was a depletion in chromium in the reaction zone. Examination of the flat areas, in cross-section, revealed a silicon/chromium oxide layer of



9.3 Alloy H46M: detail of the reaction zone beneath the pits in the cross section of a specimen after 200h exposure in the gaseous environment at 650°C while located in a ceramic holder.

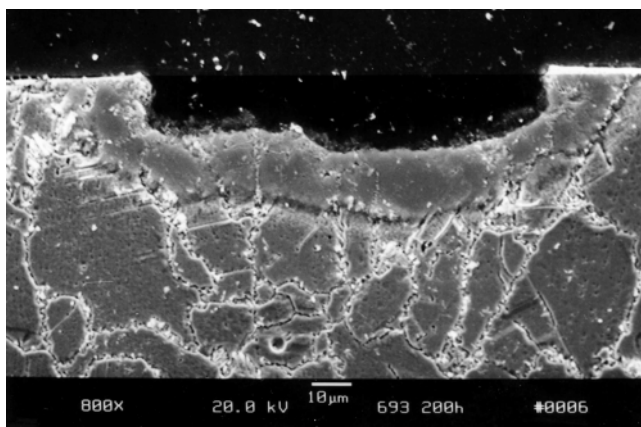
irregular thickness, which protected the surface. Moreover, traces of silicon oxide were also detected on the surfaces of the pits.

9.3.2 Alloy 693

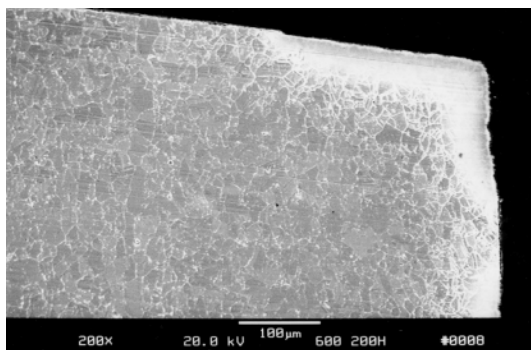
The microstructure of Alloy 693 is essentially a mono-phase solid solution of the alloying elements, characterised by equiaxed grains. After exposure to the reactive environment in the ceramic holder, some shallow pits were observed in the surfaces of the specimens, even after 100h exposure. The number of pits and their lateral size increased with time. However, for this alloy, there was no obvious correlation between the number and distribution of the pits on a given surface and its location in respect of the ceramic holder. Figure 9.4 shows one of the most common features in one of the pits. A reaction zone was again visible around the surface of the pit, although this had a relatively featureless appearance and stood slightly proud of the matrix. EPMA analysis highlighted carbon enrichment in the reaction zone surrounding the pit, with a marked enrichment at the alloy grain boundaries. In the same areas, at the grain boundaries, a high concentration of chromium was revealed. Moreover, a thin, irregular layer of aluminium oxide was detected on the flat surfaces remote from the pits, while some traces of this oxide were also observed at the interface between the pit and the carbon deposit.

9.3.3 Alloy 600

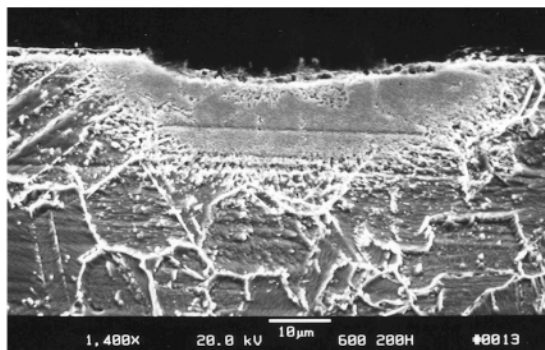
Alloy 600 is characterised by a microstructure that is mainly a solid solution of the alloying elements, with a uniform and equiaxed grain structure. Conic-



9.4 Alloy 693: etched cross-section of a pit after 200h exposure in the gaseous environment at 650°C while located in a ceramic holder.



(a)



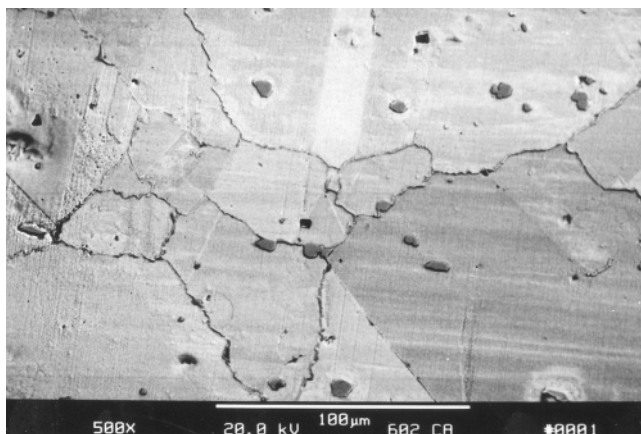
(b)

9.5 Alloy 600: cross-section of specimen after 200h exposure in the gaseous environment at 650 °C while located in a ceramic holder.

(a) Showing extensive damage adjacent to the edge of the specimen;

(b) showing a reaction zone beneath a localised pit in the surface of the specimen.

shaped, localised deposits of graphitic carbon were formed on the specimens after exposure to the carbonaceous environment in the ceramic holder. After 100h exposure, these deposits were located at the edges and lateral sides; with increasing exposure time, the deposits developed over the specimen surfaces and thickened until, after 1000h, all surfaces were covered by a conspicuous stratum of graphite and corrosion products. Fig. 9.5a shows significant metal loss at, and adjacent to, the specimen edge after relatively short periods, while localised pits were observed on the surfaces (Fig. 9.5b). The extent of such damage increased with increasing time. Again, characteristic reaction zones developed in the alloy surfaces beneath the pits and damaged areas, as shown in Fig. 9.5. At the edges (Fig. 9.5a), the reaction zone has the appearance of a continuous stratum; the reaction zone beneath the pits (Fig. 9.5b) has the typical semicircular shape of the pit in the alloy. EDX analyses did not indicate any significant compositional change in the reaction zone. In



9.6 Alloy 602CA: etched cross-section of the alloy, as received.

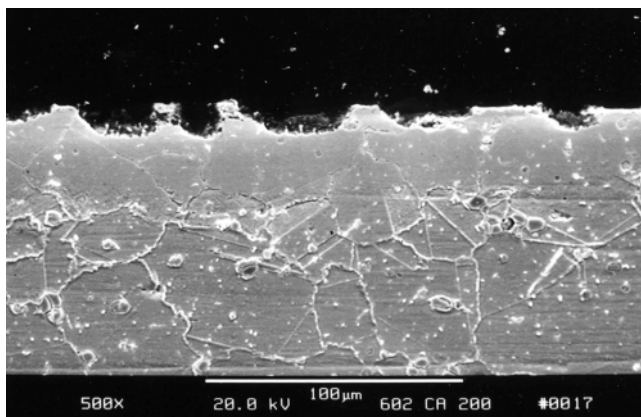
areas where little damage was observed, a thin and discontinuous chromium oxide scale was detected.

9.3.4 Alloy 602CA

The microstructure of Alloy 602CA is characterised by the high carbon content that gives rise to carbide precipitates, in both the grain boundaries and the grains (Fig. 9.6). After 100h exposure, the specimens in the ceramic crucible holders were completely covered by a thick layer of carbon deposit and corrosion products. After each further interval of exposure, the amount of deposit increased very considerably; it appeared from the morphology that layers of graphite were sequentially detached from the surfaces of the specimens and replaced by new layers. After cleaning the specimens of the carbonaceous deposit, it was observed that significant metal loss occurred on all surfaces, in the form of localised pitting damage; eventually, the pits coalesced to form an uneven surface. Figure 9.7 shows a typical surface morphology of the sample, after 200 h exposure, in cross-section. The area is characterised by a relatively thick ($\sim 30 \mu\text{m}$), uniform and continuous reaction zone, beneath the pits. EDX and XPS analyses detected changes in concentrations of the metallic elements in the reaction zone compared with those in the bulk alloy. In particular, enrichment in carbon and chromium and depletion in aluminium were detected. Traces of aluminium oxide were found on the surfaces adjacent to the pits.

9.3.5 Nano-indentation tests

Nano-indentation testing of Alloy 693, 600, H46M and 602CA, after exposure to the metal dusting environment, showed that there was a significant increase



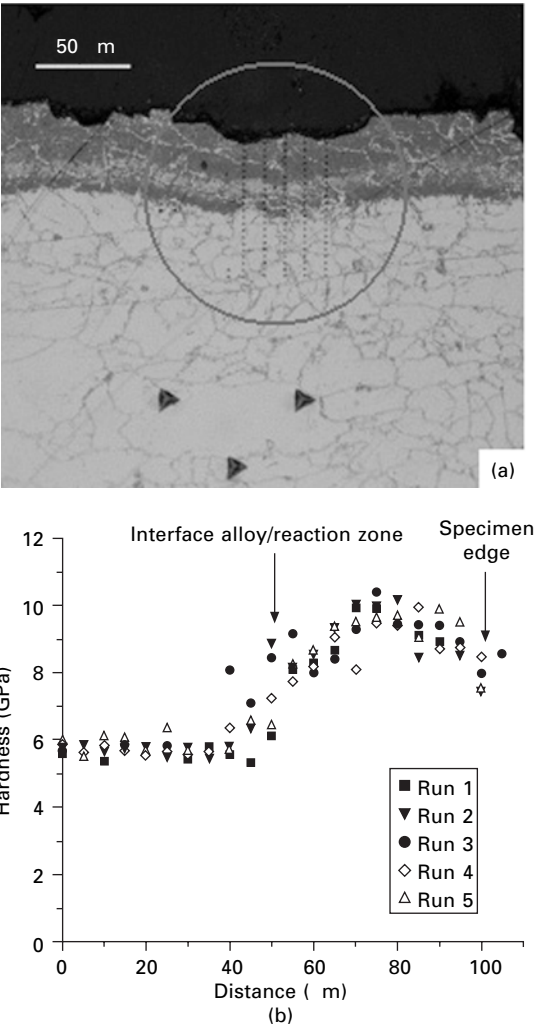
9.7 Alloy 602CA: cross-section of the pitted area after 200h exposure in the gaseous environment at 650°C while located in a ceramic holder.

in hardness in the reaction zones compared with the bulk hardness values. Figure 9.8 gives typical hardness values against distance for Alloy 693; the behaviour is common to all the alloys. A sharp rise in hardness occurred at the interface between the unreacted bulk alloy and the reaction zone surrounding the edge of the pit. The hardness continued to rise across the reaction zone, and then started to decrease in the final 10 μm towards the surface of the sample.

9.4 Discussion

An important observation has been that the initiation of metal dusting is dependent on the experimental set-up for a given set of conditions. In particular, significant carbon deposition and onset of metal dusting occurred within 100 h for the four alloys when exposed in contact with the ceramic holder, but, apart from some black staining, most of the alloys did not suffer any significant damage, even after 1000 h, when suspended from quartz hangers. The ceramic crucibles were found to be particularly active in catalysing carbon deposition on both the crucible holders and the samples, reducing the incubation time for the phenomenon to initiate. Analyses of the crucible material (by X-ray fluorescence, XRF) (Table 9.2) revealed a considerable amount of iron; this element is known to be an active catalyst for carbon deposition. The roles of iron and the other elements, such as potassium and sodium, in the ceramic matrix, were investigated and were reported in another paper [7].

The cast Alloy H46M was particularly susceptible to the effect of the holder since there was much graphite deposition on both the holder and the specimens close to the areas of contact with the holder, and dusting was



9.8 Alloy 693 after 1000h exposure, in the gaseous environment at 650°C while located in a ceramic holder: (a) optical micrograph, showing 5 rows of indents in the marked circle (b) hardness data calculated from the nano-indentation results as a function of distance, commencing 100 μm below the surface of the specimen.

significant in these locations. However, in other locations, directly exposed to the gas mixture, a protective silicon/chromium oxide scale was able to develop. For the other alloys, the effect of the holder was less obvious, since the specimens were damaged over larger areas, with less apparent influence from contact with the holder. However, the overall amount of carbon deposition and accompanying damage was significantly greater than for the corresponding specimens that were suspended from quartz hangers.

Analyses of the carbonaceous deposits and corrosion products from Alloys 600, 602CA, 693 and H46M, showed that their compositions were similar. Most analyses of the corrosion products showed the presence of chromium oxide, graphite and metal particles.

Elemental analyses of the reaction zones, immediately adjacent to the regions of surface damage, revealed chromium enrichment for Alloy 602CA, while, for Alloy H46M, there was an apparent depletion in chromium. Chromium oxide was detected in the corrosion products, but there was no evidence for chromium depletion in the area beneath the surface of Alloy 602CA. Moreover, Alloy 602CA is an alumina-forming alloy, and traces of aluminium oxide were detected on the surface of the specimens, while the reacted zones were found to be depleted in aluminium. Traces of aluminium oxide were found on the surfaces of Alloy 693 specimens, but there was no evidence for aluminium depletion in the areas beneath.

It is believed that formation of a self-healing oxide scale helps to protect against dusting attack. If the oxide scale is damaged, the resulting defects can offer preferential paths for catalysis of carbon deposit. The ability of aluminium and silicon to grow an adherent oxide film, underneath a chromium oxide scale, may provide a more effective barrier to carbon deposition, than a chromium oxide scale *per se* [8].

The behaviour of the samples suspended from the quartz hangers was markedly different. The incubation time to onset of dusting was much longer and the surfaces of the specimens were covered by localised carbon deposit, without evidence of embedded metal particles, apart from Alloy 600. The four alloys, previously tested in the ceramic crucible, showed a much higher resistance to the dusting environment. Examination of these alloys, and of the other five alloys exposed in the experiment involving the quartz hangers, in cross-section, after 1000h exposure, showed a homogeneous oxide layer on the surface. In this environment, and during all exposure times, the oxide scale was able to protect the samples from the dusting attack. It seems probable that the black stains observed would be the initiation points for the future onset of dusting attack, but no evidence for the passage from carbon deposition to attack of the metal was found, apart from Alloy 600 in the later stages of exposure. Work is being carried out to ascertain the evolution of the process.

Nano-indentation tests revealed a clear increase in the hardness of the reaction zones, compared with the bulk alloy. Possible internal diffusion of carbon and/or oxygen, may have given rise to microstructural changes, leading to an increase in hardness. In addition to any variations in the chemistry of the metal, the metal may have been hardened by such interstitial atoms. Examinations to date have not determined any internal carbides or oxides in these reaction zones; it is intended to carry out further examinations using various techniques, such as the transmission electron microscope, to ascertain whether or not any very fine precipitates are present.

9.5 Conclusions

It has been shown that the experimental set-up can affect the initiation of damage to alloys in a dusting environment. Here, the ceramic holders in which the specimens were located catalysed carbon deposition, accelerating the onset of carbon deposition and dusting of the alloys, compared with specimens that were suspended freely from quartz hangers in the same environment.

In the case of Alloy H46M, contact of the specimens with the ceramic holder was, particularly, a critical point for the onset and development of the phenomenon.

Alloys 602CA and 693 also showed onset of dusting damage in a relatively short period (100 h) when located in a ceramic holder, compared with when suspended freely from the quartz hangers, where very little damage has been observed after 100 h exposure; however, for these two alloys, there was less obvious effect of contact with the holder on the location of damage over the surfaces.

Alloy 600 showed considerable damage when located in a ceramic holder and even suffered observable damage when suspended freely from quartz hangers. Moreover, the morphologies of damage to Alloy 600 were similar for both cases.

9.6 Acknowledgements

The authors would like to thank EPSRC for funding the project, Special Metals Wiggin Ltd, Krupps VDM and Doncaster Parallooy for providing the alloys and Syntex for helpful assistance.

9.7 References

1. R. F. Hochman: *NACE Report Monograph*; 1973.
2. H. J. Grabke, R. Krajak, J. C. Nava Paz: *Corr. Sci.* **35**; 1141 1993.
3. H. J. Grabke: *Mat. and Corr.* **49**; 303 1998.
4. J. C. Nava Paz, H. J. Grabke: *Ox. Met.* **39**; n.5/6; 437 1993.
5. R. Kirchheiner, J. L. Jiménez Soler: *Conf. Proc.: Corrosion 2001*, paper 01374, NACE 2001.
6. D. C. Agarwal, U. Brill, J. Kloewer: *Conf. Proc.: Corrosion 2001*, paper 01382, NACE 2001.
7. F. Di Gabriele, F. H. Scott, Z. Liu: 'Effect of experimental conditions on the metal dusting phenomenon in several commercial nickel-base alloys'. *Materials and Corrosion*, **58**; n.2;81 2007.
8. B. A. Baker, G. D. Smith, V. W. Hartmann, L. E. Shoemaker, S. A. McCoy: *Conf. Proc.: Corrosion 2002*, paper 02394, NACE 2002.

Metal dusting of ferritic Fe–Al–M–C (M = Ti, V, Nb, Ta) alloys in CO–H₂–H₂O gas mixtures at 650°C

A SCHNEIDER and J ZHANG, Max-Planck-Institut für
Eisenforschung GmbH, Germany

10.1 Introduction

Alloys based on the iron aluminides Fe₃Al and FeAl are regarded as promising for high-temperature applications in the petrochemical industry because of their resistance to high-temperature oxidation and sulphidation [1, 2]. Only a little information is available about carburisation and metal dusting of Fe–Al alloys [1, 3].

Metal dusting is a high-temperature corrosion process which attacks iron, low- and high-alloy steels and Co- or Ni-based alloys in strongly carburising gas atmospheres with carbon activities $a_C \gg 1$ in the temperature range 400–1000 °C [4]. Metal dusting of iron and steels at various conditions such as temperature and carbon activity has been studied [5–16] using CO–H₂–H₂O and CH₄–H₂ gas mixtures.

The metal dusting of iron and low-alloyed steels during exposure to CO–H₂–H₂O mixtures with carbon activities $a_C > a_C(\text{Fe}/\text{Fe}_3\text{C})$ has been explained by the following reaction mechanism [5–9]: (i) rapid supersaturation of the metal phase with dissolved carbon by transfer from the gas phase, (ii) growth of a cementite layer at the surface, (iii) graphite deposition, (iv) subsequent cementite decomposition $\text{Fe}_3\text{C} \rightarrow 3 \text{Fe} + \text{C}$ into graphite and fine metal particles, which (v) act as catalysts for coke deposition. Catalytic coke deposition can be observed in thermogravimetric experiments by a drastic acceleration of the mass gain kinetics. Transmission electron microscopy (TEM) investigations of the decomposition product on carburised iron samples revealed a coke layer on the cementite surface which consists of graphite and finely dispersed iron particles [9] or carbide particles [12, 16].

The concept of protective oxide layers was tested for the case of chromia-forming alloys [17–19]. Chromium-containing alloys generally show resistance against metal dusting at surface areas covered with chromium oxide. Local metal dusting was observed at defects of the chromia layers.

Alumina formers, such as Fe–Al alloys are most promising for application in the petrochemical industry with environments with very low oxygen partial

pressures owing to the possibility of formation of a stable protective alumina scale. First experiments on the metal dusting behaviour of Fe_3Al were performed by Grabke and coworkers [3]. The constitution of the Fe-Al-C was investigated by Palm and Inden [20]. A ternary carbide Fe_3AlC_x (ϵ -phase) exists in this system which might play an important role as suggested by Grabke and coworkers [3], but his first experiments on metal dusting of Fe_3Al revealed only the presence of cementite after carburisation. The mechanisms of metal dusting of iron aluminium alloys are still not understood. The susceptibility of Fe-Al-Cr alloys for metal dusting was investigated by Klöwer [1]. The results showed that these alloys are very resistant against corrosive attack in $\text{CH}_4\text{-H}_2$ gas mixtures at 850, 1000 and 1100 °C.

Fundamental studies on iron aluminium alloys have started to study the effects of strengthening precipitates for clarifying the possibilities and prospects of respective alloy developments for high-temperature application. Since iron aluminium alloys are possible high-temperature materials for application in the petrochemical industry, in this work metal dusting is tested for such alloys. The alloys Fe-15Al-2M-1C ($\text{M} = \text{Ti, V, Nb or Ta}$) (compositions are given in at.%) have been selected to produce microstructures with strengthening carbides and Laves phase [21].

10.2 Experimental procedure

The Fe-15Al and Fe-15Al-2M-1C ($\text{M} = \text{Ti, V, Nb, Ta}$) alloys were processed by vacuum induction melting. The melts were cast into cylindrical copper moulds (32 mm in diameter by 186 mm in length). The as-cast alloys were then cut by spark-erosion to obtain disks with $d = 1$ mm in thickness. Quarter segments of the disks were used for the metal dusting experiments. Before starting the experiment the samples were annealed at 850 °C for 1 h in a pure hydrogen atmosphere and then ground (1000 grit). Thermogravimetric analysis (TGA) was carried out by measuring the mass gain using a microbalance with an accuracy of 1 μg . The samples were fixed at the mass balance by quartz filaments. At the end of the treatment the quartz filaments holding the sample were broken so that the sample fell on a quartz plate in the cold region of the TGA apparatus.

Gas mixtures of $\text{CO-H}_2\text{-H}_2\text{O}$ were used for the metal dusting treatment. The carbon activity of the $\text{CO-H}_2\text{-H}_2\text{O}$ gas mixture was calculated according to Grabke *et al.* [22]. The water vapour pressure was established by passing H_2 through a mixture of oxalic acid and its dihydrate at a certain temperature [23]. The gas velocities were controlled by capillary flow meters. The flow rate of the gas mixtures was fixed at 2 ml/s and the total pressure of the gas mixture was 1 bar. The diameter of the reaction tube was 27 mm.

The phases on the carburised samples were determined by X-ray diffraction

(XRD) using Cr-K radiation. The carburised samples were coated with nickel and then analysed by means of metallographic cross-sections.

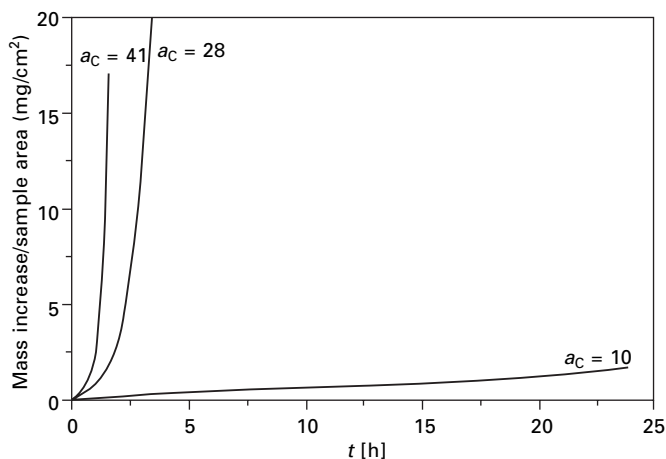
Surface analysis of the carburised samples was performed by conventional scanning electron microscopy (SEM). In order to identify small precipitates, additional EBSD (electron backscattered diffraction) measurements were performed using a high-resolution SEM (FEG-SEM JEOL JSM 6500).

10.3 Thermodynamic calculations

Thermodynamic calculations were performed using the software ThermoCalc [24] with the SGTE SSOL database [25]. The γ -phase Fe_3AlC_x was introduced separately as a line compound with an average fixed composition $\text{Fe}_3\text{AlC}_{0.565}$ according to Kumar and Raghavan [26]. In the calculations, the carbides, Laves phase and ferrite were considered to be possible components in the phase equilibria of the alloys. For the Ta-containing system it is not possible to perform the calculations, because there is no thermodynamic description of TaC available in the SSOL database. Graphite formation was not considered in the calculations.

10.4 Results

The TGA results in Fig. 10.1 represent the mass gain kinetics of the carburisation of binary Fe–15Al samples in $\text{CO-H}_2\text{-H}_2\text{O}$ gas mixtures at 650°C with carbon activities $a_C = 10, 28$ and 41 . It should be noted that the mass gain in metal dusting experiments of Fe–Al–based alloys in $\text{CO-H}_2\text{-H}_2\text{O}$ mixtures can be attributed to different processes: (i) the alumina formation at the surface, (ii) the carburisation, i.e. transfer of carbon in solid solution, (iii) the growth of carbides, and (iv) coke deposition, causing increasing mass gain rates and indicating the start of metal dusting. Figure 10.1 shows that with increasing thermodynamic driving force (carbon activity) for carbon deposition, the onset of metal dusting is shifted to a shorter time indicated by the change in curvature to an almost quadratic mass gain kinetics. The metallographic cross-section of the sample carburised at $a_C = 28$ at 650°C for 4 h is shown in Fig. 10.2(a). The coarsely serrated matrix/coke interface clearly reveals general metal wastage. Corresponding surface observation by SEM shows filamentous carbon with bright metal containing particles (Fig. 10.2(b)). The cross-section of this sample (coke layer close to the matrix/coke interface) was further analysed by SEM. Figure 10.3(a) shows that the metal-containing particles are not homogeneously distributed in the coke. These particles and their distribution are more clearly seen in the back-scattered, electron (BSE) image in Fig. 10.3(b). In order to identify the constituents of the coke, additional elemental energy dispersive X-ray (EDX) mapping was performed for iron, aluminium, carbon and oxygen (Figs 10.3(c-f)). The bright spots

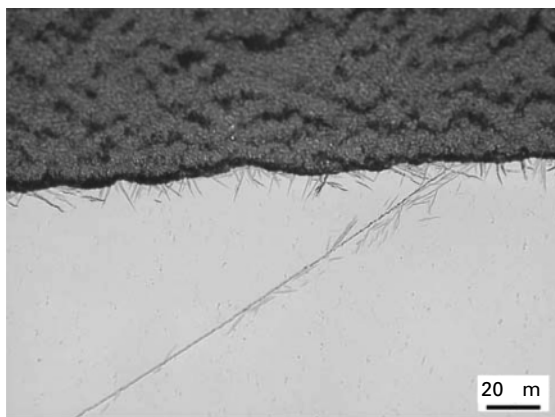


10.1 TGA of Fe-15Al samples carburised in CO-H₂-H₂O mixtures at $a_C = 10, 28$ and 41 at 650°C.

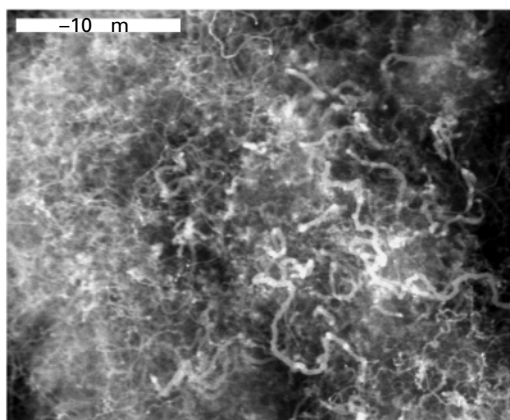
shown in the BSE image in Fig. 10.3(b) represent iron containing particles as can be seen in Fig. 10.3(c). The areas that contain iron are deficient in carbon (see Fig. 10.3(e)). The aluminium distribution does not correlate with the positions of the iron-containing particles, as can be seen by comparing Figs 10.3(c) and (d). Oxygen can be found over the entire coke area with the exception of the iron-containing areas (Fig. 10.3(f)). The presence of cementite together with graphite was detected by XRD analysis of the carburised Fe-15Al sample (see Fig. 10.4). XRD analysis of the coke after removal from the sample yields the same result. Thus, cementite and not iron is proved to be the iron-containing phase present in the coke. Aluminium oxide was not detected by XRD analysis.

SEM of the carburised Fe-15Al alloy shows oriented plate- or needle-shaped Fe₃AlC_x carbides at grain boundaries and at the sample surface (Figs 10.5(a) and (b)). The phase identification was performed by means of EBSD. It is oriented growth of Fe₃AlC_x in the Fe(Al) matrix. A finely structured layer between matrix and coke is observed by SEM. Owing to the small size of the layer and difficulties in sample preparation it was not possible to identify this layer with respect to crystal structure and chemical composition with the techniques available.

In the following the metal dusting experiments were performed at carbon activity $a_C = 28$, where a considerable attack can be expected. The influence of the alloying elements in the Fe-15Al-2M-1C (M = Ti, V, Nb or Ta) on metal dusting was also tested. A characterisation of the as-cast microstructures of these samples is given in Schneider *et al.* [21]. A common feature of all alloys is the presence of MC carbides with different morphologies. Thermogravimetric analysis of samples carburised at 650°C and at $a_C = 28$



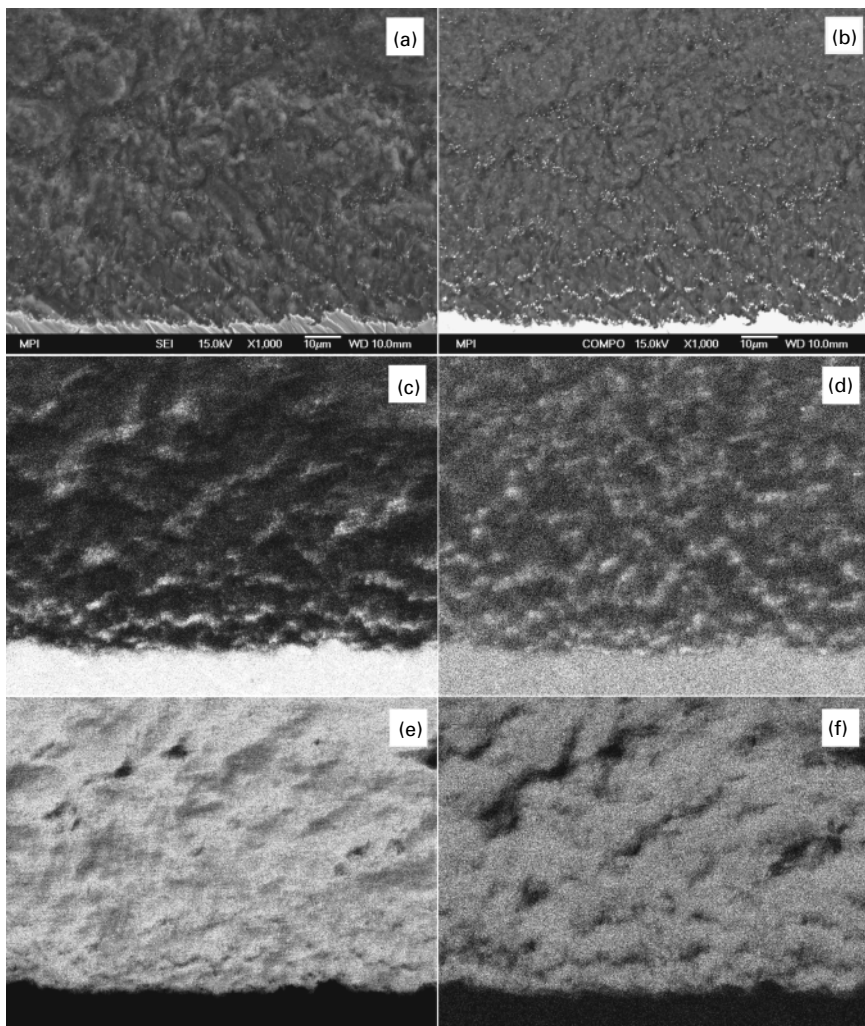
(a)



(b)

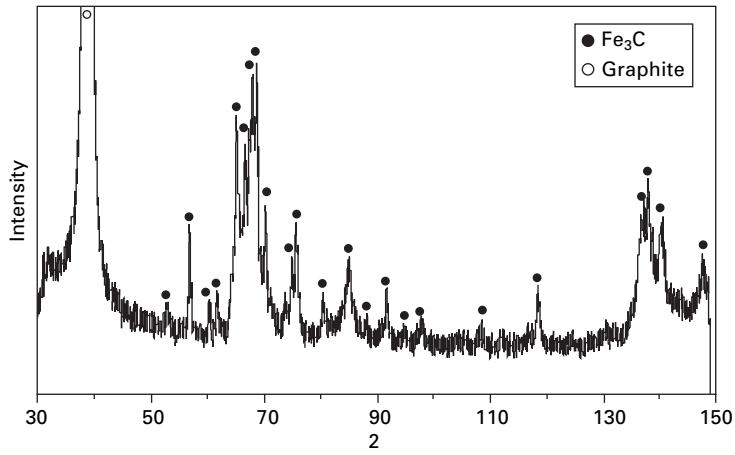
10.2 (a) Metallographic cross-section and (b) SEM surface observation of a Fe–15Al sample carburised at $a_C = 28$ at 650°C for 4 h.

shows decreasing mass gain kinetics with the alloying elements Nb, Ta, V and Ti in combination with C (Fig. 10.6). The main effect of the alloying elements is a shift of the onset of metal dusting to longer times. In the case of Fe–15Al–2Ti–1C occurrence of metal dusting can not be detected using TGA. Figure 10.7 shows typical cross section micrographs of the alloyed samples after carburisation. The alloys Fe–15Al–2Nb–1C and Fe–15Al–2Ta–1C (Figs 10.7(a) and (b)) show local pitting and coke growth. For both alloys precipitates with needle- or plate-like appearance are observed in the matrix close to the decomposition interface. Their morphology is comparable to that of the γ -phase detected in the carburised Fe–15Al sample. EDX analysis of a Fe–15Al–2Ta–1C sample carburised at 650°C and at $a_C = 28$

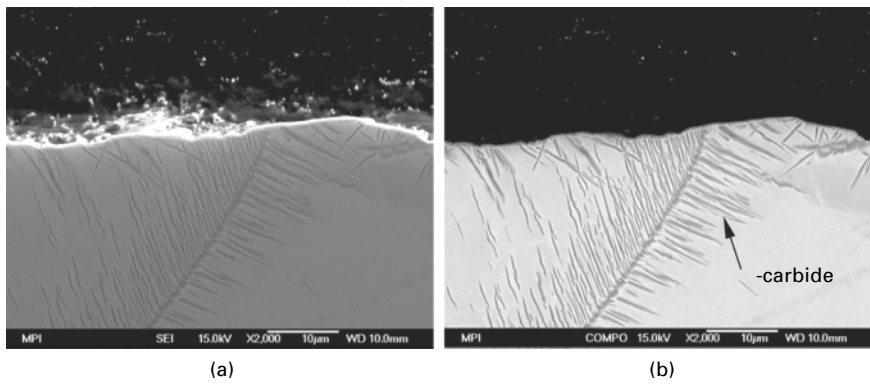


10.3 SEM images in the (a) SE and (b) BSE mode and EDX element mappings ((c) iron, (d) aluminium, (e) carbon, and (f) oxygen) of the coke of a Fe-15Al sample carburised at $a_c = 28$ at 650°C for 4 h (cross-section).

for 50h reveals white Ta and C-rich carbides present in the whole sample and grey needle- or plate-like carbides mainly containing Fe, Al and C present close to the decomposition interface (see BSE images in Figs 10.8(a) and (b)). For the alloys Fe-15Al-2V-1C and Fe-15Al-2Ti-1C almost no metal dusting attack is observed by light optical microscopy (LOM) (see Figs 10.7(c) and (d)). Only some graphite deposition can be seen on top of the flat surface.



10.4 XRD spectrum of a Fe–15Al sample carburised at $a_c = 28$ at 650°C for 4h.

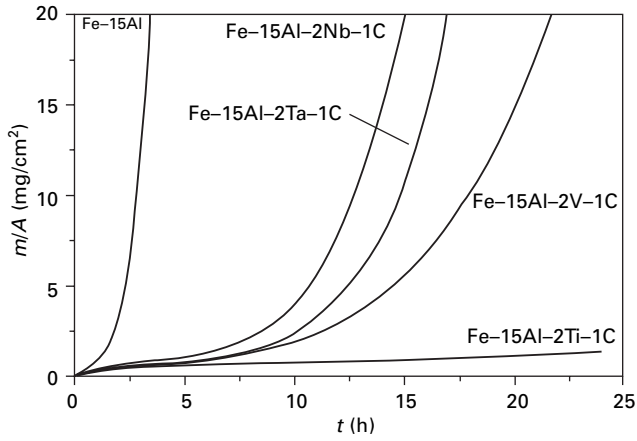


10.5 SEM image in the (a) SE and (b) BSE mode of a Fe–15Al sample carburised at $a_c = 28$ at 650°C for 4h (cross-section).

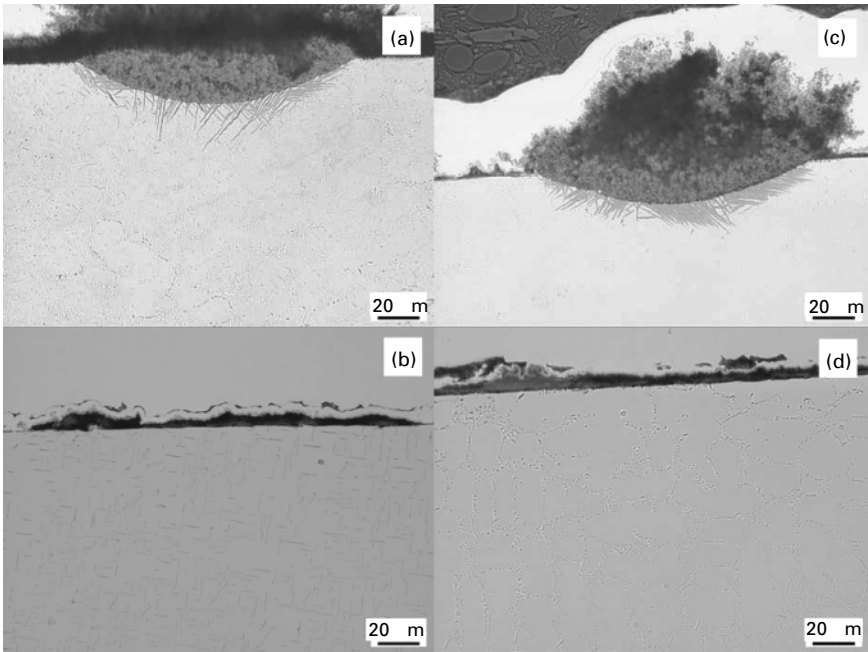
SEM analysis of the surfaces of the carburised alloys was performed to determine the coke morphology. Mainly fine carbon filaments were detected. Some parts of the sample surface are covered with bulk graphite with metal containing particles with diameters below 1 μm (see SE images of the carburised samples Fe–15Al–2Nb–1C and Fe–15Al–2Ti–1C in Figs 10.9(a) and (c) and BSE images in Figs 10.9(b) and (d)).

10.5 Discussion

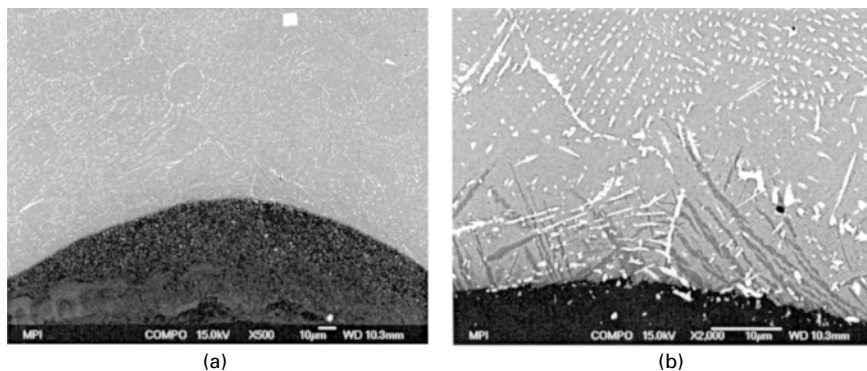
During carburisation of iron aluminium alloys in CO–H₂–H₂O gas mixtures the formation of carbides, graphite and also aluminium oxide can be expected.



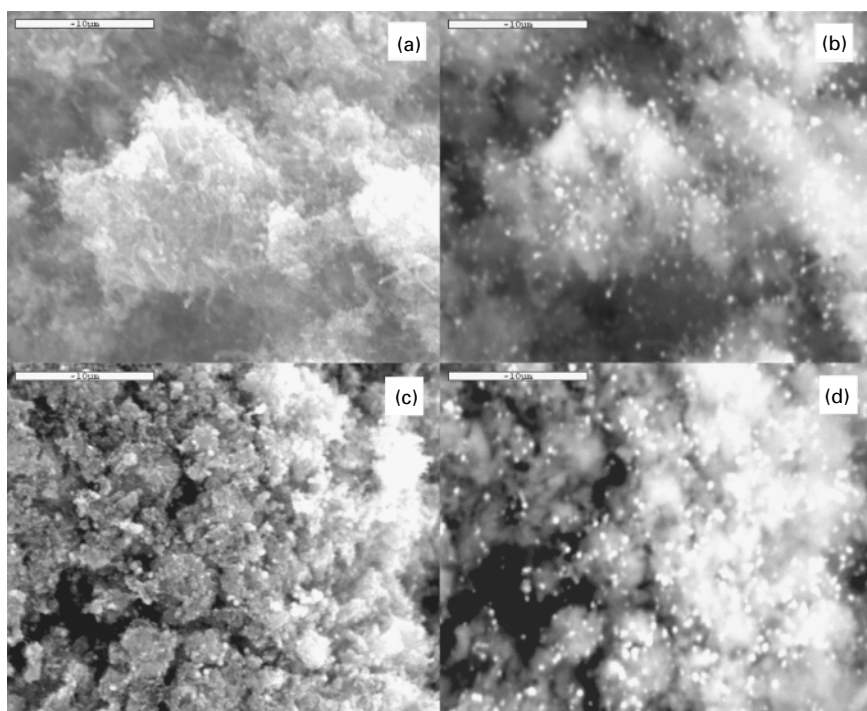
10.6 TGA of Fe-15Al-2M-1C (M = Ti, V, Nb or Ta) samples carburised at 650°C and at $a_C = 28$.



10.7 Metallographic cross-section of Fe-15Al-2M-1C samples carburised at 650°C and at $a_C = 28$ ((a) M = Nb, $t = 19.3$ h; (b) M = Ta, $t = 24$ h; (c) M = V, $t = 23.5$ h; (d) M = Ti, $t = 24$ h).



10.8 SEM image in the BSE mode of a Fe–15Al–Ta–1C sample carburised at $a_C = 28$ at 650 °C for 50 h (cross-section).

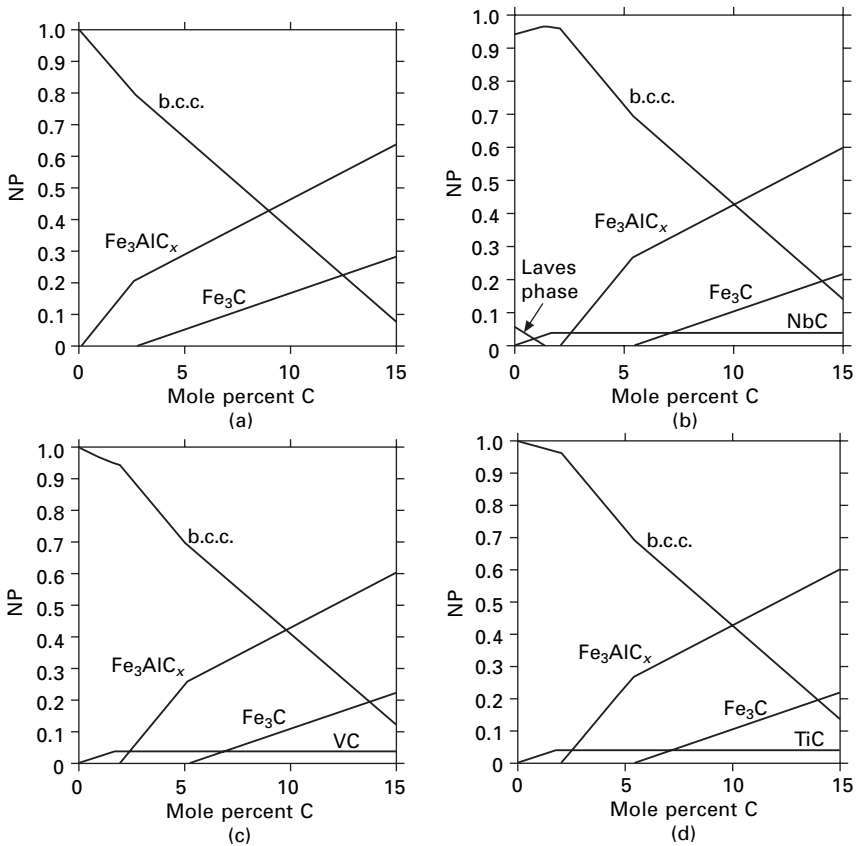


10.9 SEM surface observation of the coke of a Fe–15Al–2Nb–1C sample ((a) SE and (b) BSE mode) and of a Fe–15Al2Ti–1C sample ((c) SE and (d) BSE mode).

In this study the alloys were not pre-oxidised to form a protective alumina layer. The presence of alumina was not detected but its formation can be assumed. A partial coverage with a protective layer can be assumed for the

Fe–15Al–2M–1C alloys with $M = \text{Ti, V, Nb, Ta}$, especially in the case of Ti and V (see Fig. 10.7), because no or only local metal dusting attack is observed.

If there are significant defects carburisation will take place, resulting in a carbon profile with decreasing carbon content from the surface to the matrix. Thermodynamic calculations using the software Thermo-Calc with the SGTE SSOL database were performed to determine the phases in relation to carbon content. According to the results shown in Fig. 10.10(a) it is expected that for a binary Fe–15Al alloy at the very beginning of the carburisation reaction, i.e. for low carbon contents, a two-phase equilibrium of Fe(Al, C) and γ -phase Fe_3AlC_x will form at the near-surface region. With increasing time and therefore with increasing carbon content at the surface additional cementite



10.10 Calculated phase fractions in relation to carbon content of the alloys (a) Fe–15Al–xC, (b) Fe–15Al–2Nb–xC, (c) Fe–15Al–2V–xC, and (d) Fe–15Al–2Ti–xC with constant contents of aluminium and $M = \text{Ti, V, Nb}$ (15 wt% Al, 2 wt% M) at 650°C.

formation can be expected. It is shown by XRD and EBSD of the Fe–15Al sample that after carburisation the ϵ -phase and also cementite are present. Cementite is detected to be present in the coke which is followed by an unidentified layer (see Fig. 10.5) and then by the matrix with plate- or needle-like Fe_3AlC_x precipitates (Figs 10.2(a), and 10.5(a), and (b)). Therefore the proposed sequence of precipitates as predicted by the thermodynamic calculation (Fig. 10.10(a)) is proved. Since graphite formation is not considered in the thermodynamic calculations the metastable cementite appears at high carbon contents. The experimental observation of cementite present in the coke leads to the assumption that there are similarities between metal dusting of iron and of iron aluminium. As can be derived from the presence of Al and O in the coke (see Figs 10.3(d) and (f)), aluminium oxide is detached from the alloy surface during metal dusting.

For the Fe–15Al–2M–1C (M = Ti, V or Nb) alloys generally the same situation can be expected as can be seen in the diagrams in Figs 10.10(b–d) showing phase fractions versus carbon content. Metal dusting is not completely inhibited by alloying Fe–15Al with M = Ti, V, Nb or Ta and C. Even for Fe–15Al–2Ti–1C with a slow carbon mass gain (see TGA result in Fig. 10.6) and flat surface without pitting or serration metal wastage is detected by BSE analysis as shown in Fig. 10.9(d). Therefore it seems to be reasonable to start testing of pre-treatment of iron aluminium alloys to form a protective layer without defects.

10.6 Conclusions

Metal dusting experiments with Fe–15Al and Fe–15Al–2M–1C alloys (in at.%) with M = Ti, V, Nb or Ta were conducted at 650°C in $\text{CO-H}_2\text{-H}_2\text{O}$ gas mixtures with the carbon activity $a_C = 28$. TGA shows decreasing mass gain kinetics with the alloying elements Nb, Ta, V and Ti in combination with C. SEM analysis of the surfaces of the carburised alloys was performed to determine the coke morphology. Mainly fine carbon filaments with iron-containing particles were detected. A formation sequence of the ϵ -phase Fe_3AlC_x and subsequent cementite is predicted by Thermo-Calc calculations and proved experimentally. The role of the carbides in the decomposition process is still unknown.

10.7 Acknowledgements

The authors would like to thank Prof. Dr G. Inden and Prof. Dr G. Frommeyer for their support of this work and for helpful discussions. The authors are grateful to Dr S. Zaefferer for the EBSD measurements and helpful discussions. The authors would also like to thank Mrs K. Angenendt and M. Nellesen for SEM analysis and Mrs H. Falkenberg for preparing the metallographic cross-

sections. Support of this work by the Deutsche Forschungsgemeinschaft is gratefully acknowledged.

10.8 References

1. J. Klöwer: High temperature corrosion behaviour of iron aluminides and iron aluminium-chromium alloys, in: H. J. Grabke and M. Schütze (Eds), *Oxidation of intermetallics*, Wiley-VCH, Weinheim (1997), 203.
2. F. H. Stott, K. T. Chuah, L. B. Bradley: Oxidation-sulphidation of iron aluminides, in: H. J. Grabke and M. Schütze (Eds), *Oxidation of intermetallics*, Wiley-VCH, Weinheim (1997), 221.
3. S. Strau , R. Krajak, M. Palm, H. J. Grabke: *Mater. Corros.* **47** (1996) 701.
4. H. J. Grabke: Mechanisms of carburisation, metal dusting and coking – ways and means for protection, in: E. Bardal (Ed.), *Proceedings of Eurocorr '97*, Vol. II, European Federation of Corrosion, Trondheim, 1997 pp. 1–8.
5. H. J. Grabke, R. Krajak, J. C. Nava Paz: *Corros. Sci.* **35** (1993) 1141.
6. J. C. Nava Paz, H. J. Grabke: *Oxid. Met.* **39** (1993) 437.
7. H. J. Grabke, R. Krajak: *Härterei-Tech. Mitt.* **49** (1994) 150.
8. H. J. Grabke: *Solid State Phen.* **41** (1995) 3.
9. E. Pippel, J. Woltersdorf, H. J. Grabke, S. Strau : *Steel Res.* **66** (1995) 217.
10. H. J. Grabke: *Mater. Corros.* **49** (1998) 303.
11. H. J. Grabke, E. M. Müller-Lorenz, A. Schneider: *ISIJ Int.* **41** (Suppl. S1) (2001).
12. A. Schneider, G. Inden, H. J. Grabke, Q. Wei, E. Pippel, J. Woltersdorf: *Steel Res.* **71** (2000) 179.
13. A. Schneider, H. Viefhaus, G. Inden: *Mater. Corros.* **51** (2000) 338.
14. A. Schneider: *Corros. Sci.* **44** (2002) 2353.
15. J. Zhang, A. Schneider, G. Inden: *Corros. Sci.* **45** (2003) 283.
16. J. Zhang, A. Schneider, G. Inden: *Corros. Sci.* **45** (2003) 1329.
17. H. J. Grabke, E. M. Müller-Lorenz, B. Eltester, M. Lucas, D. Monceau: *Steel Res.* **68** (1997) 179.
18. T. A. Ramanarayanan, R. A. Petkovic, J. D. Mumford, A. Ozekcin: *Mater. Corros.* **49** (1998) 226.
19. B. Ganser, K. A. Wynns, A. Kurlekar: *Mater. Corros.* **50** (1999) 700.
20. M. Palm, G. Inden: *Intermetallics* **3** (1995) 443.
21. A. Schneider, L. Falat, G. Sauthoff, G. Frommeyer: *Intermetallics*, in press.
22. H. J. Grabke, D. Grassl, H. Schachinger, K. H. Weisssohn, J. Wünnig, U. Wyss: *Härterei-Tech. Mitt.* **49** (1994) 306.
23. G. P. Baxter, J. E. Lansing: *J. Amer. Chem. Soc.* **42** (1920) 419.
24. B. Jansson, M. Schalin, B. Sundman: *J. Phase Equilibria* **14** (1993) 557.
25. Thermo-Calc SSOL (Solid Solution Data Base) Foundation of Computational Thermodynamics, Royal Institute of Technology – Stockholm, Sweden.
26. K. C. H. Kumar, V. Raghavan: *J. Phase Equilibria* **12** (1991) 275.

-Fe layer formation during metal dusting of iron in CO–H₂–H₂O gas mixtures

J ZHANG, A SCHNEIDER and G INDEN,
Max-Planck-Institut für Eisenforschung GmbH, Germany

11.1 Introduction

The catastrophic carburisation process, metal dusting, attacks iron, low- and high-alloy steels, and Co or Ni-based alloys in strongly carburising gas atmospheres with carbon activity $a_C > 1$ at elevated temperatures. The processes and mechanisms of metal dusting have been studied over decades, and substantial, but not complete, understanding has been achieved. A general mechanism [1–6] proposed for iron-based alloys involves a supersaturation of iron with carbon and subsequent growth of a cementite layer at the surface which acts as a barrier for further carbon transfer. Consequently, graphite is deposited on the cementite surface, lowering the carbon activity to one in the Fe₃C/graphite interface and initiating cementite decomposition. The particles formed during the decomposition process then strongly catalyse further carbon deposition causing a vast growth of the reaction product ‘coke’.

The formation of iron carbide and its decomposition have been reported extensively in metal dusting of iron and in cementite production in the iron-making process [1–8]. It was found that the rates of cementite formation and its decomposition depend on the composition of the reaction gases and on temperature [6–8]. Recently the formation of iron particles or even an iron layer between cementite and graphite was observed on iron at 700 °C in H₂–CO–H₂O gas mixtures [9, 10]. It was proved that the iron at the cementite/graphite interface is a reaction product from cementite decomposition [9].

In this report, the process of iron layer formation already reported in [9, 10] is further studied with emphasis on the effect of gas composition and temperature. The experiments were performed at both 600 and 700 °C in H₂–CO–H₂O gas mixtures. The results provide new information for the understanding of the phenomenon of iron layer formation during cementite decomposition and of the mechanism of metal dusting as well.

11.2 Experimental procedure

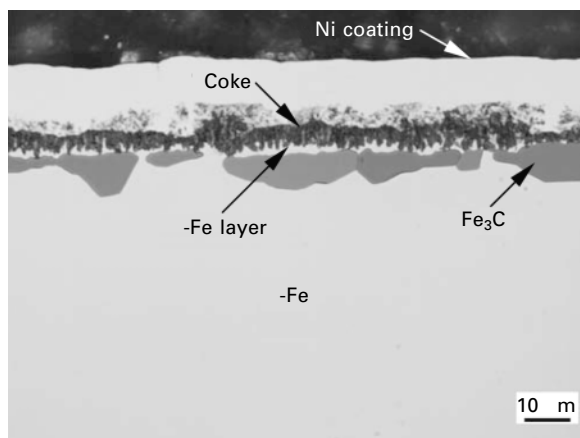
Pure iron samples (discs of 20 mm in diameter and 1.1 mm in thickness) were used for all metal dusting experiments. At first, samples were annealed at 850 °C for 1 h in a pure H₂ gas atmosphere, and then ground on SiC paper to 1000 grade. Afterwards, a sample was hung on a microbalance (Sartorius 7287 with an accuracy of 1 µg) by silica hooks. Helium gas was introduced into the chamber of the microbalance in order to protect the balance. The reaction gases were composed of H₂, CO and H₂O. The H₂O content was established by passing H₂ through a mixture of oxalic acid and its dihydrate at a certain temperature [11] and fixed at 0.2 vol.% for all experiments. At first the sample was heated in pure hydrogen. After reaching a stable temperature, the reaction gases were introduced into the reaction tube. The gas compositions were controlled by capillary flow meters. The gas flow rate was fixed at 2 ml/s. The weight change of the sample during the reaction was recorded continuously.

After reaction, the quartz filament holding the sample was broken to let the sample drop down into the cold zone for quenching. The surface of the sample was analysed by scanning electron microscopy (SEM). Then the specimens were cut to obtain cross-sections for optical microscopy. In order not to alter the surface by preparation the samples were coated with nickel and then mounted in epoxy resin. Mounted samples were polished and etched by hot solution of alkaline sodium picrate for optical microscope observation. In order to detect the phases present in the dust, the coke layer was carefully removed from the surface and analysed by X-ray diffraction (XRD). XRD analysis was performed using monochromatic Co radiation.

11.3 Results

11.3.1 Influence of gas composition on γ -Fe layer formation at 700 °C

The formation of an γ -Fe layer at the cementite/graphite interface was observed at first during metal dusting of iron in CO–H₂–H₂O gas mixtures at 700 °C with low CO contents. Figure 11.1 shows the metallographic cross-section of an iron sample carburised in a gas mixture with 3 vol.% CO for 5 h at 700 °C. This micrograph clearly reveals that an iron layer has formed between cementite and graphite. Figure 11.1 also shows that the interface between graphite and the iron layer is highly serrated. Iron layer formation is also observed in a gas mixture with 5 vol.% CO. The cross-sections of samples in different stages of carburisation in this atmosphere are shown in Fig. 11.2. After 1 h reaction, cementite is found at the surface covered by a thin layer of graphite (Fig. 11.2a). After 3 h reaction, iron particles are observed at the



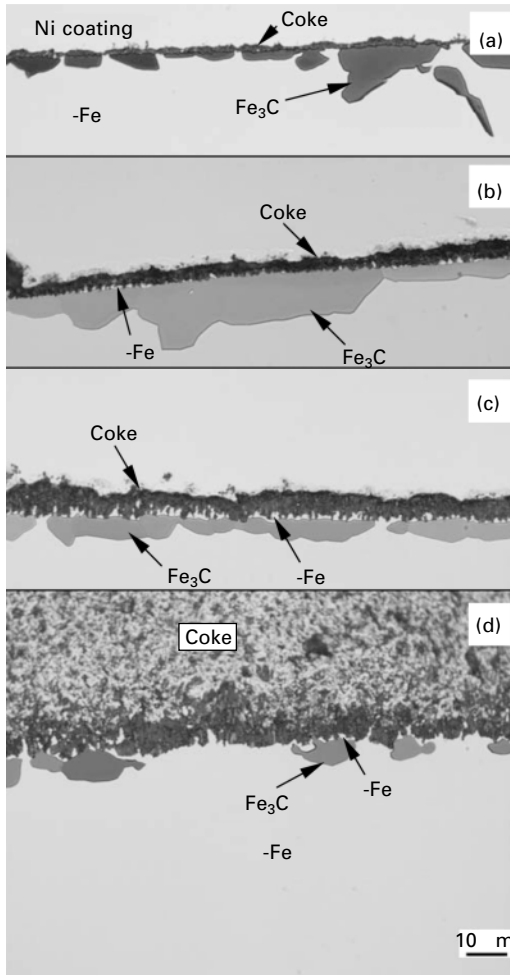
11.1 Metallographic cross-section of the iron sample carburised in the gas mixture of 3%CO–96.8% H_2 –0.2% H_2O at 700 °C for 5 h.

interface between cementite and graphite (Fig. 11.2b). With increasing reaction time to 5 h the amount of iron increases and forms a layer between cementite and graphite (Fig. 11.2c). Increasing the reaction time to 20 h results in the formation of a very thick coke layer (Fig. 11.2d). In this case, some cementite has disappeared (Fig. 11.2d).

With increasing CO content in the CO– H_2 – H_2O gas mixture, the tendency of iron particle/layer formation decreased. Figure 11.3 shows the metallographic cross-sections of samples carburised in the gas mixtures with different CO contents. With 20 vol.% CO only a small amount of iron particles is found in the interface (Fig. 11.3c). After increasing the CO content to more than 50 vol.% no iron is detected in the interface by optical microscopy (Fig. 11.3d).

The surface layers of samples after carburisation in the gas mixture with 5 vol.% CO have been analysed by SEM. Figure 11.4 shows the top-view of the graphite layers of the samples after 2 h and 18 h carburisation. After 2 h reaction, both filaments and graphite particle clusters are observed (Fig. 11.4a). The backscattered electron image shows many metallic particles embedded inside of the graphite particle clusters (Fig. 11.4b). Energy dispersive X-ray (EDX) analysis shows that these metallic particles are iron-containing phases. After 18 h reaction, only thick graphite particle clusters are observed on the surface (Fig. 11.4c). The backscattered electron image also shows some metallic particles inside (Fig. 11.4d).

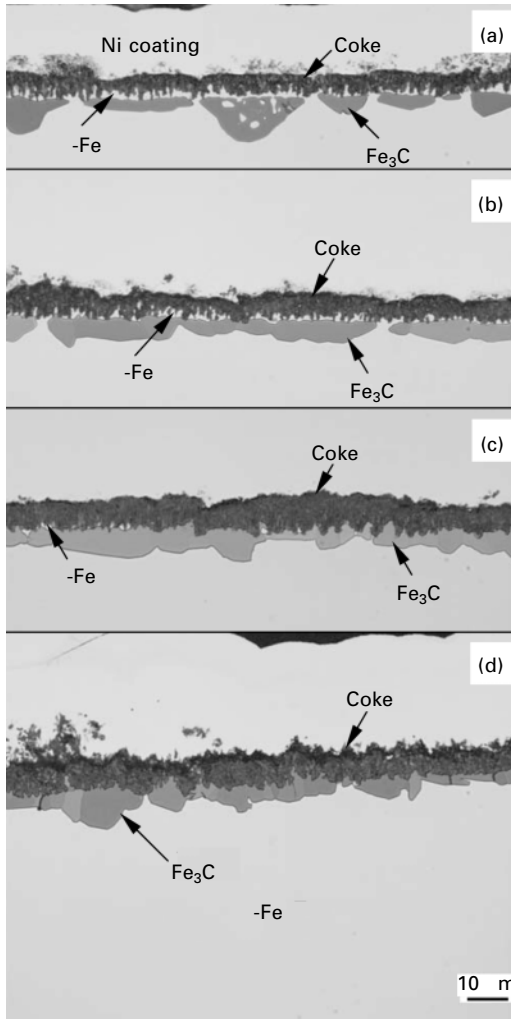
The coke of the sample carburised for 16.5 h in a gas mixture with 5 vol.% CO was analysed by XRD. The XRD analysis shows the presence of both iron and cementite in the coke (Fig. 11.5).



11.2 Metallographic cross-sections of iron samples carburised in the gas mixture of 5%CO–94.8% H_2 –0.2% H_2O at 700°C for (a) 1 h; (b) 3 h; (c) 5 h; and (d) 20 h.

11.3.2 Influence of gas composition on γ -Fe layer formation at 600°C

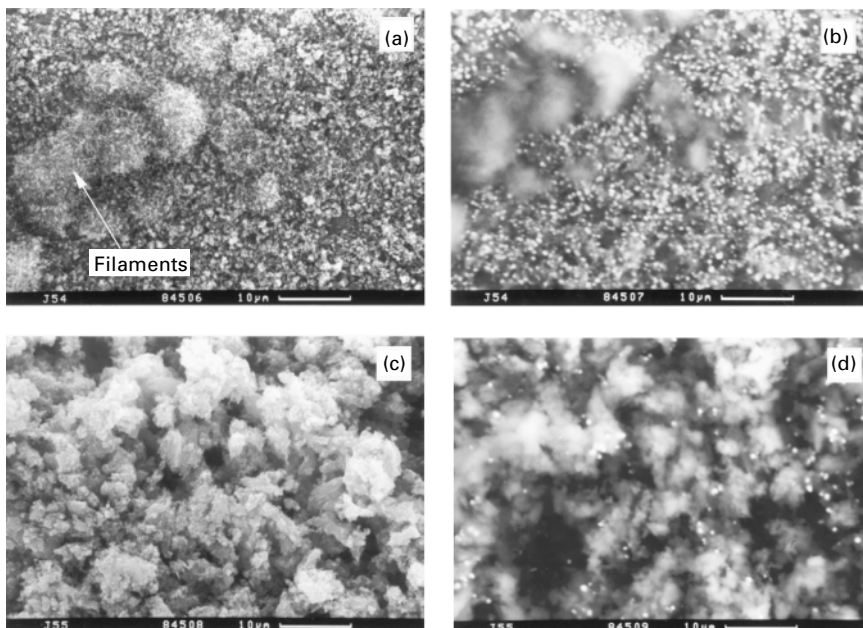
The formation of an γ -Fe layer between cementite and graphite was also observed during metal dusting of iron at 600°C but for the gas with much lower CO contents, e.g. 1 vol.% CO. Metallographic cross-sections of specimens after different stages of carburisation with 1 vol.% CO are shown in Fig. 11.6. After 4.5 h reaction, cementite was formed and graphite was deposited on its surface (Fig. 11.6a). Some iron particles are also detected between cementite and graphite (Fig. 11.6a). As the reaction time was increased



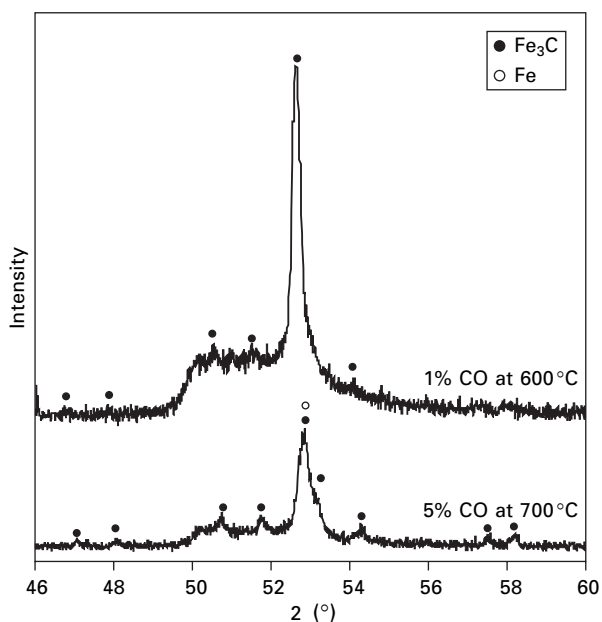
11.3 Metallographic cross-sections of iron samples carburised at 700°C for 5 h for (a)–(c), and 4 h for (d) in CO–H₂–H₂O gas mixtures (H₂O fixed at 0.2%) with the CO contents of (a) 3%; (b) 5%; (c) 20%; and (d) 50%.

to 9 h the thickness of graphite and also the amount of iron between cementite and graphite increased (Fig. 11.6b). After 21.5 h reaction, however, cementite is completely dissolved (Fig. 11.6c).

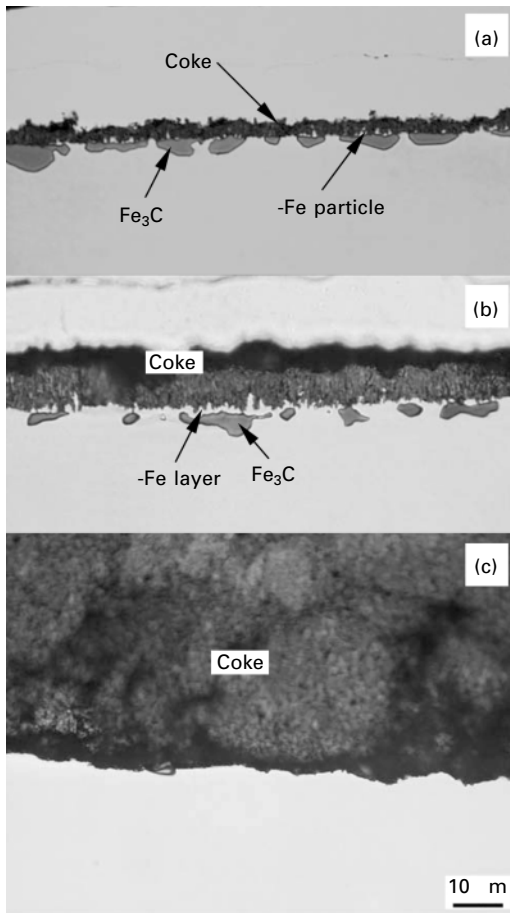
Iron layer formation does not occur at CO concentrations ≥ 5 vol.%. The metallographic cross-sections of samples after carburisation in gas mixtures with 5 vol.% and 30 vol.% CO show a thin layer of cementite and a thick graphite layer on the top but no iron particles or iron layer between them (Fig. 11.7b–c).



11.4 Surface graphite morphologies of iron samples carburised in the gas mixture of 5%CO–94.8% H_2 –0.2% H_2O at 700 °C for (a)–(b): 2 h and (c)–(d): 18 h. (b) and (d) are back-scatter electron images of (a) and (c), respectively.

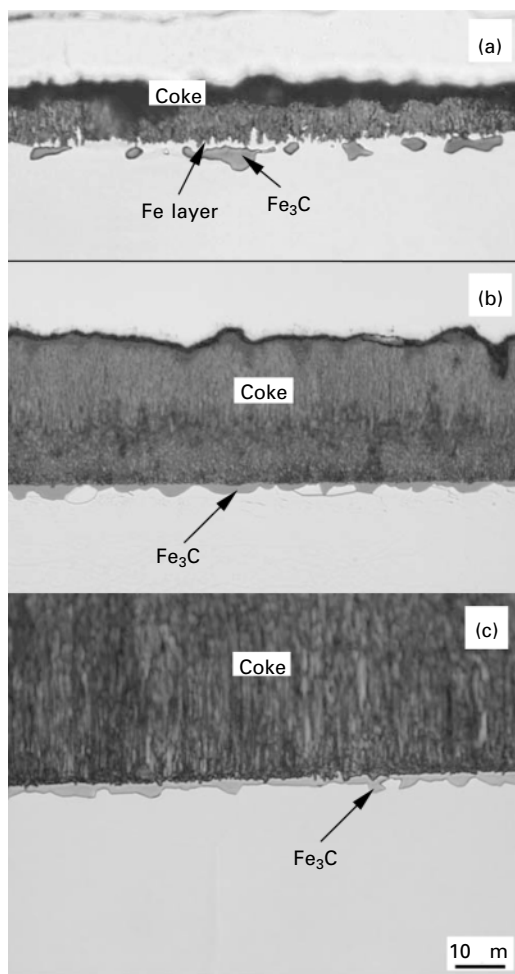


11.5 XRD spectra of the coke obtained from iron samples carburised in CO– H_2 – H_2O gas mixtures (H_2O fixed at 0.2%) with 1% CO at 600 °C for 21.5 h and with 5% CO at 700 °C for 16.5 h.



11.6 Metallographic cross-sections of iron samples carburised in the gas mixture of 1%CO–98.8%H₂–0.2%H₂O at 600°C for (a) 4.5 h; (b) 9 h; and (c) 21.5 h.

Figure 11.8 shows the morphologies of graphite on top of the sample surfaces after 21.5 h carburisation with 1 vol.% CO. Figure 11.8a shows a structure of filaments (diameter about 30 nm) densely located on the top of a columnar bulk graphite. Figure 11.8b represents a high magnification of these filaments with a diameter about 30 nm. In addition to this filamentous carbon, another kind of graphite was also found as shown in Fig. 11.9. Its morphology in the low-magnification image is similar to a coral structure as shown in Fig. 11.9a. The corresponding high-magnification image in Fig. 11.9c shows a structure with graphite particle clusters. The corresponding backscattered electron images show small metallic particles embedded inside these graphite particles (Figs. 11.9b, d).

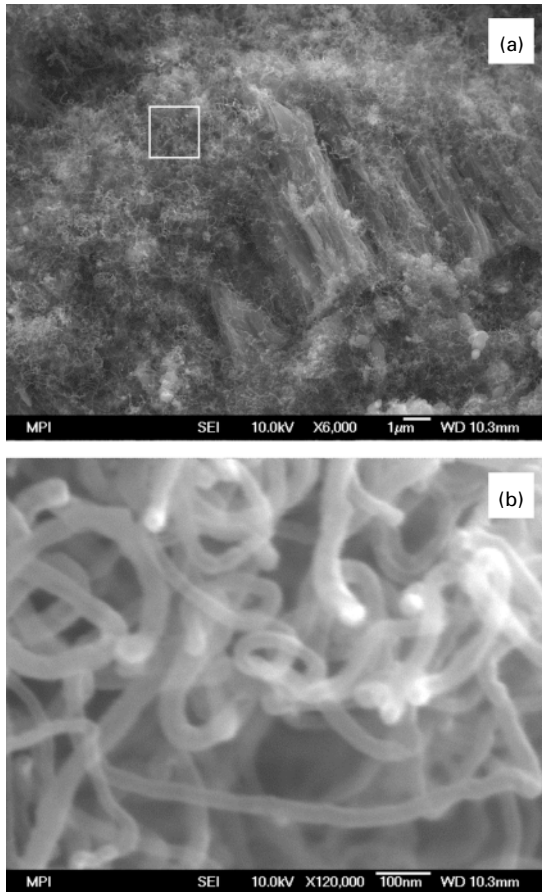


11.7 Metallographic cross-sections of iron samples carburised at 600 °C in CO-H₂-H₂O gas mixtures (H₂O fixed at 0.2%) with (a) 1% CO for 9 h; (b) 5% CO for 5 h; and (c) 30% CO for 4 h.

The coke of this sample was also analysed by XRD. The XRD analysis also shows the presence of both iron and cementite in the coke as can be seen in Fig. 11.5.

11.4 Discussion

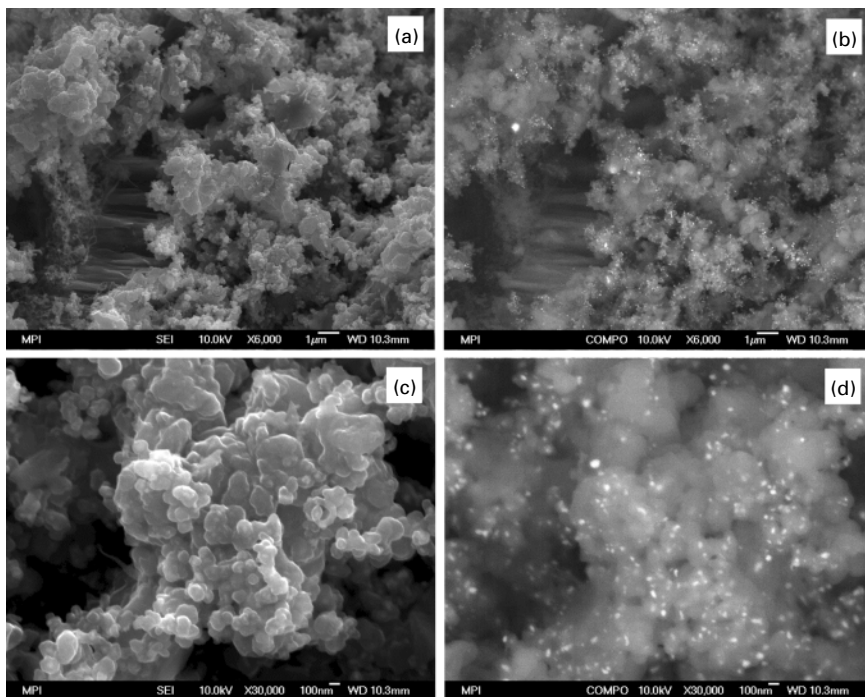
According to the mechanism of metal dusting [1–6], iron is at first subjected to carburisation in CO-H₂-H₂O gas mixtures. As a result cementite is formed on the sample surface. Subsequently, graphite is deposited on the cementite



11.8 Morphologies of graphite on the surface of the iron sample carburised at 600°C in the gas of 1% CO–98.8% H₂–0.2% H₂O for 21.5h: (a) low magnification showing very fine filaments and bulk columnar graphite, and (b) high magnification of fine filaments as indicated by a white square in (a).

surface, which initiates cementite decomposition. Figures 11.2 and 11.6 show different stages of this process at 600°C and 700°C. In earlier studies [9, 10] it was proved that γ -Fe in cementite/graphite interface is a reaction product of cementite decomposition.

The formation of an iron layer between cementite and graphite was observed at low CO contents in the CO–H₂–H₂O mixtures. The range of CO contents where this phenomenon is observed depends on the temperature. This work shows that the iron layer formation occurs for gas mixtures with CO contents 5 vol.% at 700°C. The corresponding carbon activity is $a_C = 15.8$. However, at 600°C this critical CO content becomes 1 vol.% with the calculated carbon



11.9 Morphology of graphite particle clusters formed on the surface of the iron sample carburised at 600°C in the gas of 1% CO–98.8% H₂–0.2% H₂O for 21.5h: (a) and (b) low magnification and (c) and (d) high magnification of this structure. ((a) and (c): secondary electron images; (b) and (d) corresponding back-scatter electron images.)

activity 22.2. The very close carbon activities corresponding to the critical CO contents at these two temperatures suggest that the formation of iron layer between cementite and graphite is determined by the carbon activity of the gas mixture. Therefore the same phenomenon should also occur at other temperatures in gases with similar carbon activities but different critical CO contents.

It is also clear from this work that no iron layer is formed at the cementite/graphite interface when the CO contents are larger than the critical values. In fact cementite directly in contact with graphite is the most general observation for metal dusting of iron [1–6, 12, 13]. In this case, the decomposed cementite particles are detached from the cementite/graphite interface forming filamentous graphite because of the high carbon activities in the gas atmospheres. Filamentous graphite was observed in the coke by many researchers [6, 10, 12, 13]. The amount of filaments increases with increasing CO contents in CO–H₂–H₂O gas mixtures [10].

The kinetics of cementite decomposition was investigated by Zhang and

Ostrovski [7] in their study of iron carbide production. They found that cementite produced from iron ore reduction and carburisation by $\text{CH}_4\text{-H}_2$ gas decomposes into iron and graphite in both carburisation gas atmosphere and non-carburising atmosphere (Ar gas). They also found that the cementite decomposes with the fastest rate at 600°C . By comparing the results obtained at 600°C and 700°C in this work, it is found that the rate of cementite decomposition at 600°C is faster than that at 700°C . For the case of iron particles and layer formation between cementite and graphite, after 21.5 h reaction, the cementite layer disappears completely at 600°C . (Fig. 11.6c). In contrast, at 700°C , after 20 h reaction cementite still exists, although the amount has decreased (Fig. 11.2d). For the cases without iron particles or an iron layer formation, the cross-sections show a very thin layer of cementite together with very thick graphite on the top, (Figs 11.7b, c). It implies that the decomposition of cementite is very fast at 600°C . The decomposed cementite then catalyses the massive graphite formation. In fact the metal dusting of iron was reported to be the worst at about 575°C by Chun *et al.* [6], which is very close to 600°C .

11.5 Conclusions

The formation of an iron layer between cementite and graphite was observed during metal dusting of iron in $\text{CO-H}_2\text{-H}_2\text{O}$ gas mixtures. The influences of gas composition and temperature on this phenomenon were investigated by varying the gas composition at both 600 and 700°C . It was found that iron layer formation occurs when the CO content is lower than a critical value which depends on temperature. At 600°C this phenomenon occurs when the CO content is less than 1 vol.%, while at 700°C this critical CO content becomes 5 vol.%. For CO contents higher than the critical value, no -Fe layer is detected at the cementite/graphite interface by optical microscopy. Consequently cementite contacts directly with the coke layer. The morphologies of the coke formed at low CO contents were also analysed. Three graphite morphologies in the gas with 1 vol.% CO at 600°C can be identified as filamentous carbon, bulk dense graphite with columnar structure, and graphite particle clusters with many fine iron-containing particles embedded inside. At 700°C with 5 vol.% CO the graphite particle clusters become the main form of graphite in the coke although filamentous carbon can also be seen at the early stage of reaction. Corresponding coke analyses show that both -Fe and Fe_3C are present in the coke.

11.6 Acknowledgements

The authors would like to thank Professor H. J. Grabke for many useful discussions. The authors would also like to thank Mrs H. Falkenberg, Mrs

M. Nellessen and Mrs K. Angenendt, MPI für Eisenforschung GmbH Düsseldorf, for preparing the metallographic cross-sections and for SEM analysis. Support of this study by the Deutsche Forschungsgemeinschaft is gratefully acknowledged.

11.7 References

1. H. J. Grabke, R. Krajak, J. C. Nava Paz: *Corros. Sci.* **35** (1993) 1141.
2. J. C. Nava Paz, H. J. Grabke: *Oxid. Met.* **39** (1993) 437.
3. H. J. Grabke, E. M. Müller-Lorenz, A. Schneider: *ISIJ Int.* **41** (2001) Supplement S1.
4. H. J. Grabke: *Mater. and Corros.* **49** (1998) 303.
5. E. Pippel, J. Woltersdorf, R. Schneider: *Mater. and Corros.* **49** (1998) 309.
6. C. M. Chun, T. A. Ramanarayanan, J. D. Mumford: *Mater. and Corros.* **50** (1999) 634.
7. J. Zhang, O. Ostrovski: *ISIJ Int.* **41** (2001) 333.
8. J. Zhang, O. Ostrovski: *ISIJ Int.* **41** (2001) 340.
9. A. Schneider: *Corros. Sci.* **44** (2002) 2353.
10. J. Zhang, A. Schneider, G. Inden: *Corros. Sci.* **45** (2003) 281.
11. G. P. Baxter, J. E. Lansing: *J. Amer. Chem. Soc.* **42** (1920) 419.
12. E. M. Müller-Lorenz, H. J. Grabke: *Mater. and Corros.* **50** (1999) 614.
13. M. J. Bennett: *Mater. and Corros.* **49** (1998) 345.

Coke formation during metal dusting of iron in CO–H₂–H₂O gas with high CO content

J ZHANG, A SCHNEIDER and G INDEN,
Max-Planck-Institut für Eisenforschung GmbH, Germany

12.1 Introduction

The experimental results in Zhang *et al.* [1] show that, at low CO contents in carburising atmospheres, γ -Fe forms at the Fe₃C/graphite interface. This γ -Fe is in the form of particles at the beginning and then further grows to be a ferrite layer between cementite and graphite. Above a critical CO content (e.g. 1% CO at 600°C and 5% CO at 700°C) this phenomenon does not occur. The metal particles in the coke were characterised to be γ -Fe and Fe₃C in the case of the γ -Fe layer formed. The coke layer contains graphite particle clusters with metal particles embedded and also graphite filaments.

The formation of filaments was often observed in the metal dusting and catalytic research [2–7]. For Fe-based materials, these filaments start from small γ -Fe or Fe₃C particles which are detached from the surface. The particles take up carbon from the atmosphere by a catalytic reaction. This carbon is then deposited to be graphite by surface diffusion and bulk diffusion through the particles. By this process the particles are pushed away from the surface and filamentous carbon is formed [6, 7].

It was often suggested that the fine metal particles in the coke should be in the form of γ -Fe according to the proposed mechanism of metal dusting [8–12] as being due to a decomposition of cementite into graphite and γ -Fe. Iron particles were indeed detected in the dust of pure iron by using transmission electron microscopy (TEM) [12, 13]. However, iron carbide was also found in the coke and sometimes it was the only iron-containing phase [3, 4, 14–17]. The coke analyses in Zhang *et al.* [1] indicate the coexistence of γ -Fe and Fe₃C in the coke prepared in the condition to form a γ -Fe layer between cementite and graphite. The present work will show the changes in the coke associated with a high CO content.

In this work, pure iron was carburised in a gas mixture of 75%CO–24.8%H₂–0.2%H₂O at 600 and 700°C. The coke formation was investigated by examining the coke layer in different stages of reaction. The coke was

characterised by scanning electron microscopy (SEM), X-ray diffraction (XRD) and transmission electron microscopy (TEM).

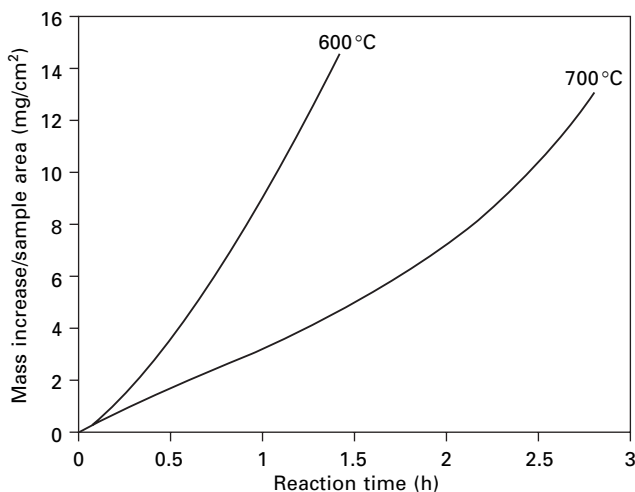
12.2 Experimental procedure

The details of sample preparation, experimental apparatus and experimental procedures can be seen in Zhang *et al.* [1]. The reaction gas for the investigation in this work was fixed at 75 vol.% CO, 24.8 vol.% H₂ and 0.2 vol.% H₂O with a calculated carbon activity 61.4 at 700°C and 418 at 600°C. The weight change of the sample during reaction was recorded using thermogravimetric analysis (TGA). The surface of the sample was analysed by SEM. The coke was identified by XRD and TEM. For TEM analysis, coke powder was fixed onto a copper grid and examined in a Philips CM20-(S)TEM operated at 200 kV.

12.3 Results

12.3.1 Iron carburisation and coke formation during metal dusting of iron

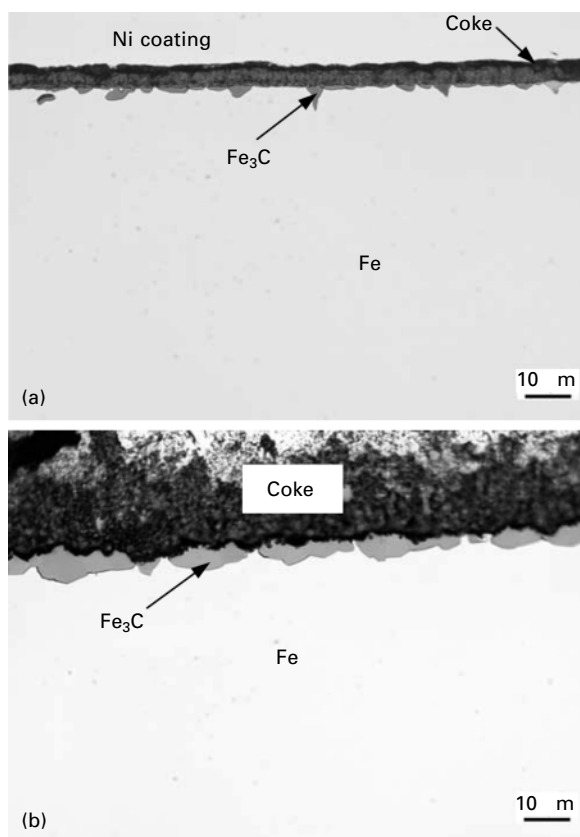
The rate of iron carburisation during metal dusting was investigated by recording weight gains in the process of reaction. Figure 12.1 shows the TGA results of iron samples carburised in the same gas atmosphere of 75%CO–24.8%H₂–0.2%H₂O at 600 and 700°C. It is clear that the rate of iron carburisation is fast in the case of 600°C. Cross-section observation of samples



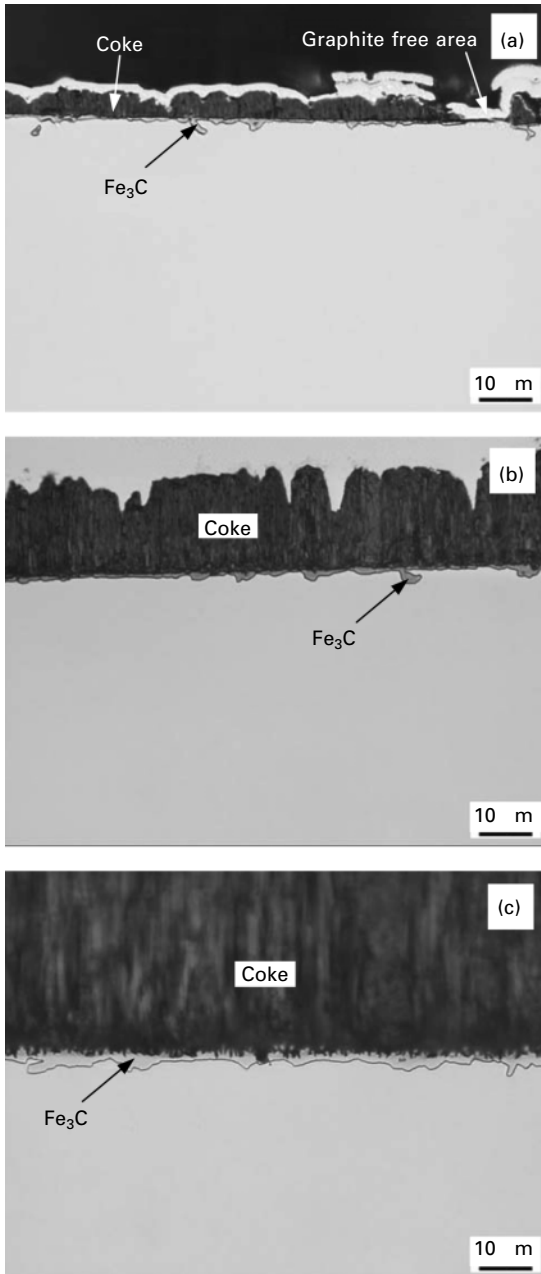
12.1 TGA results of iron samples carburised in 75%CO–24.8%H₂–0.2%H₂O gas mixture at 600 and 700°C.

shows that at 700°C, after 10 min reaction a thin cementite layer forms on the surface, together with a coke layer on the top (Fig. 12.2a). After 4 h carburisation, the thickness of both layers increases (Fig. 12.2b). This increase is particularly significant for the coke layer (Fig. 12.2b). A similar observation was made in the carburisation of iron at 600°C (Fig. 12.3). However, the cementite layer is thinner and the coke layer is thicker than at 700°C. In all cases no iron was observed at the interface between cementite and graphite.

The morphologies of graphite formed at the top of samples in different stages of reaction were examined by SEM. Figure 12.4 shows surface graphite morphologies in the process of carburisation at 700°C. After 10 min reaction at 700°C, the surface of the sample is covered by graphite islands. Very small bright particles and short filaments can be seen clearly along the sides of graphite islands (Fig. 12.4a). By increasing the reaction time to 30 min,



12.2 Cross-section observations of iron samples carburised in 75%CO–24.8%H₂–0.2%H₂O gas mixture at 700°C for (a) 10 min and (b) 4 h.



12.3 Metallographic cross-sections of iron samples after (a) 10 min, (b) 0.5 h and (c) 2 h carburation in the gas mixture of 75%CO–24.8%H₂–0.2%H₂O at 600 °C.

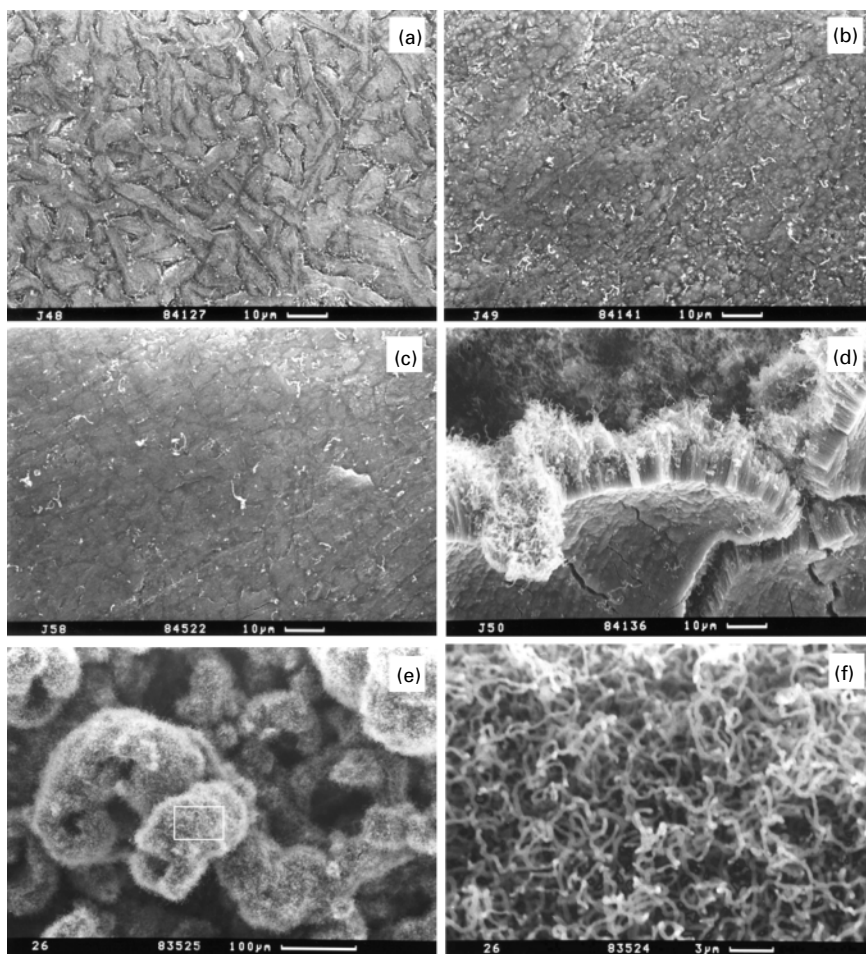
more graphite is deposited on the surface. In this case most of the graphite islands have coagulated. Some bright particles and filaments are still observed on the surface (Fig. 12.4b). After 1 h reaction, a compact graphite layer was formed on the top. The surface of this compact graphite becomes smooth, indicating a thick graphite formation. Energy dispersive X-ray (EDX) analysis shows that there is no iron in this layer. Some filaments are found near the cracks of graphite (Fig. 12.4c).

With further increased reaction time up to 2 h, this compact graphite suffers serious deformation and fracture (Fig. 12.4d). Very dense interwoven filaments can be seen underneath the compact graphite (Fig. 12.4d). The growth of these filaments seems to push the graphite plates outwards. This observation indicates that the coke consists of two layers with distinct morphologies of graphite. The inner layer is rougher and essentially consists of nodules of interwoven filaments. The outer layer is of fairly uniform thickness (5–15 μm). It exhibits a columnar layered structure which is vertical to the surface as can be seen from the fracture of this graphite (Fig. 12.4d).

When the reaction time is increased to 4 h, the pieces of compact graphite bend further such that they seem to be surrounded by filaments. This morphology is presented in Fig. 12.4e. High magnification image of these filaments is shown in Fig. 12.4f. The diameter of these filaments is about 0.2–0.3 μm and bright points are found at the filament tips or within the filaments.

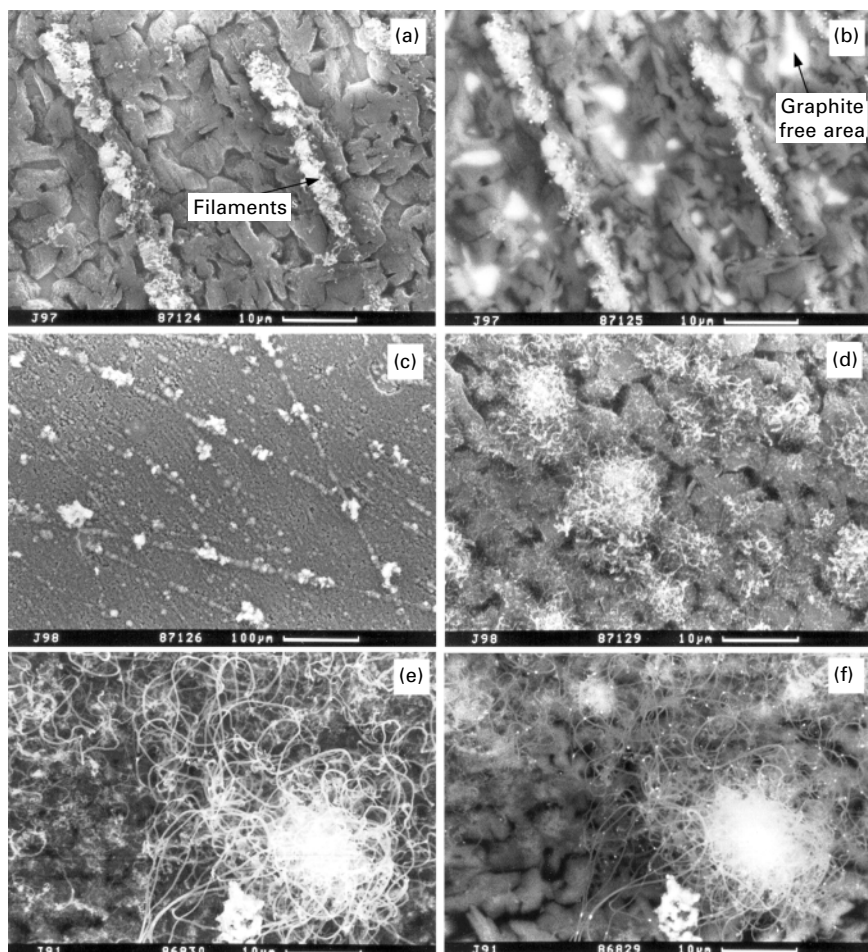
The different stages of coke formation during carburisation at 600 °C was also investigated. Figure 12.5 shows the morphologies of graphite at the top of the sample surface after 10 min, 0.5 h and 2 h reaction. After 10 min reaction, bulk dense graphite islands are formed on the sample surface after 10 min (Fig. 12.5a). Some areas of surface are still graphite-free as indicated as bright areas in the back-scatter electron image of Fig. 12.5b. Short filaments are mainly accumulated along grinding scratches (Fig. 12.5a) and are also bright in the back-scatter electron image but with many white points inside (Fig. 12.5b). After 0.5 h reaction, the whole surface is covered by bulk graphite. Filaments are distributed non-uniformly on the top of bulk graphite and preferably along grinding scratches. (Fig. 12.5c). The graphite blocks have not yet coagulated to form a compact layer and there remains space between them (Fig. 12.5d). Filaments grow out from these spaces. By further increasing reaction time to 2 h, these filaments grow further to form a long filamentous carbon cluster (Fig. 12.5e and 12.5f). A back-scatter electron image in Fig. 12.5f shows that there are still many gaps between these graphite blocks.

In order to see the interior structure of the coke, the cross-section of the coke layer was analysed by SEM. Figure 12.6 shows the cross-section of the coke sample after 2 h carburisation at 600 °C just after cutting. The low magnification image in Fig. 12.6a presents the area with a bulk graphite



12.4 Morphologies of graphite at the top of sample surface in the different stages of reaction: (a) 10 min; (b) 0.5 h; (c) 1 h; (d) 2 h; and (e–f) 4 h ((e) low magnification image, (f) high magnification showing filaments in the white rectangle in (e)) in the gas mixture of 75%CO–24.8% H_2 –0.2% H_2O at 700°C.

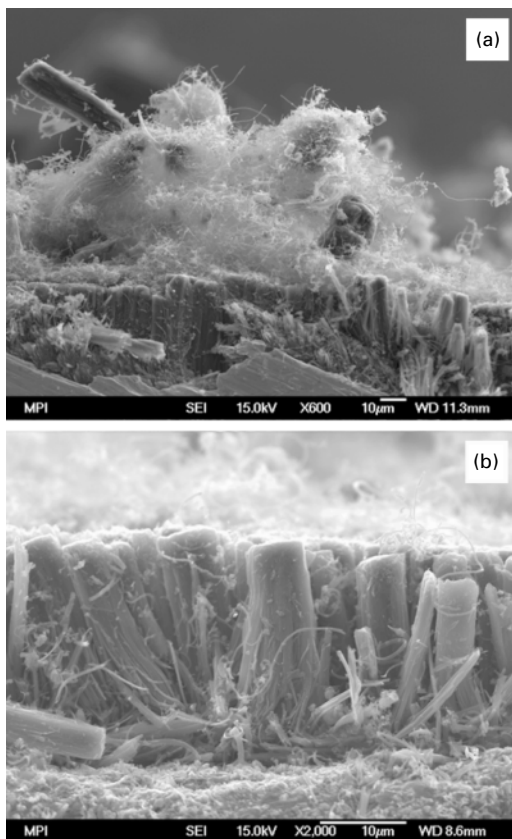
layer and fine filament clusters on the top. High magnification of the bulk graphite layer, Fig. 12.6b, shows that this layer is also composed of graphite columns which are loosely piled and are vertical to the surface. The thickness of this layer was fairly uniform. Filaments are growing between these columns and in some areas had protruded outside. Each column formed many fine fibres as shown in Figs. 12.7 and 12.8. Figure 12.7 gives the observation of these fibres from the broken graphite columns. Figure 12.8 shows the cross section of the columnar graphite which was obtained by embedding the coke sample and polishing. Many fine fibres can be seen inside the columns



12.5 Carbon deposits on the surface of iron samples carburised in the gas mixture of 75%CO-24.8%H₂-0.2%H₂O at 600°C for (a-b) 10 min; (c-d) 0.5 h; and (e-f) 2 h. (b) and (f): back-scatter electron images corresponding to their secondary electron images (a) and (e), respectively.

which are in parallel to the columnar axis. The diameter of these fibres is about 0.2 μm. A back-scatter electron image of the coke layer in Fig. 12.8b and 12.8c shows some iron-containing particles (bright particles) inside this section.

The interface of cementite and graphite was directly observed by the removal of graphite from the surface as can be seen in Fig. 12.9. This observation shows that many fine protrusions were formed on this surface with still some remaining graphite among the protrusions. The protrusions



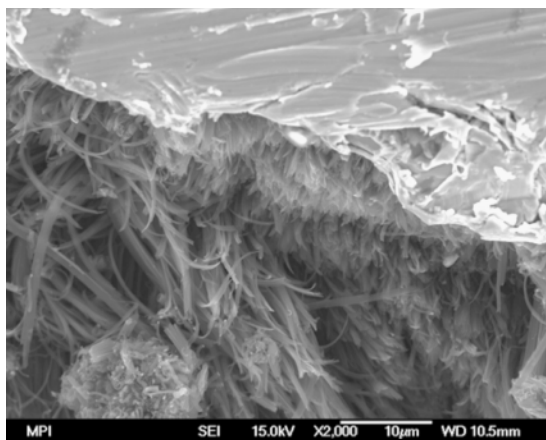
12.6 Coke layer cross-section SEM observation of the sample carburised at 600 °C for 2 h in the gas mixture of 75%CO–24.8% H_2 –0.2% H_2O (sample after just cutting). (a) Low magnification image showing the area with bulk graphite layer and dense filaments on the top; (b) high magnification image showing the columnar structure of bulk graphite layer.

seem to have a tendency to detach from this surface to form the particles. EDX analyses show that these protrusions contain iron and carbon.

12.3.2 Characterisation of coke formed during metal dusting of iron

The coke formed from iron carburisation in the gas mixture of 75%CO–24.8% H_2 –0.2% H_2O at 600 °C for 2 h and at 700 °C for 4 h was characterised by XRD. The results are shown in Fig. 12.10. Both XRD patterns show that there is only cementite in the coke.

In order to further corroborate the structure of the iron-containing particles at the tip of carbon filaments, TEM analysis of a coke powder obtained after

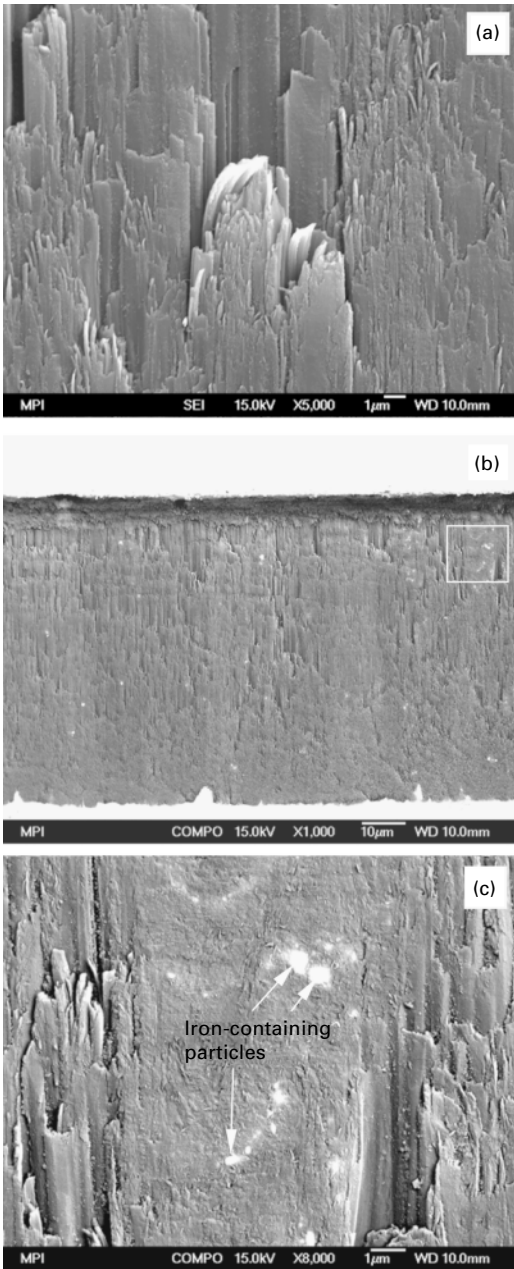


12.7 SEM observation of graphite fibres from broken graphite columns (the sample carburised at 600°C for 2 h in the gas mixture of 75% CO –24.8% H_2 –0.2% H_2O).

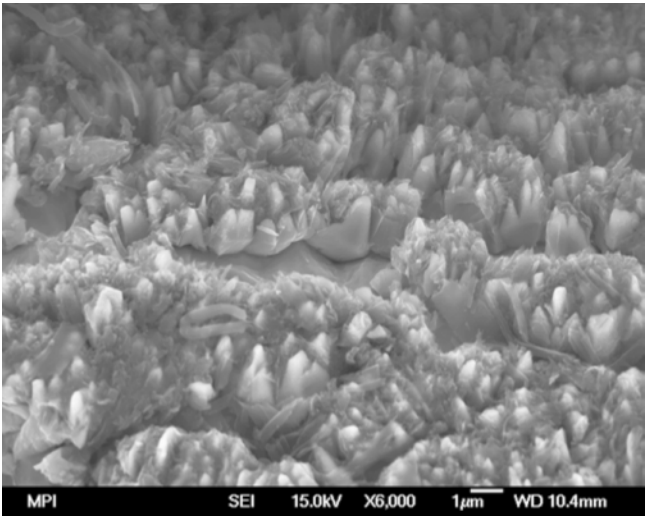
4 h carburisation of iron at 700°C was performed. The TEM images of the coke are presented in Fig. 12.11 which shows that the filaments are bent and often twisted, with random shapes. The diameter of most filaments is about 200 nm. All filaments appear to be solid rather than hollow, and generally have iron-containing particles at their tips or encapsulated along the filaments (Figs 12.11a, 12.11b). The diffraction pattern (Fig. 12.11c) from one of these particles (particle A in Fig. 12.11b) can be indexed in accordance with the [001] zone axis of cementite, which is an orthorhombic phase with the following lattice parameters: $a = 0.5089$, $b = 0.6743$ and $c = 0.4523$ nm. The diffraction patterns of other particles were all consistent with cementite.

12.4 Discussion

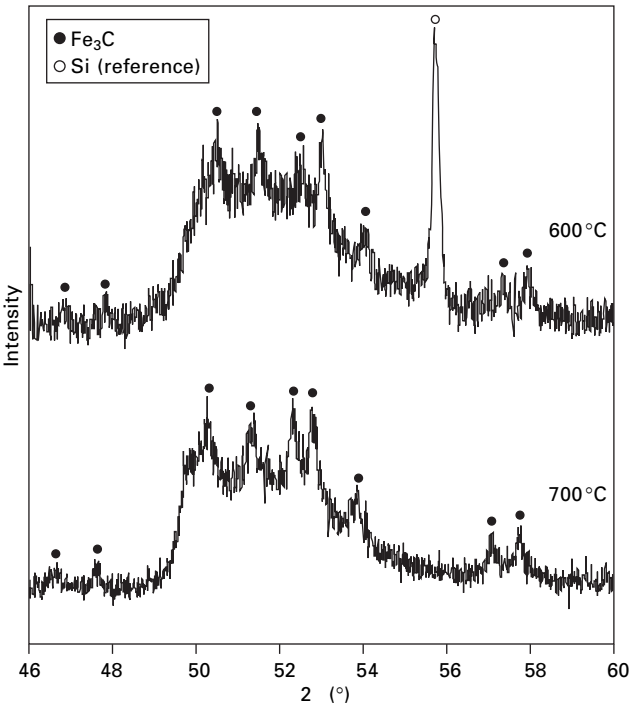
The metal dusting of iron starts with carbon dissolution in iron and growth of a cementite layer at the surface. Because of cementite formation, the further carbon dissolution into iron slows down. As a result graphite deposits on the cementite surface to form graphite islands, as can be seen in Figs 12.4a, 12.5a. This carbon deposition on cementite was claimed to be responsible for a decomposition of cementite into the stable phases -Fe and graphite [8–11]. The present observations do not corroborate this interpretation. Graphite deposition on the cementite surface induces local fluctuation of carbon activity which leads to instabilities. These instabilities result in surface protrusions by massive diffusional processes in the metal surface and in the formation of small particles giving rise to the growth of filamentous graphite. This kind of protrusion and following particle formation are clearly seen in Fig. 12.9 of the interface observation in this work and were also reported by Brown



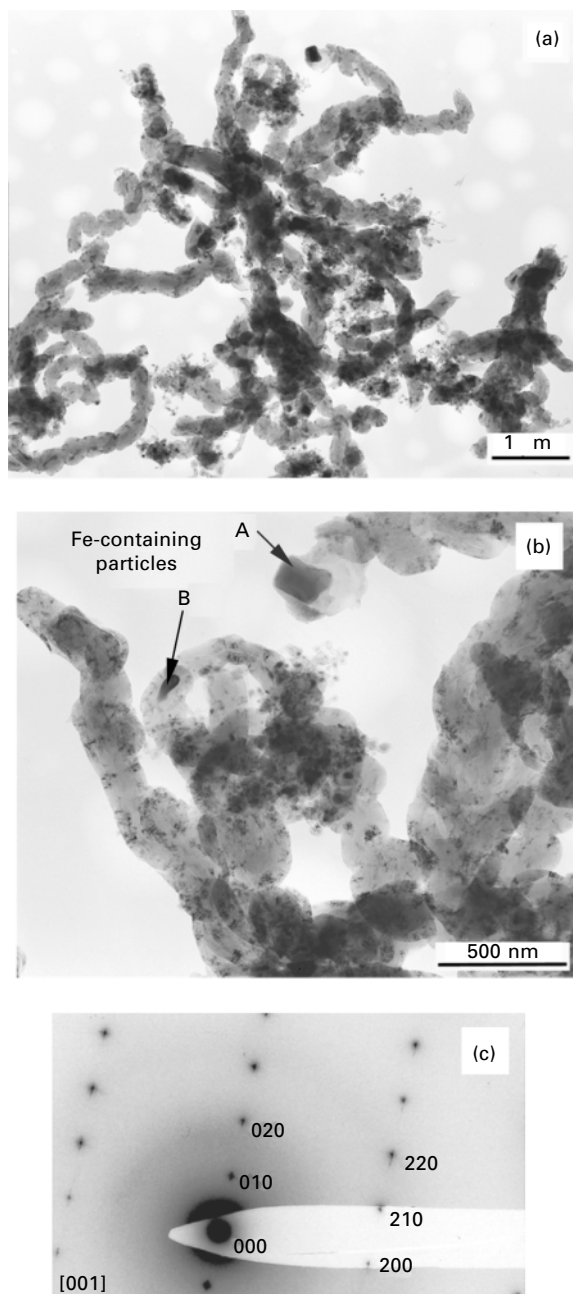
12.8 Coke layer cross-section SEM observation of the sample carburised at 600°C for 2 h in the gas mixture of 75%CO–24.8% H_2 –0.2% H_2O (sample after cutting, embedding and polishing). (a) secondary electron image; (b)–(c) back-scatter electron images, (c) high magnification image of the area marked by white square in (b).



12.9 SEM interface observation of cementite/graphite after the removal of graphite in the coke (the sample carburised at 600 °C for 2 h in the gas mixture of 75%CO–24.8% H_2 –0.2% H_2O).



12.10 XRD spectra of the coke prepared in the gas mixture of 75% CO–24.8% H_2 –0.2% H_2O for 2 h at 600 °C and 4 h at 700 °C.



12.11 TEM micrographs of carbon filaments in the coke of the sample carburised in the gas mixture of 75%CO–24.8% H_2 –0.2% H_2O for 4 h at 700 °C. (a) Overview of filaments; (b) highlight the filaments with Fe-containing particles at the tip and along the length; (c) diffraction pattern of the particle A indicated by an arrow in (b).

and Hill [18] and Schmid *et al.* [19] in their *in situ* observation of the process of iron carburisation and coke formation.

The present work shows a two-layer graphite structure in the coke at 700 °C. The inner layer comprises interwoven graphitic filaments. The outer deposit layer is of uniform thickness and shows a columnar dense structure. SEM observation indicates iron-containing particles at the tip of filaments or within the filaments. This suggests that graphite in this inner layer is formed by heterogeneous catalytic reactions. The outer layer, however, does not show metallic particles inside, indicating the homogeneous decomposition of the carbon-containing gas. This product is physically condensed and more coherent. The preferential growth direction of this carbon is vertical to the surface. Similar observation of two layers of graphite was also reported by Bennett and Price [20] in their investigation of carbonaceous deposits on HK 40 steel tubes during cracking naphtha-steam. The physical, chemical and structural properties of both layers are very similar to those described in this report.

The coke formation at 600 °C is found to be different from that at 700 °C. The bulk graphite layer is composed of graphite columns. Each column consists of many fine fibres which grow vertically to the surface. The diameters of these fibres are similar to the filaments. They may be formed by the same mechanism as filament formation. The iron-containing particles detected in this layer (Fig. 12.8b–8c) support this assumption. By comparing Fig. 12.5a, 5d, 5f and 12.6b, it is found that the diameter of the column is comparable to the grain size of cementite, suggesting that the individual graphite columns reflect the underlying cementite grain structure. The rather uniform thickness of this columnar layer indicates similar growth conditions everywhere on the surface. The mechanism of this graphite formation is not very clear and needs further investigation.

The formation of filaments is enhanced along grinding scratches. Similar observations were reported by Schmid *et al.* [19] and Strauß and Grabke [21]. The effect of surface preparation on metal dusting was investigated in our laboratory. It was found that the process of metal dusting is accelerated in the case of a rough surface, e.g. produced by grinding, compared with a polished surface.

According to the mechanism of metal dusting proposed by Grabke and coworkers [8–11] and some other researchers [12, 13] the iron-containing particles in the coke were expected to be γ -Fe, since they are in direct contact with graphite. This assumption is not convincing. Cementite particles in contact with graphite are in metastable equilibrium. Nucleation of ferrite at the graphite/cementite interface is difficult, since cementite is a stoichiometric phase with a very small homogeneity range. In fact, cementite was found to be the major part of iron-containing particles in the coke or even the only iron-containing phase [3, 4, 14–17]. Hochman [14] identified the particles in

the filaments to be iron and in some cases carbide, but he did not give details of this result. Wei *et al.* [15] reported that iron particles were present in the coke if low carbon activity gas (e.g. $a_C = 3.3$) was used, while with extremely high carbon activities (e.g. $a_C = 4580$ at 500°C) only carbide was detected [15, 17]. Toh *et al.* [4] used XRD and TEM to analyse a coke of Fe–25Cr–(0–25)Ni carburised by 68% CO–26% H₂–6% H₂O at 680°C ($a_C = 2.9$). They found that for the steel with low contents of Ni (0–5 wt%) only cementite was detected in the coke and at the tip of filaments. For alloys with high Ni contents (10–25 wt%), in addition to carbide, some austenite was detected. Zeng *et al.* [16] reported that cementite is the only detectable iron-containing phase in the coke of iron carburised at 593°C in the gas of 72.4% H₂–8.1% CO₂–17.2% CO–2.3% H₂O ($a_C = 27.3$). These reports imply that the type of metal-containing phase in the coke, iron or carbide depends on the alloying elements in the sample and on the reaction conditions. The coke analyses presented in this work and in Zhang *et al.* [1] show that the nature of the particles also depends on the gas atmosphere. At high CO contents and thus high carbon activities the particles consist only of cementite.

12.5 Conclusions

Coke formation during metal dusting of iron has been investigated in the gas mixture of 75% CO–24.8% H₂–0.2% H₂O at both 600 and 700°C . Metallographic cross-section observation and thermogravimetric analysis reveal a stronger carburisation and coke formation at 600 compared with 700°C . The morphologies of the coke were analysed by SEM. Two kinds of graphite were identified: compact bulk graphite with a rather uniform thickness and columnar structure, and filamentous carbon with iron-containing phases at the tip or along its length. A two-layer structure of the coke was observed at 700°C . The inner layer is composed of filaments, while the outer layer consists of compact columnar graphite. The further growth of the catalytic filaments pushes the top compact graphite layer to form fractures. These filaments then grow outside from these fractures and finally cover the whole surface. At 600°C , however, the coke layer contains mainly graphite columns which are loosely piled and are vertical to the surface. Each graphite column is found to be composed of many fine coherent graphite fibres in parallel with the columnar axis. Filaments grow outside preferably from the gaps among these graphite columns and along the grinding scratches with a non-uniform distribution on the surface. TEM analysis of the coke detects very convoluted filaments with iron-containing particles at the tip or along their length. XRD and TEM analyses show that these particles are Fe₃C rather than metallic iron.

12.6 Acknowledgements

The authors would like to thank Professor H. J. Grabke, Max-Planck-Institut für Eisenforschung GmbH Düsseldorf, for many useful discussions. The authors would also like to thank Mrs H. Falkenberg, Mrs M. Nellesen, Mrs K. Angenendt and Mrs E. Bartsch, MPIE in Düsseldorf, for preparing the metallographic cross-sections, the SEM analysis and the TEM analysis. Support of this study by the Deutsche Forschungsgemeinschaft is gratefully acknowledged.

12.7 References

1. J. Zhang, A. Schneider, G. Inden: EFC workshop No. 258, Frankfurt am Main, Germany, 30–31 January 2003.
2. J. Zhang, A. Schneider, G. Inden: *Corros. Sci.* **45** (2003) 281.
3. J. Zhang, A. Schneider, G. Inden: *Corros. Sci.* **45** (2003) 1329.
4. C. H. Toh, P. R. Munroe, D. J. Young: *Oxid. Met.* **58** (2002) 1.
5. P. L. Walker, Jr., J. F. Rakaszawski and G. R. Imperial: *J. Phys. Chem.* **63** (1959) 140.
6. R. T. K. Baker, M. B. Barber, P. S. Harris, F. S. Feates, R. J. Waite: *J. Catal.* **26** (1972) 51.
7. J. R. Rostrup-Nielsen, D. L. Trimm: *J. Catal.* **48** (1977) 155.
8. H. J. Grabke, R. Krajak, J. C. Nava Paz: *Corros. Sci.* **35** (1993) 1141.
9. J. C. Nava Paz, H. J. Grabke: *Oxid. Met.* **39** (1993) 437.
10. H. J. Grabke, E. M. Müller-Lorenz, A. Schneider: *ISIJ Int.* **41** (2001) Supplement S1.
11. H. J. Grabke: *Mater. and Corros.* **49** (1998) 303.
12. C. M. Chun, T. A. Ramanarayanan and J. D. Mumford: *Mater. and Corros.* **50** (1999) 634.
13. E. Pippel, J. Woltersdorf, R. Schneider: *Mater. Corros.* **49** (1998) 309.
14. R. F. Hochman: *Proceedings of the symposium on properties of high temperature alloys with emphasis on environmental effects*, 1976, 715.
15. Q. Wei, E. Pippel, J. Woltersdorf, H. J. Grabke: *Mater. Corros.* **50** (1999) 628.
16. Z. Zeng, K. Natesan, V. A. Maroni: *Oxid. Met.* **58** (2002) 147.
17. A. Schneider, G. Inden, H. J. Grabke, Q. Wei, E. Pippel, J. Woltersdorf: *Steel Res.* **71** (2000) 179.
18. A. M. Brown, M. P. Hill in: M. J. Comstock (Ed.), *Coke formation on metal surfaces*, Am. Chem. Soc., 1982.
19. B. Schmid, N. Aas, Ø. Grong, R. Ødegård: *Appl. Catal. A: General* **215** (2001) 257.
20. M. J. Bennett, J. B. Price: *J. Mater. Sci.* **16** (1981) 170.
21. S. Strauß, H. J. Grabke: *Mater. Corros.* **49** (1998) 321.

Morphologies and mechanisms of metal dusting on high-alloy steels

P S Z A K Á L O S, Swedish Institute for Metals Research
(SIMR), Sweden

13.1 Introduction

It has long been known that iron can be attacked by an atmosphere of high carbon activity [1–3]. In addition to dissolving carbon, the iron acts as a catalyst for the formation of graphite and the graphitization reaction breaks off fragments of iron, forming a metal dust mixed with graphite (coke). Recently this process has attracted considerable attention, and pure iron as well as steels of various alloy contents have been studied [4–12]. However, the mechanism and driving force for metal dusting (MD) has so far not been fully understood [11]. The present study encompasses ferritic steels, including pure iron, a FeCr steel and a FeCrAl alloy. The results will be explained taking into account the effects of alloying elements and oxygen.

The phenomenon of metal dusting may be divided into three main mechanism ‘building blocks’, denoted Type I, Type II and Type III. Type I, first described by Hochman [3] and further refined by Grabke [4], involves decomposition of metastable cementite. Type II may be described as disintegration of a carbon supersaturated phase by precipitated graphite and was described by Hultgren and Hillert [1] in the 1950s and studied in detail by Pippel *et al.* [12]. Type III, which operates on high-alloyed steels and Ni-base alloys, has been proposed recently [7–10] and involves selective oxidation of alloyed carbides. A fourth mechanism, Type IV, will be introduced in this chapter and may be described as continued disintegration of the corrosion products, resulting in nano-sized particles.

It should be mentioned that there is seldom only one MD mechanism operating on a steel. For example, Types III and II operate conjointly in austenitic stainless steels and Ni-base alloys [7–9]. It will be shown in this chapter that with these four mechanism ‘building blocks’, a consistent MD process with well-defined driving forces can be presented for iron, low- and high-alloyed steels. It is also applicable to Ni-base alloys.

13.2 Experimental procedure

The laboratory exposures were conducted at 600–650 °C in a quartz tube furnace with a diameter of 25 mm. The chemical composition of the ferritic steels studied is given in Table 13.1. The test samples were prepared by grinding to 600 mesh and cleaning in acetone prior to testing and placed in the cold furnace. To reach a low oxygen partial pressure, pure hydrogen was flushed through the furnace for 3 h before heating to 600–650 °C. The input composition of the reaction gas, which was introduced during heating, was 25%CO + 3%H₂O + 72H₂, with a calculated equilibrium oxygen partial pressure of $p_{\text{O}_2} = 10^{-24}$ at 650 °C [7,8]. The flow rate was 250 ml/min, which corresponds to a gas velocity over the specimen of 9 mm/s.

The pure iron sample of dimensions $12 \times 7 \times 2 \text{ mm}^3$ was exposed in two shorter periods, 48 h and 100 h at 650°C . The ferritic 26Cr-steel was exposed intermittently for 3–1000 h at 650°C . The surfaces were partially scratched with 120 SiC paper after 2000 h exposure. The sample dimensions were $12 \times 12 \times 4 \text{ mm}^3$ and $12 \times 4 \times 0.5 \text{ mm}^3$. The FeCrAl alloy sample of dimensions $12 \times 12 \times 1 \text{ mm}^3$ was exposed intermittently for a total of 5000 h: 4–1000 h at 650°C + 1000 h at 600°C . The surfaces were partially scratched with 120 SiC paper after 2000 and after 3000 h exposure in order to disturb the oxide formation.

The post-exposure metallographic examination was made with JEOL JSM-6400 scanning electron microscope (SEM) and the analyses were made with a Link-Inca energy dispersive spectrometer (EDS). Micrographs were also taken with a field emission gun-SEM Leo-1530 (FEG-SEM) and with light optical microscopy (LOM). The analysis of the corrosion products (coke) was made with a Guinier–Hagg powder diffraction camera, using Cu-radiation and Si as an internal reference.

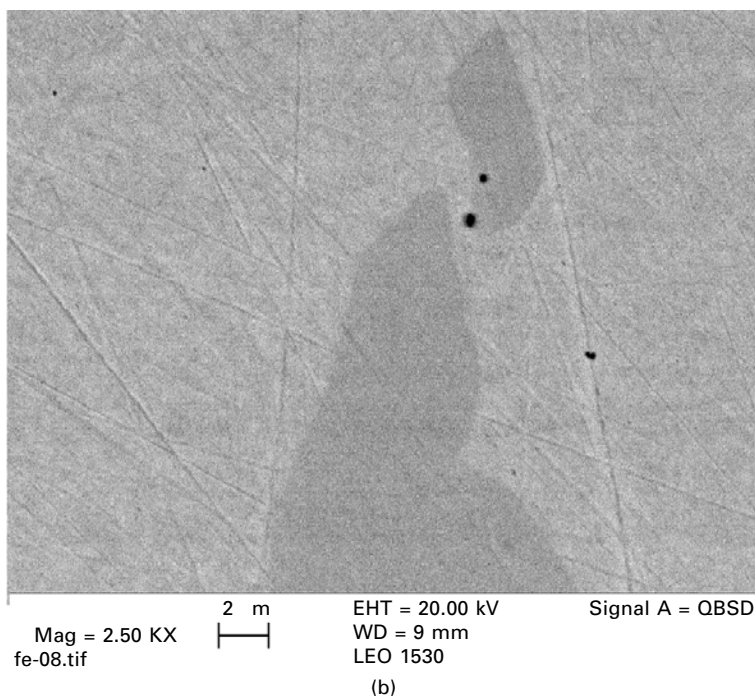
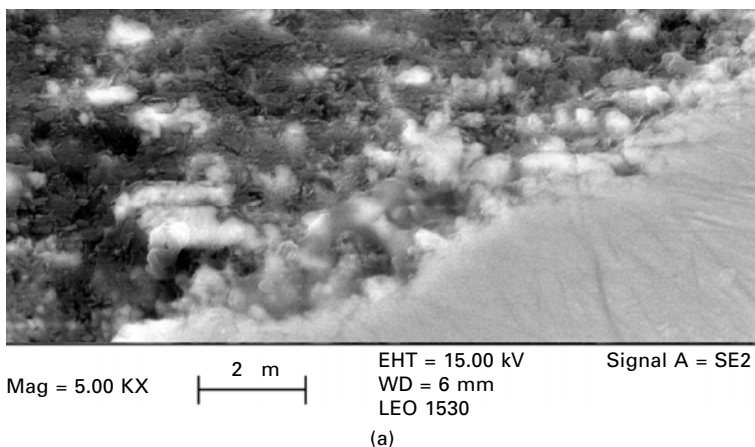
The thermodynamic modelling was conducted with ThermoCalc (TC) [13] database and software. Two databases were combined for the calculations, the SSUB database for the gas phases and the FEDAT database for the phases in the steel with additional thermodynamic data for oxides (spinel).

Table 13.1 Chemical composition of the steel investigated (wt%)

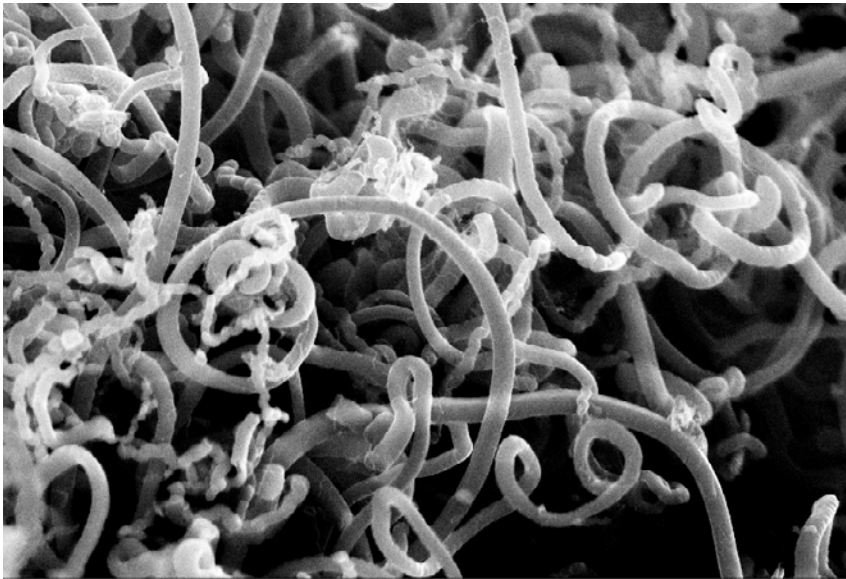
[illegible]

13.3 Results

Post-exposure metallography of pure iron is shown in Figs 13.1–13.2 and of the alloyed ferritic steels in Figs 13.3–13.8. ThermoCalc modelling of the stainless steels is shown in Figs 13.9–13.11.



13.1 (a) FEG-SEM secondary electron image. The steady state metal dusting reaction front of pure iron in cross-section. The steady state situation had appeared by 48 h, though these micrographs were taken after 100 h exposure at 650°C in 25CO–72H₂–3H₂O. (b) Some cementite was detected, but not at the reaction front.

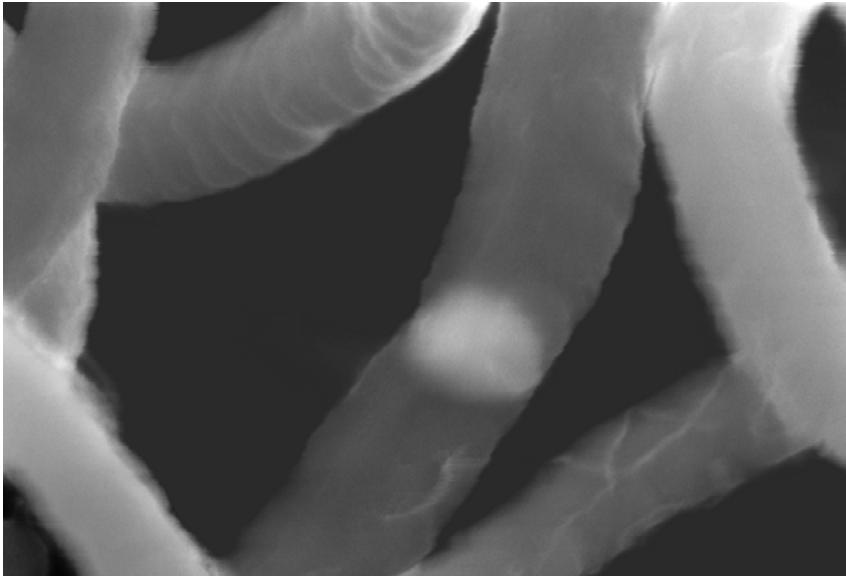


Mag = 10.00 K X | 1 m |
carbon_06.tif

EHT = 10.00 kV
WD = 7 mm
LEO 1530

Signal A = InLens

(a)



Mag = 75.00 K X | 100 nm |
carbon_08.tif

EHT = 10.0 kV
WD = 7 mm
LEO 1530

Signal A = InLens

(b)

13.2 Carbon nanotubes formed in the coke after exposure of iron in a $\text{CO-H}_2\text{-H}_2\text{O}$ gas mixture.

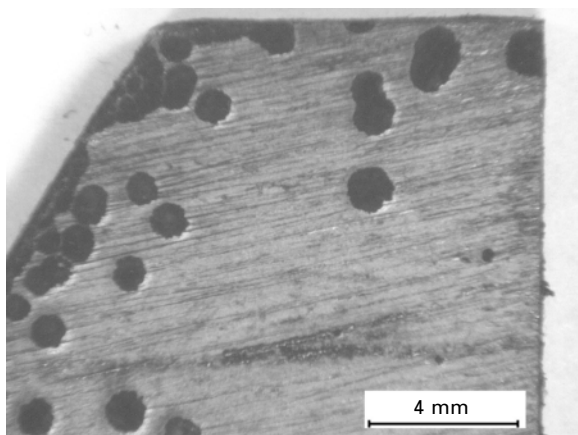
13.3.1 Ultra-pure iron

The sample surface was covered with porous coke mixed with dense graphite after 48h and the metallographic cross-section showed general MD attack with metal fragments released from the 100% ferritic surface. SEM investigations were made after 100h exposure and showed the same appearance; see Fig. 13.1a. Less than 1% cementite was present in the bulk and no cementite was found in the reaction front, as shown in Fig. 13.1b.

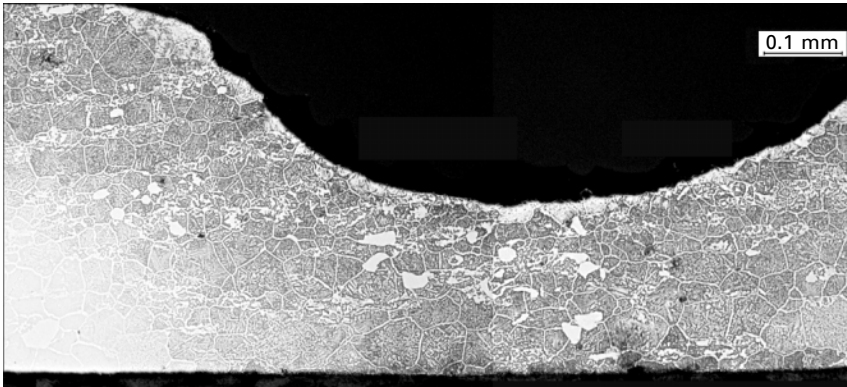
Further away from the surface, nanoparticles typically 150nm in diameter were found; see Fig. 13.2. These particles were in direct contact with filamentous carbon. This phenomenon was studied by Hillert and Lange in the 1950s [14], and is now known as carbon nanotube formation. No graphite flakes were detected in contact with these nanoparticles. Powder diffraction analysis of the coke gave graphite lines and some very weak signals, possibly cementite (JCPDS 35-0772). However, Natesan and coworkers [11] have shown that the particles indeed consist of cementite during similar exposures of iron.

13.3.2 Ferritic 26Cr–steel

A macrograph of the attacked surface with several MD pits is shown in Fig. 13.3. A cross-section of the thinner sample is shown in Fig. 13.4. The darker etched area shows the carburized zone surrounding the metal dusting pit. It should be noticed that the carburized zone has penetrated the remaining sample thickness towards the chromia layer on the opposite side. SEM micrographs with EDS analysis from the metal dusting reaction front are



13.3 Macrograph of the 26Cr steel surface after 3000h exposure at 650°C. All metal dusting pits grew during the final 1000h exposure.

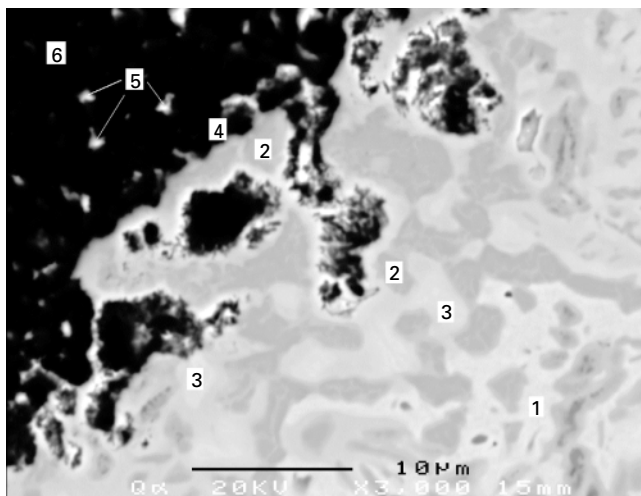


13.4 LOM image of 26Cr steel etched in nital. Cross-section of the sample through a metal dusting pit. Dark etching: carburized zone. White grains: Cr-Fe cementite.

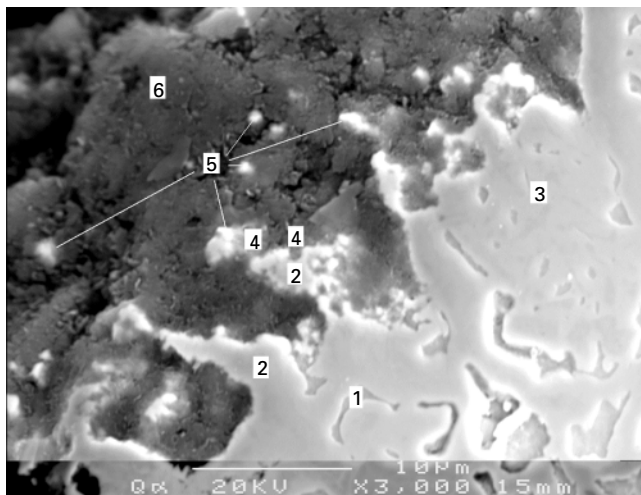
shown in Fig. 13.5a, b. The structure consists almost completely of carbides and the carbide fragments released from the metal surface were partially covered by oxides. The powder diffraction data from three different positions from the coke growing out from a metal dusting pit showed almost the same composition. Large amounts of graphite were detected, with wide lines indicating a fine crystallite size and with d -values corresponding to JCPDS 1-0640. The second strongest lines correspond to Fe-Cr spinel (JCPDS 34-140). The widening of the spinel lines indicates variation in Cr content. The third crystalline phase detected was cementite (JCPDS 35-0772), again with broad intensity peaks. The cementite lines were significantly lower in intensity compared with the spinel lines, indicating there is more spinel in the corrosion end products. These findings correspond well to the TC modeling shown in Figs 13.10 and 13.11. The metal containing corrosion end products at $p_{O_2} = 10^{-24}$ bar are predicted to consist of 60–70% spinel and 40–30% cementite or ferrite particles, depending on the carbon activity as shown in Fig. 13.11. However, during exposures in MD environments, the carbon activity in the coke is normally high enough to stabilize unalloyed cementite as discussed in Section 13.1. The Cr-alloyed cementite is even more stable and, therefore, the situation in this and other studies, for instance by Young and coworkers [15], corresponds to the TC modelling shown in Fig. 13.10b.

13.3.3 Ferritic FeCrAl alloys

Two different phases formed in the MD reaction front as shown in Figs 13.6 and 13.7. A line analysis of the phase fractions in the outermost reaction front gave approximate 34% M_7C_3 -carbide, 35% of a plate-shaped dark phase which is probably a ternary FeCrAl carbide and 33% ferrite. According



(a)



(b)

13.5 (a) Backscatter electron image of a mechanically polished surface. (b) Secondary electron image slightly etched in nital resulting in a deep etched ferrite phase. SEM micrographs of 26Cr steel exposed in a metal dusting environment for 3000h showing the cross-sections of the reaction front in the bottom of a metal dusting pit. EDS-analysis in atomic% is shown in Table 13.2.

to the TC modelling, see Fig. 13.9a, up to 40% M_7C_3 carbide is expected. No ternary $FeCrAl$ carbide is described in the TC database and the only phase found in the literature that is probable is the perovskite -carbide Fe_3AlC [16, 17]. The EDS analysis (Fig. 13.7, marker c) of the dark phase fits quite well with -carbide, albeit there is some Cr present. A calculation of the

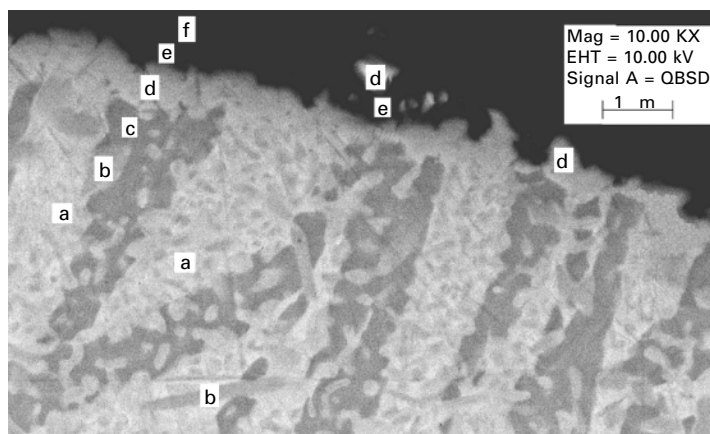
Table 13.2 EDS analysis of 26 Cr-steel (at.%)

Marker	Phase	Cr	Fe	Mn	O	C
1	Ferrite	4	93	–	–	2
2	M_7C_3 carbide	48–57	22–10	1	–	~30
3	M_3C carbide	7–12	78–73	0.4	–	~25
4	Oxide	25–45	14–26	0–2	40–50	Excluded*
5	Particle	7–10	93–90	–	–	Excluded*
6	Coke	0.7	3	–	3	93

*As carbon is excluded, the compositions are normalized to 100%.



13.6 FeCrAl alloy exposed in a metal dusting environment for 5000 h. SEM cross-section of the reaction front in bottom of a metal dusting pit. Light grey in contrast are M_7C_3 carbides, dark in contrast are possibly M_3AlC carbide with strong orientational growth in the ferritic lattice.

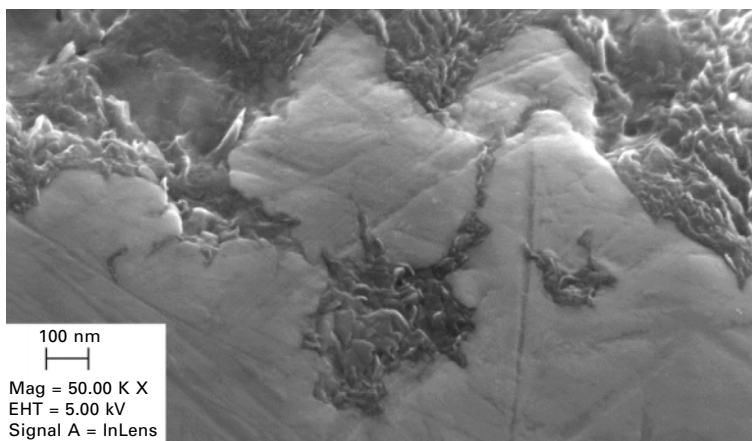


13.7 FeCrAl alloy exposed in a metal dusting environment for 5000 h. FEG-SEM backscatter electron image, polished cross-section of the reaction front in bottom of a metal dusting pit. Average EDX analysis of the different phases in atomic% are shown in Table 13.3.

Table 13.3 Average EDX analysis of different phases of FeCrAl-alloy (the values are slightly 'smeared' because of the fine structure)

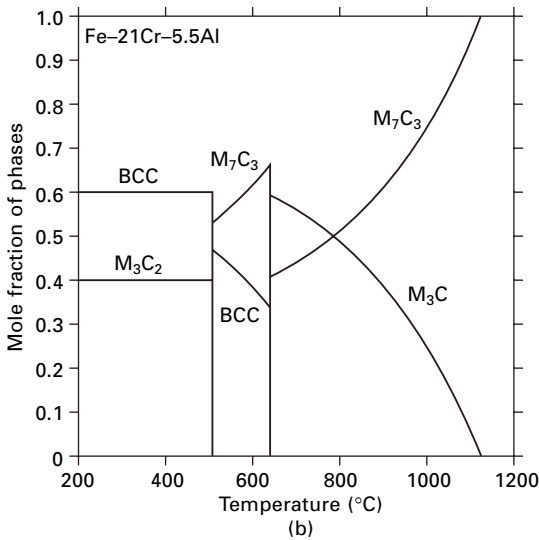
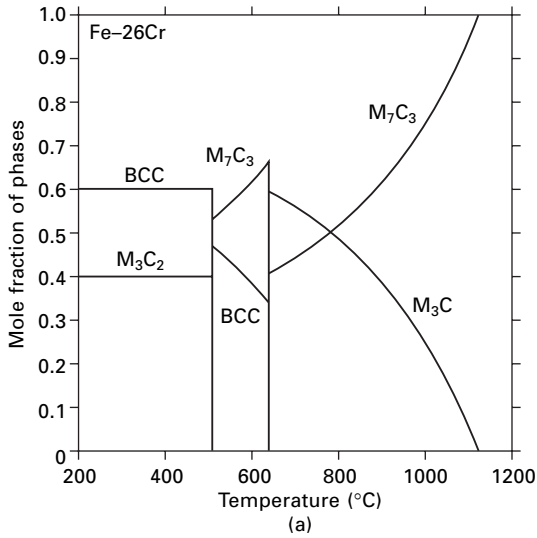
Marker	Phase	Cr	Al	Fe	O	C
a	Ferrite + M_7C_3	14	6	65	–	8
b	Grey contrast (M_7C_3)	30	4	40	–	24
c	Dark: - carbide (?)	13	13	55	–	13
d	Ferrite	10	5	83	–	Excluded*
e	Oxide	5–15	5–15	40–60	10–30	Excluded*
f	Coke	1	0.5	10	6	80
	FeCrAl-bulk composition	20.4	10.6	69	–	0.03

* As carbon is excluded, the compositions are normalized to 100%.

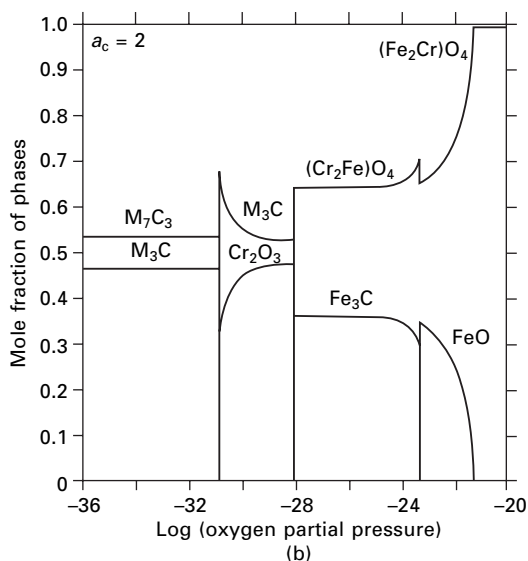
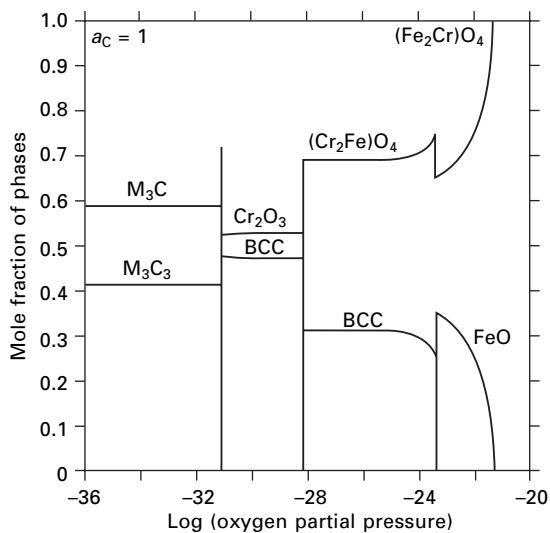


13.8 Detail from Fig. 13.7. FEG-SEM secondary electron image of the ferritic border in the reaction front. The outermost ferrite border is penetrated by graphite structures. The oxides (oxygen signals) are detected mostly around the particles and in metal/coke interface, as seen in Fig. 13.7.

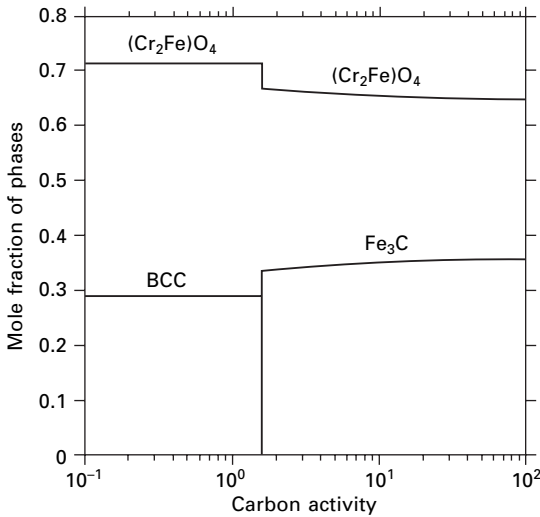
maximum carbide content in a carbon-saturated FeCrAl alloy gives approximately the following volume fractions: 35 vol% M_7C_3 carbide and 40 vol% Fe_3AlC and 25 vol% ferrite. These phase calculations and phase compositions support the possible identification as perovskite -carbide. A close-up of the carbide-free ferrite border is shown in Fig. 13.8, comparable with the carbide-free and Cr-depleted austenite border observed on austenitic stainless steels [7,8]; see Section 13.4.4.



13.9 Mole fraction of stable phases as a function of temperature with $a_C = 1$ and graphite excluded in the calculations, 26Cr steel (a) and FeCrAl alloy (b). The 26Cr steel may form 100% carbides ($M_7C_3 + M_3C$) in the reaction front, in contrast to the FeCrAl-alloy that forms a mix of ferrite (BCC) and M_7C_3 carbide during metal dusting conditions at 650°C. The γ -carbide (Fe_3AlC) is not included in the calculation. Carbide composition in 26Cr steel approximately ($Fe_{2.5}Cr_{0.5}$)C and ($Fe_{3.7}Cr_{3.3}$)C₃. Phase composition in FeCrAl alloy: Ferrite with 1.7 at.% Cr and 15.8 at.% Al and carbides with an approximate composition of ($Cr_{4.6}Fe_{2.4}$)C₃.



13.10 Mole fraction of stable phases in the 26Cr steel–C–O–H system at 650°C as a function of oxygen partial pressure with a fixed carbon activity $a_C = 1$ (a) and $a_C = 2$ (b) with graphite excluded in the calculations. For the equilibrated gas composition used in this study, with $p_{O_2} = 1.6 \times 10^{-24}$, the stable phases will be (a) BCC-ferrite or (b) cementite and Cr–Fe spinel oxide. Schematically, the diagram can be seen as a cross-section of the thin metal dusting front from the metal interface (at low p_{O_2}) towards the gas phase (high p_{O_2}). The equilibrium Cr content is at the most 2.3 at% at $p_{O_2} = 1 \times 10^{-31}$, rapidly dropping with higher p_{O_2} , in both ferrite (BCC) and cementite (Fe_3C) in equilibrium with oxide.



13.11 Mole fraction of stable phases in 26Cr steel as a function of carbon activity with graphite excluded in the calculations and a fixed oxygen partial pressure of $p_{\text{O}_2} = 1.6 \cdot 10^{-24}$ at 650°C. The threshold carbon activity value between ferrite (BCC) and cementite is at $a_{\text{C}} = 1.7$. The spinel oxide is stable, even at high carbon activities.

13.4 Discussion

13.4.1 Metal dusting on pure iron

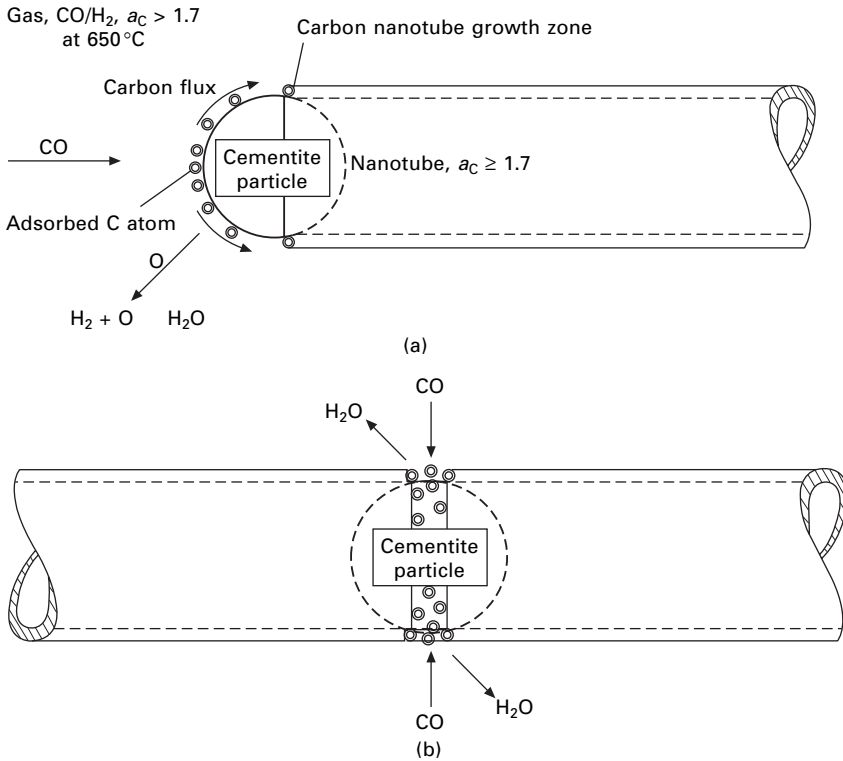
It is well known that it is difficult or impossible for graphite to nucleate directly from a gas phase even if the carbon activity is rather high. On the other hand, metals such as Fe, Ni and Co are very efficient catalysts [18]. A CO molecule can be adsorbed on the surface and dissociate into free C and O. The C atom may then dissolve in the iron due to the considerable solubility and diffusivity and the O atom stay on the surface until it is combined with other atoms to form a gas molecule, e.g. H_2O or CO_2 . As more and more C dissolves in the Fe phase, the carbon activity increases in the material and carbon can precipitate as graphite at an activity over 1.0 and as cementite at a higher activity, the critical value depending on the temperature. From a thermodynamic point of view, one would thus expect graphite to form first, but it has greater difficulty in nucleating and is slow to grow, at least inside the Fe phase. Usually, cementite will thus be the first phase to form. Eventually, graphite will form inside the material and it usually results in the cementite dissolving. One may even identify this as an eutectoid reaction; cementite $\text{Fe}(\text{C}) + \text{graphite}$. When graphite forms within the surface layer, it happens by interstitial diffusion of carbon, which does not itself provide any volume for the growing graphite. Instead, the growing graphite will deform the Fe matrix, which results in fragments of iron breaking off [5, 6], i.e. the Type II

mechanism. In the subsequent process, cementite will play a lesser role because it is more difficult for the carbon activity to exceed the critical value for cementite when graphite particles are present inside the material. In fact, it is not possible to explain the driving forces of MD on iron if there is an inward growing cementite layer present during the steady state process since that would need carbon diffusion in the opposite direction to the carbon activity gradient. It is now proposed that the simple solution to this problem is that there is such a layer only during the *initial stages of MD*. These initial stages, studied by several researchers [3–5, 11, 12, 19, 20] seem to continue for more than 20 h [20] but not more than 48–100 h at 650–700 °C, as seen in the reaction front in Fig. 13.1.

Carbon nanotube formation: Type IV mechanism

The ferritic fragments broken off from the bulk material will still act as catalysts and dissolve carbon and precipitate it as graphite. The fragmentation may thus continue and the particle size will decrease gradually. It is proposed that the particles finally may be too small to allow further precipitation in their interior and the continued formation of solid carbon will occur on their surface. For energetic reasons one could primarily expect that the graphite lattice would be oriented with its hexagonal planes more or less parallel to the surface of the metallic particle. The growth will occur at the interface and most of the available sites for carbon would then represent the beginning of a new hexagonal plane. Such sites should be less favourable than those where carbon atoms can attach themselves to the edge of an hexagonal plane. This would result in the graphite tending to shoot out from the particle more or less tangentially. It is proposed that this is the mechanism behind the formation of nanotubes on the very small particles and would explain why the diameter of the nanotubes corresponds to the diameter of the particles. The principal growth mechanism of nanotubes is shown in Fig. 13.12a,b. The same micromechanism may occur on the metallic surface of the bulk of the specimen but there it would not result in nanotubes, for geometric reasons. Instead, a much more irregular structure would form. It is often described as coke. The Type IV mechanism represents a self-assembling system; the larger ferrite fragments are subjected to the Type II mechanism with irregular graphite formation until they reach a suitable size for nanotube formation.

It should be mentioned that there is a different hypothesis about the formation of the small particles acting as catalysts for the formation of nanotubes. This proposes that Fe atoms (or other metal atoms) dissolve in the graphite that grows on the surface and protrudes into the specimen. These atoms are proposed as diffusing outwards and finally precipitating and agglomerating inside, or at the outer side, of the surface layer of graphite (coke). To the present author this mechanism seems less likely. It would depend on the



13.12 (a) A mechanism for nanotube formation in CO/H₂-containing gases at high carbon activities is proposed. CO molecules dissociate at the cementite surface, carbon diffuses towards the lower carbon activity at the carbon nanotube growth zone and oxygen reacts with hydrogen to form water vapour. (b) Two nanotubes may grow from one particle.

solubility and diffusivity of Fe in graphite and on a driving force for outward diffusion, which has not yet been identified. The Type IV mechanism, the nanotube process, represents only a secondary MD effect, i.e. further disintegration of the corrosion products. However, there is an interest in these small tubes in material science in general and particularly in nanotechnology.

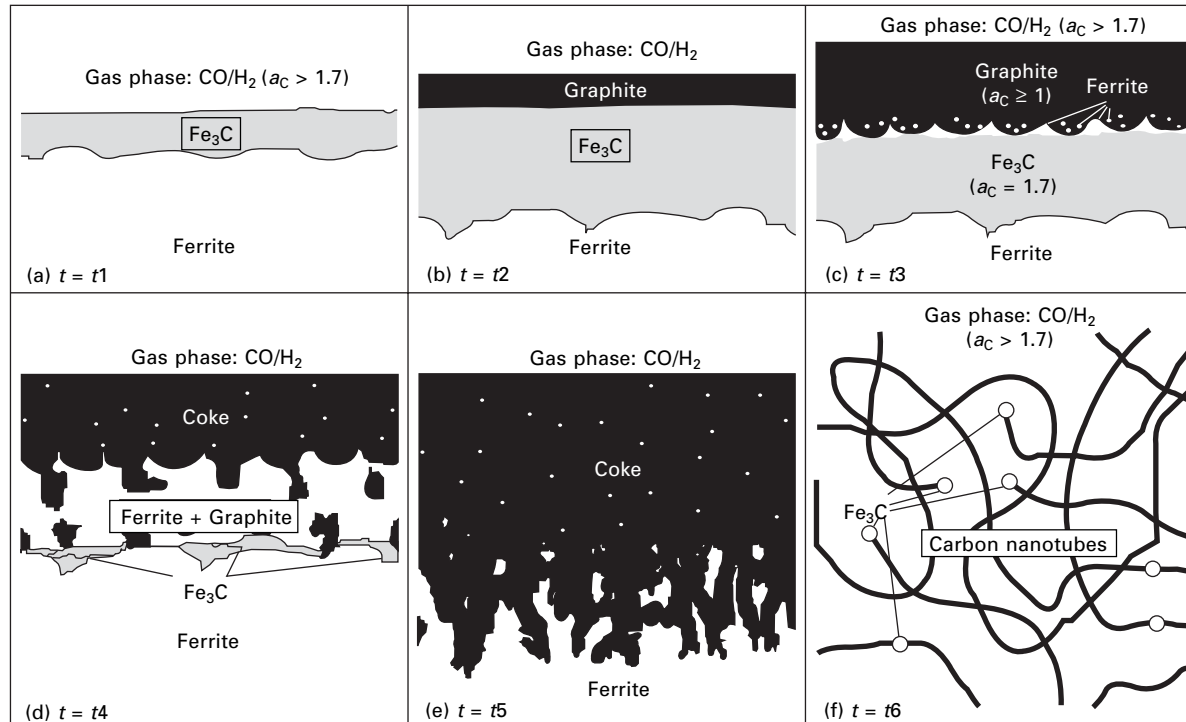
Carbon activity

It is relevant to discuss the carbon activity of the various types of carbon mentioned here. Perfectly developed graphite should by definition have a carbon activity of 1.0, and higher values are expected as a consequence of imperfections. The type described here as coke (mix of defective graphite, amorphous carbon and/or nanotubes) or porous coke (basically consisting of

carbon nanotubes) should thus have an activity considerably higher than 1.0 but it is difficult to judge how much higher. The compact graphite layer on the initially formed cementite initiates the decomposition process, indicating a carbon activity not higher than 1.7 at 650 °C, as shown in Figs 13.11 and 13.14c(below). However, the ferritic fragments released during the steady state MD process, form catalytic nanoparticles consisting of cementite [11], indicating a carbon activity higher than 1.7 in the now prevalent porous coke. This means that the dissociation of carbon from the gas phase represents a higher driving force than the precipitation of solid carbon on the base of the growing nanotube. Studies of the internal structure of nanotubes indicate that they may have a perfect structure. On the other hand, they have a very high surface-to-volume ratio, which will increase the carbon activity. The carbon activity in the surface layer will initially increase gradually to well above 1.0 to make the formation of cementite possible. After graphite has started to form, the activity decreases and cementite starts to dissolve. However, it is most probable that the activity is even higher than that of the defective graphite, because the driving force for internal graphite formation is high enough to cause fragments of metal to break off. This is possible because the gas is able to penetrate a layer of porous coke and interact with the metallic surface without losing too much carbon to the graphite formation in the coke layer. This may explain why cementite prevails for a certain time after the formation of graphite in the ferrite. However, all cementite has been found to disappear eventually in pure Fe specimens.

Schematic presentation of the different MD steps on pure iron

The main steps of the MD process on pure iron are shown in Fig. 13.13. In the first step a cementite layer forms on the surface (Fig. 13.13a) followed by a graphite layer on the cementite (Fig. 13.13b). As the graphite layer grows thicker and tighter, the carbon activity drops towards unity and cementite starts to decompose, i.e. the Type I mechanism (Fig. 13.13c). The eutectoid reaction (cementite = ferrite + graphite) may be fast enough to form an intermediate layer of ferrite and graphite (Fig. 13.13d). Cementite contains 25 at.% carbon and 75 at.% Fe which corresponds to an eutectoid structure with approximately 19 vol. % graphite and 79 vol. % iron. However, the carbon diffusion is fast at 650–700 °C and some of the carbon may diffuse to the existing surface graphite, resulting in a structure with locally less graphite. The likelihood to observe this intermediate ‘iron layer’-step [20], i.e. the degenerated eutectoid structure, should be favoured by lower carbon activities because the fragmentation process of the same layer by graphitization (Type II) is slower under these conditions. This Type II mechanism constitutes the steady state process and a well-defined driving force, and no more cementite forms in contact with the graphite (Fig. 13.13e). A close-up from the coke



13.13 A consistent description of the mechanisms that cooperate on pure iron or low alloyed steels during metal dusting is proposed. Parts (a–f) represent increasing exposure times. Cementite formation on the ferrite surface (a). Graphite formation on the cementite layer (b). As the graphite layer grows thicker and tighter the carbon activity drops to unity and cementite starts to decompose, i.e. Type I mechanism (c). The eutectoid reaction may be fast enough to form an intermediate eutectoid layer; cementite + ferrite + graphite (d). No more cementite forms in contact with graphite in the coke, i.e. the steady state process has started, the Type II mechanism (e). Close up from the coke; corrosion of the corrosion products to a steady state size, i.e. Type IV mechanism (f).

shows the steady state situation of the corrosion end products with small catalytic cementite particles producing carbon nanotubes, i.e. the Type IV mechanism (Fig. 13.13f). As observed, the carbon activity in the coke is high enough to transform ferrite to cementite particles.

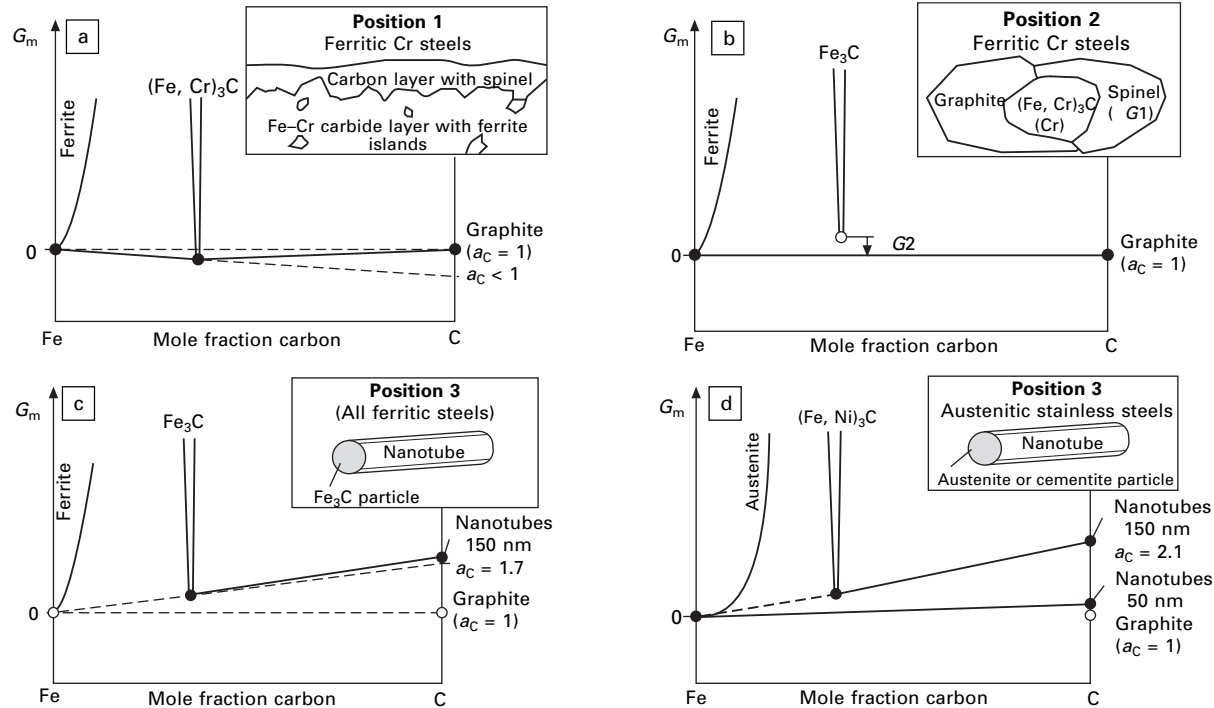
13.4.2 Metal dusting on Cr steels

In contrast to pure iron, which forms metastable carbides, Cr-alloyed steels form stable carbides such as M_3C and M_7C_3 , which change the MD process. These alloyed carbides are stable even at very high carbon activities but they will *dissolve by selective oxidation*. The oxygen partial pressure in a CO-containing metal dusting environment is always high enough to form Cr-rich oxides such as chromia and (Cr, Fe)-spinel. The important difference from the initially protective chromia layer on the surface is that the oxides formed from selective oxidation of carbides are very porous and non-protective; in fact, the spinel oxide is totally mixed with coke, as seen in Fig. 13.5. The mechanisms of MD on Cr steels may be described by schematic Gibbs energy diagrams as shown in Fig. 13.14. Position 1 (Fig. 13.14a) is at the metal dusting reaction front on a ferritic Cr steel. Two equilibria are possible: ferrite–alloyed cementite and alloyed cementite–graphite. Since the cementite is alloyed with a sufficient amount of Cr (~12 at.%, according to Fig. 13.9) it is stable at carbon activities significantly lower than $a_C = 1$, as shown schematically with the extended line. The ferrite–graphite equilibrium is marked by a broken line at $G_m = 0$ J/mole as ferrite and graphite are set as reference states.

The alloyed carbides are more stable and thus not subject to carbon-induced MD. However, the oxygen partial pressure is high enough to selectively oxidize the Cr-rich carbides, i.e. the Type III mechanism, which results in spinel oxides and more or less pure Fe_3C particles (Fig. 13.14b). The cementite may now be subjected to the Type I mechanism; decomposition of metastable cementite into iron and graphite. The fragmentation process continues until the particles can no longer nucleate graphite flakes. Instead the Type IV mechanism takes place (Fig. 13.14c), see page 226. The carbon activity in the porous coke is high enough to transform ferrite into cementite particles, see Sections 13.3.2 and page 227.

The steps and operating mechanisms during MD on ferritic Cr steels can be summarized as follows:

1. Carburization and carbide formation; initially $M_{23}C_6$ carbides, then M_7C_3 and M_3C carbides at higher carbon activity up to a phase fraction of 100%.
2. Partial M_3C carbide dissolution by selective oxidation. M_7C_3 carbides may oxidise completely under (Cr–Fe)-spinel formation (Type III mechanism).



13.14 Principal Gibbs energy diagram as function of carbon content at 650°C explaining the mechanisms and driving forces of metal dusting on ferritic Cr steel. Positions 1–3 correspond to a movement towards the gas phase, i.e. towards higher carbon activity and higher oxygen partial pressure. The positions may also be seen as time steps during the metal dusting process. Position 1 (a) represents the MD reaction front on a ferritic Cr steel. Position 2 (b) shows the situation when cementite fragments are exposed to the higher oxygen partial pressure prevalent in the coke. Position 3 (c) is in the coke, away from the surface and shows the situation when the cementite particles are sufficiently small to be in equilibrium with nanotubes. As comparison, the corresponding situation (position 3) for a stainless steel is shown in (d).

3. Release of M_3C carbide fragments due to oxidation (Type III mechanism) and by graphite inward growth (Type II mechanism).
4. The M_3C carbide fragments with high Cr content continue to dissolve under more Cr–Fe spinel formation until a (low) equilibrium Cr content is reached in the cementite, depending on p_{O_2} and carbon activity, see Fig. 13.10.
5. Local decomposition of iron cementite fragments in contact with graphite into smaller and smaller cementite fragments and graphite/ferrite eutectoid (Type I).
6. The carbon activity in the porous coke is high enough to stabilize cementite and these nano-particles act as catalysts for carbon nanotube formation (Type IV, see page 226).

The corrosion end products are thus Cr–Fe spinel oxides, cementite metal dust and carbon in different forms. Cr is a cementite stabilizer, which is in accordance with the observed cementite dust.

An estimation of the MD corrosion rate of 26Cr steel is possible, as some very small metal dusting pits were detectable after 2000h exposure and during the next 1000h exposure the largest pits were about 1.3 mm in diameter and 0.45 mm in depth. This gives a corrosion rate of 0.45 m/h, which is about half the corrosion rate of austenitic stainless steels [7, 8].

13.4.3 Metal dusting on FeCrAl steels

Alumina formers like FeCrAl alloys or alloys containing substantial amounts of Al have the best MD resistance among the engineering alloys used today [21]. However, after longer incubation periods, these alloys will suffer from MD. In this study, the protective oxide on the sample surface was partially disturbed by light grinding. Nevertheless, it took 5000h to produce a significant MD attack. The mechanism of MD is similar to that of austenitic stainless steels (see Section 13.4.4) and involves dissolution of carbides by selective oxidation to give a carbide-free ferritic surface layer with a decreasing Cr and Al gradient towards the (Cr, Al, Fe)-oxides on the surface. The ferritic surface layer is thinner than the corresponding (FeNi)-austenite layer on austenitic steels and also without graphite channels, indicating lower metal flux and slower MD kinetics. A very simple approach is to use Einstein's random walk model, $d^2 = 2Dt$, to calculate the diffusion times required. The effective metal diffusion distance is set to $d = 0.3$ m, i.e. the approximate thickness of the carbide-free and (Cr-Al)-depleted ferrite border seen in Fig. 13.7. The bulk diffusion coefficient of Cr and Al in ferrite is $6.1 \cdot 10^{-18}$ m²/s and $3 \cdot 10^{-17}$ m²/s respectively, at 650 °C [22,23].

$$t_{Cr} = \frac{d^2}{2D_{eff}} = \frac{(0.3 \cdot 10^{-6})^2}{2 \cdot 6.1 \cdot 10^{-18}} = 7353s \quad 2h \quad 13.1$$

$$t_{\text{Al}} = \frac{d^2}{2D_{\text{eff}}} = \frac{(0.3}{2} \frac{10^{-6}}{3} \frac{10^{-17}}{10^{-17}})^2 = 1500\text{s} \quad 0.4\text{h} \quad 13.2$$

This means that chromium diffusion through the ferrite border is the rate-limiting step and MD corrosion may progress at a rate of $0.3/2 = 0.15$ m/h. This is about seven times slower than the metal dusting rate on 304L austenitic steel [7, 8]. The ferrite border probably has defects and grain boundaries, which enhance the Cr diffusion and corrosion rate, but FeCrAl alloys are nevertheless expected to display much lower MD corrosion rates compared to austenitic steels.

The steps and operating mechanisms during MD on FeCrAl-alloys can be summarized as follows:

1. Carburization and carbide formation, initially $M_{23}C_6$ carbides, then M_7C_3 and Fe_3AlC (perovskite -carbide) at higher carbon activity to an observed carbide fraction of 69% (34% M_7C_3 + 35% -carbide).
2. Complete dissolution by selective oxidation of all carbides formed, i.e. a ferrite-border forms, through which Cr and Al diffuse under subsequent Cr–Al–Fe oxide formation (Type III).
3. Simultaneous fragmentation of the ferrite border due to the graphitization process (Type II), as seen in Fig. 13.8.
4. The metal dust may act as a catalyst for filamentous carbon formation (Type IV). The corrosion products are thus Cr–Al–Fe oxides, ferritic metal dust, and carbon in different forms. Al is a ferrite stabilizer, which is in accordance with the observed ferritic border and the ferritic metal fragments. However, at a later stage, when Cr and Al are consumed in the ferritic fragments by oxidation, the ferrite may transform to cementite dust, thus being the corrosion end product.

13.4.4 Austenitic stainless steels

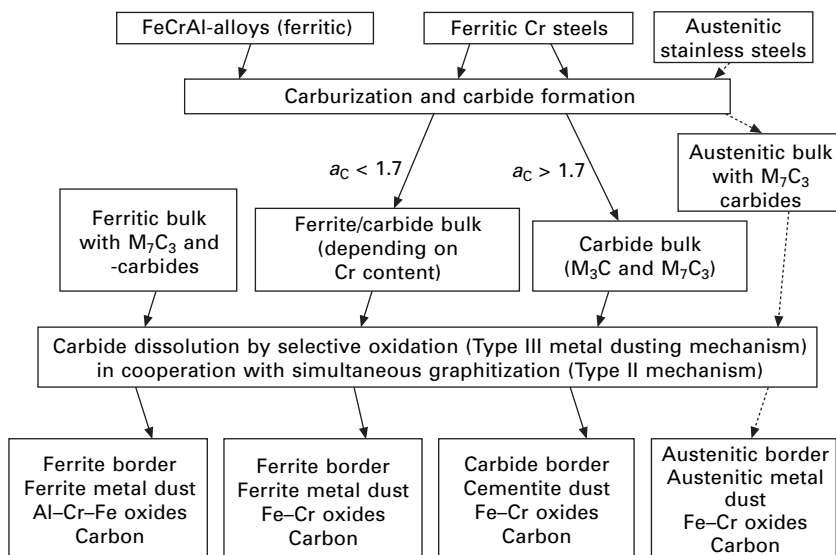
For comparison, a description of the MD process on austenitic stainless steels, which is described in detail in [7, 8] is included:

1. Carburization and carbide formation, initially $M_{23}C_6$ carbides, then M_7C_3 and M_3C carbides form at higher carbon activity up to a phase fraction of 85%.
2. Complete dissolution by selective oxidation of all carbides, resulting in a carbide-free austenite-border with a graphite channel substructure. These graphite channels enhance the Cr diffusion through the layer with subsequent Cr–Fe oxide formation in the metal/coke interface (Type III mechanism). The Cr diffusion is the rate-limiting step for the MD process.
3. Simultaneous fragmentation of the austenite border into smaller and smaller austenitic metal dust particles due to the graphitization process (Type II).

4. The austenite dust acts as catalyst for carbon nanotube formation (Type IV). The end corrosion products are thus chromia, Cr–Fe spinel, austenitic metal dust and carbon in different forms. Ni is an austenite and graphite stabilizer, which is in accordance with the observed austenite-border with graphite channels and the austenite metal dust.

The principal Gibbs energy diagram describing the situation in step (4) above, is shown in Fig. 13.14d. In this case, two equilibria are possible; austenite/nanotubes (small diameter) or Ni-alloyed cementite/nanotubes (larger diameter). However, only austenitic particles were detected in the coke [7, 8]. This indicates that the carbon activity in the porous coke is lower than 2.1 [7, 8] (the a_C needed for Fe–Ni cementite formation) but higher than 1.7 (since Fe_3C is formed in the same environment).

A summarizing MD mechanism chart for ferritic and austenitic stainless steels is given in Fig. 13.15.



13.15 Schematic metal dusting mechanism chart for ferritic and austenitic stainless steels. The marked carbon activity is calculated at 650 °C; however, the principles are applicable in a wide temperature range. Al is a ferrite stabilizer and subsequently ferritic dust is formed. Cr is a cementite stabilizer and preferably cementite dust is formed. However, the carbon activity is high enough to form cementite nanoparticles even in the case of pure iron. Ni is an austenite stabilizer and subsequently austenitic metal dust is formed.

13.5 Conclusions

In contrast to pure iron, it is not possible to explain the MD process on high-alloyed steels by a solely carbon-induced corrosion. The dissolution of the alloyed carbides by selective oxidation during metal dusting is one of the key mechanisms, denoted Type III. The driving force for MD in pure iron (and low-alloyed steels) is explained by separating the initial, cementite-formation stages (Type I), from the steady state MD process, which may be described as disintegration of supersaturated ferrite by graphite formation, denoted the Type II mechanism. The important conclusion is that there is no inexplicable step or phenomenon included in the different metal dusting processes that occurs in pure metals or engineering alloys. In fact, all the observed and reported observations are readily explained with four fundamental mechanisms, Types I, II, III and IV, which follows the known thermodynamics in the respective system $\text{Me}-\text{C}-\text{H}-\text{O}$. The Type IV mechanism, presented in detail in this chapter, may be described as continued disintegration of the corrosion products resulting in nanoparticles and carbon nanotube formation.

13.6 Acknowledgements

This work was financed by the High Temperature Corrosion Centre (HTC), Sandvik Materials Technology AB, Kanthal AB, AvestaPolarit AB, and financial support for writing this chapter, was provided by Professor Christofer Leygraf (KTH). Special thanks are expressed to Professor Mats Hillert (KTH), Rachel Pettersson and Staffan Hertzman for valuable discussions and comments on the manuscript. Thanks are expressed to Alexandra Kusoffsky for help with the thermodynamic calculations and to Joacim Hagström and Ulla Gustavsson for help with the FEG-SEM analysis and SEM-EDS analysis respectively and to Lars Göthe (SU) for the X-ray diffraction analyses. Thanks are also expressed to Bevis Hutchinson for supplying the ultra-pure iron samples.

13.7 References

1. A. Hultgren, M. Hillert, 'Betingelser för bildning av cementit vid uppkolning av nickelstål' *Jernkont. Ann.* **137**, 7, 1953.
2. F. Eberle, R.D. Wylie, 'Attack on metals by synthesis gas from methane-oxygen combustion' *Corrosion* **15**, 12 622t–626t, 1959.
3. R.F. Hochman, 'Catastrophic deterioration of high temperature alloys in carbonaceous atmospheres' *Electrochemical Society Inc. Proc.*, **77-1**, 715–732, 1976.
4. H.J. Grabke, 'Metal dusting of low- and high-alloy steels' *Corrosion* **51**, (9) 711–720, 1995.
5. E. Pippel, J. Woltersdorf, R. Schneider, 'Micromechanisms of metal dusting on Fe-base and Ni-base alloys' *Materials and Corrosion*, **49**, (5), 309–316, 1998.
6. R. Schneider, E. Pippel, J. Woltersdorf, S. Strauss, H.J. Grabke, 'Microprocesses of metal dusting on nickel and Ni-base alloys' *Steel Research*, **68**, (7), 326–332, 1997.

7. P. Szakálos, R. Pettersson, S. Hertzman, 'An active corrosion mechanism for metal dusting on 304L stainless steel' *Corrosion Science*, **44**, (10), 2253–2270, 2002.
8. P. Szakálos, 'Mechanisms of metal dusting on stainless steels' Licentiate Thesis, ISBN 91-7283-260-6, Stockholm, 2002.
9. P. Szakálos, L. Liu, 'Mechanisms of metal dusting – Application to alloy composition, temperature and pressure' *15th International Corrosion Conference ICC*, Granada, Sept. 2002.
10. P. Szakálos, 'A new corrosion mechanism for metal dusting on 304L stainless steel' *International Workshop on Metal Dusting*, Chicago, 26–28 Sept 2001.
11. Z. Zeng, K. Natesan, V.A. Maroni, 'Investigation of metal dusting mechanism in Fe-base alloys using Raman spectroscopy, X-ray diffraction and electron microscopy' *Oxidation of Metals*, **58** (1), 147–170, 2002.
12. E. Pippel, J. Woltersdorf, H.J. Grabke, S. Strauss, 'Microprocesses of metal dusting on iron' *Steel Research*, **66**, (7), 217–221, 1995.
13. B. Sundman, B. Jansson, J-O. Andersson, *CALPHAD* **9**, 153–190, 1985.
14. M. Hillert, N. Lange, 'The structure of graphite filaments' *Zeitschrift für Kristallographie* **111**, 1, 1958.
15. C.H. Toh, P.R. Munroe, D.J. Young, 'Metal dusting of Fe–Cr and Fe–Ni–Cr alloys under cyclic conditions' *Oxidation of Metals*, **58** (1) 1–21, 2002.
16. R.G. Baligidad, A. Radhakrishna, 'Effect of hot rolling and heat treatment on structure and properties of high carbon Fe–Al alloys' *Materials Science and Engineering A Switzerland*, **308**, (1-2) 136–142, 2001.
17. M. Ozbayramoglu, M.V. Akdeniz, 'Structural examinations on iron aluminides' *8th International Metallurgy and Materials Congress*, Istanbul, Turkey, 6–9 June 1995.
18. R.E. Smalley, M.P. Grosboll, P.A. Willis, W.C. Kittrell, 'Process utilising two zones for making single-wall carbon nanotubes' US Patent no: US0202682, 2002.
19. C.M. Chun, J.D. Mumford, T.A. Ramanarayanan, 'Mechanisms of metal dusting corrosion of iron' *J. Electrochem. Soc.* **149** (7), B348–B355, 2002.
20. A. Schneider, 'Iron layer formation during cementite decomposition in carburising atmospheres' *Corr. Sci.* **44** (10), 2353–2365, 2002.
21. B. A. Baker, G. D. Smith, 'Metal dusting in a laboratory environment-alloying addition effects', *International Workshop on Metal Dusting*, ANL, Argonne, Illinois 26–28 Sept. 2001.
22. I. Kaur, W. Gust, L. Kozma, *Handbook of Grain and Interphase Boundary Diffusion Data*, 1989.
23. J. Fridberg, L-E. Törndahl, M. Hillert, Diffusion in iron, *Jernkont. Ann.* **153**, 263–276, 1969.

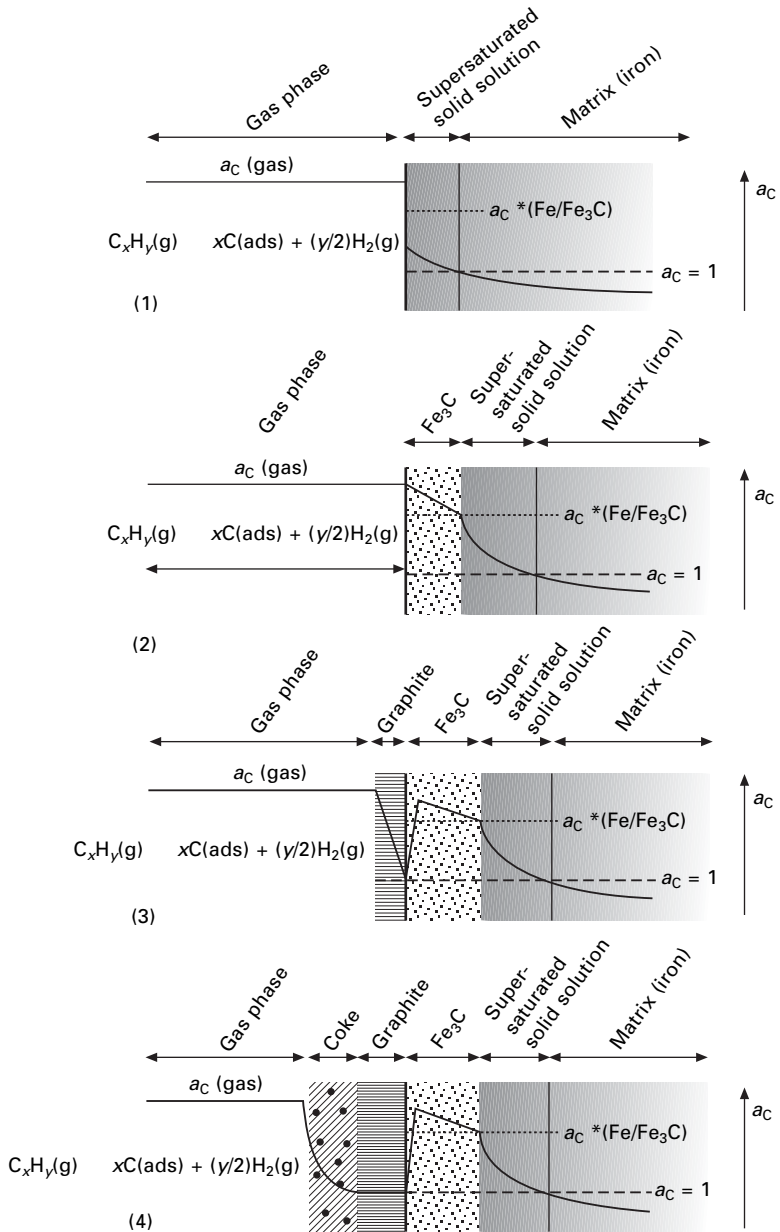
Filamentous carbon formation caused by catalytic metal particles from iron oxide

F BONNET and F ROPITAL,
Institut Français du Pétrole, France and
Y BERTHIER and P MARCUS,
Laboratoire de Physico-Chimie des Surfaces, France

14.1 Introduction

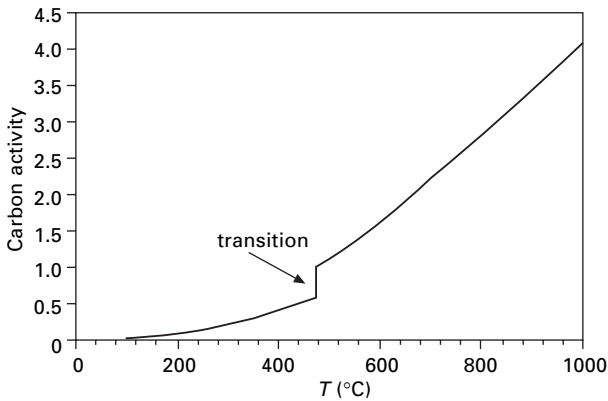
The formation of carbon filaments, which occurs at carbon activities $a_C > 1$ over a range of temperatures 450–700 °C, is a major problem in many chemical and petrochemical processes where hydrocarbons or other strongly carburising atmospheres are involved. The carbon deposition on reactor walls induces localised disruption in the process such as heat-transfer reduction and pressure drops. Excessive carbon deposition causes deterioration of the furnace alloys and high cleaning cost. The iron-catalysed formation of filamentous carbon has been studied from carbon monoxide and a variety of saturated and unsaturated hydrocarbons. Several investigations performed by Hochman [1, 2] and Grabke and coworkers [3–5] provide a good understanding of the thermodynamics, the kinetics and the mechanisms of coke deposition. One of the mechanisms has been proposed for iron and low-alloyed steels. Coke formation involves reactions at the gas/metal interface and carbon diffusion within the metal. Fundamental studies with transmission electron microscopy (TEM) observations [6, 7] have clearly shown that the unstable carbide M_3C , which is formed at the iron surface after supersaturation, is an intermediate of the reaction. The formation of catalytic particles on iron and on low-alloy steels is generally explained by the following reaction mechanisms (Fig. 14.1).

1. Decomposition of hydrocarbons at the metal surface (adsorption and dissociation of hydrocarbons molecules) and supersaturation of the metallic phase with dissolved carbon by transfer from the carburising gas mixture;
2. When the carbon activity in the metal is higher than the carbon activity for cementite (Fe_3C) formation ($a_C > a_{Fe/Fe_3C}$) Fig. 14.2, the supersaturation of carbon in the metal causes nucleation and growth of cementite at the metal surface and at the grain boundaries.
3. The carbon diffusion is very slow through the cementite in the temperature range 400–700 °C [8]. Consequently, the cementite layer acts as a barrier for further carbon transfer from the gas phase to the metal.



14.1 Mechanism currently proposed to explain the catalytic particle formation on iron and low alloy steels (adapted from [1–5]).

4. The precipitation of graphite at the cementite surface leads to a carbon activity of $a_C = 1$ at the graphite/cementite interface. Cementite becomes unstable and starts to decompose according to the following reaction: $\text{Fe}_3\text{C} \rightarrow 3\text{Fe} + \text{C}$.



14.2 Influence of the temperature on the carbon activity for cementite formation in γ -iron.

5. Carbon atoms resulting from Fe_3C decomposition are attached to the basal planes of graphite that grow into the cementite [9, 10]. Because of the concentration gradient, iron atoms diffuse through the graphite to the outer surface and agglomerate to small particles (about 20 nm diameter). Formation of metal particles is energetically more favourable than complete layers.
6. These particles act as a catalyst for further carbon deposition and growth of graphitic filaments.

It was accepted relatively early that the mechanism of carbon filament growth is based on the catalytic decomposition of hydrocarbons by particles present at the filament tips. Graphitic filaments are formed when carbon deposition occurs from the gas phase on one side of the active catalyst particle, followed by diffusion through the catalytic particle, and finally precipitation as graphite at the metal–carbon filaments interface. The driving force for the diffusion process would be the carbon activity gradient [11, 12].

The nature of the catalytic particle has been discussed for the iron-catalysed filament growth. Measurements of carbon deposition rates were done by Baker *et al.* [13, 14] in controlled atmosphere electron microscopy (CAEM). They showed that the activation energy associated with the growth of filaments is closed to the activation energy of carbon diffusion in the corresponding metal. These experiments were performed with different metals such as Ni, γ -Fe, α -Fe, Co, V, Mo and Cr. They concluded that the carbon diffusion through the catalytic particle is the rate-limiting step. A surface diffusion mechanism was also postulated. These results suggest that the catalytic particle is the reduced metal. Other studies have concluded that bulk carbides [15] or surface carbides are the active catalyst. Bianchini and Lund [16] proposed that when carbon activity in the gas phase is above the thermodynamic limit

for the formation of carbide, nucleation of this phase occurs on the reactive face of the catalytic particle. This surface carbide separates the metallic bulk of the catalyst from direct contact with the surrounding atmosphere.

In spite of the disagreement on the nature of catalytic particles (metal or carbide), there is some agreement that protective oxide scales, including iron oxides, can prevent surface carburisation and coke deposition. In the industrial cracking furnace tubes where pyrolysis reactions take place, various oxide scales are found at the metal surface. The formation of these oxides occurs during the start of the process or during the 'decoking' operations in which coke is burnt in an oxidising gas atmosphere such as steam or air. The solubility of carbon in the iron oxides such as FeO and Fe₃O₄ has been measured by Wolf and Grabke [17] to be below 0.01 ppm even at 1000 °C. This low solubility is expected to prevent any bulk diffusion of carbon in iron oxides and thus carburisation of the metal. However, when the oxide scales are exposed to reducing and carburising atmospheres, such as hydrocarbon feeds, interfacial reactions between the oxide layer and the hydrocarbon species can occur.

Baker *et al.* [18] compared the catalytic reactivity of metallic iron (Fe), wustite (FeO) and haematite (Fe₂O₃) as precursors for the formation of carbon filaments from ethane and acetylene. Their results lead to the conclusion that the order of activity is FeO > Fe ~ Fe₂O₃. It was proposed that the high catalytic activity of FeO could be attributed to the formation of iron-rich sponge-like product of high surface area. Moreover, small metallic particles can be formed from FeO reduction, which would lead to the rapid production of graphitic filaments. Similarly Grabke [19] proposed, in the case of Fe–Cr alloys, that the reduction of mixed oxides (Fe, Cr)₂O₃ in a reducing and carburising atmosphere can induce the formation of catalytic particles.

Tokura *et al.* [20] investigated the reactivity of pre-oxidised iron samples in CH₄–H₂ gas atmospheres at 1000 °C. They compared the kinetics of the coke deposition for different pre-oxidised surface states. The coke formation rate increased with the initial oxide layer thickness. This was interpreted by the formation of an active 'metallic' surface generated by the reduction of the oxide scale.

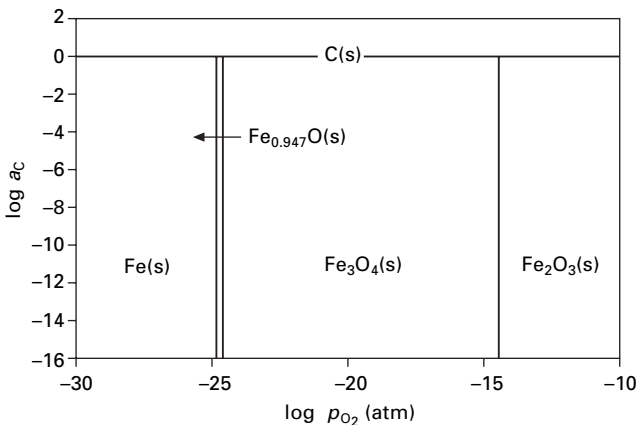
To summarise, three mechanisms are currently proposed to explain the participation of iron oxide in catalytic coking:

1. Iron oxides, once reduced, increase the surface area which increases the kinetics of the carburisation step.
2. Iron oxides are reduced in fine metallic particles and act as catalysts for graphitic filament growth.
3. Finally, iron oxides or partially reduced iron have a catalytic activity in the hydrocarbon decomposition processes.

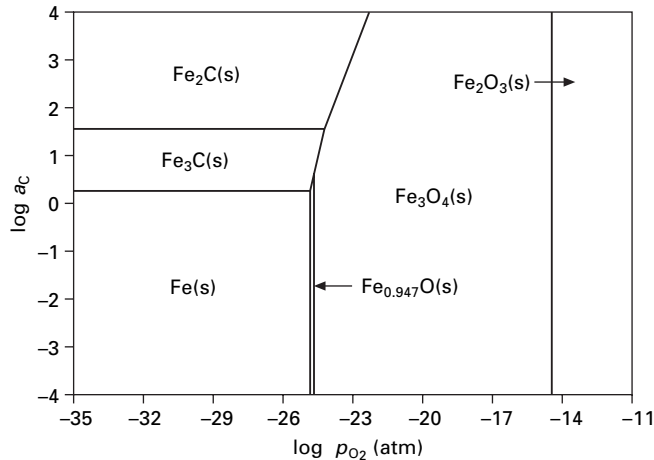
In the present study, the metastable Fe–C–O phase diagram was calculated over the range of temperatures where catalytic coke is formed, to define the different reactions that can occur at the oxide/gas interface in a reducing and carburising atmosphere. The kinetics of coke formation on reduced and pre-oxidised iron surfaces was investigated with a thermobalance (ATG) and the different steps of the reaction were studied by sequential exposure experiments. Scanning electron microscopy (SEM) observations and X-ray diffraction (XRD) analysis were performed to investigate the iron oxide behaviour and to identify the phase transformations. The objective of this work is to elucidate the role of iron oxides in the mechanism of coke deposition.

14.2 Thermodynamic calculations

To define the different reactions that can occur at the metal/gas interface and oxide/gas interface in isobutane/hydrogen mixtures, the Fe–C–O phase diagram has been calculated according to the oxygen partial pressure and carbon activity. In a carburising atmosphere, iron carbides are thermodynamically unstable with respect to graphite. However, the formation rate of graphite is so slow at 600 °C that cementite is generally formed as a metastable phase. Therefore, the Fe–C–O phase diagram was calculated (Figs 14.3 and 14.4) for stable and metastable conditions. Numerous iron carbides are reported in the metallurgical literature with compositions ranging from Fe_3C to Fe_2C when the carbon activity in the gas phase increases. Cementite is the most commonly formed iron carbide phase, but other metastable iron carbides (Fe_7C_3 and Fe_5C_2) have also been identified in association with the formation of filamentous carbon [21, 22]. From a thermodynamic point of view, only two of them (Fe_3C and Fe_2C) have been studied under metastable equilibrium conditions. Thermodynamic data are available only for these two compounds.



14.3 Stable Fe–C–O phase diagram at 600 °C.



14.4 Metastable Fe-C-O phase diagram at 600 °C.

Table 14.1 Variation of the Gibbs energy during the formation of the different phases in Fe-C-O system

Reaction	$\text{f}G^\circ = A + BT$ (T in K) (cal/mol)	Uncertainty on $\text{f}G^\circ$ (cal/mol)	Range of temperature (K)
$0.947\text{Fe(s)} + 1/2\text{O}_2(\text{g}) \rightleftharpoons \text{Fe}_{0.947}\text{O(s)}$	$-63\,222 + 15.80T$	± 1000	843–1650
$3\text{Fe(s)} + 2\text{O}_2(\text{g}) \rightleftharpoons \text{Fe}_3\text{O}_4(\text{s})$	$-265\,772 + 78.40T$	± 2000	473–1870
$2\text{Fe(s)} + 3/2\text{O}_2(\text{g}) \rightleftharpoons \text{Fe}_2\text{O}_3(\text{s})$	$-195\,479 + 61.24T$	± 3000	473–1735
$3\text{Fe(s)} + \text{C(gr)} \rightleftharpoons \text{Fe}_3\text{C(s)}$	$6926.9 - 6.78T$	± 100	473–1273
$2\text{Fe}_3\text{C(s)} + \text{C(gr)} \rightleftharpoons 3\text{Fe}_2\text{C(s)}$	$4850 - 2.5T$	–	443–1296

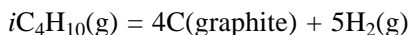
The thermodynamic equilibrium between metallic iron (Fe), iron oxides (FeO, Fe₃O₄ and Fe₂O₃), iron carbides (Fe₃, Fe₂C) and isobutane/hydrogen mixture were calculated at 600 °C. Thermodynamic data for the iron oxide and cementite were provided by Thermodata¹. The values of Browning *et al.* were used for the Hägg carbide Fe₂C [23] Tables 14.1 and 14.2.

The discussion will be developed in terms of the thermodynamic carbon activity a_C . Formally, a_C is the ratio of carbon fugacity as it exists in the reaction environment to the fugacity of carbon in its standard state (graphite) at the same temperature. In processes involving hydrocarbon and hydrogen, carbon activity can be calculated from the following equilibrium:

¹ Thermodata, 1001 Avenue Centrale, BP 66 Grenoble Campus, – 38402 Saint Martin d'Hères cedex, France.

Table 14.2 Stability fields of iron, iron carbide, iron oxide and graphite

Chemical equilibrium	Stability fields
$0.947\text{Fe(s)} + \frac{1}{2}\text{O}_2\text{(g)} \rightleftharpoons \text{Fe}_{0.947}\text{O(s)}$	$\ln p_{\text{O}_2} = \frac{2}{RT} {}_fG_{\text{Fe}_{0.947}\text{O}}^\circ$
$3\text{Fe(s)} + 2\text{O}_2\text{(g)} \rightleftharpoons \text{Fe}_3\text{O}_4\text{(s)}$	$\ln p_{\text{O}_2} = \frac{{}_fG_{\text{Fe}_3\text{O}_4}^\circ}{2RT}$
$3\text{Fe}_{0.947}\text{O(s)} + 0.394\text{O}_2\text{(g)} \rightleftharpoons 0.947\text{Fe}_3\text{O}_4\text{(s)}$	$\ln p_{\text{O}_2} = \frac{0.947 {}_fG_{\text{Fe}_3\text{O}_4}^\circ - 3 {}_fG_{\text{Fe}_{0.947}\text{O}}^\circ}{0.394 RT}$
$2\text{Fe}_3\text{O}_4\text{(s)} + \frac{1}{2}\text{O}_2\text{(g)} \rightleftharpoons 3\text{Fe}_2\text{O}_3\text{(s)}$	$\ln p_{\text{O}_2} = \frac{6 {}_fG_{\text{Fe}_2\text{O}_3}^\circ - 4 {}_fG_{\text{Fe}_3\text{O}_4}^\circ}{RT}$
$3\text{Fe}_{0.947}\text{O(s)} + 0.947\text{C(gr)} \rightleftharpoons 0.947\text{Fe}_3\text{C(s)} + \frac{3}{2}\text{O}_2\text{(g)}$	$\ln p_{\text{O}_2} = \frac{6 {}_fG_{\text{Fe}_{0.947}\text{O}}^\circ - 1.894 {}_fG_{\text{Fe}_3\text{C}}^\circ}{3RT} + \frac{2}{3} \ln a_{\text{C}}^{0.947}$
$\text{Fe}_3\text{O}_4\text{(s)} + \text{C(gr)} \rightleftharpoons \text{Fe}_3\text{C(s)} + 2\text{O}_2\text{(g)}$	$\ln p_{\text{O}_2} = \frac{{}_fG_{\text{Fe}_3\text{O}_4}^\circ - {}_fG_{\text{Fe}_3\text{C}}^\circ}{2RT} + \frac{1}{2} \ln a_{\text{C}}$
$2\text{Fe}_3\text{O}_4\text{(s)} + 3\text{C(gr)} \rightleftharpoons 3\text{Fe}_2\text{C(s)} + 4\text{O}_2\text{(g)}$	$\ln p_{\text{O}_2} = \frac{2 {}_fG_{\text{Fe}_3\text{O}_4}^\circ - 3 {}_fG_{\text{Fe}_2\text{C}}^\circ}{4RT} + \frac{3}{4} \ln a_{\text{C}}$
$3\text{Fe(s)} + \text{C(gr)} \rightleftharpoons \text{Fe}_3\text{C(s)}$	$\ln a_{\text{C}} = \frac{{}_fG_{\text{Fe}_3\text{C}}^\circ}{RT}$
$2\text{Fe}_3\text{C(s)} + \text{C(gr)} \rightleftharpoons 3\text{Fe}_2\text{C(s)}$	$\ln a_{\text{C}} = \frac{3 {}_fG_{\text{Fe}_2\text{C}}^\circ - 2 {}_fG_{\text{Fe}_3\text{C}}^\circ}{RT}$



$$a_C = \frac{K(p_{iC_4H_{10}})^{1/4}}{p_{H_2}^5}$$

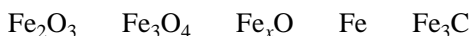
with $\ln(K) = 30.43$ at 600°C .

K is the equilibrium constant of the chemical reaction and $p_{iC_4H_{10}}$, p_{H_2} are the partial pressures of the gases iC_4H_{10} and H_2 respectively. The experimental conditions used in this study (30% iC_4H_{10} , 30% H_2 , 40% Ar) establish a carbon activity of $a_C = 6710$ at 600°C .

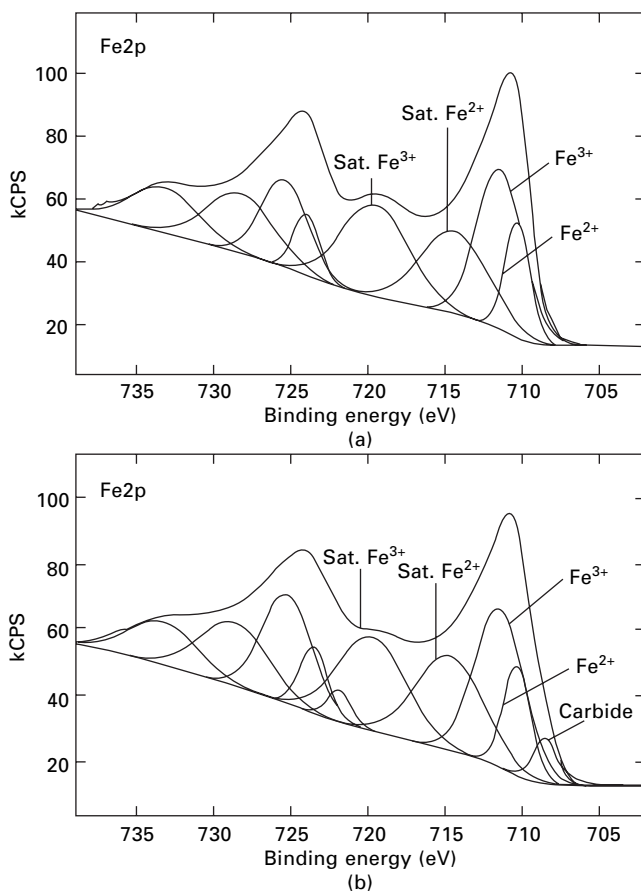
On the basis of the metastable diagram, iron oxides can be directly converted into carbides in carburising and reducing atmospheres. The phases involved in the oxide/carbide transition depend on the carbon activity and on the temperature. At 600°C Fe_3C can be produced from Fe_3O_4 for carbon activities larger than 3.6 Fig. 14.4. Intermediate oxycarbide species $Fe_xC_yO_z$ may be formed during this reaction.

This transformation is well known [24] for chromium oxide Cr_2O_3 and occurs when the alloy is covered with a graphite layer and heated to temperatures $> 1050^\circ\text{C}$. The atmosphere at the oxide/metal interface has a carbon activity $a_C = 1$ (equilibrium with graphite) and its oxygen activity decreases because of the reducing gas mixture. These conditions induce a shift of the equilibrium Cr_2O_3/Cr_3C_2 in favour of the carbide. Our calculations show that this oxide/carbide transition also exists for iron oxide.

However, kinetic factors must be taken into account in the transformation. Indeed, another path, different from the thermodynamic prediction, can occur if the rate of the oxide/carbide conversion is impeded. The iron oxides can be progressively reduced in iron and then converted into carbide:

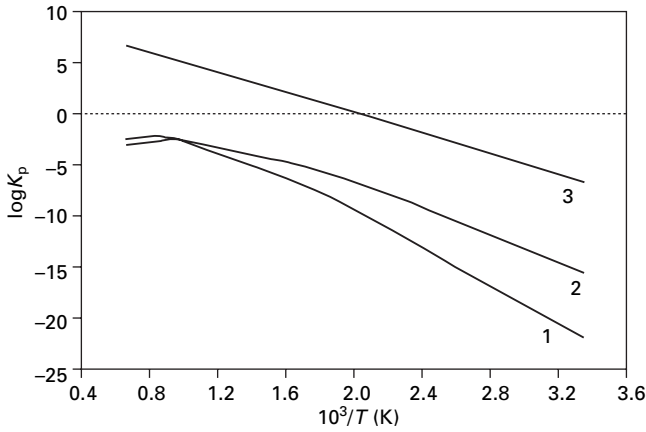


Previous studies [25] have been performed to identify the first stages of the oxide/carbide transformation in strongly carburising atmosphere. Iron samples with pre-oxidised surfaces were maintained in contact with isobutane/hydrogen gas mixture ($a_C = 2887$) at 550°C . The oxide/carbide transition was characterised by X-ray photoelectron spectroscopy. The results show that iron carbide is obtained on the sample surface after 30 min in the reducing and carburising gas mixture (Fig. 14.5). No metallic iron was detected, which indicates that iron carbide is present in the oxide layer. This gives evidence that the iron oxides present initially on the surface sample can be directly converted into iron carbide without the formation of metallic iron. Experimental works performed by Nakagawa *et al.* [26] confirm these results: Fe_3O_4 (face-centred cubic) may be directly transformed in Fe_3C (hexagonal) in $CO-CO_2$ mixture at 550°C .

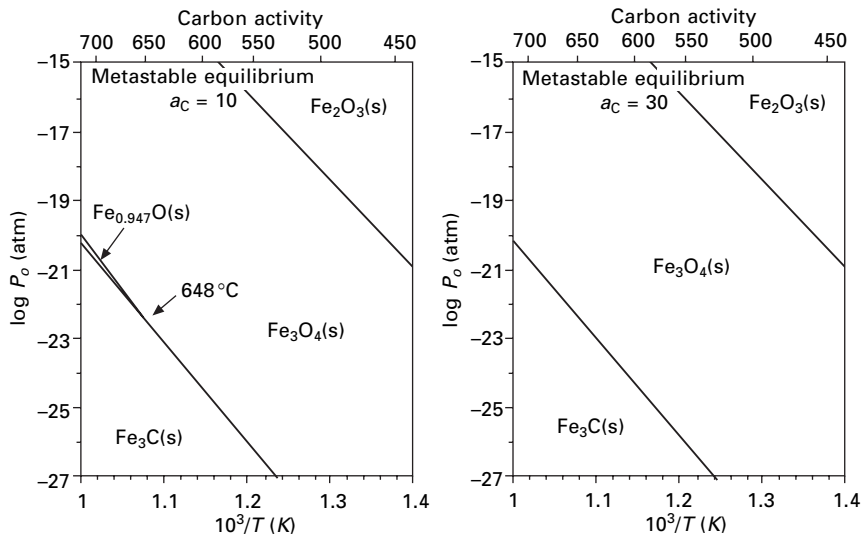


14.5 XPS spectra of Fe2p region obtained on the oxidised (a) and coked (b) iron surface after 30 min in 50% H_2 –50% $i\text{C}_4\text{H}_{10}$ gas mixture at 550 °C [25].

Thermodynamic calculations show that iron carbide Fe_3C , once formed, can also participate in the reduction of Fe_2O_3 [27]. The reduction reaction is possible at temperatures above 230 °C (Fig. 14.6). To ensure that the oxide/carbide transformation occurs in the overall temperature range where catalytic coke is formed (450 °C–700 °C), we studied the influence of the temperature on the different equilibria that occur in the Fe–O–C system (Fig. 14.7). The oxide/carbide transition occurs in the entire domain where catalytic coke is formed. Only the nature of the chemical species involved in the transformation varies with temperature. The triple point Fe_3C – $\text{Fe}_{0.947}\text{O}$ – Fe_3O_4 is shifted toward the high temperatures when carbon activity increases.



14.6 Equilibrium constant dependency on temperature for iron oxide reduction by iron carbide: 1, $\text{Fe}_3\text{O}_4 + \text{Fe}_3\text{C} = 3\text{FeO} + 3\text{Fe} + \text{CO}$; 2, $\text{FeO} + \text{Fe}_3\text{C} = 4\text{Fe} + \text{CO}$; 3, $3\text{Fe}_2\text{O}_3 + \text{Fe}_3\text{C} = 2\text{Fe}_3\text{O}_4 + 3\text{Fe} + \text{CO}$.



14.7 Influence of the temperature, carbon activity and oxygen partial pressure on the stability of iron oxides and iron carbides.

14.3 Experimental procedure

Thermogravimetric analyses (TGA) were performed on polycrystalline iron samples (10 mm \times 5 mm \times 1 mm) provided by Weber (purity > 99.9%). The chemical analysis is given in Table 14.3. Before inserting the samples into the furnace, they were first mechanically polished to 1200 grit SiC, cleaned

Table 14.3 Analysis of the iron samples (contents in mass %)

C	Mn	S	P	Cu	N
0.003	0.04	0.002	0.004	0.008	0.005

with ethanol and annealed for 12 h at 700 °C in hydrogen flow. In the thermobalance, the samples were suspended with a quartz filament and exposed to a flowing carburising atmosphere (30% H₂, 30% iC₄H₁₀, 40% Ar) at 600 °C under 1 atm. The mixture and the flow rate (50 ml/min) were controlled by mass flow meters. All the experiments were performed with a 'Setaram TG-DTA 92' apparatus.

In the thermobalance, the samples were first heated in a hydrogen flow up to 600 °C. Hydrogen was replaced by the gas mixture as soon as the temperature was reached and the mass of coke was continuously recorded. The iron samples were exposed during different time periods of coking. To stop the reaction, the gas mixture was replaced by pure argon (purity > 99.9996%) and the furnace was switched off. The samples remained in the furnace during cooling (30 min).

The evolution of the iron surface and the initial stages of the coke formation were characterised by SEM. The different phases present on the carburised sample were identified by XRD with Co-K α radiation.

The experiments were performed with two different initial surface states of iron: reduced and oxidised. To prepare the oxidised surface state, the samples could be initially heated in an oxidising gas flow up to 600 °C before inserting the coking gas mixture. However, the evolution of the carbon activity at the beginning of the experiment will be different from that obtained with hydrogen flow and the kinetics of the coking reaction could not be directly compared. So, the protocol used to prepare both surface states should not modify the evolution of carbon activity during the first step of the coking reaction. The oxygen content of the isobutane was used to prepare the initial surface states of iron. The higher oxygen content of isobutane N25 (Table 14.4) was used to obtain the oxidised surface state. As the activities of both carbon and oxygen increase during the introduction of the gas mixture (isobutane + hydrogen), the iron oxides Fe₃O₄ and Fe₂O₃ are momentarily stable until the gas mixture becomes reducing and carburising. This protocol allows us to obtain a reproducible oxidised iron surface. The isobutane N35 was used to prepare the reduced surface state. In both cases, when the hydrogen is replaced by the gas mixture at 600 °C, the carbon activity evolution in the thermogravimetric reactor is the same for both surface states' studies.

Table 14.4 Composition of the isobutane grade provided by 'Air liquide' and used in the coking experiments (in ppm) to obtain the reduced and oxidised surface states

Isobutane	Purity	H ₂ O	O ₂	CO ₂	Surface state
N25	>99.5%	–	100	–	Oxidised state
N35	>99.95%	5	10	10	Reduced state

14.4 Results

14.4.1 Characterisation of the initial surface states

In the reactor, the samples were exposed to the hydrogen/isobutane mixture for five minutes before stopping the reaction by replacing the gas mixture by pure argon. The surface state of the samples was characterised by SEM (Fig. 14.8) whereas the chemical composition and the thickness of oxide scales were given by XRD (Fig. 14.9) and electronic microprobe analyses. After 5 min contact with N25 isobutane, the iron sample is covered by an oxide layer of 1 μm composed of Fe_2O_3 ($25 \pm 10\%$) and Fe_3O_4 ($75 \pm 10\%$). According to the Fe–C–O phase diagram, when the atmosphere becomes reducing with $a_{\text{C}} = 6710$, haematite should be reduced in magnetite, and magnetite should be converted into Fe_3C . When N35 isobutane is used, no iron oxides are detected on the surface samples with the same techniques.

14.4.2 Kinetics of the catalytic coke formation

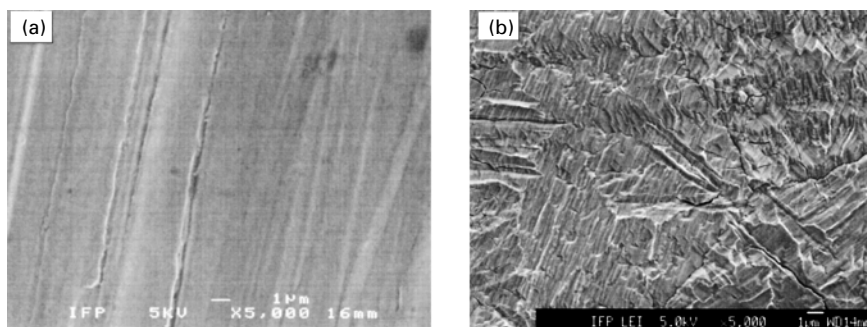
The mass of coke was measured after exposures for different lengths of time. The different stages of the reaction on the reduced and pre-oxidised iron samples were characterised by SEM and the nature of the reaction products was identified by XRD with Co K α radiation.

Coke formation on the reduced surface state

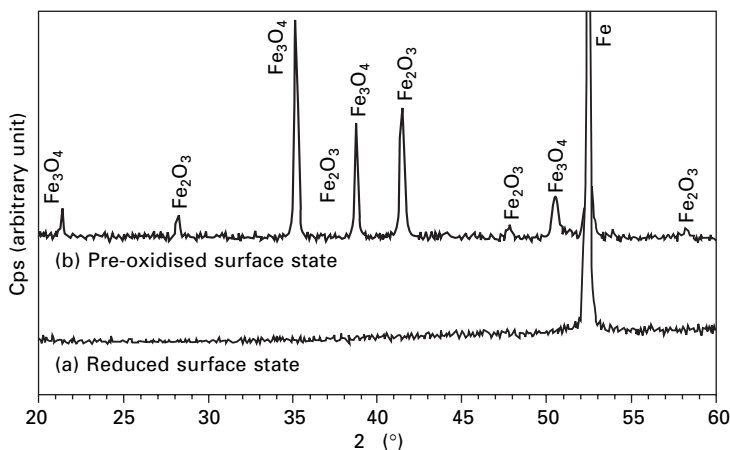
The mass of coke versus time is plotted in Fig. 14.10 and the SEM images are shown in Fig. 14.11. Nucleation and growth of graphite needles are observed on the iron surface after exposure of 10 min to isobutane. Nucleation occurs first at the grain boundaries. After 50 min, 95% of the surface is covered by carbon and small particles start to appear on the graphitic surface. The maximum size of the particles is about 0.1 μm . The number of particles increases with time and the particles induce the growth of filaments. Graphitic filaments appear on the surface after ~ 70 min.

Coke formation on the pre-oxidised surface state

Thermogravimetric measurements show that the rate of coke deposition is higher when the iron surface is initially pre-oxidised (Fig. 14.12). After 10

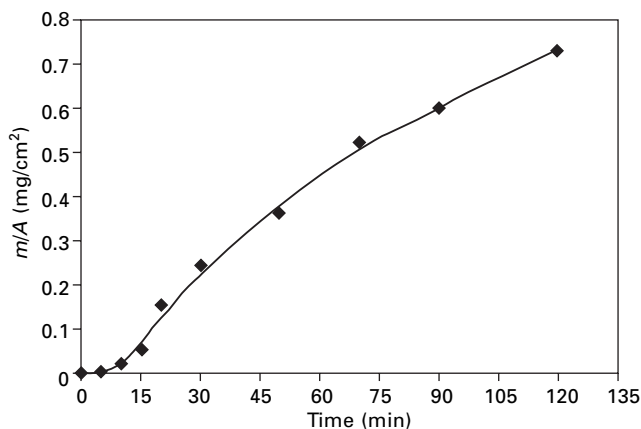


14.8 SEM characterisation of the iron surface after 5 min in contact with iC_4H_{10} - H_2 -Ar gas mixture at 600°C (total pressure = 1 atm): (a) initial reduced state, (b) initial pre-oxidised state.

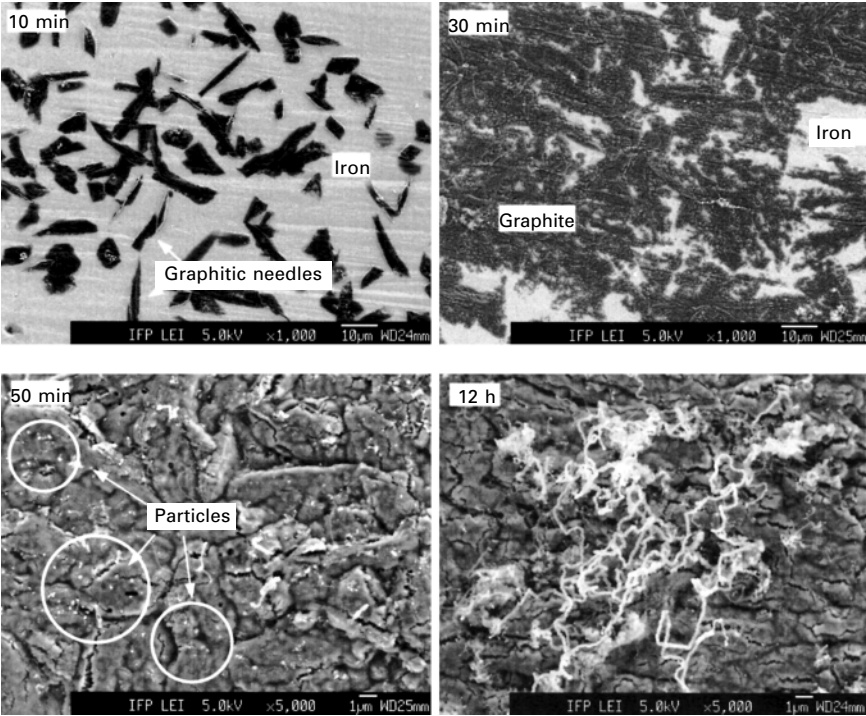


14.9 XRD analysis of the iron surface state after 5 min in contact with iC_4H_{10} - H_2 -Ar gas mixture at 600°C (total pressure = 1 atm) : (a) initial reduced state; (b) initial oxidised state.

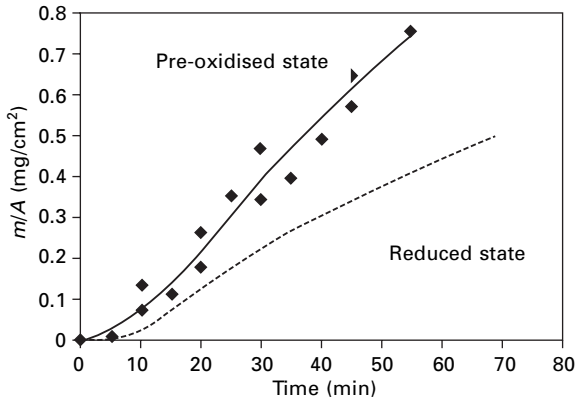
min in the gas mixture, the iron oxide layer is still present on the surface, but cementite and graphite are also detected. Another mechanism of catalytic particle formation is observed when the surface is initially pre-oxidised. In the carburising and reducing atmosphere, fragmentation of the oxide layer occurs and metallic particles with a size range of 50–400 nm are formed (Fig. 14.13). At the same time, graphite nucleation occurs on the metal surface. The size of metallic particles decreases with time. In contact with graphite, they are progressively transformed into particles that catalyse the graphitic filaments formation (Fig. 14.14). The first filaments appear after 20 min and their density increases rapidly with time. After 45 min, the iron surface is completely covered by graphitic filaments, whereas many hours are necessary on the reduced surface.



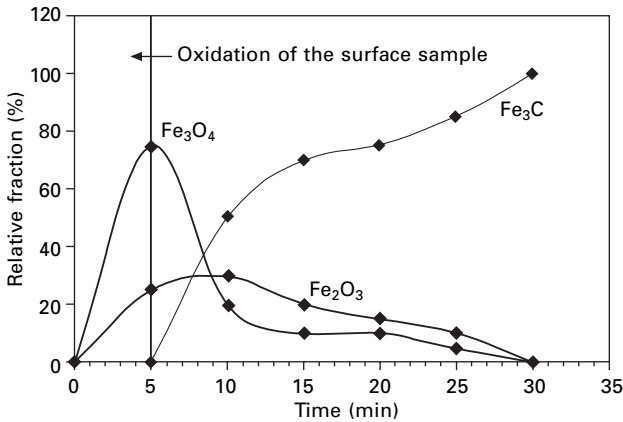
14.10 Mass gain versus time for iron samples (reduced surface) carburised in 30% iC_4H_{10} -30% H_2 -40% Ar gas mixture at 600°C (total pressure = 1 atm).



14.11 Evolution of the reduced iron surface after sequential exposure in iC_4H_{10} - H_2 -Ar atmosphere at 600°C.

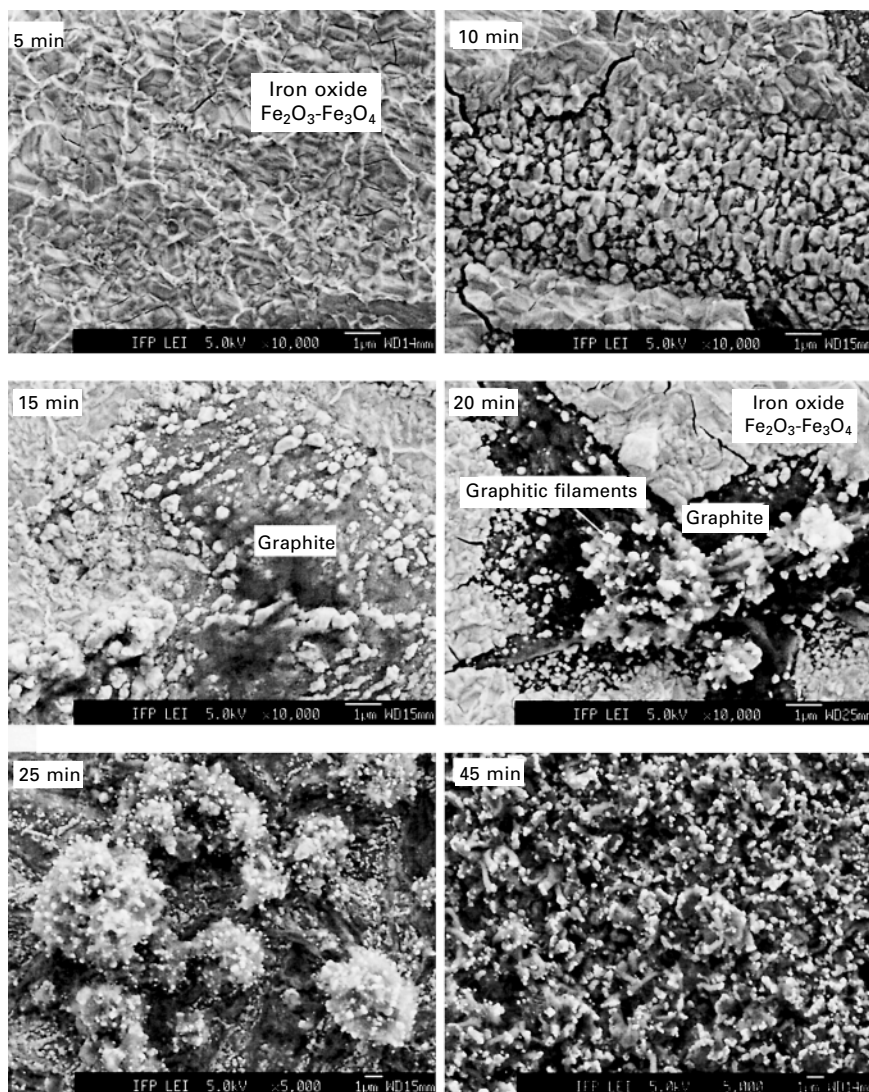


14.12 Mass gain versus time for iron (pre-oxidised and reduced surface state) samples carburised in 30% $i\text{C}_4\text{H}_{10}$ –30% H_2 –40% Ar gas mixture at 600°C (total pressure = 1 atm).



14.13 Evolution with time of the relative fractions of haematite (Fe_2O_3), magnetite (Fe_3O_4) and cementite (Fe_3C) present on the sample surfaces (initially pre-oxidised) exposed to a mixture of 30% $i\text{C}_4\text{H}_{10}$ –30% H_2 –40% Ar at 600°C.

A time of 30 min is required to eliminate the iron oxides from the surface. The relative fraction of magnetite (Fe_3O_4) decreases rapidly compared with the fraction of haematite (Fe_2O_3). This result is consistent with thermodynamic data. Haematite must be reduced in magnetite before its conversion into carbide. Wustite (Fe_xO), which is formed during the reduction of magnetite in metallic iron, is not detected during coke formation. This result is consistent with a direct conversion of iron oxide into carbide without the formation of metallic iron. The iron carbide that is formed is cementite (Fe_3C), which is different from thermodynamic predictions. Metallographic cross-sections show that cementite is also formed at the metal/oxide interface. The average size



14.14 Evolution of the oxidised iron surface after sequential exposure in 30% $i\text{C}_4\text{H}_{10}$ –30% H_2 –40%Ar atmosphere at 600 °C.

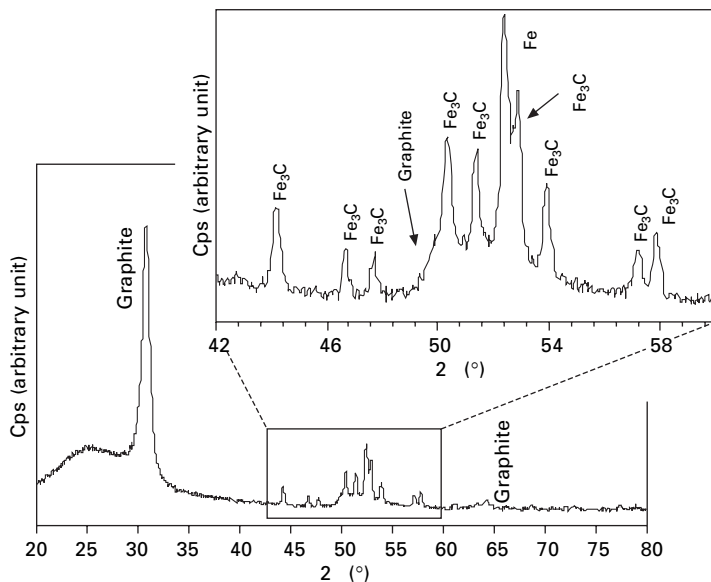
and the distribution of the precipitates are similar to those observed when the iron surface is initially reduced.

Characterisation of the catalytic particles

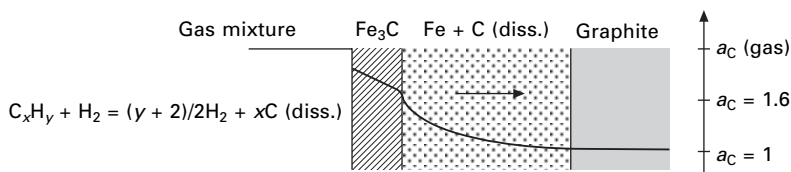
Iron samples with an initial reduced and pre-oxidised surface state are coked in the gas mixture 30% $i\text{C}_4\text{H}_{10}$ –30% H_2 –40%Ar for 11 h at 600 °C. After this

treatment, the coke deposition is removed from the surface samples, and the chemical nature of the catalytic particles is analysed using XRD. Catalytic particles are composed of metallic iron (Fe) and iron carbides (Fe_3C and Fe_2C) (Fig. 14.15). These results are consistent with the observations previously performed by the authors and carried out by TEM [28]. No difference was observed between the reduced or pre-oxidised surface states.

Thermodynamic calculations show that metallic iron is unstable with respect to the carburising atmosphere. Moreover, catalytic particles cannot be composed of pure iron carbide. Indeed, the carbon diffusion through cementite is very slow. The presence of cementite bulk should induce graphite nucleation around the particles and the deactivation of their catalytic properties. As already proposed by Bianchini and Lund [16], the catalytic particles are probably composed of a mixture of metallic iron and iron carbides. A carbide layer on the leading faces of the catalytic particles probably separates the metallic bulk of the catalyst from direct contact with the carburising atmosphere. The nature of the carbide layer depends on the carbon activity in the gas phase. More and more carbon-rich phases from Fe_3C (25 at.%C) via Fe_5C_2 (28.6 at.%C) to Fe_2C (33 at.%C) are formed with increasing carbon content in the iron. The different interfaces associated with the particles (gas/carbides/iron/graphite) induce a carbon activity gradient (Fig. 14.16). The carbon from the gas phase can diffuse through the catalytic particles to feed filament growth.



14.15 XRD analysis of the coke deposition present on an iron samples after exposure of 11 h in 30% $i\text{C}_4\text{H}_{10}$ –30% H_2 –40% Ar atmosphere at 600 °C.



14.16 Carbon activity gradient at 600°C through the catalytic particles.

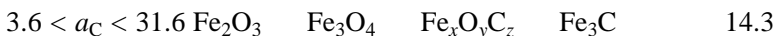
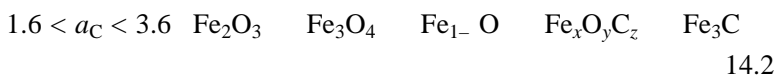
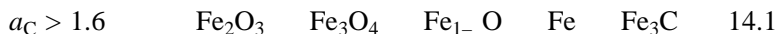
14.5 Discussion

14.5.1 Formation of catalytic particles on reduced iron surfaces

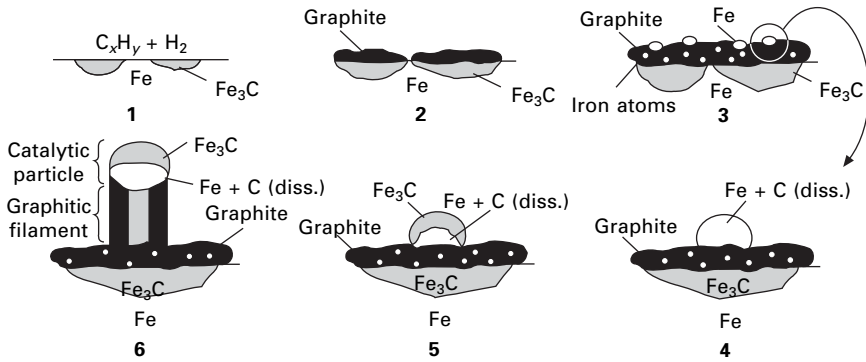
The observations performed on the initially reduced iron surfaces are consistent with the mechanism currently proposed to explain the formation of catalytic particles on iron. The different steps of this mechanism are summarised in Fig. 14.17: (1) carburisation of the iron surface, (2) graphite nucleation on cementite precipitates, (3) decomposition of iron carbide in contact with graphite and formation of metallic particles after diffusion of iron atoms through graphite layer, (4) carburisation of metallic particles, (5) formation of a carbide layer on the leading face of the catalytic particles and (6) filament growth.

14.5.2 Formation of catalytic particles on pre-oxidised iron surfaces

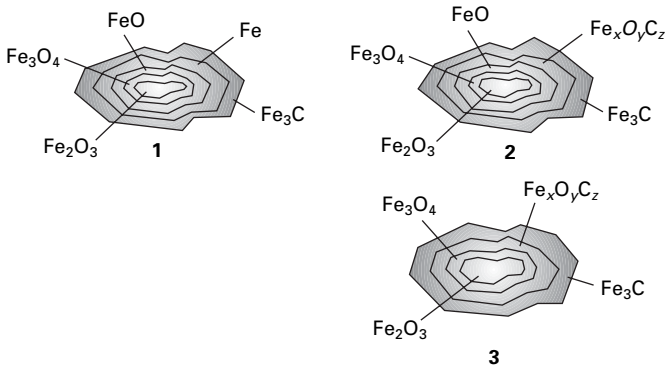
In reducing and carburising atmosphere, two mechanisms are proposed to explain the transformation of iron oxides. Iron oxides can be progressively reduced in metallic iron which is carburised to give cementite (reaction 14.1). Moreover the oxides can be directly converted into carbides probably through the formation of oxycarbide species (reactions 14.2 and 14.3). In the following reactions, the different steps and the carbon activity ranges are given for a temperature of 600°C:



The reduction of haematite pellets (Fe_2O_3) occurs by the growth of successive iron oxide layers as oxygen content decreases. The reduction reactions take place at the interface of the different oxide layers. The different mechanisms of transformation proposed are described in Fig. 14.18.



14.17 Mechanism currently proposed to explain the formation of catalytic particles on initially reduced iron surfaces.



14.18 Schematic representation of mechanisms of transformation of haematite pellets in a reducing and carburising atmosphere at 600 °C for different carbon activities; (1) $a_C > 1.6$; (2) $1.6 < a_C < 3.6$; (3) $3.6 < a_C < 31.6$.

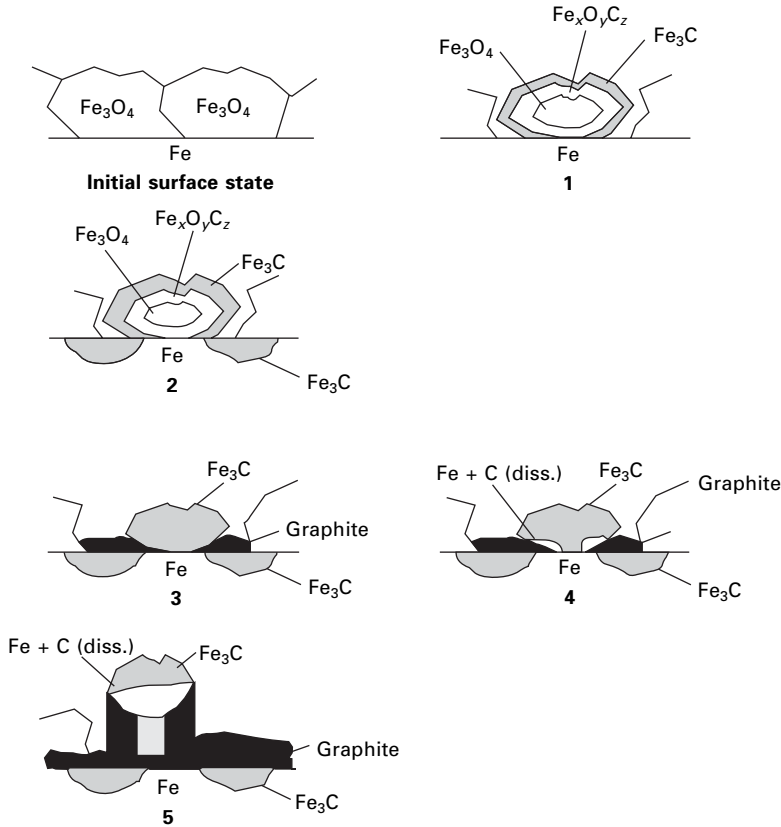
The thermodynamic calculations Fig. 14.4 and the previous results from X-ray photoelectron spectroscopy [25] showed that in strongly carburising atmosphere, the oxide/carbide transition occurs without the formation of metallic iron. Consequently, only mechanisms 2 and 3 in Fig. 14.8 can occur. The fragmentation of the iron oxide layer that occurs in the early stage of the reaction can be explained by the difference of the molar volume between the different iron oxides and the cementite (Table 14.5). For the $\text{Fe}_3\text{O}_4/\text{Fe}_3\text{C}$ transformation, the molar volume is divided by a factor of about 2.

A new mechanism is postulated to account for the transformation of the iron oxide in catalytic particles for carbon filament growth. This mechanism can be divided into five steps (Fig. 14.19):

1. In contact with reducing and carburising atmosphere, magnetite is transformed into cementite probably via an 'oxycarbide' species $\text{Fe}_x\text{O}_y\text{C}_z$.

Table 14.5 Volumetric mass and molar volume of haematite, magnetite, wustite, iron and cementite. These values are given for stoichiometric compounds

Phase	Fe_2O_3	Fe_3O_4	FeO	Fe	Fe_3C
Volumetric mass (10^3) (kg/m ³)	5.24	5.18	5.87	7.88	7.67
Molar volume (10^5) (m ³ /mol)	3.03	4.45	1.22	0.71	2.34



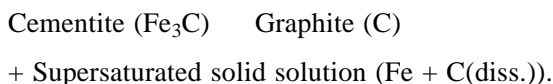
14.19 New mechanism proposed to explain the formation of catalytic particles on initially pre-oxidised iron surfaces (transformation of magnetite (Fe_3O_4) in catalytic particles).

The difference of molar volume between these different phases induces a fragmentation of the oxide scale. During the transformation, a cementite layer encompasses the magnetite grains.

- In the same time, through the cracks in Fe_3O_4 , hydrocarbon molecules reach the metal surface and their decomposition at the gas/metal interface (adsorption and dissociation of hydrocarbons molecules) induces carbon supersaturation of the metallic phase. When the carbon activity in the

metal is higher than the carbon activity for cementite formation, the supersaturation of carbon in the metal causes nucleation and growth of cementite at the metal surface and at the grain boundaries.

3. The carbon diffusion is very slow through the cementite in the temperature range 400–700 °C [8]. Consequently, the cementite layer acts as a barrier for further carbon transfer and the precipitation of graphite occurs on the cementite precipitates.
4. Cementite becomes unstable in contact with graphite and starts to decompose according to the following reaction:



The solid solution is formed at the graphite/cementite interface and induces the decomposition of cementite. At this step, the catalytic particles are composed of a mixture of cementite and iron supersaturated with carbon. The different layers induce a carbon activity gradient through the catalytic particles.

5. Carbon from the gas phase can diffuse through the catalytic particles via the cementite decomposition and precipitate in graphite, inducing a separation of the catalytic particles from the graphite surface. The particles act as catalysts for further carbon deposition and the continuous carbon diffusion induced the graphitic filament growth.

The mechanism currently proposed by Grabke *et al.*,¹⁹ which occurs on the reduced surface state, can then take place at the same time after the fragmentation of the oxide scale.

14.6 Conclusion

The thermodynamic equilibria between iron, iron oxides and iron carbides were calculated at 600 °C. According to the metastable Fe–C–O phase diagram, iron oxides can be directly converted into carbide in a reducing and carburising atmosphere without the formation of metallic iron. The chemical species involved in the oxide/carbide transition depend on the temperature and carbon activity. In the range of temperature where catalytic coking occurs, haematite (Fe₂O₃) must be reduced into magnetite (Fe₃O₄) before its conversion into carbide. The kinetics of the coke formation were studied by thermogravimetry in isobutane/hydrogen/argon mixture with $a_C = 6710$. A comparison was made between iron surfaces that were initially reduced or pre-oxidised. The observations performed on the initially reduced surface are consistent with the mechanism currently proposed to explain the formation of catalytic particles on iron. A new mechanism is proposed to explain the formation of catalytic particles on iron surfaces initially oxidised. In a carburising and reducing

atmosphere, iron oxides are progressively transformed into carbide. This reaction induces a fragmentation of the oxide scale and the formation of graphite on the iron surface. In contact to graphite, iron carbides become unstable and a carbon activity gradient occurs through carbides which can act as catalyst for the graphitic filaments' growth. This mechanism of catalytic particle formation increases the rate of coke deposition compared to an initially reduced iron surface.

14.7 References

1. R.F. Hochman, *Proc. 4th Int. Congr. Metal Corrosion* (eds. N.E. Hammer, NACE, Houston) (1972).
2. R.F. Hochman, *Proc. of the Symp. on 'Properties of High Temperatures Alloys with Emphasis on Environmental Effects'* (eds. Z.A. Foroulis and F.S. Pettit), The Electrochemical Society (1977) 715.
3. J.C. Nava Paz, H.J. Grabke, *Oxid. Metals* **39** (1993) 437.
4. H.J. Grabke, *Corrosion Sci.* **51** (1995) 711.
5. H.J. Grabke, *Mater. Corrosion* **49** (1998) 303.
6. E. Pippel, J. Woltersdorf, R. Schneider, *Mater. Corrosion* **49** (1998) 309.
7. Q. Wei, E. Pippel, J. Woltersdorf, H.J. Grabke, *Mater. Corrosion* **50** (1999) 628.
8. B. Ozturk, V.L. Fearing, J.A. Ruth, G. Simkovich, *Metall. Transactions* **13A** (1982) 1871.
9. E. Pippel, J. Woltersdorf, H.J. Grabke, *Steel Res.* **66** (1995) 217.
10. C.M. Chun, T.A. Ramanarayanan, J.D. Mumford, *Mater. Corrosion* **50** (1999) 634.
11. J.R. Rostrup-Nielsen, D.L. Trimm, *J. Catalysis* **48** (1977) 155.
12. M. Audier, M. Coulon, *Carbon* **23** (1985) 317.
13. R.T.K. Baker, M.A. Barber, F.S. Feates, P.S. Harris, R.J. Waite, *J. Catalysis*, **26** (1972) 51.
14. R.T.K. Baker, P.S. Harris, R.B. Thomas, R.J. Waite, *J. Catalysis* **30** (1973) 86.
15. A.J.H.M. Kock, P.K. De Bokx, E. Boellard, J.W. Geus, *J. Catalysis* **96** (1985) 468.
16. E.C. Bianchini, C.R.F. Lund, *J. Catalysis*, **117** (1989) 455.
17. I. Wolf, H.J. Grabke, *Solid State Comm.* **54** (1985) 5.
18. R.T.K. Baker, J.R. Alonzo, J.A. Dumesic, D.J.C. Yates, *J. Catalysis* **77** (1982) 74.
19. H.J. Grabke, *Mater. Corrosion* **50** (1999) 673.
20. S. Tokura, N. Otsuka, T. Kudo, *Corrosion* **49** (1993) 561.
21. P. Thacker, Jr. A. Sacco, *Proc. 8th Int. Congr. Catal.* **2** (1985) 647.
22. A. Schneider, G. Inden, H.J. Grabke, Q. Wei, E. Pippel, J. Woltersdorf, *Steel Res.* **71** (2000) 179.
23. L.C. Browning, T.W. De Witt, P.H. Emmett, *J. Am. Chem. Soc.* **72** (1950) 4211.
24. W.F. Chu, A. Rahmel, *Oxidation of metals* **151** (1981) 331.
25. F. Bonnet, F. Ropital, P. Lecour, D. Espinat, Y. Huiban, L. Gengembre, Y. Berthier, P. Marcus, *Surf. Interface Anal.* **34** (2002) 418.
26. H. Nakagawa, T. Murayama, Y. Ono, T. Matsunaga, *Tetsu to Hagane*, **85** (1999) 14.
27. J. Birmantas, *Chemija T.* **10** (1999) 167.
28. F. Bonnet, PhD Thesis, Paris VI University, 2001.

Typical failures in pyrolysis coils for ethylene cracking

D J A K O B I Schmidt + Clemens Group, Germany and
R G O M M A N S, Gommans Metallurgical Services,
The Netherlands

15.1 Introduction

Pyrolysis coils in ethylene cracking furnaces are exposed to very severe conditions, e.g. high temperatures up to 1150 °C, severe start/stop and decoke cycles, oxidizing and nitriding flue gases at the outside and carburizing atmospheres at the tube inside surface. Therefore, high-alloyed centrifugal cast Ni–Cr–Fe alloys with adequate high-temperature corrosion resistance, good high-temperature strength, and good machinability and weldability (even after years of service) are required.

The principal alloys for ethylene cracking furnaces are shown in Table 15.1.

Different alloys are used in a radiant coil, each for specific parts in the coil. Generally speaking, high-carbon-containing alloys are used inside the firebox, and low-carbon-containing alloys outside the firebox. The highest Ni–Cr-containing alloys are used for the parts with the highest temperatures.

Table 15.1 Alloys for pyrolysis furnaces

Common name	S+C Grade Märker®G/ Centralloy®CA	C, %	Cr, %	Ni, %	Nb, %	W, %	Other
HK40	4848	0.40	25	20	–	–	Si
–	4868	0.50	30	30	–	–	
–	4868	0.50	30	30	–	–	Microalloy additions
HP Mod Nb	4852	0.40	25	35	1	–	–
HP Mod W	4857 W	0.40	25	35	–	4.0	–
HP Micro	4852	0.45	25	35	1	–	Microalloy additions
35/45	ET 45	0.45	35	45	1	–	Microalloy additions
Micro	Micro						
Alloy 800	4859	0.10	20	32	1	–	–
HP LC	H 101	0.10	25	35	1.0	–	–

Radiant coils have a limited life and failure is caused by a variety of factors, many being related to furnace operation. However, each pyrolysis plant experiences specific operational conditions and operational philosophies. Therefore, each plant has typical causes for radiant coil failure and it is important that operators analyse and understand the typical failure mechanisms. This will enable them to consider the material grades, which would be best suited for those particular conditions and also to keep failures within limits by proper furnace operation.

15.2 Damage mechanisms

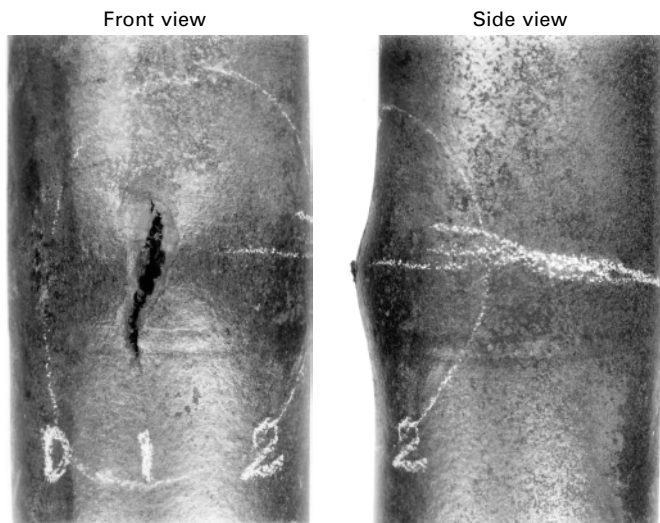
15.2.1 Radiant tubes

The two main failure mechanisms for radiant tubes are:

- ductile failures caused by carburization and creep ductility exhaustion; and
- brittle failures caused by thermal shock.

These mechanisms are causing the majority of failures in radiant tubes. Other failure mechanisms (such as stretching, overheating, nitriding and chromia evaporation) are also described in this section.

Ductile failure can be recognized by a bulge on the tube and a short longitudinal crack on top of the bulge (see Fig. 15.1). In the micro-structure creep voids can be observed between matrix and carbides. Further explanation and the metallurgical background to carburization and ductility exhaustion are given in Section 15.3.1.



15.1 Typical ductile failure of a radiant tube in a pyrolysis coil.

Brittle fracture can be recognized by a long longitudinal crack which 'ends' in a fork-like appearance (see Fig. 15.2). Sometimes, the cracks result in circumferential rupture or 'windows' that fall out of the tube. The cracks can be many metres long, and a thick coke layer is often present inside the tube.

In the micro-structure it can be observed that the carbides have split. This is a marked difference from the ductile fracture and can be recognized easily. Further explanation is given in Section 15.3.2.

Creep elongation (also called stretching) occurs because of creep by the weight of the tube and the coke layer present in the tube. It is influenced by temperature, the load-carrying cross-section of the tube, and the material used. It is generally known that non-carburized HP micro-types creep less than 45Ni/35Cr types. However, carbon uptake (carburization) leads to a higher specific volume of newly formed carbides and therefore to internal stresses which cause an increase in creep rate. The creep elongation of carburized ex-service centrifugal cast, high-carbon tube material has been examined in several studies. Investigations and calculations show that carburization is a major contributor to longitudinal creep growth and thus shortening of tube life (Guttmann and Bürgel 1980, Guttmann *et al.* 1988, Hendrix and Clark 1985, Hendrix, 1998).

A consequence of a high creep rate is the need to shut down the furnace and to shorten the coils. Failures can occur if tubes are not shortened before they reached the heater floor. The coils are warped and bowed, resulting in higher tube stresses and creep rates. There is also a difference in the height



15.2 Typical brittle failure of a radiant tube in a pyrolysis coil.

of the firebox. In general, modern higher furnaces suffer more from creep elongation than older, smaller furnaces.

Another failure mechanism is *overheating*, which results in local melting or overall melting of the tubes. Such overheating can happen due to lack of flow, coke blockage or burner problems (flame impingement). Lack of flow can occur when inlet valves fail or in the case of compressor problems. An example of overheated tubes is given in Fig. 15.3.

Above 1100°C *nitriding* (internal nitride formation) occurs from the outer diameter of the radiant tube (flue gas side). Nitrogen penetrates the oxide and reacts with chromium by precipitation of nitrides. The precipitation in most cases starts with the conversion of carbides into carbonitrides $M_2(C, N)$, $M(C, N)$ and $M_6(C, N)$ which grow by uptake of chromium and nitrogen (Aydin *et al.* 1980). Also, the lack of oxygen in the flue gas plays a role. Under reducing conditions (often caused through flame impingement by badly adjusted burners), this can result in severe loss of wall thickness by



15.3 Overheating failure of radiant tubes.

alternating oxidation and nitriding. The nitrides then cause spallation of the oxides. As a result a thick layer of oxides (up to 10–20 cm (4–8") thick!) can be found on the furnace floor. This is also known as oxide shedding. The rough as-cast surface disappears because of nitriding and the surface has a smooth and glazed appearance, see Fig. 15.4a, b.

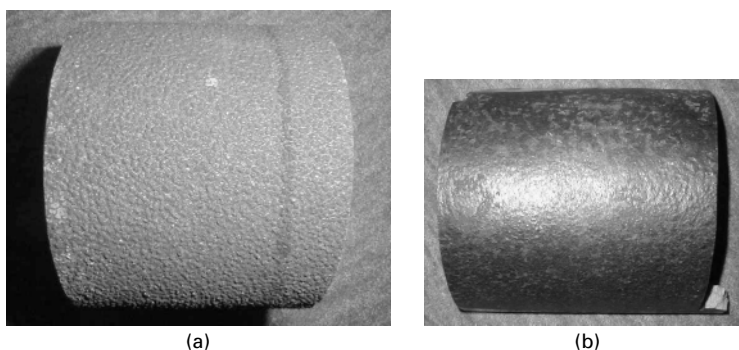
The changes in material properties caused by nitriding and carburization are very similar (see Section 15.3.1). In both cases internal precipitates are formed and the matrix is more or less depleted of chromium.

Chromia evaporation may become a problem for chromia forming at high surface temperatures $>1050^{\circ}\text{C}$ and high oxygen pressures, as in the flue gases of pyrolysis furnaces. Strong chromium depletion in the alloy subsurface region can be the consequence and also the formation of a thick carbide-free zone which advances into the alloy. In this area there are no carbide precipitates available for alloy strengthening and the 'sound wall thickness' of the alloy is reduced.

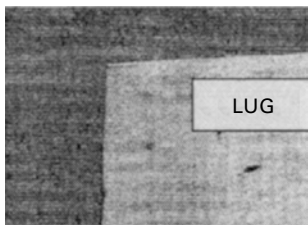
15.2.2 Bends and outlet parts

Erosion can be observed in 90° or 180° bends or in Y-pieces; an example is given in Fig. 15.5. The most accepted theory is that erosion is caused by hard coke particles during decoking. Some investigators believe that this erosion is caused by coke particles, which are present during normal operation. The remedy is to modify the decoking procedure, so that the coke is gasified instead of being spalled. The second remedy is to lower the gas velocity during decoke below 200 m/s. The third remedy is to apply 'internally stepped fittings', which have been applied successfully on many occasions.

Thermo-wells also suffer from erosion by coke particles. Successful solutions include, for example, thermo-wells fully made of Stellite and the rotation of the thermo-well at regular intervals.



15.4 (a) Rough (as-cast) outer surface: typical of new or aged condition. (b) Smooth (glazed) outer surface: typical of nitrided condition.



15.5 Example of erosion in the cross-section of a 90° outlet bend.

As in the radiant tubes, *carburization* also occurs in fittings (bends, Y-pieces, tetra fittings, etc.). In general, such carburization does not limit the life of the coils, because the radiant tubes will fail before the fittings do. This is because of the high wall-thickness of the fittings.

Thick-walled bends and outlet fittings (Y-piece, tetra-fittings, flanges) may suffer from *carburization and thermal fatigue*. The carburized zone is brittle and already cracks at low strains. The thermal stresses during start/stop-operation and decoke cycles cause thermal fatigue at the inside of such thick-walled components. A distinct feature is that the cracks are oriented in many directions and are opened widely. Some people call this ‘mud cracking’ or ‘crazy cracking’ because of this marked appearance; see Fig. 15.6. This type of cracking is not considered to limit the life of the component.

15.3 Metallurgical background of the main failure mechanisms

15.3.1 Carburization and creep ductility exhaustion

Carburization is an internal carbon enrichment and carbide formation which occurs mainly in industrial processes where Cr–Ni–Fe alloys are applied at high temperatures ($T > 800^{\circ}\text{C}$) in carbonaceous atmospheres. The carburization rate is related to the carbon activity of the gas (occurs at carbon activities $a_{\text{C}} < 1$) and progresses exponentially in relation to temperature (Bagnoli and Krupowicz 1992; Grabke 1998, 2000).

Carbon pick-up increases the metal volume resulting in internally induced stresses. It progresses from the tubes inside surface, causing compressive stresses in the inner wall (carburized tube material) and tensile stresses at the outside (non-carburized tube material). Intergranular cracking results, starting from the middle of the tube wall (Bagnoli and Krupowicz; 1992; Grabke 1998).

Carburization should be negligibly slow at temperatures below 1000°C for the usual materials with 25% Cr. They form protective scales composed of an outer spinel layer (Mn, Cr oxide) and an inner chromia layer (Cr_2O_3)



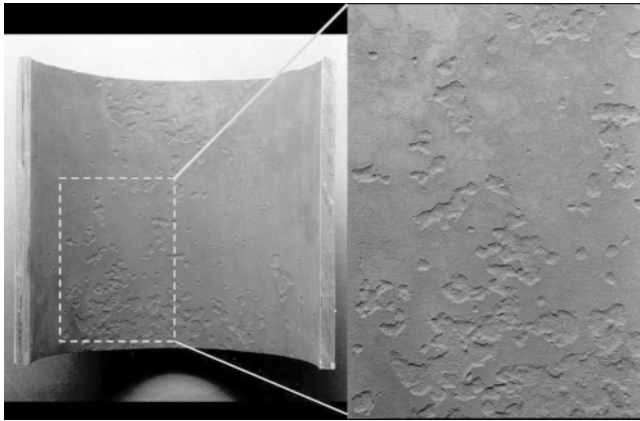
15.6 Thermal fatigue and carburization in a return bend of a pyrolysis coil (also called 'mud cracking' because of its marked appearance).

which are nearly impermeable for carbon diffusion from the atmosphere, since carbon solubility in these oxides is extremely low. However, there are several mechanisms leading to the failure of the oxide scale:

- Too large diffusion distance through the de-chromized zone: The periodic process of chromium oxide growth and spallation results in a gradual depletion of Cr in the alloy subsurface region. A critical thickness of the Cr-denuded zone is reached in operation at about 200 μm (Petkovic-Luton and Ramanarayanan 1990; Ramanarayanan, *et al.* 1998).
- Conversion of Cr oxides to non-protective carbide phases at high temperatures above 1050°C and high carbon activities $a_C \geq 1$. The surface carbides do not provide much protection against internal carburization (Grabke 1998; Grabke *et al.* 1976; Ramanarayanan *et al.* 1998).
- Structural defects in the protective oxide layer (pores, cracks, etc.), e.g. cracks formed as a result of thermal cycling (Wolf and Grabke 1985; Wolf *et al.* 1988).

Figure 15.7 shows an example of an inner surface of a tube where the protective oxide scale has failed and carburization has occurred. Figure 15.8 show the cross-section of a pyrolysis tube with carburized areas. These pictures clearly show the patchy nature of carburization, which is caused by local failure of the oxide scale.

The resistance of materials against carburization is given by the Ni content and the presence of Si, which forms a silica sub-scale. Therefore, modern materials have a high Ni content (well above 40%) and Cr contents of minimum 25–30% and contain 1.5–2.5% Si. The most modern Cr oxide-forming material in this respect is the 45Ni/35Cr material (such as ET45 Micro) with certain alloying additions (rare earth elements) in order to improve the oxide scale adherence (Kirchheiner and Jimenez 2001).



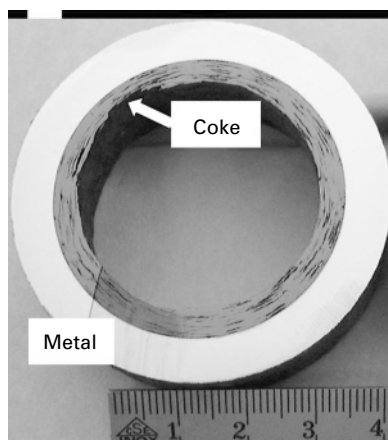
15.7 Inner surface of a tube where the protective oxide scale has failed and carburization has occurred.



15.8 Cross-section of a pyrolysis tube with (patchy) carburized areas.

Creep ductility exhaustion is a complex mechanism in which the creep ductility is exhausted by cyclic operation (such as decoke stops, plant shut-downs and trips). During normal operation a coke layer is deposited at the inner diameter of the tube. At the end-of-run (EOR) such coke layers can be up to 20mm thick. During the decoking, the coke is gasified, with the purpose that the tube is clean after the decoke. However, during the change between normal operation and decoking, a temperature drop occurs. Because the thermal expansion coefficient of the metal is much higher than the coefficient of the coke, the metal-tube shrinks on the 'coke-tube'. Because of the high compressive strength of coke, the metal does not crush the coke. This causes high tensile stresses in the tube metal, which relax during the (on-line) decoking procedure. The strain range that occurs is proportional to the difference in thermal expansion coefficient and the temperature range T according to:

$$\epsilon = \alpha \Delta T \quad 15.1$$



15.9 Pyrolysis tube and deposited coke layer inside the tube. The strain range during a decoke cycle is proportional to the temperature drop. $\epsilon_{\text{Metal}} = 19 \text{ m/m/k}$. $\epsilon_{\text{Coke}} = 4 \text{ m/m/k}$.

During a normal decoke such a temperature drop can be 100–200 °C, which causes a strain range of 0.15–0.30% corresponding to high stress levels. During the subsequent decoking procedure, these high stresses relax because of creep. The damage mechanism is thus cyclic creep relaxation. During each cycle the tube creeps a small amount; and at end-of-life the material reaches its creep ductility. That is where the name ‘creep ductility exhaustion’ comes from. Tube life is thus dependent on:

- the number of decoke cycles (n);
- the severity of the cycle (start/stop, on-line or off-line decoke, ΔT); and
- creep parameters (temperature, material, creep rate, creep ductility).

The combination of *carburization and creep ductility exhaustion* is the ‘normal’ failure mechanism for pyrolysis tubes in ethylene plants. It results in bulges, ovalization and, sometimes, tube bending as has been described in Section 15.2.1. Each single occurrence is relatively simple to explain, but the complete process is complex and not yet fully understood.

15.3.2 Brittle fracture caused by furnace trips

As described in the previous section, the metal-tube shrinks on the ‘coke-tube’ during a temperature drop. During a normal decoke the temperature drop is limited to about 100–200 °C. During a furnace trip such a temperature drop can be 500–1000 °C. The strain during such a furnace trip is then 0.75–1.5%. This equals the rupture ductility of aged, carburized and nitrided material between room temperature and ~600 °C. Since materials tend to

crack when their rupture ductility is reached; furnace tubes also crack. Because aged, nitrided and carburized furnace tube materials are brittle at these temperatures, they crack. These brittle cracks can extend for many metres.

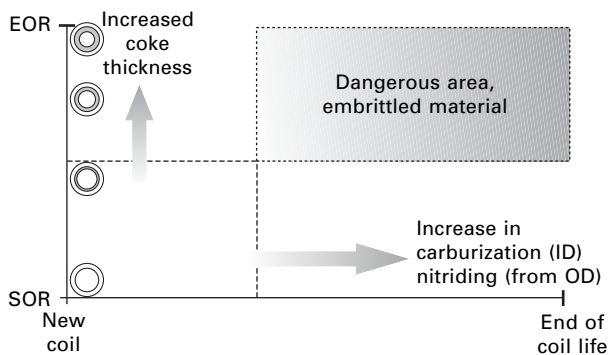
The risk for brittle cracks is dependent upon:

- the severity of the trip (temperature drop);
- the thickness of the coke layer inside the tube; thin coke layers at start-of-run (SOR) will be crushed, but thick coke layers at EOR will not;
- the degree of brittleness of the material, which is determined by the amounts of ageing and carburization.

As a guideline, brittle fracture occurs most frequently when the tubes are already a few years old *and* when the furnace is in the second half of its operation run. This 'dangerous area' is given in Fig. 15.10.

15.4 Process technological background

The underlying problem for the main failure mechanisms of radiant tubes is deposition of coke at the ID of the tube. The coke deposition results in higher tube wall temperatures. For a tube life of about 6 years in high-severity cracking furnaces EOR-temperatures can be up to 1100°C for HP materials (such as G4852 and derivatives) and 1125°C for 45Ni/35Cr materials (such as ET 45 Micro). At these high temperatures the materials carburize and creep harder. Therefore, many problems are related to furnace operation. Overheating, flame impingement, nitriding, oxide shedding, reducing flue gases, erosion, and especially brittle fracture can all be prevented by proper furnace operation. Creep elongation, carburization and creep ductility exhaustion can be kept within limits by proper furnace operation, proper material choice and good design.



15.10 'Dangerous area' for brittle cracking of pyrolysis tubes.

Furnace inspections may give early detection of approaching failures, and should therefore be performed at regular intervals (e.g. during decoke stops). It can be helpful to measure *carburization*. Several companies offer traditional carburization meters based on magnetic principles (permeability, eddy current, etc.). Recently, Shell Global Solutions International presented a new pulsed Eddy Current technique, which showed promising results. However, a fully carburized tube can have a remnant life of 1–2 years (if no furnace trips occur).

Dimension measurements can be helpful as well. If creep elongation (stretching) limits the life of the furnace, it can be monitored by the position of guide tubes. In most cases creep in the circumferential direction (tube swelling, bulging and ovalization) will shorten working life. Diameter measurements by simple strapping can be helpful. However, there will be tubes that fail at low ductilities (a few per cent) and tubes that will fail at higher ductilities (up to 15% has been observed). This is dependent on the method of furnace operation and the type of material (HK40, HP-Nb or 45Ni/35Cr), but also significant scatter between the individual tubes exists. Accelerated creep testing of ex-service material is not suitable to determine the remnant life of pyrolysis coils, because the relevant failure mechanisms (combined carburization and cyclic relaxation) cannot be taken into account by a simple creep test.

For the time being, visual inspections and strapping (diameter measurements) are the best inspection tools. One should look for bulging, ovalization and appearance (smooth vs. rough). The results obtained can be used for identifying trends. Many operators replace tubes about 9–12 months after the first bulges and ovalities are observed.

However, significant developments are being made in modelling the relevant failure mechanisms. Also, statistical approaches are under development. The Schmidt + Clemens Group is developing a statistical method to determine residual coil life based on operating conditions.

15.5 Conclusions

The dominant failure mechanisms for radiant tubes are: (a) the combined action of carburization and creep ductility exhaustion, and (b) brittle fracture during furnace trips. The first mechanism results in bulging, bending and ovalization of the tubes. The second mechanism results in large, longitudinal cracks.

The metallurgical background of the combined action of carburization and creep ductility exhaustion are explained. The carburization rate is determined by the presence of protective oxide scales, and the nickel and silicon content of the matrix. Creep ductility exhaustion is determined by the number of cycles (start/stop and decoke cycles) and the nature (or severity)

of these cycles. Other mechanisms include creep elongation (stretching), overheating, nitriding, oxide shedding, thermal fatigue and erosion.

Many failures are related to furnace operation and can be prevented or can be kept within limits by proper furnace operation, material choice and good design. Regular furnace inspections may give an early warning of approaching failures.

15.6 Acknowledgement

The authors would like to thank the Schmidt + Clemens management for permission to publish this paper.

15.7 References

- Aydin, I.; Bühler, H. E.; Rahmel, A.; *Werkstoffe und Korrosion* **31** (1980), 675.
- Bagnoli, D. L.; Krupowicz, J. J.; 'Experiences with Ethylene Heater Tube Carburization', *Corrosion* 92, Paper No. 307 (1992).
- Grabke, H. J.; *Carburization – A High Temperature Corrosion Phenomenon*, MTI Publications No. 52, St. Louis, Elsevier Science, Amsterdam, New York (1998).
- Grabke, H. J.; 'Corrosion by carbonaceous gases, carburization and metal dusting, and methods of prevention', *Materials at high temperatures* **17** (4) 483–487 (2000).
- Grabke, H. J.; Gravenhorst, U.; Steinkusch, W.; *Werkstoffe und Korrosion* **27**, 291 (1976).
- Guttmann, V.; Bürgel, R.; 'The creep behavior of HK-40 and Alloy 800H in a carburizing environment', In *Corrosion and Mechanical Stress at High Temperatures*, Applied Science Publishers, Ltd. London, 1980.
- Guttmann, V.; Beck, K. E.; Bürgel, R.; 'A comparison of the creep behavior of various austenitic steels under carburizing conditions', *Mat.-wiss. U. Werkstofftech.* **19**, 104–111 (1988).
- Hendrix, D. E.; 'Comparative performance of six cast tube alloys in an ethylene pyrolysis test', *Corrosion* 98, Paper No. 430, Houston, TX, NACE International, 1998.
- Hendrix, D. E.; Clark, M. W.; 'Contributing factors to the unusual creep growth of furnace tubing in ethylene pyrolysis service', *Corrosion* 85, Paper No. 21, Houston, TX, NACE International, 25–29 March, 1985.
- Kirchheiner, R.; Jimenez, J. L.; 'Correlation of oxidation, carburization and metal dusting; controlling corrosion by corrosion', *Corrosion* 2001, Paper No. 01374, NACE Conference, Houston, TX, NACE International, 2001.
- Petkovic-Luton, R.; Ramanarayanan, T.; 'Mixed oxidant attack of high temperature alloys in carbon- and oxygen containing environments', *Oxidation of Metals*, **34**, 381 (1990).
- Ramanarayanan, T. A.; Petrovic, R. A.; Mumford, J. D.; Ozekcin, A.; 'Carburization of high chromium alloys', *Materials and Corrosion* **49** (1998).
- Wolf, I.; Grabke, H. J.; *Solid State Communications*. **54**, 5 (1985).
- Wolf, I.; Grabke, H. J.; Schmidt, H. P.; *Oxidation of Metals*, **29**, (1988) 289.

Thermodynamic characteristics and numerical modelling of internal nitridation of nickel-base alloys

H - J CHRIST, S - Y CHANG and U KRUPP,
Universität, Siegen, Germany

16.1 Introduction

In many high-temperature applications, alloys are exposed to gaseous environments that contain nitrogen (e.g. air or ammonia). Internal nitridation of nickel-base alloys usually takes place as a consequence of spalling and cracking of a protective oxide scale, which can be considered as impermeable to nitrogen [1, 2]. Nickel-base superalloys usually contain alloying elements such as Ti and Al which can form thermodynamically stable nitrides. In the case of most precipitation-hardened nickel-base superalloys, a near-surface depletion of the strengthening γ' -phase ($\text{Ni}_3(\text{Al}, \text{Ti})$) may lead to a deterioration of the creep resistance at high temperatures as a consequence of the consumption of Ti and Al for nitride formation. Furthermore, owing to the molar volume difference between the alloying elements and their nitrides, internal nitride precipitation can give rise to internal stresses and can lead to embrittlement in the near-surface layer [3, 4].

The phenomenon of internal nitridation has been observed for numerous nickel-base alloys. In oxygen-free atmospheres, where superficial oxide formation is negligible, the nitrogen attack was found to follow a parabolic rate law [5–8]. This indicates that the process is controlled by diffusion, i.e. the inward diffusion of nitrogen in combination with the outward diffusion of the nitride-forming elements are the rate-controlling steps. Following the well-known theory of internal oxidation of Carl Wagner [9], the dissolved concentrations of nitrogen c_N and solute element c_B in the alloy as a function of time t and location x is determined by Fick's second law:

$$\frac{\partial c_N}{\partial t} = D_N \frac{\partial^2 c_N}{\partial x^2} \quad \text{and} \quad \frac{\partial c_B}{\partial t} = D_B \frac{\partial^2 c_B}{\partial x^2} \quad 16.1$$

where D_N and D_B denote the diffusion coefficients of nitrogen and solute element B in the alloy. If one nitride of type BN_v , of high thermodynamic stability, is formed and the following expression is fulfilled:

$$\frac{D_B}{D_N} \ll \frac{c_N^s}{c_B^0} \ll 1 \quad 16.2$$

where c_N^s is the surface concentration of dissolved nitrogen, and c_B^0 is the initial concentration of solute element B, Equation (16.1) can be solved using some mathematical simplifications. Then, the penetration depth of the internal nitrides as a function of exposure time t can be calculated analytically as proposed by Wagner for internal oxidation [9]:

$$x^2 = 2k_N t = 2 \frac{D_N c_N^s}{c_B^0} t \quad 16.3$$

where k_N denotes the parabolic nitridation rate constant. According to Equation (16.3), the nitridation kinetics is determined by the diffusivity and solubility of the interstitially dissolved nitrogen.

The solubility of nitrogen depends significantly on the composition of the alloy as well as the nitridation temperature [10]. Nitrogen dissolves in metals according to the following reaction [11]:



The nitrogen solubility in nickel-base alloys is extremely small. Hence, the experimentally determined data show a large scatter [12, 13]. The nitrogen solubility can be predicted theoretically using the CALPHAD (calculation of phase diagrams) method by applying a two-sublattice model. In this study, the calculations were carried out using ChemSage, a software package for Gibbs energy minimisation calculations [14].

As stated above, internal precipitation can be described by Wagner's theory of internal oxidation [15, 16] in simple cases. However, modelling of more complex internal precipitation reactions that involve more than one compound or moderate stability of the reaction product and varying boundary conditions (e.g. temperature changes) requires a numerical treatment of both the diffusion and the thermochemical processes in the alloy [17, 18]. For this purpose, a computer simulation was developed, in which the commercial thermodynamic software ChemApp is combined with a finite-difference diffusion calculation using the explicit method [19]. The calculation of the concentration profiles and the resulting penetration depths of the internal nitridation zones is based on a simple numerical treatment of the relevant diffusion processes which are the diffusion of nitrogen into the alloy and the counter-diffusion of the alloying elements towards the surface. After each single diffusion step, the precipitated nitride concentration as well as the concentration of nitrogen and the alloying elements are determined assuming local chemical equilibrium. It is shown in this chapter that this calculation technique provides a quantitative description of the internal nitridation process of the nickel-base model alloys.

Furthermore, this time and location resolved calculation method gives a sound basis for model expansions which aim at a consideration of superimposed effects such as superficial oxide formation and spallation.

16.2 Experimental procedure

The chemical compositions of the alloys studied are listed in Tables 16.1 and 16.2. Table 16.1 contains the compositions of the commercial nickel-base superalloys CMSX-2, CMSX-6 and SRR99 (single-crystalline alloys) and the polycrystalline alloy Nicrofer 7520. These materials were obtained as cylindrical rods of 10–12 mm diameter. The model alloys used in this study are listed in Table 16.2. The alloys were produced by vacuum arc melting and provided as cylindrical rods with a diameter of 10 mm.

For the nitriding experiments, specimens of approximately 1 mm in thickness were cut using a low-speed saw. Their surfaces were wet ground with SiC paper down to grade 1200 and polished with 3 μ m and 1 μ m diamond suspensions. Prior to exposure the specimens were ultrasonically cleaned and degreased in ethanol.

Thermogravimetric measurements were carried out in a thermobalance having a sensitivity of 10^{-6} g. Supplementary long-term nitridation experiments were performed in a vacuum-tight annealing apparatus. As the nitriding atmosphere, a gas mixture consisting of 45 vol.% He, 5 vol.% H, and 50 vol.% N₂ at a constant flow rate of 6 litres per hour was used. This gas was led through a small package of porous Ti sponge located immediately in

Table 16.1 Composition of the commercial nickel-base alloys studied (in wt%)

	Ni	Cr	Al	Ti	Co	Ta	Mo	W	Fe	Re	Hf	C
CMSX-2	(66.4)	7.9	5.6	1.0	4.6	6.0	0.6	7.9	–	–	–	–
CMSX-6	(71.6)	9.6	4.7	4.6	4.8	1.8	2.8	0.1	–	–	–	–
SRR99	(65.6)	8.5	5.6	2.2	5.2	2.8	0.6	9.5	–	–	–	0.014
Nicrofer 7520	(75.3)	20.2	1.6	2.7	0.01	–	–	–	0.18	–	–	0.045

Table 16.2 Composition of the nickel-base model alloys studied (in wt%) and (at.%)

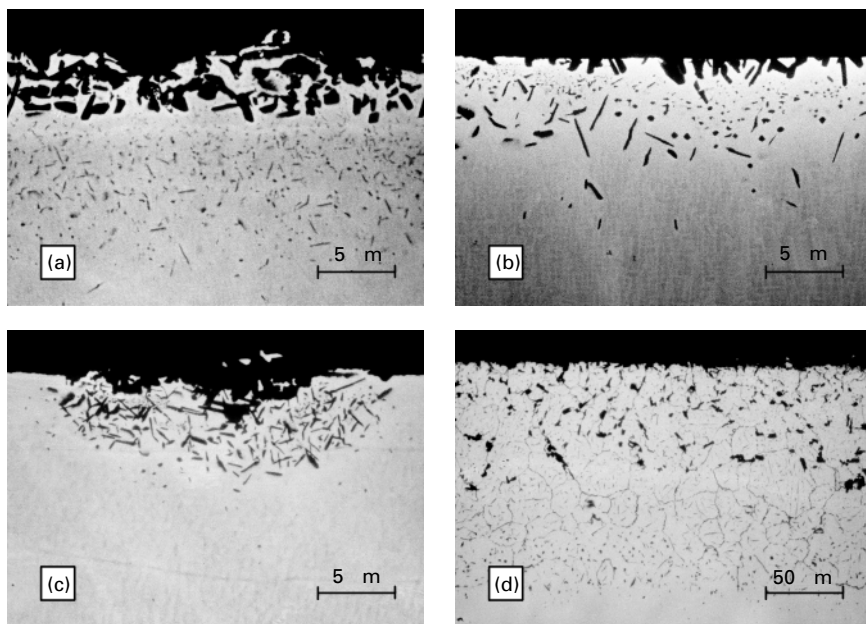
Alloy	Ni		Cr		Ti	
	wt%	at.%	wt%	at.%	wt%	at.%
NiTi2	98	97.6	–	–	2	2.4
NiCr5Ti2	93	92.0	5	5.6	2	2.4
NiCr10Ti2	88	86.5	10	11.1	2	2.4
NiCr20Ti2	78	75.7	20	21.9	2	2.4
NiCr20Ti6	74	71.2	20	21.7	6	7.1
NiCr30Ti2	68	65.2	30	32.5	2	2.3

front of the specimen. The high oxygen affinity of Ti in combination with the H_2 content of the gas mixture reduces the oxygen partial pressure down to a value smaller than $p_{O_2} = 10^{-18}$ Pa. The composition, phases and morphology of the products formed as well as the nitridation kinetics were investigated applying analytical scanning electron microscopy, transmission electron microscopy and X-ray diffraction (XRD).

16.3 Results and discussion

16.3.1 Behaviour of commercial nickel-base alloys

Exposure to the nitriding atmosphere leads, in the case of the commercial alloys, which contain 1.6–5.6 wt% Al and 1.0–4.6 wt% Ti, to an internal reaction zone with precipitates of AlN and TiN. SEM micrographs of this nitrided zone are shown in Fig. 16.1. Needle-shaped precipitates of AlN were formed beneath the surface and were clearly seen as black coarse precipitates in the cross-section. The TiN precipitates also showed needle-like shape, but they were smaller and their precipitation zone extended significantly deeper into the alloy. The larger size of the AlN particles is probably a consequence of a higher phase-boundary energy and a smaller

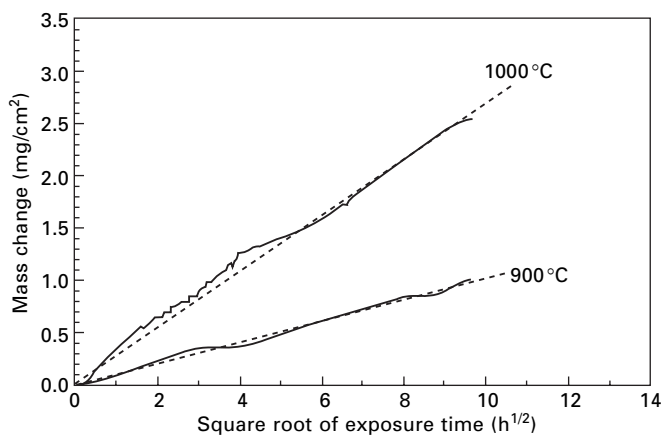


16.1 SEM micrographs of internal precipitation zones formed at 1000°C in a nitriding atmosphere (45 vol.% He, 5 vol.% H_2 and 50 vol.% N_2): (a) CMSX-2 (192 h), (b) SRR99 (192 h), (c) CMSX-6 (192 h) and (d) Nicrofer 5720 (150 h).

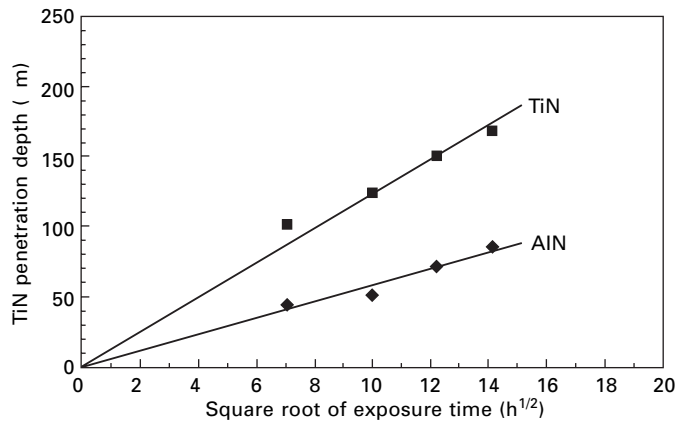
thermodynamic stability as compared with TiN. Hence, the critical nucleus size is increased, thereby reducing the nucleation rate.

Figure 16.2 shows the gravimetrically determined weight gain as a function of time for the alloy Nicrofer 7520 in a representation of the mass gain per surface area versus the square root of time. Results of metallographic examinations of cross-sections are shown in Fig. 16.3. Both figures confirm that the internal nitridation process obeys a parabolic rate law, justifying the assumption that overall nitridation kinetics is diffusion controlled.

The parabolic nitridation rate constant k_N as defined in Equation (16.3) was calculated from the experimentally determined depths of the internal



16.2 Thermogravimetrically measured weight change plotted versus the square root of time for Nicrofer 7520 exposed to the nitriding atmosphere at 900 and 1000 °C.



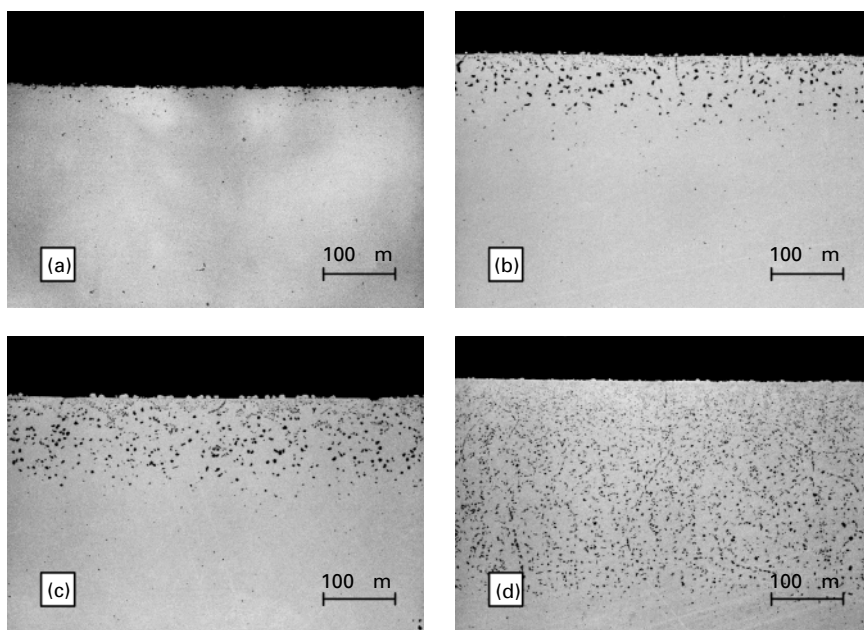
16.3 Penetration depths of internal TiN and AlN precipitation in Nicrofer 7520 at 1000 °C plotted versus square root of time.

nitridation. The resulting values of the parabolic nitridation constants of TiN and AlN at 1000 °C for Nicrofer 7520 are 2.1×10^{-8} and $4.8 \times 10^{-9} \text{ mm}^2 \text{ s}^{-1}$, respectively.

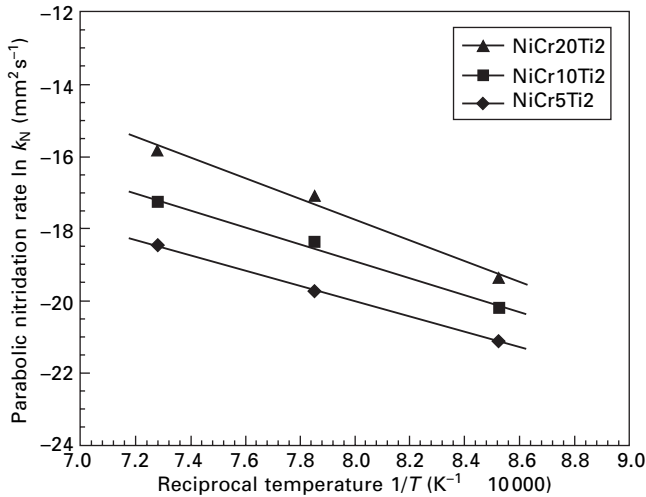
16.3.2 Behaviour of NiCrTi model alloys

Figure 16.4 shows the micrographs of cross-sections of Ni–Cr(0–20)–Ti2 alloys after nitridation at 1100 °C for 100 h. In these model Ni–Cr–Ti alloys, only TiN precipitates were observed, which form a well-defined zone of internal nitridation. Clearly, the TiN precipitation zone depth increases strongly with increasing Cr content. For each temperature, again a parabolic rate law holds true, indicating that the nitridation process is diffusion controlled. An Arrhenius diagram of the logarithm of the parabolic rate constant versus the reciprocal temperature for the internal nitridation of NiCrTi2 alloys is given in Fig. 16.5.

In order to reveal the effect of chromium on the nitridation rate, thermodynamic equilibrium calculations were carried out using the computer program ChemSage in combination with a thermodynamic database for the system Ni–Cr–Al–Ti–N–O. According to the calculated results, the nitrogen solubility in *pure* nickel can be expressed by the following equation:



16.4 Internal precipitation of TiN in Ni–Cr–Ti₂ alloys exposed to nitriding atmosphere for 100 h at 1100 °C: (a) NiTi₂, (b) NiCr5Ti₂, (c) NiCr10Ti₂, and (d) NiCr20Ti₂.



16.5 Arrhenius-type plot of the parabolic rate constant of internal nitridation for various Ni-Cr-Ti alloys.

$$c_N = 0.039 \exp \frac{-45645 [\text{J/mol}^{-1}]}{RT} \sqrt{p_{N_2} [\text{bar}]} \quad [\text{at.}\%] \quad 16.5$$

The effect of chromium on the internal nitrogen behaviour can be attributed to its influence on the activity coefficient of nitrogen in solid solution. Following the formula of Wagner and Chipman, the logarithm of the nitrogen activity coefficient f_N can be expressed as [20]:

$$\log f_N = e_N^{\text{Cr}} c_{\text{Cr}} + \frac{c_{\text{Cr}}^2}{N} c_{\text{Cr}}^2 \quad 16.6$$

where e_N^{Cr} and $\frac{c_{\text{Cr}}^2}{N}$ are the first and second order interaction coefficients between nitrogen and chromium. The nitrogen concentration c_N can be calculated according to the equation:

$$c_N = \frac{a_N}{f_N} \quad 16.7$$

Combining Equation (16.6) and Equation (16.7) yields the expression:

$$\log c_N = \log a_N - e_N^{\text{Cr}} c_{\text{Cr}} - \frac{c_{\text{Cr}}^2}{N} c_{\text{Cr}}^2 \quad 16.8$$

A second order polynomial fit was applied to the results obtained by the ChemSage calculation. The dissolved nitrogen concentration for Ni-Cr alloys at a nitrogen partial pressure of 0.5 bar at 1000 °C can be written as:

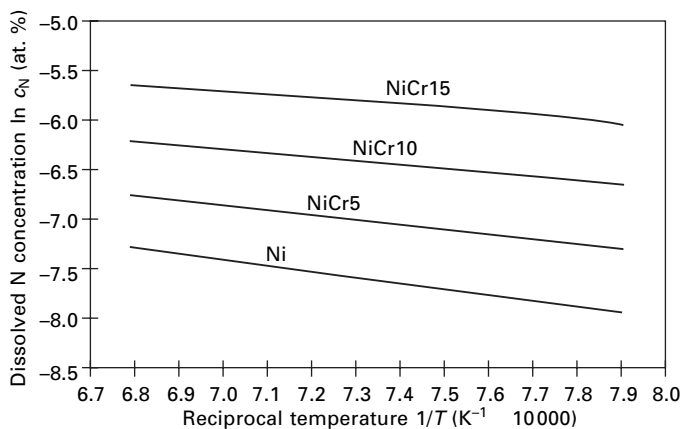
$$\log c_N [\text{at.}\%] = -3.43 + 0.055 c_{\text{Cr}} [\text{at.}\%] + 7 \cdot 10^{-5} (c_{\text{Cr}} [\text{at.}\%])^2 \quad 16.9$$

Figure 16.6 shows the dissolved nitrogen concentration versus the reciprocal temperature for four Ni–Cr alloys in an Arrhenius-type representation. It should be noted that in Ni–Cr–Ti alloys the zone of internal nitridation, in which the dissolved nitrogen diffuses, is almost completely depleted of Ti owing to the high thermodynamic stability of the TiN formed. Hence, the consideration regarding the effect of Cr on the equilibrium surface concentration of nitrogen in Ni–Cr alloys can be transferred to Ni–Cr–Ti alloys. The calculation results document clearly that the nitrogen solubility increases strongly with increasing temperature as well as with increasing Cr concentration.

According to Equation (16.3), a second reason for acceleration of the nitridation rate with chromium concentration might be an increase of the nitrogen diffusion coefficient. Nitrogen diffuses along interstitial lattice sites and consequently diffusivity is much faster than that of the substitutionally dissolved alloying elements. Hence, Equation (16.2) is fulfilled and Wagner's theory can be employed to express the internal nitridation rate constant. By means of the calculated values of c_N^s and the experimentally observed values of k_N , the effective diffusion coefficient of nitrogen can be obtained:

$$D_N = \frac{k_N c_B^0}{c_N^s} \quad 16.10$$

Table 16.3 lists the nitrogen concentrations that are dissolved in Ni–Cr–Ti alloys as well as the metallographically determined parabolic nitridation rate constants. The calculated values of D_N indicate that the diffusion coefficient increases with increasing Cr concentration. An Arrhenius-type representation of the effect of Cr concentration on the diffusion of nitrogen is shown in



16.6 Solubility of nitrogen in Ni–Cr–Ti alloys at 1000°C and a nitrogen pressure of 0.5 bar.

Table 16.3 Experimentally observed values for the parabolic nitridation rate constant, thermodynamically calculated nitrogen solubilities (at a nitrogen pressure of 0.5 bar) and nitrogen diffusion coefficients (as derived from Wagner's parabolic rate law)

Alloy	T (°C)	k_N (mm ² s ⁻¹)	c_N [at. %]	D_N (cm ² s ⁻¹)
NiCrTi2	900	6.84 10^{-10}	5.08 10^{-4}	3.27 10^{-8}
	1000	2.68 10^{-9}	6.98 10^{-4}	9.30 10^{-8}
	1100	9.66 10^{-9}	9.15 10^{-4}	2.57 10^{-7}
NiCr10Ti2	900	1.66 10^{-9}	9.46 10^{-4}	4.24 10^{-8}
	1000	1.06 10^{-8}	1.33 10^{-3}	1.93 10^{-7}
	1100	3.11 10^{-8}	1.66 10^{-3}	4.52 10^{-7}
NiCr20Ti2	900	3.74 10^{-9}	1.01 10^{-3}	8.81 10^{-8}
	1000	3.80 10^{-8}	2.86 10^{-3}	3.16 10^{-7}
	1100	1.38 10^{-7}	5.56 10^{-3}	5.91 10^{-7}

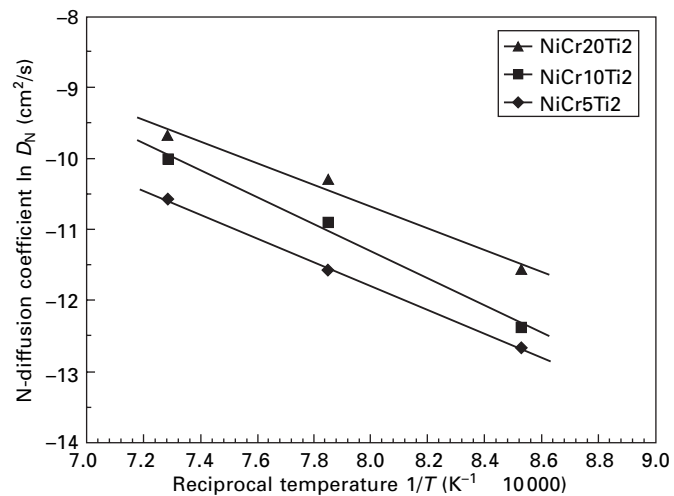
Figure 16.7. The activation energies for nitrogen diffusion in NiCr5Ti2, NiCr10Ti2 and NiCr20Ti2, as obtained from the slopes of the Arrhenius plots, appear to be somewhat different. However, the low number of data points per alloy does not justify a sound conclusion. An average value of 135 ± 12 kJ/mol can be derived.

The calculation of D_N shows that the concentration of Cr in the Ni–Cr–Ti alloys affects not only the nitrogen solubility but also the diffusion of nitrogen. Hence, the observed change of nitridation kinetics with Cr concentration results from both an increased solubility and an enhanced diffusivity at increased chromium concentration.

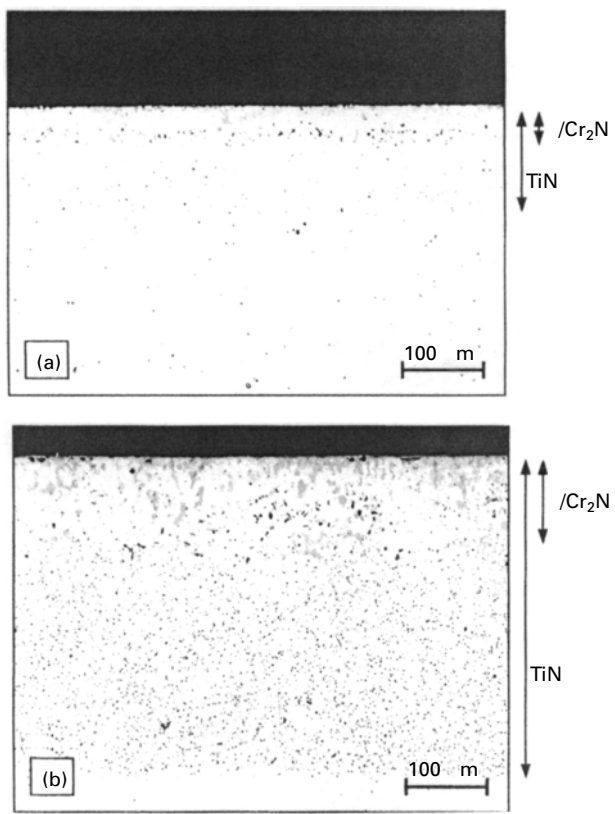
16.3.3 Thermodynamic prediction of the range of stability of γ phase

The predictive capacity of the numerical thermodynamic calculation becomes evident when alloys with even higher Cr content are considered. As an example, the nitridation of NiCr30Ti2 at temperatures below 1100 °C leads to the formation of further phases in the zone of internal nitridation. Needle-shaped Cr₂N precipitates as well as the so-called γ -phase [10, 21] precipitate and forms a clearly visible nitridation zone close to the surface which is embedded in the deep TiN zone (Fig. 16.8).

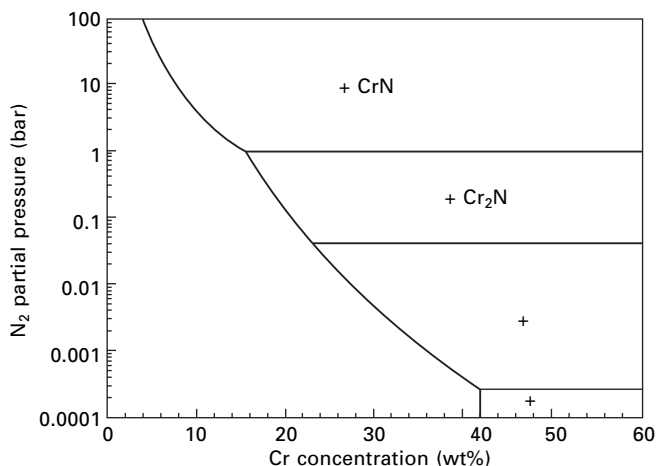
Using the thermodynamic program ChemSage, isothermal Ni–Cr–N equilibrium diagrams were calculated. Figure 16.9 shows such a diagram for the temperature of 1000 °C. Taking into account that the nitrogen partial pressure was limited to 0.5 bar in this work, the thermodynamic calculation predicts the experimentally observed phases very accurately. As an example, the stability diagram shows that γ -phase formation is confined to high-Cr contents above 22.8 wt% at 1000 °C.



16.7 Arrhenius-type plot of the nitrogen diffusion coefficient for various Ni-Cr-Ti alloys.



16.8 Internal precipitation of TiN, Cr₂N and γ -phase in NiCr30Ti2 exposed to the nitriding atmosphere for 100 h at (a) 900 °C and (b) 1000 °C.



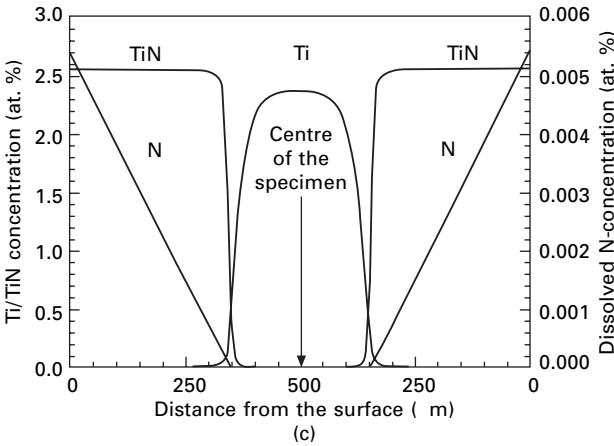
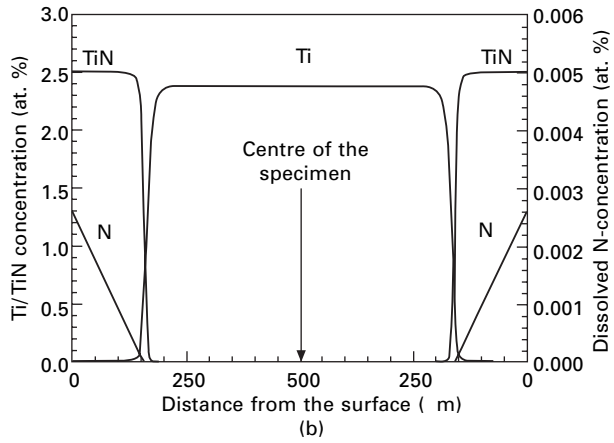
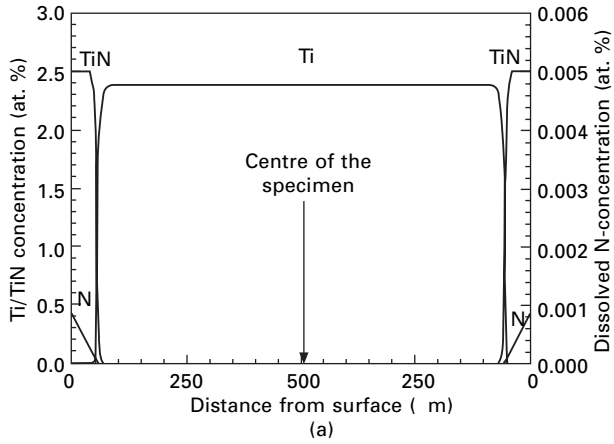
16.9 Calculated stability diagram for the Ni-Cr-N system at 1000°C.

16.3.4 Simulation of internal nitridation

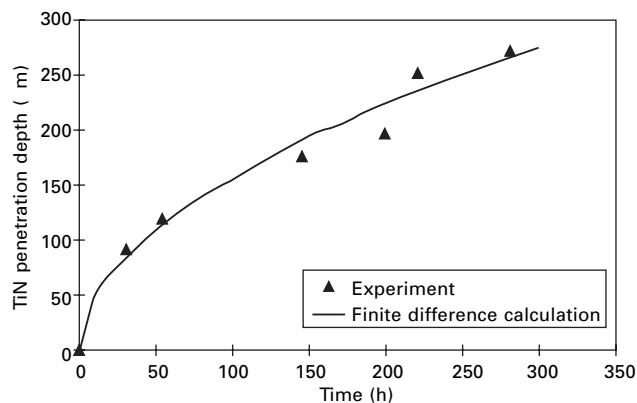
The numerical simulation of the internal nitridation process is based on a calculation of the diffusion of nitrogen into the alloy and the counter-diffusion of the alloying elements. Fick's second law is solved applying an explicit finite-difference method [19]. For this purpose, time and location are subdivided into intervals and after each time step the concentrations resulting from diffusion are calculated for all positions. Before the diffusion calculation is continued by increasing time by one time interval, the precipitated nitride concentrations are determined assuming local thermodynamic equilibrium. A detailed description of the calculation method is presented in Krupp and Christ [6].

Figure 16.10 depicts the calculated concentration profiles of the reacting elements for the internal nitridation reaction of a NiCr20Ti2 alloy. In Fig. 16.11, the experimentally observed depths of TiN precipitation are compared with calculated results.

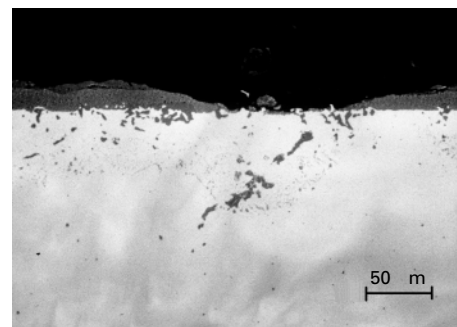
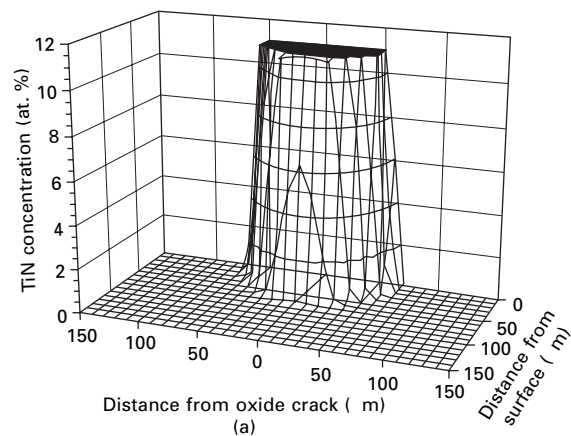
As a first step towards an extension of the simulation in such a way that the superficial processes can be taken into account, a two-dimensional simulation model was developed. One application of this model is the calculation of internal nitridation as a consequence of a cracked oxide scale. For an experimental verification of the calculated results (Fig. 16.12a), a crack in the oxide scale of a pre-oxidized specimen of NiCr20Ti6 was generated using diamond wire saw. Then the specimen was exposed for 100h at 1000 °C to an oxygen-free nitrogen atmosphere. Figure 16.12b shows that TiN precipitation depth underneath the crack is obviously larger than the depth below the oxide scale. A comparison of the nitridation depth underneath the crack and the numerical prediction shows a reasonable agreement between experimental and calculated data.



16.10 Calculated concentration profiles of the internal nitridation of NiCr20Ti2 for an exposure time of 100 h at (a) 900°C, (b) 1000°C and (c) 1100°C.



16.11 Comparison of the prediction (solid line) with the experimentally determined internal nitridation depths (data points) for NiCr20Ti2 at 1000°C and a nitrogen pressure of 0.5 bar.



16.12 Internal nitridation of NiCr20Ti6 as a consequence of a crack in the oxide scale after 100 h at 1000°C in a 0.5 bar N₂ atmosphere: calculated TiN concentration profile and (b) cross-section of a sample, the oxide scale of which was locally removed after pre-oxidation (1000°C, 100 h, air).

16.4 Conclusions

The growth rate of the internal precipitation zone obeys a parabolic rate law in all cases studied. Hence, the internal nitridation of nickel-base alloys is diffusion-controlled. A detailed analysis proved that the process can be described by the classical theory of internal oxidation by Carl Wagner.

The diffusivity and solubility of nitrogen in nickel-base alloys were found to depend strongly on alloy composition. In Ni–Cr–Ti model alloys the influence of Cr content on the maximum dissolved concentration of nitrogen was confirmed theoretically by means of thermodynamic calculations. Using this data of the nitrogen solubility, the simple Wagner equation for internal oxidation yields an increase of the nitrogen diffusion coefficient with increasing Cr concentration.

At a Cr content higher than 20 wt%, a peritectic reaction of Cr_2N with Ni can lead to the formation of the ternary γ phase. The occurrence of Cr_2N and the γ phase is in accordance with the predictions of thermodynamic equilibrium calculations.

A numerical simulation model was developed and used to describe quantitatively the internal nitridation process. The distribution of the various elements within the diffusion zone during internal precipitation can reasonably be predicted based on a combination of kinetic and thermodynamic considerations.

An extension to a two-dimensional calculation was carried out, in order to take oxide scale failure into account. First results indicate the close correlation of internal nitridation and oxide scale integrity.

16.5 Acknowledgement

Financial support of this study by Deutsche Forschungsgemeinschaft is gratefully acknowledged.

16.6 References

1. S. Han, D. J. Young, *Oxid. Metals* 2001, **55**, 223.
2. S. Y. Chang, U. Krupp, H.-J. Christ, in: *Cyclic Oxidation Testing as a Tool for High-Temperature Materials Characterisation* (Ed. M. Schütze and W. J. Quadakkers), EFC Publications, London, 1999, 63.
3. H. Rolleck, in *Binäre und ternäre Karbid- und Nitridsysteme der Übergangsmetalle*, Gebrüder Borntraeger, Berlin, 1984.
4. S. Y. Chang, U. Krupp, H.-J. Christ, *Mater. Sci. Engng A* 2001, **301**, 196.
5. U. Krupp, H.-J. Christ, *Oxid. Metals* 1999, **52**, 277.
6. U. Krupp, H.-J. Christ, *Oxid. Metals* 1999, **52**, 299.
7. R. P. Rubly, D. L. Douglass, in: *High Temperature Corrosion of Advanced Materials and Protective Coating* (Ed. Y. Saito, B. Öney and T. Mamyama), Elsevier Science Publisher, Tokyo, 1992, 133.

8. K. Tjokro, D. J. Young, *Oxid. Metals* 1995, **44**, 453.
9. C. Wagner, *Zeitschr. Elektrochem.* 1959, **63**, 772.
10. U. Krupp, S. Y. Chang, H.-J. Christ, *Z. Metallkde* 2000, **91**, 1006.
11. E. J. Mittemeijer, J. T. Slycke, *Härterei-Techn. Mitt.* 1995, **50**, 114.
12. H. A. Wriedt, O. D. Gonzalez, *Trans. Met. AIME* 1961, **221**, 532.
13. E. Fromm, E. Gebhard, *Gase und Kohlenstoff in Metallen*, Springer-Verlag, Berlin, 1976.
14. E. Königsberger, G. Eriksson, *CALPHAD* 1995, **19**, 207.
15. R. A. Rapp, *Corrosion* 1965, **21**, 382.
16. F. H. Stott, G. C. Wood, *Materials Science and Technology* 1988, **4**, 1072.
17. H. C. F. Rozendaal, E. J. Mittemeijer, P. F. Colijn, P. J. Van der Schaaf, *Met. Trans. A* 1983, **14**, 395.
18. J. A. Nesbitt, *Oxid. Metals* 1995, **44**, 309.
19. J. Crank, *The Mathematics of Diffusion*, 2nd Edition, Clarendon Press, Oxford, 1986.
20. M. Herrera-Trejo, D. Ablitzer, *Canadian Metallurgical Q.* 1997, **36**, 341.
21. A. A. Kodentsov, J. H. Gilpen, C. Cserhati, J. K. Kivilahti, F. J. J. Van Loo, *Met. Mater. Trans. A* 1996, **27**, 59.

HJ GRABKE, S STRAUSS and D VOGEL,
Max-Planck-Institut für Eisenforschung GmbH, Germany

17.1 Introduction

The behaviour of steels and alloys in nitriding and oxidizing atmospheres is of interest for some industrial processes in which organic N-compounds (Melamin) are produced and for the possible application of $\text{NH}_3\text{--H}_2\text{O}$ mixtures in power plants. By using $\text{NH}_3\text{--H}_2\text{O}$ (Kalina cycle) instead of only water vapour (Rankine cycle) the efficiency of power plants might be improved by 5–6%. The Kalina cycle has been under discussion for more than a decade [1–3]; a pilot plant using this process had been operating, but there are still severe doubts considering possible corrosion of the metallic components in a power plant. For thermodynamic reasons one might expect formation of a protective magnetite scale on the steels used for tubes and turbines, but if these steels were to be nitrided in long-term operation, the embrittlement and volume increase would be most dangerous [4–12]. Since corrosion in $\text{NH}_3\text{--H}_2\text{O}$ atmospheres at elevated temperatures had not been studied before, a research project was conducted on the corrosion behaviour of several steels used in power plants, but also of iron, nickel and a Ni-base alloy.

17.2 Experimental procedure

The exposures were conducted on iron, nickel and some steels which are used in power plant construction, in addition a nickel-base alloy was tested. The chemical composition of the commercial materials is given in Table 17.1.

Samples of $20 \times 10 \times 1 \text{ mm}^3$ were exposed, ground to # 600, cleaned in acetone and weighed. The samples were hung from a sample holder made of quartz, which was introduced into the reaction tube within a horizontal furnace after heating to 500°C . During heating the system was flushed with He; after introduction of the sample holder, the gas supply was changed to He– H_2O or $\text{NH}_3\text{--H}_2\text{O}$. The flow velocities of He and NH_3 were controlled by capillary flowmeters. H_2O was added while the gas flow passed a column, filled with glass tube sections at 200°C , by dosing with a minipump. Exposures in He–

Table 17.1 Composition of the tested materials (contents in wt%)

	Cr	Ni	Mo	Mn	Al	Si	C
13CrMo44	0.98		0.52	0.55		0.22	0.14
120CrMo910	2.25		1.05			0.35	0.13
P91	8.6	0.26	0.93	0.41			0.10
12CrMoV lo	10.4	0.66	0.83	0.52		0.27	0.20
12CrMoV hi	11.2		0.86	0.50		0.32	0.12
Sicromal	18.0			<1.0		0.7–1.4	0.12
18Cr – 9Ni	17.6	8.66		0.83	0.014	0.55	0.03
Alloy 800	20.4	30.6		0.70	0.28	0.38	0.068
Alloy 600	16.2	73.7		0.21	0.11	0.26	0.03

30% H_2O were conducted for 50 h to observe the oxidation behaviour of the materials in the absence of NH_3 . The exposures in 70% $\text{NH}_3\text{--}30\%\text{H}_2\text{O}$ were performed for 50 and 200 h. After the exposures the surfaces were studied by scanning electron microscopy (SEM) and sometimes X-ray diffraction (XRD). Metallographic cross-sections were prepared and investigated by optical microscopy.

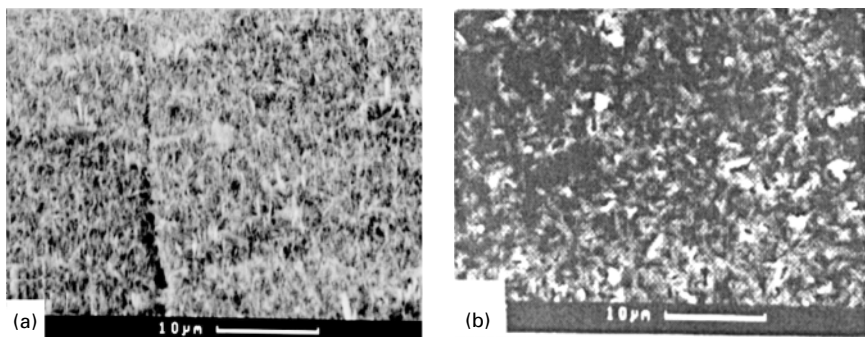
17.3 Results

17.3.1 Iron

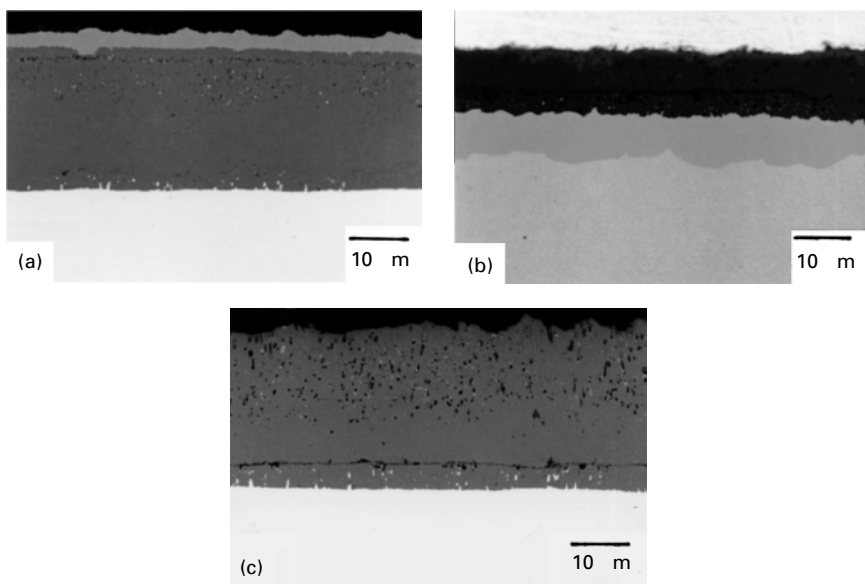
The oxidation of iron in $\text{He--}30\%\text{H}_2\text{O}$ after 50h led to formation of oxide layers, an inner layer of Fe_3O_4 and an outer layer of Fe_2O_3 needles (Fig. 17.1a). Both oxides can be seen in the metallographic cross-section (Fig. 17.2a) and were detected by XRD. After 50h in 70% $\text{NH}_3\text{--}30\%\text{H}_2\text{O}$ the appearance of the scale is different: a sponge-like porous structure was obtained, and XRD showed presence of Fe_3O_4 , Fe_2O_3 , Fe_2N and Fe_4N . After 200h in $\text{NH}_3\text{--H}_2\text{O}$ the porous structure was still observed (Fig. 17.1b) and XRD showed prevailing Fe_3O_4 . The cross-section after 50h showed nitridation, but after 200h the nitrided layer was consumed by oxidation (Figs 17.2b,c). Also in the cross-section the oxide scale appears porous; most probably the pores are caused by the N_2 which is set free by oxidation of the nitrided layer.

17.3.2 Low-alloy steels

In the oxidation of the 1%CrMo and the 2.25%CrMo steel, double layers of magnetite are formed, as well known by inward and outward growth, and some needles of haematite on the surface (Fig. 17.3a). The morphology after reaction in $\text{NH}_3\text{--H}_2\text{O}$ again is clearly different, sponge-like and porous (Fig. 17.3b). The cross-sections taken after 50h show internal nitridation, after



17.1 Scanning electron micrograph of the surface of iron after 50 h reaction: (a) in He-H₂O, dense structure of oxide needles; (b) in NH₃-H₂O, sponge-like porous oxide structure.

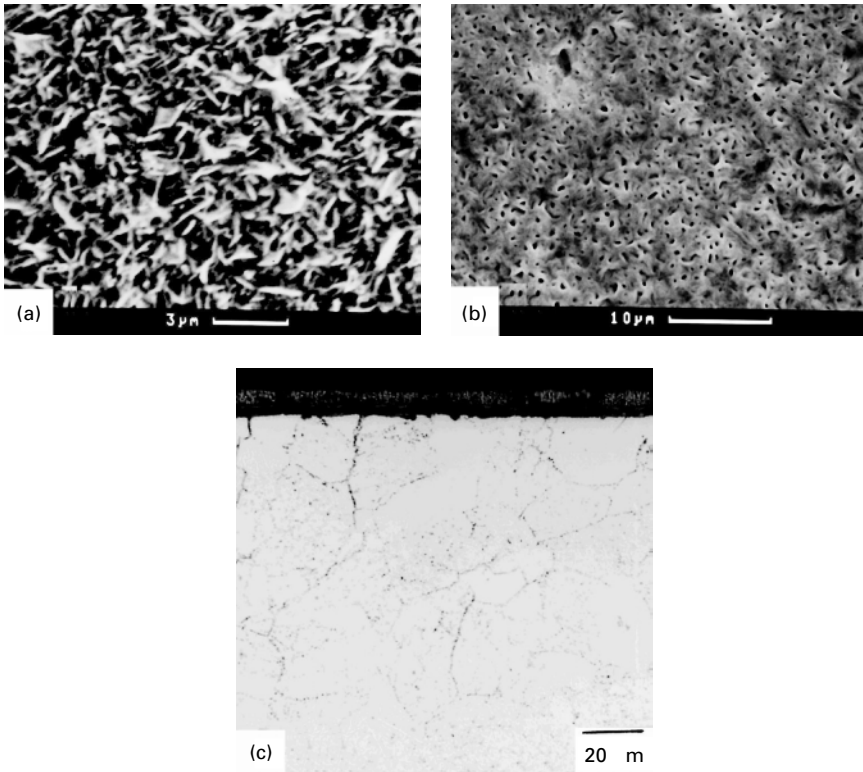


17.2 Metallographic cross-section of iron (unetched) optical micrographs: (a) after 50 h in He-H₂O, dense Fe₂O₃/Fe₃O₄-scale; (b) after 50 h in NH₃-H₂O, porous oxide scale and nitrided layer; (c) after 200 h in NH₃-H₂O, porous oxide scale (the nitride layer is oxidized).

200 h differences occurred: the 1%CrMo steels has pores and in the 2.25%CrMo steel there are already cracks (Fig. 17.3c) due to the compressive stresses caused by CrN precipitation.

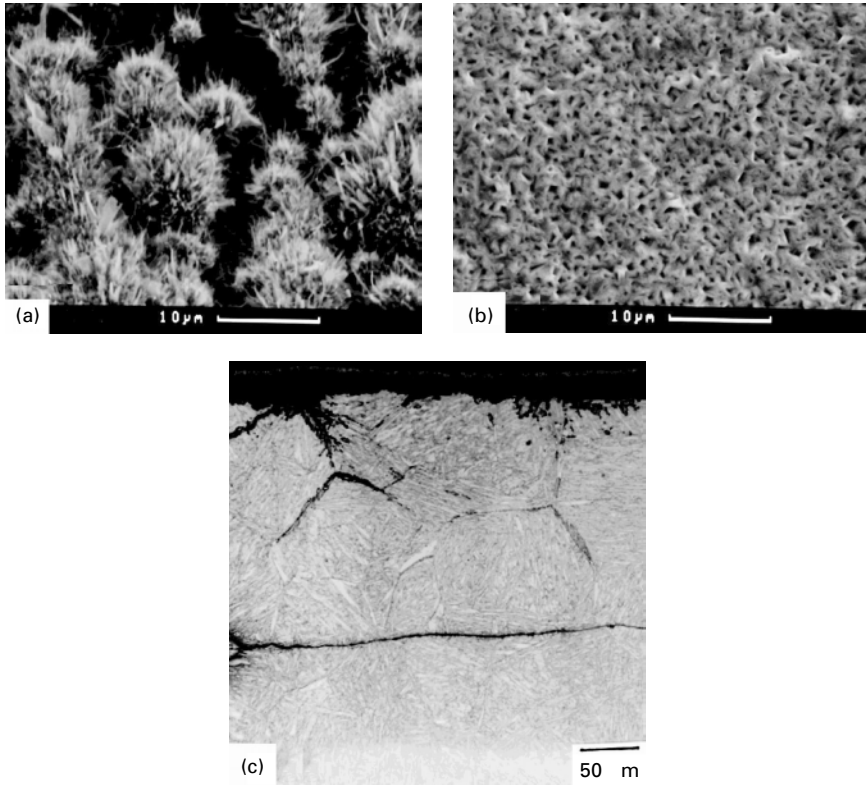
17.3.3 Ferritic 9–18%Cr steels

The oxidation in He-30% H₂O of these steels led to a more or less dense protective scale; the lower the Cr content of the steel, the more often there



17.3 2.25%Cr – 1%Mo – steel: (a) after 200 h in $\text{He--H}_2\text{O}$, SEM photo of the surface, needle-like iron oxides; (b) after 200 h in $\text{NH}_3\text{--H}_2\text{O}$, SEM photo of the surface, sponge-like, porous oxide structure; (c) metallographic cross-section, shows porous oxide and nitriding in the interior, intergranular cracking starts.

are protrusions of outgrowing iron oxides (Fig. 17.4a). Again the morphology after reaction in $\text{NH}_3\text{--H}_2$ is different, on the 9–12%Cr steels a sponge-like porous structure is observed (Fig. 17.4b) and dense oxide needles on the 18%Cr steel. These oxide structures allow nitrogen transfer by NH_3 , since internal nitridation occurs. At high magnification fine CrN-particles can be seen, which precipitate in the microstructure of these steels, especially at grain boundaries and martensite laths. The resulting compressive stresses cause cracking at grain boundaries but also transgranular cracking parallel to the surface (Fig. 17.4c). If the cracks are connected to the surface, H_2O had entered and caused internal oxidation. Most severe was the attack on the steel with highest Cr content (Sicromal), where intergranular disintegration occurred, owing to internal nitridation, cracking and oxidation of the cracks (Figs 17.5a, b).



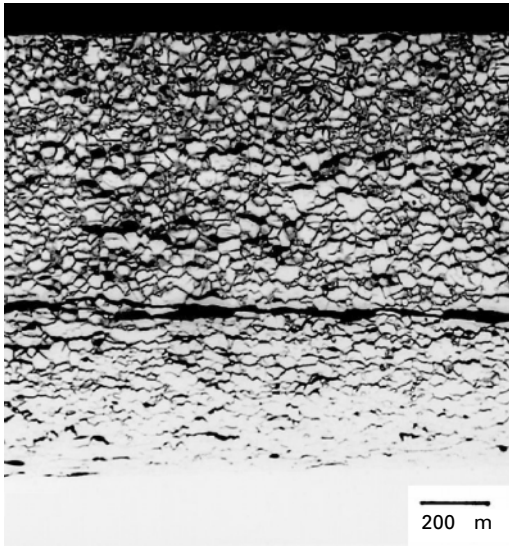
17.4 10.4%-Cr-steel: (a) after 200 h in He-H₂O, SEM photo of the surface, thin Cr-rich oxide scale with protrusions of Fe-oxides; (b) after 200 h in NH₃-H₂O, SEM photo of the surface with porous oxide scale; (c) metallographic cross-section, shows internal nitridation and cracking.

17.3.4 Austenitic 18%Cr–9%Ni and 20%Cr–32%Ni steel

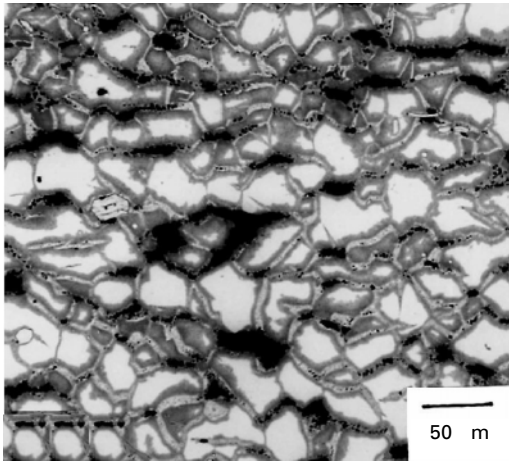
The ‘stainless’ 18%Cr–9%Ni steel after 200 h in NH₃–H₂O is deeply nitrided. In the unetched cross-section the internally nitride zone is nearly invisible, but after etching (V2A) this zone appears dark (Fig. 17.6). Internal cracking did not occur in the 200 h exposure, but owing to the compressive stresses, locally some metal phase is pressed outward through the oxide scale and is oxidized. The 20%Cr–32%Ni steel is attacked locally: here internal nitridation can be seen after etching (Fig. 17.7b), and the area disintegrates into flakes (Fig. 17.7a).

17.3.5 Nickel and Ni-base alloy

Nickel and the Ni-base Alloy 600 do not form an oxide scale in NH₃–H₂O. In nickel the nitride Ni₃N was observed, a very unstable nitride which



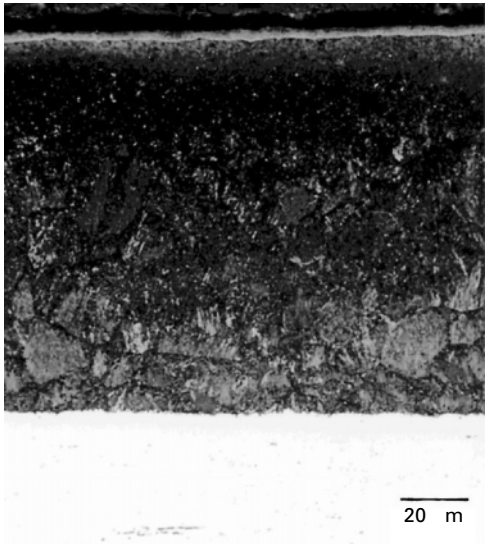
(a)



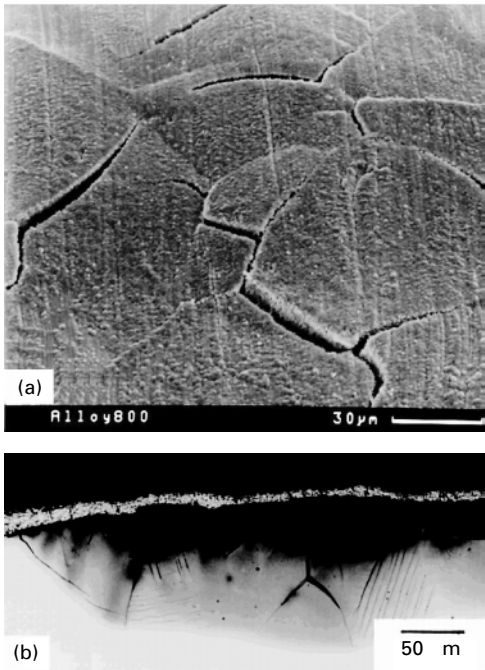
(b)

17.5 18%Cr steel (Sicromal) after 200 h in $\text{NH}_3\text{-H}_2\text{O}$: (a) and (b) metallographic cross-section at different magnification, shows internal nitridation, cracking and oxidation of the crack flanks.

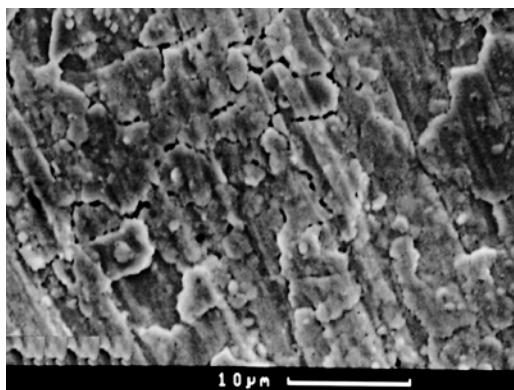
immediately decomposes according to $2\text{Ni}_3\text{N} \rightarrow 6\text{Ni} + \text{N}_2$. The nitrogen evolved at high pressure causes pore formation. Internal nitridation and pore growth led to internal stresses and surface cracks (Fig. 17.8a, b). In the Alloy 600, as in Alloy 800, internal CrN precipitation causes stresses and intergranular cracks and Ni grains are pressed out from the material (Fig. 17.9a, b).



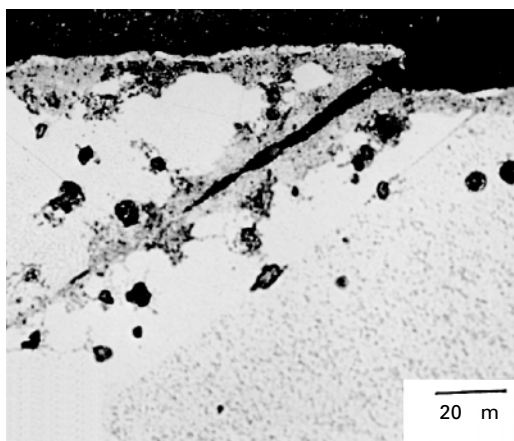
17.6 18%Cr-9%Ni steel after 200h in $\text{NH}_3\text{-H}_2\text{O}$, metallographic cross-section (etched), thin oxide scale and nitrided layer beneath, with very fine CrN precipitates.



17.7 32%Cr-20%Ni steel (Alloy 800) after 200h in $\text{NH}_3\text{-H}_2\text{O}$: (a) SEM-topview of the cracked surface; (b) etched cross-section, shows local internal nitridation and cracking.



(a)



(b)

17.8 Nickel after 200 h in $\text{NH}_3\text{--H}_2\text{O}$: (a) REM-topview of the cracked surface; (b) metallographic cross-section (etched) shows internal Ni_3N -formation and pores formed by its decomposition, and cracking by compressive stresses.

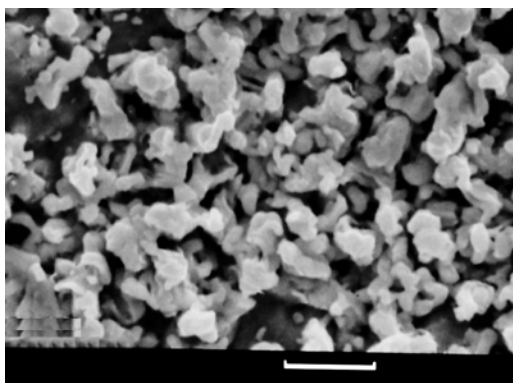
17.4 Discussion

17.4.1 Thermodynamics

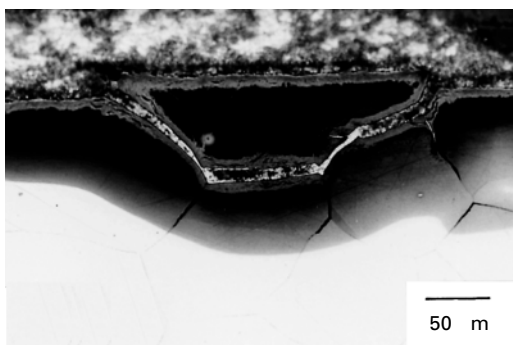
The experiments were performed in flowing 70% NH_3 –30% H_2O mixtures at 500 °C and 1 bar. NH_3 is not stable under these conditions and should decompose largely to N_2 and H_2 (whereas in planning the Kalina process it was assumed that the decomposition was negligible). The decomposition reaction



could lead to high nitrogen pressures. Assuming that 1% H_2 is formed, the virtual nitrogen pressure would result:



(a)

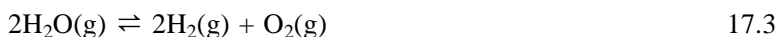


(b)

17.9 Nickel-base alloy Ni-16%Cr-10%Fe (Alloy 600) after 200 h in $\text{NH}_3\text{-H}_2\text{O}$: (a) SEM topview of the surface, Ni-grains have been pressed outwards; (b) cross-section showing internally nitrated region, dark zone with very fine CrN precipitates, intergranular cracking and oxidized crack flanks, the Ni-grains which have been pressed outward appear as a white layer on the surface and in the cracks.

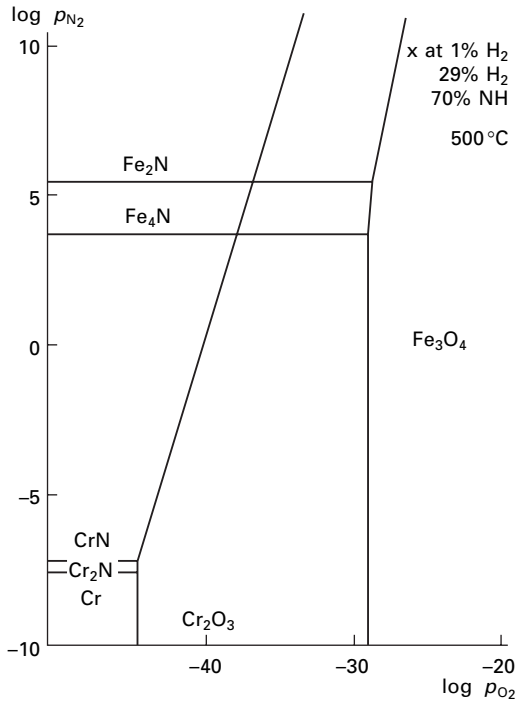
$$p_{\text{N}_2} = K_1 (p_{\text{NH}_3}^2 / p_{\text{H}_2}^3)^2 = 3 \quad 10^8 \text{ bar} \quad 17.2$$

The oxygen pressure results from the reaction



$$p_{\text{O}_2} \rightleftharpoons K_2 (p_{\text{H}_2\text{O}} / p_{\text{H}_2})^2 = 1 \quad 10^{-25} \quad 17.4$$

These data for p_{N_2} and p_{O_2} yield one point in the thermochemical stability diagram of the systems Fe-N-O and Cr-N-O, see Fig. 17.10. This point is in the stability field of Fe_3O_4 , i.e. magnetite would be the stable phase on iron and low-alloy steels, for equilibrium with the atmosphere (Cr_2O_3 or FeCr_2O_4 for high-alloy steels). But nitrides can be formed in the first attack of the atmosphere on the blank metal surface – in this ‘transient state’ all

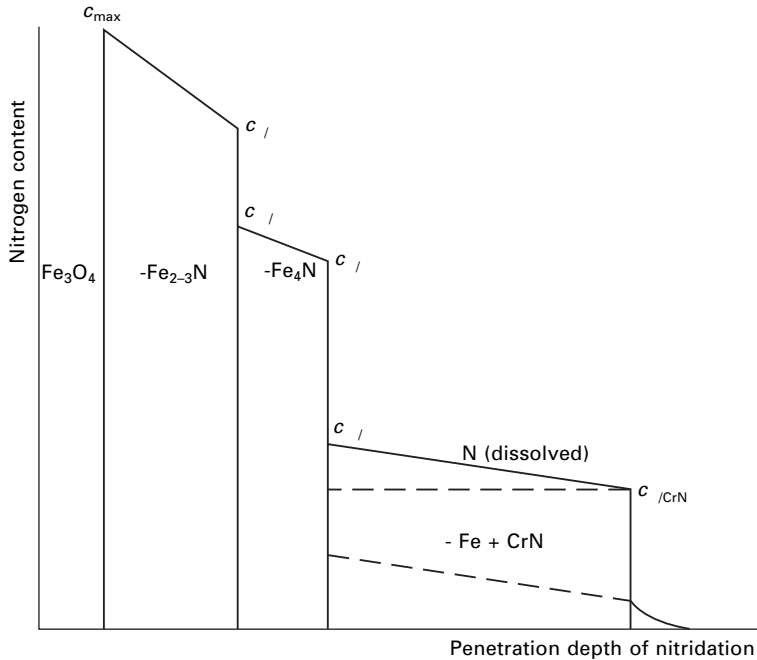


17.10 Thermochemical stability diagram of the systems Fe–O–N and Cr–O–N at 500°C – the point marks the thermodynamics of the Kalina cycle.

compounds may grow for which the formation pressure is exceeded, including the nitrides Fe_2N , Fe_4N and CrN and the oxides mentioned. But, also below a magnetite scale these nitrides can be formed, since below the scale and in the metal phase p_{O_2} decreases. Therefore below the outer Fe_3O_4 layer, the iron nitrides can be expected and in the metal phase internal nitridation will occur, i.e. precipitation of CrN in the metal matrix will occur. Only if the outer Fe_3O_4 layer is perfectly dense and shows no pores or cracks would this nitridation be suppressed. The present studies have shown that this is not the case: the scales formed in $\text{NH}_3\text{-H}_2\text{O}$ are clearly porous.

17.4.2 Kinetics

For the system p_{N_2} and p_{O_2} are rather high and the nitrides CrN , Mo_2N , $\text{-Fe}_4\text{N}$, $\text{-Fe}_{2-3}\text{N}$ and the oxides Fe_3O_4 , Cr_2O_3 and FeCr_2O_4 can be formed on a Cr steel. The processes and the structure of the corrosion layers caused by nitridation can be derived from kinetic considerations, which is known from experience with nitriding [13, 14] and oxinitriding [15, 16]. Figure 17.11 shows the layers formed by ingress of nitrogen, upon oxidation



17.11 Schematic of the oxinitrided surface region of a Cr steel.

growth of the oxides Fe_3O_4 and FeCr_2O_4 should occur by outward diffusion of cations.

The following processes need to be considered:

- Transfer of nitrogen from the gas phase into the solid phase according to reaction



which was studied in detail on iron foils [17–19] and inward diffusion of dissolved N into the metal matrix.

- Internal nitride formation in steels containing Cr, Mo, V, Ti, Al and other nitride-forming elements [20, 21] by reaction of the inward diffusing nitrogen with these alloying elements, as soon as the solubility product is exceeded which is given for a nitride MN by

$$K_L = a_M (p_{\text{N}_2})^{1/2} = \exp(-G_{\text{MN}}/RT) \quad 17.6$$

where a_M is the activity of alloying element M in the steel and G_{MN} the free energy of nitride formation. A front of precipitation moves inward into the steel and the penetration depth X of internal nitridation is given by

$$x^2 = 2 \frac{D_N c_N}{c_M} t \quad 17.7$$

where D_{N} is the diffusivity and c_{N} is the solubility of N in the metal matrix (after precipitation of the nitride). In this study, mainly CrN will be formed and at the relatively low temperature as a finely divided precipitate, the particles are only detectable by electron microscopy [20].

The internal nitridation is retarded with decreasing nitrogen diffusivity D_{N} and solubility c_{N} , i.e. for increasing Ni content; thus the nitridation of Ni-base alloys is slower than that of steels. The nitridation is also retarded with increasing concentration c_{M} of nitride-forming elements. On the other hand, at high c_{M} the large amount of precipitates causes internal stresses, dislocation nets and stress fields, in which additional nitrogen is trapped [21]. Thus high Cr steels and alloys tend to embrittlement and cracking in the zone of internal nitridation, and this study confirms that the embrittlement and cracking increases with Cr content of the steels and alloys.

As explained before, the nitrogen pressure of the Kalina cycle is very high (infinity, when no H_2 present), so the iron nitrides Fe_3N and Fe_4N can be formed. The growth of Fe_4N is described by the parabolic law $x^2 = k_{\text{p}} \cdot t$ and values for k_{p} have been determined at 505°C [22]. After five years a layer of about 0.5 mm Fe_4N is to be expected.

The growth of Fe_3N -nitride cannot be predicted exactly since the external nitrogen pressure is not well defined, but the experience from nitriding indicates that the Fe_3N -layer is generally thicker than the Fe_4N -layer, and that pores appear in this layer, because of nitride decomposition under N_2 formation [13, 14].

The $\text{NH}_3\text{--H}_2\text{O}$ is also oxidizing, and according to the experience from 'gas oxinitriding' an oxide layer grows on the iron nitrides, which is porous so that nitrogen can penetrate [15, 16]. It is reported that the nitridation rate is even enhanced in the presence of oxidizing gases H_2O , CO_2 or air. The oxide layer is mainly Fe_3O_4 , for which the growth rate is well known from studies on oxidation by water vapour in power plants [23].

Altogether, on a steel in the $\text{NH}_3\text{--H}_2\text{O}$ mixture of the Kalina cycle a sequence of layers should develop as shown in Fig. 17.11. For the 1%CrMo steel the total corrosion layer would have a thickness of about 15 mm after 5 years, as calculated on the base of data from the cited publications [13, 14, 22, 23].

17.5 Acknowledgement

This study was supported by the Deutsche Forschungsgemeinschaft.

17.6 References

1. Young M. Park, R.E. Sonntag, *Int. J. Energy Research* **14** (1990) 153.
2. H.A. Mlcak, *Proceed. American Power Conf. Illinois Inst. Technology, Chicago, Illinois* 1995.

3. R.W. Bjorge, J.C. Corman, R.W. Smith, *Power Gen. Europe '96*, Budapest 1996.
4. J.J. Moran, J.R. Mihalisin, E.N. Skinner, *Corrosion NACE* **17** (1961) 115.
5. A. Rahmel, H.J. Schütter, P. Schwaab, W. Schwenk, *Bänder, Bleche, Rohre* **5** (1964) 245.
6. J.R. Schley, F.W. Bennett, *Corrosion NACE* (1967) 276.
7. M. Vyklicky, M. Mericka, *Werkstoffe u. Korrosion* **19** (1968) 580.
8. U. Jäkel, W. Schwenk, *Werkstoffe u. Korrosion* **27** (1971) 1.
9. W. Steinkusch, *Werkstoffe u. Korrosion* **27** (1976) 91.
10. I. Aydin, H.E. Bühler, A. Rahmel *Werkstoffe u. Korrosion*, **31** (1980) 67.
11. A.A. Kodentsov, J.H. Gülpen, C. Cerhati, J.K. Kivilthi, F.J.J. van Loo, *Met. Mat. Trans.* **27A** (1996) 59.
12. U. Krupp, H.J. Christ, *Nichtmetalle in Metallen '98*, Herausgeber D. Hirschfeld, GDMB Clausthal-Zellerfeld 1998, 89.
13. M.A.J. Somers, E.J. Mittemeijer, *Met. & Mat. Trans* **26A** (1995) 57.
14. M.A.J. Somers, E.J. Mittemeijer, *Nitrieren und Nitrocarburieren*, Berichtsband, Hrsg. E.J. Mittemeijer, J. Grosch, AWT Wiesbaden 1991.
15. H.J. Spies, F. Vogt, *Härterei-Techn. Mitteilungen* **52** (1997) 6.
16. H.J. Spies, P. Schaaf, F. Vogt, *Mat.-wiss. u. Werkstofftechn.* **29** (1998) 588.
17. H.J. Grabke, *Ber. Bunsenges. Physik. Chem.* **72** (1968) 533–541.
18. H.J. Grabke, *Ber. Bunsenges. Physik. Chem.* **72** (1968) 541–548.
19. H.J. Grabke, *Z. Physik. Chem. N.F.* **100** (1976) 185–200.
20. B. Mortimer, P. Grieveson, K.H. Jack, *Scand. J. Metallurgy* **1** (1972) 203.
21. H.H. Podgurski, R.A. Oriani, F.N. Davis, *Trans Met. Soc. AIME* **245** (1969) 1603.
22. K. Schwerdtfeger, P. Grieveson, E.T. Turkdogan, *Trans. Met. Soc. AIME* **245** (1969) 2461.
23. J. Robertson, *Corr. Sci.* **29** (1989) 1275.

- Alloy 10CrMo9 10 104, 105, 106,
 - 109–18, 146
 - coating process 109–12, 113, 114
 - metal dusting behaviour 112–18, 119, 120
- Alloy 600 16, 17, 92
 - metal dusting behaviour 163, 165, 168–70, 174
 - nitridation in ammonia-water vapour mixtures 290–1, 294
 - welded nickel-based alloys with different surface finishes 59, 60, 61, 62, 63–9, 70, 73, 74, 75
- Alloy 601 16–17, 92, 155–6
 - welded nickel-based alloys with different surface finishes 59, 60, 62, 64, 65, 69–71, 72, 73, 75
- Alloy 602 16, 17, 92
- Alloy 602CA 17
 - metal dusting behaviour 163, 165, 170, 171, 173, 174
 - welded nickel-based alloys with different surface finishes 59, 61, 62, 63, 64, 65, 71, 73, 74, 75
- Alloy 690 92
- Alloy 693 163, 165, 168, 174
- Alloy 800 2, 12, 13
 - diffusion coatings 104, 105, 142–6
 - coating process 142–3, 144, 145, 146
 - metal dusting behaviour 143–6, 147, 148, 149, 150, 151
- failure cases
 - direct reduction furnace 97, 100
 - heat exchanger for synthesis gas 20, 92–4, 95
 - nitridation in ammonia-water vapour mixtures 290, 292
 - welded nickel-based alloys with different surface finishes 59, 60, 61, 62, 63, 66, 73, 75
- Alloy H46M 163, 166–8, 173, 174
- Alloy P91 104, 105, 118–24, 146
 - coating process 118–19, 121
 - metal dusting behaviour 119–24, 125, 126
- Alloy X10CrAl18 104, 105, 124–32, 146
 - coating process 124–6, 128, 129
 - metal dusting behaviour 126–32, 133, 134
- Alloy X18CrN28 104, 105, 132–42, 146
 - coating process 132–6, 137
 - metal dusting behaviour 136–42
- alloying elements 92
 - corrosion products on high-temperature alloys 166
 - iron aluminium alloys 178–81, 182, 183–4, 185
 - role in metal dusting of high-alloy steels 12–14
- alumina (aluminium oxide) 14, 152
 - high-temperature alloys 168, 170, 173
 - iron aluminium alloys 175–6, 181–3
- aluminium 14, 17, 23
 - Alloy X10CrAl18 *see* Alloy X10CrAl18
 - Cr-44Fe-5Al 154, 157, 158, 159
 - diffusion coatings 103, 146, 152
 - Alloy 10CrMo9 10 109
 - Alloy 800 142–3, 147, 148
 - Alloy P91 118, 120, 122, 123

- Alloy X10CrAl18 125, 127, 128, 130, 131, 132
- Alloy X18CrN28 132–5, 138, 139, 141
- Si-Al *see* silicon-aluminium co-diffusion coating
- Si-Ti-Al *see* silicon-titanium-aluminium co-diffusion coating
- Ti-Al *see* titanium-aluminium co-diffusion coating
- two-step chromium-aluminium diffusion coating 106–7, 109–11, 114, 115, 119, 152
- diffusion in ferrite 232–3
- iron aluminium alloys 175–86
- iron-chromium-aluminium alloys 215, 219–23, 232–3, 234
- aluminium nitride 274–6
- ammonia plant heat exchanger 99, 101
- ammonia-water vapour mixtures 286–98
- amorphous carbon 29–34, 40, 41–3, 46, 47
- Arrhenius diagrams 8–10
- Auger electron spectroscopy (AES) 22, 77–8, 79
- austenite 7, 212
 - coking and metal wastage rates 8–10
- austenitic steels 91
 - mechanisms of metal dusting 214, 231, 233–4
 - nitridation in ammonia-water vapour mixtures 290, 292
- bends 263–4
- Boudouard reaction 3–4
- brittle failures 260, 261, 267–8
- brushed surface nickel-based alloys 61–2, 67, 69
- bulk graphite 203–4, 205, 206, 212
- carbides, internal *see* internal carbides
- carbon activity 2–3, 108
 - catalytic particles 237, 239–40, 242–6
 - carbon activity gradient 253–4
 - types of carbon and 227–8
- carbon diffusion 257
 - in cementite and Hägg carbide 81–3
 - diffusion control 6, 7
- carbon filaments *see* filaments, carbon
- carbon-iron system 84
- carbon-iron-oxygen phase diagram 241–6
- carbon monoxide
 - methanation 4
 - reduction 2–4
- carbon monoxide-hydrogen-water vapour mixtures
 - with high carbon monoxide content and coke formation during metal dusting of iron 199–213
 - iron aluminium alloys 175–86
 - iron layer formation 187–98
 - carbon monoxide content 188–9, 190–1, 193, 194, 195–6, 197
- carbon nanotubes 214, 217, 218, 226–7, 228, 229, 230, 234
- carburisation
 - and coke formation during metal dusting of iron in carbon monoxide-hydrogen-water vapour mixtures 200–6, 207, 208, 209
 - direct carburisation on steels with varying concentrations of chromium 44, 45
 - effect of hydrogen sulphide on carburisation kinetics 77–81, 82
 - joint mechanism of carburisation, metal dusting and oxidation in high-alloy steels 10–12
 - measurement 269
 - pyrolysis coils 261, 264–6
 - carburisation and thermal fatigue 264, 265
- catalytic metal particles 237–58
 - characterisation of 252–4
 - characterisation of initial surface states 248
 - experimental procedure 246–8
 - formation on pre-oxidised iron surfaces 254–7
 - formation on reduced iron surfaces 254, 255
 - kinetics of catalytic coke formation 248–54
 - thermodynamic calculations 241–6
- cementite 1, 25, 76, 256
 - carbon diffusion in 81–3
 - decomposition 84–6, 257
 - kinetics 196–7
 - formation of catalytic metal particles 225–7, 237–9, 257

- catalytic coke formation 251–2, 253
- iron aluminium alloys 178, 181, 184–5
- iron in carbon monoxide-hydrogen-water vapour gas
 - characterisation of coke 206–7, 209, 210
 - cementite/graphite interface 205–6, 209
 - high carbon monoxide content and cementite in iron-containing particles 211–12
- iron layer formation at cementite/graphite interface 187–98, 199
- iron-nickel alloys 55–8
- metal dusting mechanism of low-alloy steels 5–7, 76, 90
- metal dusting of iron 5–7, 49–50, 76, 90, 225–6, 228, 229
 - effect of hydrogen sulphide on 78, 79
- steels with varying concentrations of chromium 26, 29–30, 34, 35, 40
 - ferritic 26Cr-steel 219, 224, 225
 - mechanisms of metal dusting 44, 45–6, 47
- sulphur protection 19–20
- ceramic crucibles 163, 165–70, 171–3
- cerium (Ce) 13–14
- chlorine 97, 101
- chromia (chromium oxide) 87, 154, 175
 - evaporation 263
 - high-alloy steels 10–12, 23
 - high-temperature alloys 166, 170, 173
 - metal dusting resistance of high-chromium alloys 158–61
 - protective scale 20, 23, 91–2, 152
 - on Alloy 800 144, 149
 - silicon/chromium oxide layer 167–8
 - steels with varying concentrations of chromium 38–40, 44–5, 48
- chromium 17, 23
 - Alloy 10CrMo9 10 *see* Alloy 10CrMo9 10
 - Alloy X10CrAl18 *see* Alloy X10CrAl18
 - Alloy X18CrN28 *see* Alloy X18CrN28
 - chromium-denuded zone 265
 - diffusion coatings 103
 - Alloy 10CrMo9 10 109–11
 - chromium-aluminium two-step coating 106–7, 109–11, 114, 115, 119, 152
 - diffusion in ferrite 232–3
 - high-chromium alloys *see* high-chromium alloys
 - iron-chromium-aluminium alloys 215, 219–23, 232–3, 234
 - metal dusting of steels with varying concentrations of chromium 25–48
 - $1\frac{1}{4}\text{Cr}-\frac{1}{2}\text{Mo}$ and $5\text{Cr}-\frac{1}{2}\text{Mo}$ steels 26, 28–34, 35, 40–3
 - 9Cr–1Mo and 13Cr steels 26, 34–8, 43–6
 - 20Cr steel 26, 38–40, 43–6
 - accurate corrosion quantification 28
 - effect of temperature 28–34, 35, 40–1
 - experimental approach 26–7
 - mechanisms of metal dusting 41–6, 47
- nickel–chromium–nitrogen system 279–81
- nickel-chromium–titanium model alloys 273, 276–83
- porous 154, 157, 158–60
- chromium-nickel steels 1, 2
 - nitridation in ammonia-water vapour mixtures 290, 292
- chromium nitride 279–81, 288, 289, 291, 292, 294, 295, 296
- chromium–nitrogen–oxygen system 294–5
- chromium steels 1, 10
 - ferritic 9–18% Cr steels in ammonia-water vapour mixtures 288–90, 291
- morphologies and mechanisms of metal dusting on ferritic 26Cr-steel 215, 218–19, 220, 221, 223, 224, 225, 230–2, 234
- coke/coking 1, 2, 90
 - constituents of coke on iron aluminium alloys 177–8, 179, 180, 181, 183
 - formation on iron in carbon monoxide-hydrogen-water vapour mixture 189, 192, 194
 - characterisation of coke 206–7, 209, 210

- with high carbon monoxide content 199–213
 - iron carburisation and coke formation 200–6, 207, 208, 209
 - formation on welded nickel-base alloys 59–60, 63, 64, 65
 - inside radiant tubes 266, 267–8
 - kinetics of catalytic coke formation 248–54
 - kinetics of coking on iron and low-alloy steels 8–10
- columnar graphite 193, 195, 197
 - iron in carbon monoxide-hydrogen-water vapour with high carbon monoxide content 203, 204, 206, 211, 212
- commercial nickel-based alloys 273, 274–6
- compact graphite layer 203–4, 205, 206, 212
- continuous catalyst regeneration (CCR) units 87, 96–7, 98–9, 101
- cracking tubes 86
- cracks 288, 289, 290, 291, 292, 293, 294
- creep ductility exhaustion 266–7
- creep elongation (stretching) 261–2
- decoking 266–7
- diffusion 271–2
 - aluminium in ferrite 232–3
 - carbon diffusion 6, 7, 257
 - in cementite and Hägg carbide 81–3
 - chromium in ferrite 232–3
 - Fick's second law 271, 281
 - nitrogen diffusion coefficient 278–9, 280
- diffusion coatings 103–53
 - Alloy 10CrMo9 10 104, 105, 106, 109–18, 119, 120, 146
 - Alloy 800 104, 105, 142–6, 146, 147, 148, 149, 150, 151
 - Alloy P91 104, 105, 118–24, 125, 126, 146
 - Alloy X10CrAl18 104, 105, 124–32, 133, 134, 146
 - Alloy X18CrN28 104, 105, 132–42, 146
 - coatings 104–7
 - metal dusting tests 107
 - metallographic examination 108–9
 - substrates 104, 105
 - test atmospheres 107–8
- diffusion control 6, 7, 271–2
- dimension measurements 269
- direct carburisation 44, 45
- direct reduction furnace 97, 100, 101
- direct reduction plants 87
 - gas heaters 94–6, 101
- ductile failures 260, 264–7
- electropolishing 92
- erosion 263, 264
- etching 21–2, 108–9
 - high-temperature alloys 163, 166–7
- ethylene cracking, pyrolysis coils for 259–70
- eutectoid layer 225, 228, 229
- failures 90–102
 - brittle failures 260, 261, 267–8
 - direct reduction furnace 97, 100, 101
 - ductile failures 260, 264–7
 - gas heaters of a direct reduction plant 94–6, 101
 - heat exchanger of an ammonia plant 99, 101
 - heat exchanger for synthesis gas 20, 92–4, 95
 - platformer unit in a refinery 96–7, 98–9, 101
 - pyrolysis coils for ethylene cracking 259–70
- ferrites 7
 - coking and metal wastage rates 8–10
- fibres, graphite 204–5, 207, 211, 212
- Fick's second law 271, 281
- filaments, carbon 5, 6, 31, 32, 41, 46, 47
 - caused by catalytic metal particles 237–58
 - iron aluminium alloys 177, 179
 - iron in carbon monoxide-hydrogen-water vapour 189, 192, 193, 195, 196, 197
 - characterisation of coke 206–11
 - high carbon monoxide content 199, 201–3, 204, 205, 206, 212
- fine-grained microstructure 20–1, 91–2
- fittings 263–4
- fractures 203, 204, 212
- furnace inspections 268–9

- furnace trips 267–8
- gas heaters of a direct reduction plant 94–6, 101
- gas-metal reaction thermodynamics and kinetics 1–4, 5
- Gibbs energies 242
 - austenitic stainless steels 231, 234
 - cementite 84, 85
 - Hägg carbide 84, 85
 - metal dusting on ferritic chromium steels 230, 231
 - metal dusting process 1–2
- graphite 1, 76
 - bulk (compact) graphite 203–4, 205, 206, 212
 - columnar *see* columnar graphite
 - effect of hydrogen sulphide on graphite formation 77–81, 82
 - fibres 204–5, 207, 211, 212
 - formation from Hägg carbide 86
 - iron layer formation at cementite/graphite interface 187–98
 - islands 201–3, 204, 205, 207
 - lattice planes 5, 6, 46, 50, 51–3
 - mechanisms of metal dusting
 - iron and low-alloy steels 5–7, 90
 - nickel and nickel-based alloys 7, 90
 - metal dusting of pure iron 225–6, 228
 - metal dusting of steels with varying concentrations of chromium 29–34, 40, 41–3, 46, 47
 - morphologies of graphite on iron in carbon monoxide-hydrogen-water vapour mixtures 189, 192, 193, 195, 196, 197
 - high carbon monoxide content 201–5, 206, 211
 - particle clusters 189, 192, 193, 196, 197
- grinding 21–2, 91–2
 - and formation of filaments 211
 - nickel-based alloys 61, 66, 67, 75
- H46M 163, 166–8, 173, 174
- haematite 251, 256
 - reduction of haematite pellets 254, 255
- Hägg carbide 49, 78–9
 - carbon diffusion in 81–3
 - decomposition 84–6
 - thermodynamics of formation 83–4
- hardness of high-temperature alloys 164, 170–1, 172, 173
- heat-affected zone (HAZ) 59, 63, 66, 73
- heat exchangers
 - ammonia plant 99, 101
 - for synthesis gas 20, 92–4, 95
- helium-water vapour mixtures 286–90
- high-alloy steels 214–36
 - austenitic stainless steels 214, 231, 233–4
 - ferritic 26Cr-steel 215, 218–19, 220, 221, 223, 224, 225
 - metal dusting 230–2, 234
 - ferritic FeCrAl alloys 215, 219–23
 - metal dusting 232–3, 234
 - metal dusting 10–14
 - joint mechanism of carburisation, metal dusting and oxidation 10–12
 - role of alloying elements 12–14
 - protection against metal dusting 20, 23
- high-chromium alloys 154–61
 - Cr-5Fe-1Y₂O₃ 154, 157, 158, 160
 - Cr-44Fe-5Al 154, 157, 158, 159
 - Cr-50Ni 17, 154, 157, 158, 159, 160–1 as a metal dusting resistant coating 161
- high-temperature alloys 162–74
 - Alloy 600 163, 165, 168–70, 174
 - Alloy 602CA 163, 165, 170, 171, 173, 174
 - Alloy 693 163, 165, 168, 174
 - Alloy H46M 163, 166–8, 173, 174
 - nano-indentation tests 164, 170–1, 172, 173
- HK 40 steel 94–6, 101
- Hochman mechanism for metal dusting 25
- HVOF -TiAl spray coatings 107, 151–2
 - Alloy 800 143, 146–7, 148, 151
 - Alloy X10CrAl18 124–5, 127, 130, 131, 132, 134
- hydrocarbon cracking 86
 - failures in pyrolysis coils for ethylene cracking 259–70
- hydrogen
 - coke formation on iron in carbon dioxide-hydrogen-water vapour with high carbon monoxide content 199–213
 - iron aluminium alloys in carbon

- monoxide-hydrogen-water vapour mixtures 175–86
- iron layer formation in carbon monoxide-hydrogen-water vapour mixtures 187–98
- hydrogen sulphide 19–20, 76–89, 101
 - carbon diffusion in cementite and Hägg carbide 81–3
 - decomposition of cementite and Hägg carbide 84–6
 - effect on carburisation kinetics and graphite formation 77–81, 82
 - failure of gas heater in a reduction plant due to lack of 95, 101
 - iron sulphide formation 86
 - practical aspects of sulphur adsorption 86–7
 - thermodynamics of Hägg carbide formation 83–4
 - see also* sulphur
- internal carbides 1, 2, 91, 161, 265
 - austenitic stainless steels 233
 - catalytic particles 241–6, 253
 - pre-oxidised iron surfaces 254–5
 - reduced iron surfaces 254, 255
 - ferritic 26Cr-steel 219, 223, 224, 230–2
 - ferritic FeCrAl alloys 219–22, 223, 233
 - high-alloy steels 11, 12
 - kinetics of formation 12–13
 - steels with varying concentrations of chromium 37, 38, 39, 45, 47
 - see also* cementite; Hägg carbide; ϵ -phase carbide
- internal oxidation, Wagner's theory of 271–2
- iron 90
 - ammonia-water vapour mixtures 287, 288
 - coke formation in carbon monoxide-hydrogen-water vapour with high carbon monoxide content 199–213
 - effect of hydrogen sulphide on metal dusting 76–89
 - high-chromium alloys
 - Cr-5Fe-1Y₂O₃ 154, 157, 158, 160
 - Cr-44Fe-5Al 154, 157, 158, 159
 - iron-depleted zones in iron-nickel alloys 53–4, 55, 57–8
 - iron layer formation in carbon monoxide-hydrogen-water vapour mixtures 187–98
 - kinetics of metal wastage and coking on 8–10
 - mechanisms of metal dusting 4–7, 25, 175
 - metal dusting microprocesses 49–50
 - morphologies and mechanisms of metal dusting 215, 216, 217, 218, 225–30
 - carbon activity 227–8
 - carbon nanotube formation 226–7
 - schematic presentation of metal dusting steps 228–30
 - nickel-iron in corrosion products on high-temperature alloys 166
 - pre-oxidised *see* pre-oxidised iron
 - reduced *see* reduced iron surfaces
- iron aluminium alloys 175–86
- iron-carbon system 84
- iron-carbon-oxygen phase diagram 241–6
- iron-chromium-aluminium alloys 215, 219–23, 232–3, 234
- iron-containing particles 190, 193, 197, 199
 - carbon monoxide-hydrogen-water vapour with high carbon monoxide content 205–7, 210, 211–12
 - iron aluminium alloys 177–8, 180, 185
- iron layer formation 6, 7, 187–98, 199
 - influence of gas composition 188–94
 - at 600°C 190–4, 195, 196
 - at 700°C 188–90, 191, 192
- iron-nickel alloys 14, 15
 - microprocesses of metal dusting 49–58
- iron nitrides 287, 295, 296, 297
- iron-nitrogen-oxygen system 294–5
- iron oxide 91
 - carbon filaments caused by catalytic metal particles from 237–58
- iron sulphide 86
- islands, graphite 201–3, 204, 205, 207
- Kalina cycle 286, 293–5, 297
 - ϵ -phase carbide
 - ferritic FeCrAl alloys 219–22, 233

- iron aluminium alloys 176, 177, 178, 181, 184–5
- low-alloy steels
 - ammonia-water vapour mixtures 287–8, 289
 - kinetics of metal wastage and coking on 8–10
 - mechanisms of metal dusting on 4–7, 25, 90, 175
 - protection against metal dusting 19–20, 23
- magnetite 251, 256
 - formation of catalytic particles 255–6
- mass gain/loss
 - catalytic coke formation 248, 249, 251
 - high-chromium alloys 157
 - iron aluminium alloys 177, 178, 179, 182
 - iron in carbon monoxide-hydrogen-water vapour 200–1
 - nitridation of nickel-based alloys 273
 - protective behaviour of diffusion coatings
 - Alloy 10CrMo9 10 114, 116
 - Alloy 800 143, 148
 - Alloy P91 119–20, 123
 - Alloy X10CrAl18 126, 131
 - Alloy X18CrN28 136, 139
- mechanisms of metal dusting 4–7, 214
 - iron *see* iron
 - low-alloy steels 4–7, 25, 90, 175
 - nickel and nickel-based alloys 7, 90
 - steels with varying concentrations of chromium 26, 41–6, 47
 - type IV mechanism (carbon nanotubes) 214, 217, 218, 226–7, 228, 229, 230, 234
- metal dusting 1–24
 - current knowledge 90–2
 - definition 1
 - high-alloy steels 10–14
 - kinetics of metal wastage and coking on iron and low-alloy steels 8–10
 - mechanisms of *see* mechanisms of metal dusting
 - nickel-based alloys 14–17
 - protection against 17–23
 - thermodynamics and kinetics of gas-metal reactions 1–4
- metal wastage
 - action of sulphur 19–20
 - kinetics on iron and low-alloy steels 8–10, 90
 - surface treatments and oxide protection 21–2
 - welded nickel-based alloys 60, 65
- methanation of carbon monoxide 4
- methane, oxidation of 4
- mineral salts 99, 101
- model nickel-based alloys 273, 276–83
- molybdenum (Mo) 12–13
 - $1^{1/4}$ – $1^{1/2}$ Mo and 5Cr– $1^{1/2}$ Mo steels 26, 28–34, 35, 40–3
 - 9Cr–1Mo steels 26, 34–8, 43–6
 - Alloy 10CrMo9 10 *see* Alloy 10CrMo9 10
- mud cracking 264, 265
- multi-element co-diffusion coatings 104–6
 - see also* silicon-aluminium co-diffusion coating; silicon-titanium-aluminium co-diffusion coating; titanium-aluminium co-diffusion coating
- nano-indentation tests 164, 170–1, 172, 173
- nanotubes, carbon 214, 217, 218, 226–7, 228, 229, 230, 234
- newly developed coatings *see* diffusion coatings
- nickel 1, 90, 92, 265
 - mechanisms of metal dusting 7, 90
 - microprocesses of metal dusting 49–50
 - nickel-iron in corrosion products on high-temperature alloys 166
 - nitridation in ammonia-water vapour mixtures 290–1, 293
- nickel-based alloys 1, 23, 214
 - Cr-50Ni 17, 154, 157, 158, 159, 160–1
- iron-nickel alloys *see* iron-nickel alloys
 - mechanisms of metal dusting 7, 90
 - nitridation 271–85
 - in ammonia-water vapour mixtures 290–1, 294
 - commercial alloys 273, 274–6

- model alloys 273, 276–83
 - simulation 281–3
 - thermodynamic prediction of the
 - range of stability of phase 279–81
 - resistance to metal dusting 14–17, 92
 - welded *see* welded nickel-based alloys
- nickel–chromium–nitrogen system 279–81
- niobium 12–13
 - iron aluminium alloys 179–80, 182, 183–4, 185
- nitridation
 - in ammonia–water vapour mixtures 286–98
 - kinetics 295–7
 - of nickel-based alloys 271–85
 - radiant tubes 262–3
 - simulation 281–3
 - thermodynamics 293–5
- nitrogen
 - Alloy X18CrN28 *see* Alloy X18CrN28
 - chromium–nitrogen–oxygen system 294–5
 - diffusion coefficient for NiCrTi alloys 278–9, 280
 - iron–nitrogen–oxygen system 294–5
 - nickel–chromium–nitrogen system 279–81
 - solubility 272, 276–7
 - in NiCrTi alloys 277–9
 - nitrogen pressure 293–5
- oil refineries *see* refineries
- outlet parts 263–4
- overheating 262
- oversaturation with carbon 11
- oxidation
 - joint mechanism of carburisation, metal dusting and oxidation in high-alloy steels 10–12
 - of methane 4
 - Wagner's theory of internal oxidation 271–2
- oxide scales 91–2, 175–6, 264–5
 - Alloy 800 144–5, 149, 150
 - cracked and simulation of internal nitridation 281, 283
 - diffusion coatings 152
 - high-temperature alloys 165, 167–8, 169–70, 173
 - mechanisms leading to failure of 265
 - porous and nitridation in ammonia–water vapour mixtures 287, 288, 289, 290, 294, 295, 296, 297
 - protective 17, 20–2, 23, 91–2, 173, 240
 - rupture and steels with varying concentrations of chromium 44–5, 47–8
 - see also under individual oxides*
 - oxide shedding 263
 - oxygen
 - chromium–nitrogen–oxygen system 294–5
 - iron–carbon–oxygen phase diagram 241–6
 - iron–nitrogen–oxygen system 294–5
 - oxygen pressure 4, 294–5
 - parabolic rate constants
 - growth of cementite and Hägg carbide 81–3
 - nitridation rate constant 272, 275–6
 - parabolic rate law 271–2
 - particle clusters, graphite 189, 192, 193, 196, 197
 - penetration depth
 - internal carbide formation 12–13
 - internal nitridation 272, 275–6
 - ammonia–water vapour mixtures 296–7
 - simulation model 281, 283
 - perovskite *see* -phase carbide
 - phase 279–81
 - pickling 92
 - nickel-based alloys 59, 61, 69, 75
 - pitting 35, 42, 47, 91
 - Alloy 800 144, 149
 - gas heaters of a direct reduction plant 95, 96
 - high-temperature alloys 165, 167, 168, 169, 170, 171
 - nickel-based alloys 66–71, 72, 73–4
 - platformer unit in a refinery 96–7, 98–9, 101
 - PM 2000 154, 156–8
 - pore formation 291, 293

- pre-oxidised iron 240, 247–8, 249
 - coke formation on 248–52
 - formation of catalytic particles on 254–7
- protection against metal dusting 17–23
 - iron aluminium alloys 175–6, 181–5
 - oxide scale 17, 20–2, 23, 91–2, 173, 240
 - sulphur 17–20, 23, 86–7, 91
 - see also* diffusion coatings
- pyrolysis coils 259–70
 - damage mechanisms 260–4
 - bends and outlet parts 263–4
 - radiant tubes 260–3
 - metallurgical background of failure mechanisms 264–8
 - brittle fracture caused by furnace trips 267–8
 - carburisation and creep ductility exhaustion 264–7
 - process technological background 268–9
- quartz hangers, suspension from 163, 164–5, 173
- radiant tubes 259, 260
 - damage mechanisms 260–3
- Raman spectroscopy 41–2
- rate equation 3
- rate law 8
- reaction zones 165–6, 167, 168, 169, 170, 173
 - hardness 171, 172, 173
- reduced iron surfaces 247–8, 249
 - coke formation on 248, 250, 251
 - formation of catalytic particles on 254, 255
- refineries 86–7
 - failure of a platformer unit 96–7, 98–9, 101
- ripple effect 42, 43
- sandblasting 59, 61, 69
- secondary ion mass spectrometry (SIMS) 42, 43
- selective corrosion effect 57–8
- Sicromal 289, 291
- silicon 14, 17, 23
 - diffusion coatings 103, 150, 152
 - Alloy 10CrMo9 10 111, 112, 114–16, 120
 - Alloy 800 147, 148
 - Alloy X10CrAl18 125, 128, 130, 131
 - Alloy X18CrN28 135, 138, 139
 - see also* silicon-aluminium co-diffusion coating; silicon-titanium-aluminium co-diffusion coating
 - heat exchanger for synthesis gas 94, 95
 - resistance to carburisation 265
- silicon-aluminium co-diffusion coating 150–1
 - Alloy 10CrMo9 10 111, 113, 115, 116, 120
 - Alloy 800 143, 144–5, 148
 - Alloy P91 118, 120–1, 123, 125
 - Alloy X10CrAl18 126, 128–32, 133
 - Alloy X18CrN28 135–6, 137, 139, 141–2
- silicon/chromium oxide layer 167–8
- silicon dioxide 14
- silicon-titanium-aluminium co-diffusion coating 151
 - Alloy 800 143, 144–5, 146
 - Alloy P91 118, 123, 124, 126
- simulation of internal nitridation 281–3
- single element diffusion coatings 104
 - see also under* aluminium; chromium; silicon
- spallation 120, 125, 128
- spinel 22, 44–5, 91
 - high-alloy steels 10–12
 - steels with varying concentrations of chromium 35, 36, 44–5, 47
 - ferritic 26Cr-steel 219, 224, 225, 230–2
- steam 99
- steam reforming 162
- steels 90
 - chromium steels *see* chromium steels
 - high-alloy steels *see* high-alloy steels
 - low-alloy steels *see* low-alloy steels
 - metal dusting of steels with varying concentrations of chromium 25–48
- strapping (diameter measurements) 269
- stretching (creep elongation) 261–2
- sulphur

- adsorption 18–19, 76, 77, 78, 91
 - practical aspects 86–7
- failure cases and lack of 95, 97, 101
- inhibition of metal dusting 6–7, 91
- protection by 17–20, 23, 86–7, 91
 - see also* hydrogen sulphide
- surface treatments 91–2, 211
 - protection by oxide scale and 21–2
 - welded nickel-based alloys 59–75
 - see also under individual treatments*
- synthesis gas (syngas) 162
 - heat exchanger for 20, 92–4, 95
- tantalum (Ta) 179–80, 182, 183–4
- temperature
 - coke formation on iron in carbon
 - monoxide-hydrogen-water vapour with high carbon monoxide content 199–213
 - high-temperature alloys *see*
 - high-temperature alloys
 - influence of gas composition on iron
 - layer formation 188–94
 - 600°C 190–4, 195, 196
 - 700°C 188–90, 191, 192
 - iron oxide reduction by iron carbide 245–6
 - mechanisms of metal dusting on iron
 - and low-alloy steels 4–7
 - metal dusting of $1\frac{1}{4}\text{Cr}-\frac{1}{2}\text{Mo}$ and $5\text{Cr}-\frac{1}{2}\text{Mo}$ steels 28–34, 40–1
 - 650–850°F (regime I) 29–32
 - 850–1050°F (regime II) 29, 32–3
 - over 1050°F (regime III) 29, 33–4, 35
- ternary carbide *see* γ -phase carbide
- thermal fatigue and carburisation 264, 265
- ThermoCalc modelling
 - high-alloy steels 215, 219, 220, 223, 224, 225
 - iron aluminium alloys 184–5
- thermogravimetric analysis (TGA) 28
- thermo-wells 263
- titanium 13
 - diffusion coatings 103, 152
 - silicon-titanium-aluminium
 - co-diffusion coating *see*
 - silicon-titanium-aluminium co-diffusion coating
 - titanium-aluminium co-diffusion coating *see* titanium-aluminium co-diffusion co-diffusion coating
 - iron aluminium alloys 179, 180, 182, 183–4, 185
 - NiCrTi model alloys 273, 276–83
 - titanium-aluminium co-diffusion coating 151
 - Alloy 10CrMo9 10 111–12, 113
 - Alloy 800 143, 144–5, 147, 150
 - Alloy P91 118–19, 121–4, 126
 - HVOF γ -TiAl spray coating 107, 151–2
 - Alloy 800 143, 146–7, 148, 151
 - Alloy X10CrAl18 124–5, 127, 130, 131, 132, 134
 - titanium nitride 274–6, 279–81
 - simulation of internal nitridation 281–3
 - tungsten (W) 12–13
 - vanadium (V) 180, 182, 183–4, 185
 - Wagner's theory of internal oxidation 271–2
 - water vapour
 - coke formation on iron in carbon
 - monoxide-hydrogen-water vapour with high carbon monoxide content 199–213
 - iron aluminium alloys in carbon
 - monoxide-hydrogen-water vapour mixtures 175–86
 - iron layer formation in carbon
 - monoxide-hydrogen-water vapour mixtures 187–98
 - nitridation in ammonia-water vapour mixtures 286–98
 - welded nickel-based alloys 59–75
 - Alloy 600 59, 60, 61, 62, 63–9, 70, 73, 74, 75
 - Alloy 601 59, 60, 62, 64, 65, 69–71, 72, 73, 75
 - Alloy 602CA 59, 61, 62, 63, 64, 65, 71, 73, 74, 75
 - Alloy 800 59, 60, 61, 62, 63, 66, 73, 75
 - samples 61–2
 - wustite 251, 256
 - zirconium (Zr) 13